

MATER. TEHNOL.	LETNIK VOLUME	47	ŠTEV. NO.	5	STR. P.	541–681	LJUBLJANA SLOVENIJA	SEP.–OCT. 2013
-------------------	------------------	----	--------------	---	------------	---------	------------------------	-------------------

VSEBINA – CONTENTS

PREGLEDNI ČLANKI – REVIEW ARTICLES

Evaluation of ladle slag as a potential material for building and civil engineering

Ocena potenciala ponovne žlindre kot surovine za uporabo v gradbeništvu

V. Zalar Serjun, B. Mirtič, A. Mladenovič 543

IZVIRNI ZNANSTVENI ČLANKI – ORIGINAL SCIENTIFIC ARTICLES

Modelling of the lubricant-layer thickness on a mandrel during rolling seamless tubings

Modeliranje debeline plasti maziva na trnu pri valjanju brezšivnih cevi

D. Čurčija, I. Mamuzić 551

Alternative utilization of the core sand for a green-sand system

Alternativna uporaba peska za jedra v sistemu priprave livarskega peska

N. Špirutová, J. Beňo, V. Bednářová 557

Micro-abrasion wear testing of multilayer nanocomposite TiAlSiN/TiSiN/TiAlN hard coatings deposited on the AISI H11 steel

Mikroabrazijsko preizkušanje obrabe večplastne nanokompozitne trde prevleke TiAlSiN/TiSiN/TiAlN na jeklu AISI H11

H. Çalişkan, A. Erdoğan, P. Panjan, M. S. Gök, A. C. Karaoglanlı 563

Determination of the solidus and liquidus temperatures of the real-steel grades with dynamic thermal-analysis methods

Določanje solidusnih in likvidusnih temperatur realnih jekel z metodami dinamične analize

K. Gryc, B. Smetana, M. Žaludová, K. Michalek, P. Klus, M. Tkadlečková, L. Socha, J. Dobrovská, P. Machovčák, L. Válek, R. Pachlopnik, B. Chmiel 569

Synthesis of Au nanoparticles prepared with ultrasonic spray pyrolysis and hydrogen reduction

Sinteza Au-nanodelcev, pripravljenih z ultrazvočno razpršilno pirolizo in redukcijo z vodikom

S. Stopic, R. Rudolf, J. Bogovic, P. Majerič, M. Čolić, S. Tomić, M. Jenko, B. Friedrich 577

Effect of heat treatment on the microstructure and mechanical properties of piston alloys

Vpliv toplotne obdelave na mikrostrukturo in mehanske lastnosti zlitin za bate

S. Manasijević, S. Marković, Z. Aćimović - Pavlović, K. Raić, R. Radiša 585

Effect of the bonding time on the microstructure and mechanical properties of a transient-liquid-phase bonded IN718 using a Ni-Cr-B filler alloy

Vpliv časa spajanja na mikrostrukturo in mehanske lastnosti spoja s prehodno tekočo fazo pri spajanju IN718 z uporabo zlitine Ni-Cr-B za spajanje

M. Pouranvari, A. Ekrami, A. H. Kokabi 593

Electro-codeposited Cr-SiC composite coatings: effect of the pulse-current frequency on morphology and hardness

Kompozitna prevleka iz elektronanesenega Cr-SiC: vpliv frekvence pulzirajočega toka na morfologijo in trdoto

O. Sancakoğlu, M. Erol, B. Agaday, E. Çelik 601

Effect of sheet thickness on the anisotropy and thickness distribution for AA2024-T4

Vpliv debeline pločevine na anizotropijo in razporeditev debeline pri AA2024-T4

M. Dilmec, H. S. Halkaci, F. Ozturk, M. Turkoz 605

Effect of a Mo addition on the properties of high-Mn steel

Vpliv dodatka Mo na lastnosti visokovsebnostnega Mn-jekla

G. R. Razavi, M. S. Rizi, H. M. Zadeh 611

Influence of the matrix type on the temperature responsiveness of a poly-NiPAAm/chitosan microgel functionalized PES fabric

Vpliv vrste matrice na temperaturno odzivnost poli-NiPAAm/hitozan mikrogela na PES-tkanini

B. Tomšič, P. Križman Lavrič, B. Simončič, D. Jocić 615

Application of infinite-element calculations for consolidating a railway foundation of blowing sand reclamation

Uporaba izračuna z neskončnimi elementi za utrditev podlage železniške proge z drobnim peskom

K. Xie, Y. Pan, H. Ni, H. Wang 621

Experimental study on the role of the vibration damping and energy absorption of flexible function layers Eksperimentalna študija vloge dušenja vibracij in absorpcije energije v gibljivih funkcionalnih plasteh B. Yang, J. Huang, S. Mo, P. Wu.	627
Abrasive wear behaviour of SiCp-reinforced 2011 Al-alloy composites Vedenje kompozita Al zlitine 2011, ojačane z delci SiCp, pri abraziji M. Uzku	635
Influence of weld-process parameters on the material characterization of the friction-stir-welded joints of the AA6061-T₆ aluminium alloy Vpliv parametrov postopka varjenja na lastnosti tornovrtilno varjenih spojev aluminijeve zlitine AA6061-T ₆ H. Patil, S. Soman.	639
Compositional and microstructural analyses of Fe-Pd nanostructured thin films Elementna in mikrostrukturna analiza nanostrukturnih tankih plasti Fe-Pd Z. Samardžija, K. Žužek Rožman, D. Pečko, S. Kobe	647
Evaluation of the effects of surface treatments on different dental ceramic structures Ocena vpliva obdelave površine različnih dentalnih keramik E. Ertürk, M. Dalkiz, E. Özyilmaz, H. Z. Akbaş, H. A. Çetinkara, H. Aykul.	653

STROKOVNI ČLANKI – PROFESSIONAL ARTICLES

Microtomography in building materials Mikrotomografija gradbenih materialov A. Česen, L. Korat, A. Mauko, A. Legat	661
Influence of thermomechanical processing on the cold deformability of low-carbon steel Vpliv termomehanske predelave na hladno preoblikovalnost maloogljičnega jekla B. Baručija, M. Oruč, O. Beganović, M. Rimac, S. Muhamedagić	665
Oxidation of the Al₂O₃-TiB₂ composites produced with the reduction-combustion synthesis technique Oksidacija kompozita Al ₂ O ₃ -TiB ₂ , izdelanega s tehniko redukcijske zgorevne sinteze N. Ergin, Y. Garip, O. Ozdemir	669
Optimisation of the slag mode in the ladle during the steel processing of secondary metallurgy Optimiranje žlindre v ponovci pri izdelavi jekla po postopku sekundarne metalurgije L. Socha, J. Bažan, K. Gryc, J. Morávka, P. Styrnal, V. Pilka, Z. Piegza.	673
Study on the mechanical and radiation-shielding properties of borided AISI 304 stainless steels Študija mehanskih lastnosti in zaščitnih sposobnosti nerjavnega jekla AISI 304 pred sevanjem A. Çalik, S. Karakaş, N. Uçar, İ. Akkurt, A. Turhan.	679

EVALUATION OF LADLE SLAG AS A POTENTIAL MATERIAL FOR BUILDING AND CIVIL ENGINEERING

OCENA POTENCIALA PONOVCNE ŽLINDRE KOT SUROVINE ZA UPORABO V GRADBENIŠTVU

Vesna Zalar Serjun¹, Breda Mirtič¹, Ana Mladenović²

¹University of Ljubljana, Faculty of Natural Sciences and Engineering, Department of Geology, Aškerčeva c. 12, 1000 Ljubljana, Slovenia

²Slovenian National Building and Civil Engineering Institute, Dimičeva 12, 1000 Ljubljana, Slovenia
vesna.zalar@geo.ntf.uni-lj.si

Prejem rokopisa – received: 2013-02-22; sprejem za objavo – accepted for publication: 2013-03-20

An important step in secondary metallurgy of stainless steel is ladle metallurgy. Ladle slag is a by-product of ladle refining, typically specific for each steelmaking plant. Industrial secondary materials can be used for different applications, including construction and civil engineering. The use of industrial by-products requires the knowledge of the characteristics of the materials. Using metallurgical by-products that fulfil the relevant requirements can save natural resources, as well as helping to avoid impairment of the landscape through their excavation and, thus, minimizing the adverse landfilling of such materials. This paper provides an overview of possible uses of ladle slag (the slag from a ladle furnace and vacuum-oxygen-decarburization processes). As a preliminary research, ladle slag has been investigated using SEM/EDS. The commonly known hydraulic minerals, such as tricalcium aluminate, mayenite, tricalcium silicate and dicalcium silicate, were detected in this analysis. Since a large proportion of the mineral phases of ladle slag exhibit hydraulic properties, ladle slag could also have a potential use in the bonded composites in construction.

Keywords: ladle (ladle furnace, vacuum oxygen decarburization) slag, reuse, recycling, building sector, civil engineering

Ponovna tehnologija je pomemben proces sekundarne metalurgije pri proizvodnji nerjavnih jekel. Stranski produkt rafinacije jekla v ponovci je ponovčna žlindra, ki je bolj ali manj specifična za posamezno jeklarno. Industrijski stranski produkti se lahko uporabijo v različnih panogah, vključno z gradbenim sektorjem. Ključni pogoj za uporabo tehnoloških odpadkov je poznanje njihovih lastnosti. Ponovna uporaba stranskih produktov iz proizvodnje jekla z ustreznimi lastnostmi je pomemben element zmanjševanja obremenjenosti okolja, saj se s tem ohranjajo neobnovljivi naravni mineralni viri, ki se pridobivajo iz naravnih kopov ter hkrati razbremenjujejo deponije. V članku je podan pregled mogoče uporabe ponovčne žlindre (žlindre iz ponovčne peči in žlindre iz procesa vakuumskega razogljčenja (VOD)). Preliminarna raziskava ponovčne žlindre je bila izvedena s SEM/EDS. Določene so bile mineralne faze, ki izkazujejo hidravličnost, kot so trikalcijev aluminat, mayenit, trikalcijev silikat ter dikalcijev silikat. Ker ima velik del mineralnih faz v preiskovani ponovčni žlindri hidravlične lastnosti, je žlindra zato dodatno potencialno zanimiva za vezne kompozite v gradbeništvu.

Ključne besede: ponovčna (ponovčna peč, proces vakuumskega razogljčenja) žlindra, ponovna uporaba, recikliranje, gradbeni sektor, nizke gradnje

1 INTRODUCTION

In 2010, the EU steelmaking industries generated about 21.8 million tonnes of different types of slag.¹ About 13 % of this amount was generated as secondary metallurgical slag¹, arising from various secondary-metallurgy processes. One of the secondary processes in the production of high-alloyed steel is known as ladle refining or ladle metallurgy. Ladle refining consists, generally, of a ladle furnace (LF) and vacuum oxygen decarburization (VOD).² The slag resulting from this process is called ladle slag (LS) and is also known as basic, refining, reducing, or falling slag, and also as white slag.^{1,3-9}

Land disposal restrictions are becoming increasingly stringent (due to the environmental harm, the use of valuable landfill space, resources and costs). The current EU policy encourages and promotes the reuse and recycling of waste. The EU Waste Framework Directive (2008/98/ES)¹⁰ earmarks land disposal as the least acceptable alternative. Implementation of this concept

means that a material originating as waste can either be characterized as waste, or declared as a by-product.

In many EU states slag has already been declared as a by-product, a non-waste material, or a product.^{1,11} Different types of slag have different capabilities for recycling and reuse; ladle slag has the lowest such capability.⁶ Due to its fine grain size and adverse properties with regard to leaching (the presence of harmful elements such as Cr), ladle slag has a low potential for recycling.¹²⁻¹⁵ For this reason about 80 % of it is currently landfilled, taking into account the whole of the EU.¹¹

The recycling of industrial by-products has two important goals: a reduction in the amount of waste material and the minimization of the exploitation of natural resources. In order to minimize consumption in a production process, it is necessary for every country to exploit, to the maximum, every available industrial by-product.^{16,17} In the case of the concrete industry, an industrial by-product of fine gradation can be used as a filler or as a fine aggregate. Of course, there is a higher benefit, when it can be used as a binding agent, replacing

a percentage of the cement.¹⁷ Following this concept, an extensive research is in progress in order to create new opportunities for the reuse of LS.

Environmental challenges have become a key issue for the steelmaking industry, too. In recent years, methods for the recycling of slags have been improved, as the recycling approach is not only an opportunity but also a necessity for the survival of steel production,^{7,18} since, among other factors, it is not possible to return slag, or at least not all of it, into the primary steelmaking process. The ideal sector for the consumption of the excess slag is the building industry. In the construction sector two synergetic effects are achievable: large amounts of material can be consumed and, at the same time, in the case of bonded composites (e.g., concrete) the harmful elements such as Cr can be permanently immobilized through the solidification/stabilization (S/S) technology.^{14,15} An additional benefit lies in the fact that LS has (latent) hydraulic components and may be considered as a cementitious material. This attribute can be positive in the binder mixtures used in bonded composites.^{3,5,19–25} Steelmaking slags could be either low-cost materials in the applications where low demands are expected, or products with a high-added value that could improve the properties of the final products.¹⁷ At present, LS is still an innovative option, being less extensively used in the building sector than the other steelmaking slags.⁶ The applications of LS are diverse and can be extended to any realm where their use is allowed, advised or even recommended by imagination, common sense and/or good practice.⁸

Each type of steel slag has its own characteristics. Not all steel heats are similar, nor do all steel manufacturers share the same working practices, giving rise to variations in the composition of LS at different steel works, and even at the same works, due to different heats.⁸ Furthermore, local conditions, batch syntheses and scrap-metal variations also affect the composition of the produced slag.^{17,21,22} The exposure of slag stockpiles to the atmosphere must also be taken into account.⁸ Another aspect is the physical or practical procedure of dealing with the logistics of slag. Slags from different processes are sometimes mixed together in the liquid phase before being transported to the slag yard. Last but not least is the question of the handling of the slag at the slag yard. Water is often used to lower the temperature of the slag and/or to avoid the formation of dust.^{2,23} This means that every different LS must be considered as a case study.

Accurate knowledge about the chemical, mineralogical and morphological properties of steel slags is essential because their cementitious and mechanical characteristics, which play a key role in their possible reuse, are closely linked to these properties.^{19,20}

This paper provides a literature review of possible fields of application, as well as reviewing the chemical and mineralogical composition of ladle slag (LF and

VOD slag). The most common mineral composition of the LS studied by means of SEM/EDS is presented. The purpose of this work is to explore the potential (latent) hydraulic properties of LS.

2 FIELDS OF APPLICATION

The number of publications per year on the topic of ladle slag (**Figure 1**) indicates that LS has been intensely studied in recent years, from the point of view of both fundamental and applied research.

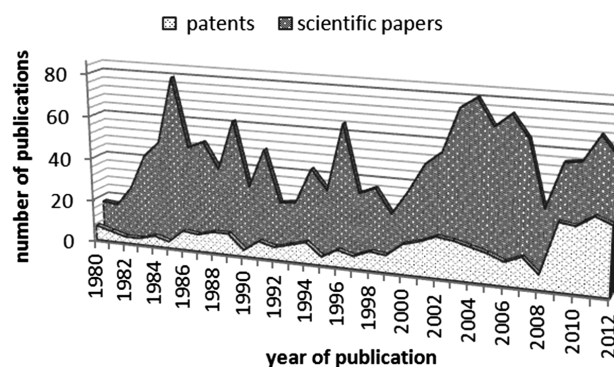


Figure 1: The number of publications per year and the publishing trend regarding the dynamics of the development in the field of ladle slag is presented using a value-added processing method. The relationship between the number of published articles and the number of patents indicates the proportion of fundamental and applied research. The data were collected from the databases: Engineering Village (Compendex) and Espacenet, for the period of 1980–2012.

Slika 1: Za sledenje usmeritev raziskav, tako temeljnih kot aplikativnih, ter za spremljanje dinamike razvoja s področja ponovne žindre, smo uporabili metodo procesiranja z dodano vrednostjo. Razmerje med članki in patenti nakazuje delež temeljnih in aplikativnih raziskav. Podatki so bili zbrani iz podatkovne baze Engineering Village ter Espacenet za obdobje 1980–2012.

According to Manso et al.²⁶ two main groups can be identified among the possibilities for the reuse of LS: those involving its industrial transformation with a significant economic cost (mainly recycling in the electric-arc furnace), and those aimed at finding an inexpensive use of LS as a construction material.

2.1 Reuse of LS

The steel-making industry can recycle LS by using it as a flux in the steel production instead of lime.^{27–30} This kind of reuse of LS is performed by injecting it into EAF, representing the so-called "hot recycling" of LS.^{7,29} Such recycling of LS can sometimes achieve interesting and advantageous results: besides decreasing the amount of dumped material and the cost of fluxes (by about 35 %), it can improve the foaminess of the EAF slag, and also increase electricity-consumption efficiency. Additionally, there is no more need for lime or this need is reduced to at least 70 %.^{16,18,29} The LS recycling using the BOF process and a LD-converter has also been shown to be a viable procedure.³⁰

2.2 Recycling of LS

In the second group, research has been performed into the use of LS in cement and the concrete industry, as well as in the slag-soil mixes in civil engineering.

2.2.1 Bricks, granulated slag: Some researchers have investigated the technology for recycling different steelmaking wastes including LS, by mixing them in furnaces to produce bricks.³¹ The manufacturing technology of granulated slag particles was introduced by Kojimori et al.³²

2.2.2 Cement: LS can be used as a raw material for the production of Portland cement (PC).^{3,8,26} LS has also been assessed as a raw material for the production of sulphoaluminate belite cement.³³

2.2.3 Mortar, concrete: There has also been research into the use of LS in other sectors of the construction industry, e.g., in the manufacturing of mortars with lime¹⁷, the application of LS as a screed material in internal premises, where there is a need for a quick repair of floors or walls²³, and for other similar products that can facilitate masonry work.^{3,26} LS could also be used, in the case of manufacturing hydraulic concrete without additives, for individual precast urban elements that have no load-bearing capacity, e.g., barriers, bannisters and curbs for pedestrianized areas⁶, and for developing concrete blocks that are used in aquiculture.³⁴ Studies on the hydraulic concrete matrixes made using LS, other residual materials and PC have also been performed.⁵ Shi and Hu⁹ investigated the hydraulic reactivity of LS fines in combination with siliceous materials (silica flour, FA, PC and hydrated lime). LS can also be used as a filler in the self-compacting concrete exposed to elevated temperatures.³⁵ The behaviour

of masonry mortars containing LS in aggressive environments was evaluated by Manso et al.⁴ A study of the physical, mechanical and durability properties of the concrete made of a combination of EAFS and LS without chemical activators against the external agents has been carried out by Polanco et al.⁶ LS can also be used as a supplementary cementing material in briquettes, containing iron and steelmaking residues³³, and as an alternative binder for low-strength applications.^{3,21,26} In order to increase the final strength of the cement composites containing LS, researchers have suggested several ways of processing LS such as re-melting²¹, the use of activators^{17,36} and screening or grinding.^{21,36}

2.2.4 Civil engineering: Surveys have proposed alternative uses of LS in landfill applications²¹, as a landfill covering structure^{24,37,38}, as filtering beds²⁶ and in other civil-engineering works, e.g., for the stabilization of soft clayey soils³⁹ in the construction of embankments.⁴⁰ Studies of the paving mixes for rural roads with low levels of traffic²⁶ have also been performed. Branca et al.⁴¹ investigated an addition of glazing powder to LS for the potential use of slag in the road construction. A survey performed by Bignozzi et al.⁴² revealed that LS is also suitable for geopolymerization.

2.2.5 Environmental engineering: There is also a further line of study, which proposes the use of LS in environmental engineering, for the fixation of ions in water depuration^{3,8}, as a neutralizing agent in bioleaching with the aim of replacing commercial-grade slaked lime in agriculture⁴³ and for acidity corrections of soil.^{3,6,8} A study published by Sun et al.⁴⁴ indicated a possibility of using LS as an industrial waste material for treating another kind of industrial waste in order to produce a high-value-added product.

Table 1: Chemical compositions of ladle slags according to the literature in mass fractions, w/%

Tabela 1: Kemijska sestava ponovčne žlindre iz literature v masnih deležih, w/%

CONSTITUENTS			w/%			REFERENCE		
A	B	C	A	B	C	A	B	C
CaO	CaO _{free}	CaO _{total}	26–66	max 20	max 51	3, 4, 6, 8, 9, 17, 20–23, 25, 26, 33, 35, 36, 40, 42, 45–52	4, 6, 8, 25, 45, 49, 52	26, 41
SiO ₂	Si _{reactive}	Al ₂ O ₃	2–50	max 20.4	1–37	3, 4, 6, 8, 9, 17, 20, 23, 25, 26, 33, 35, 36, 40–42, 45–52	25	3, 4, 6, 8, 9, 17, 20–23, 25, 26, 33, 35, 36, 40–42, 45–52
MgO	MgO _{free}	MgO _{total}	1–13.2	max 10	max 11	3, 4, 6, 8, 9, 17, 20–23, 25, 26, 33, 35, 36, 40, 41, 42, 45–52	4, 6, 8, 45	26
Fe ₂ O ₃	FeO	Fe _{total}	max 4	max 15	max 4	4, 8, 9, 21, 22, 36, 41, 42, 47, 52	17, 20, 25, 33, 35, 46, 47, 50–52	23, 49, 52
Mn ₂ O ₃	MnO	TiO ₂	max 8.1	max 10	max 2.5	33	8, 9, 20, 22, 23, 36, 42, 46, 47, 50–52	8, 9, 20, 22, 23, 33, 36, 41, 42, 50
Cr ₂ O ₃	Cr	F	max 8.1	max 0.27	max 4.4	8, 19, 35, 49, 50	46, 47	9, 36, 48
SO ₃	S	Na ₂ O	max 2.4	max 1.5	max 0.9	6, 9, 20, 22, 25, 26, 41, 42, 45	8, 36, 40, 46, 51, 52	8, 17, 20–22, 25, 33, 35, 41
P ₂ O ₅	P	Ka ₂ O	max 0.87	max 0.4	max 0.42	8, 20, 35, 42, 52	46	8, 17, 20–22, 33, 35, 40–42

Works concerning LS that characterize the product as a material, have also been published.⁵

3 CHEMICAL COMPOSITION

The chemical compositions of ladle slags (ladle-furnace slag (LFS) and vacuum-oxygen-decarburization slag (VOD)) from various studies^{3,4,6,8,9,17,20,21–23,25,26,33,35,36,40–42,45–52} are presented in **Table 1**. The contents of the major oxides (SiO₂, Al₂O₃, CaO and MgO) point to a diverse composition of LS.

Typically, LS is mostly constituted of calcium oxides, as well as silica, aluminium and magnesium oxides. Beside the major components, minor amounts of Fe, Ti, Mn, Cr and S oxides, as well as P, Na and K oxides can be present in LS.

Some other elements, such as Mo, Zn, Ni, Cu, P_{20,46,47}, soluble salts (Cl⁻, NO₃⁻, SO₄⁻)^{17,21,42}, CO₂²², C^{8,40}, ZrO₂^{9,36} and V₂O₃⁴² have also been detected, all in the quantities of less than 2 %.

The bulk chemical composition for the oxide chemical analysis was, in most cases, determined with X-ray fluorescence (XRF).^{8,20,22,40,42,47} Chemical composition was also determined by means of the inductively coupled plasma-atomic emission spectroscopy (ICP-AES).^{47,50} Papayianni and Anastasiou¹⁷ presented the chemical composition of the acid-soluble phases. Tossavainen et al.⁴⁷ used titration for an analysis of Fe and FeO and infrared adsorption spectroscopy (IR) for carbon and sulphur. Carbon and sulphur contents were also determined with a combustion analysis.^{25,33,40} Hot ethylene glycol titration for determining CaO was performed by Monkman et al.²² Manso et al.²⁶ performed specific determinations of free lime on LS according to the ASTM C 114 standard. For a quantification of the CO₂ content, an automated carbon analyzer with an induction furnace and an infrared detector has been used.²² Papayianni and Anastasiou²¹ determined the reactive silica according to the European standard EN 197-1: 2000. Chloride and sulfate contents and loss on ignition (LOI) were determined following the specific procedures for the cement chemical analysis reported in the EU standard EN 196-2 by Bignozzi et al.⁴² Böhmer et al.⁴⁹ noted the Czech standard CSN 72 2041-1.

3.1 Basicity

Chemical composition is one of the important parameters determining the hydraulic properties of slags. It is generally agreed that the reactivity and the cementitious properties of steel slag increase with its basicity/alkalinity.^{46,53} Different authors have defined basicity in slightly different ways. According to Shi⁴⁶ the mass concentration $V = w(\text{CaO})/w(\text{SiO}_2)$ is often used to characterize basicity. Posch et al.⁵⁴, Setien et al.⁸ and Manso et al.⁵, however, interpret basicity as $B = w(\text{CaO})/w(\text{Al}_2\text{O}_3 + \text{SiO}_2)$, whereas Wang et al.⁵⁵ and Xu and Li⁵⁶ have stated that the commonly used parameter for evaluating the activity of steel slag is alkalinity: $M = w(\text{CaO})/[w(\text{SiO}_2) + w(\text{P}_2\text{O}_5)]$. Yet another way of defining basicity is $M_b = w(\text{CaO} + \text{MgO})/w(\text{SiO}_2 + \text{Al}_2\text{O}_3)$.^{47, 57}

The mineralogical composition of steel slag changes with its chemical composition. The relationship between basicity, the main mineral phases and the reactivity of steel slag are summarized in **Table 2**.^{46,55,58,59}

Basicity, defined as B , also defines the main mineral phases in each basicity range ($B < 0.8$ spinels; $B > 0.8$ periclase, (Mg, Fe)-wüstite; $0.6 < B < 2.1$: C₃A, C₁₂A₇, C₂S, C₃S; $B > 2.1$ CaO_{free} occurs).⁵⁴ If the M alkalinity of the slag is higher than 1.8, it should be considered as a cementitious material.^{59,60} If M_b exceeds the value of 1, the slag is basic, which, according to Tossavainen et al.⁴⁷, results in a mainly crystalline slag. The value of M_b for LS is 1.5.⁴⁷ LS has the V basicity of around 2³⁶, the B basicity in the range of 1.6–2.4 according to Setien et al.⁸, and in the range of 0.45–2.1 according to Posch et al.⁵¹

4 MINERAL COMPOSITION

As the chemical composition of LS is variable, the mineral composition of LS also varies. LS is most frequently characterised by high calcium and alumina contents, which suggests a likely formation of calcium aluminates as the main phases, along with dicalcium silicate and some other phases.^{23,33}

According to the available literature reviews of the mineral compositions of ladle slags^{5,6,8,20–23,26,33,36,38,40,42,47,51}, the most common minerals are C₂S (β and γ), maye-

Table 2: Relationship between basicity, the main mineral phases and the reactivity of steel slag

Tabela 2: Razmerje med bazičnostjo, glavnimi mineralnimi fazami in reaktivnostjo jeklarske žlindre

Reactivity	Types of steel slag	Basicity [Reference]			Main mineral phases
		$V = w(\text{CaO})/w(\text{SiO}_2)$ 46, 58, 59	$M = w(\text{CaO})/w(\text{SiO}_2 + \text{P}_2\text{O}_5)$ 46, 58, 59	M_b 55	
LOW	olivine	0.9–1.5	0.9–1.4	< 1.8	olivine, RO phase, merwinite
	merwinite	1.5–2.7	1.4–1.6		RO phase, merwinite, C ₂ S
MEDIUM	dicalcium silicate		1.6–2.4	1.8–2.5	C ₂ S, RO phase
HIGH	tricalcium silicate	>2.7	>2.4	> 2.5	C ₃ S, C ₂ S, C ₄ AF, C ₂ F, RO phase

*The following abbreviated formulae are used in the text: C= CaO; A= Al₂O₃; S= SiO₂; F= Fe₂O₃; M= MgO; H= H₂O

Table 3: Mineral compositions of ladle slags according to the literature**Tabela 3:** Mineralna sestava ponovne žlindre

	PHASE		METHOD	REFERENCE
BEFORE WEATHERING	most common	calcium silicates (C_2S , CS , C_3S), calcium aluminates ($C_{12}A_7$, C_3A , CA), periclase, portlandite	XRD, DTA/TGA, FTIR, SEM/EDS	5, 6, 8, 20–23, 26, 33, 36, 38, 40, 42, 47, 51
	common	calcium magnesium silicates (C_3MS_2 , CMS_2 , C_2MS_2), RO and R_3O_4 phase, fluorite, calcite, jasmundite, spinel		5, 6, 8, 20–23, 26, 33, 36, 38, 40, 51
	minor	C_2AS , dolomite, $C_{20}A_{13}MS_3$, brucite, CaO , C_2F , amorphous phase, C_3AH_6 , garnet, anhydrite, uvarovite, oldhamite, quartz, iron magnesium (calcium) silicate, calcium fluoroaluminate, iron, Al metallic, $C_{54}MAS_{16}$		5, 8, 20–23, 26, 33, 36, 38, 40, 42, 47, 51
AFTER WEATHERING	primary	calcium silicates (C_2S), calcium magnesium silicates, calcium aluminates ($C_{12}A_7$, C_3A), spinel, jasmundite, fluorite, iron oxides, portlandite, periclase	XRD, DTA/TGA, FTIR, ISOTHERMAL CALORIMETRY	6, 8
	secondary	CAH phases (CAH_{10} , $C_2AH_{7.5}$, C_2AH_8 , C_4AH_{19} , C_3AH_6 , C_4AH_{13}), AH_3 , C_2ASH_8 , amakinite, portlandite, periclase, vaterite, calcite, spurrite		6, 8, 22, 23, 33

nite, tricalcium aluminate, portlandite and periclase (Table 3).

In order to investigate the self-cementing capacity of LFS, a slag paste was produced by mixing water with LFS, and the compressive strength of the hardened paste was measured. The SEM/EDX, DTA/TG analyses and X-ray diffraction analysis were used to determine the latent hydraulic character of LS.²¹ The results showed the presence of ettringite and the C-S-H compounds in small amounts and a decrease in the content of portlandite.²¹

A quantification of the LS mineral compounds was calculated directly from the chemical-composition data and X-ray diffraction data^{8,26}, and also determined by means of the semi-quantitative SEM-EDS analyses⁵⁰ and the Rietveld analysis.³³ The amorphous-phase content was determined separately, using pure quartz as an internal standard.³³ Free lime was determined by deducting the amount of $Ca(OH)_2$ determined with the DTA-TG analysis from the amount of CaO_f determined by using the relevant European standard EN 451-1.²¹ DTA-TG was also applied for the quantifications of CaO , $Ca(OH)_2$, $CaCO_3$, MgO and $Mg(OH)_2$.^{22,23,41} Monkman et al.²² applied a TGA analysis for the quantifications both before and after the accelerated carbonation.

5 VOLUME STABILITY

The presence of C_2S as a mineral phase in the slag microstructure drives the disintegration of slag into a very fine powder.⁶¹ Free C_2S can be present in LS in different phases, such as α , $\alpha'H'$, α' , β and γ . C_2S undergoes several polymorphic transformations up until the cooling process. During the cooling down of slag, α - C_2S undergoes a polymorphic solid-phase transition to β type larnite, at a temperature of about 630 °C. At the temperatures within the range of 450–500 °C larnite is partially or fully converted into the low-temperature stable form of γ C_2S .^{8,12,31,41,61} The high internal stress of LS, caused

by the conversion of the β into the γ polymorph, arising from a different crystal structure and density, results in the shattering of the matrix, accompanied by a 10–12 % volume increase. This phenomenon is responsible for the initial cracking of the LS monolithic mass and the following disintegration/self-pulverising process during the further cooling. This is the reason why LSs are also known by the name of "self-dusting" or "falling" slags.^{8,20,46,57,61}

It should be emphasized that this disintegration occurs during the cooling, making it clearly distinct from the swelling of the slag after the cooling due to lime and/or periclase, which is further discussed below.

The hydration and carbonization reactions of lime and periclase, present in LS, are, in fact, also liable to expansion. The oxides can cause long-term volume instability of the slag. Free lime, or periclase, present in the slag microstructure after the cooling, tends to react with water and CO_2 in a humid environment. The volume of the hydrates and carbonates is almost double the volume of the oxides, so that a 100 % increase in the volume can occur. Both of these ageing reactions cause a volume expansion or 'swelling', which can lead to severe valorisation issues for the reuse of this slag.^{8,31,61} The fact that lime hydrates quickly suggests that the majority of the free lime in LS will hydrate within a few days if it has access to water. The residual free lime and/or free periclase can be embedded in small pockets or inside the pits in the slag particles. Delayed volume instability (weeks to months) will occur if hydration takes place. In comparison with lime, periclase hydrates at a much slower rate.^{4,5} The spontaneous hydration of periclase requires several years.⁵ However, the vast majority of the slags generated in modern steelmaking plants have a low periclase content. If the fluxing agent used is dolomite, the periclase content in the slag increases, so that a long-term volumetric expansion is possible.^{20,46,61} Potential spontaneous changes at a later stage, such as the

hydration of calcium aluminates, do not, however, produce any further changes in the morphology (grain size) of LFS.⁸

The potential treatments of the slags containing lime and/or periclase and C_2S can be divided into two main groups: firstly, a group where the aim is to prevent the expansive transformation of the mineral, and secondly, a group where there is an outright avoidance of the presence of the mineral in the first place.

The usual way to ensure the long-term volume stability of slag particles is weathering in outdoor conditions for an extended period of time (over 6 months).⁶¹ Tossavainen et al.⁴⁷ confirmed that LS can become stable after a performance of rapid cooling, due to the formation of glass. The use of LS in ternary systems with siliceous materials and cement, as well as mixing LS with an inert material, is one of the proposed methods of avoiding the expansion phenomena.^{9,21} The carbonation treatment reduces the amounts of portlandite and extractable CaO in slag in an energy-efficient manner.²² However, action can also be taken to actually prevent the presence of lime/periclase in slag.⁶¹

Inhibiting the β - to γ -polymorph transformation of C_2S is an option that stabilizes the high-temperature C_2S polymorphs at an ambient temperature. This is carried out by depressing the required migrations of the Ca^{2+} ions and the rotations of SiO_4^{4-} tetrahedrons, using either physical or chemical methods. Physical stabilization methods for free C_2S particles include limiting the grain size, rapid cooling and constraining the particles in a matrix.^{12,23,47,62} Chemical-stabilization techniques are based on an incorporation of doping elements in the

crystal structure.^{12,62} Alternatively, slag disintegration can be averted by an outright avoidance of the presence of C_2S by modifying the slag composition.⁶³

6 PRELIMINARY/CASE STUDY

6.1 Material and methods

The analysis carried out in this study was preliminary and was based on the samples of slowly cooled (air atmosphere), wetted and aged LS. The investigated ladle slag consisted of a mixture of slags from two different ladle refining operations; the majority of the slag was the ladle-furnace slag, whereas a smaller part was the slag from the vacuum-oxygen-decarburization process. The LS used in this work was supplied by an Italian steel manufacturer, ABS.

The identification and characterization of the mineral phases and the microstructure of the samples were conducted by means of a scanning electron microscope using back-scattering electrons. The JEOL 5600 LV microscope model of was used, with a spectrometer for the chemical composition using energy dispersive spectroscopy (EDS). The excitation voltage was 20 kV and the pressure was between 10 Pa and 20 Pa.

6.2 Results and discussion

The most common mineral phases observed in the investigated LS (**Figure 2**) were C_3A , C_2S , C_3S , the melilite group (gehlenite (C_2AS)-åkermanite (C_2MS_2)), FeO (wüstite), C_4AF (brownmillerite), $C_{12}A_7$ (mayenite)

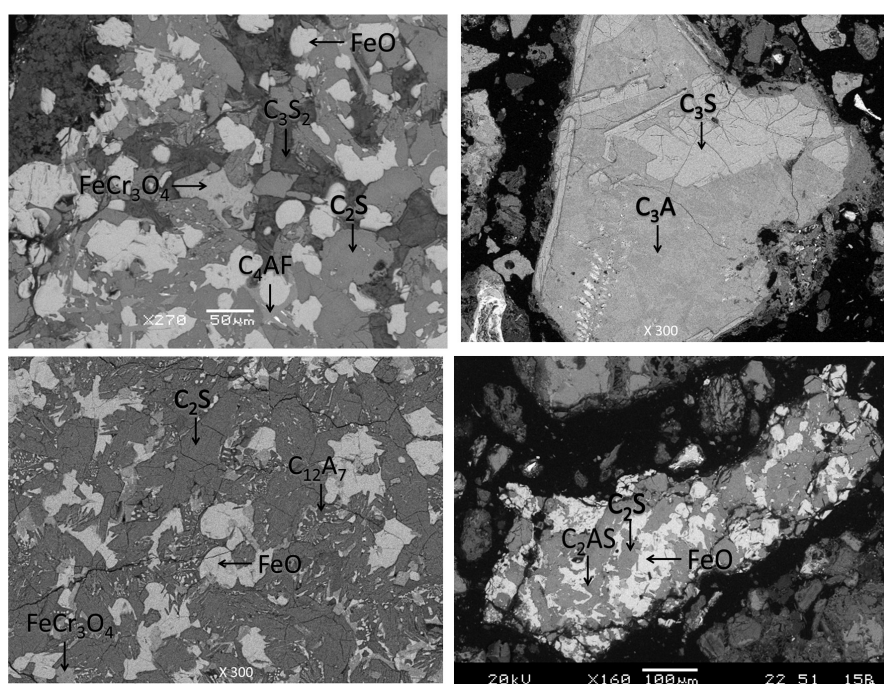


Figure 2: SEM/EDS analysis of the investigated LS

Slika 2: SEM/EDS analiza preiskovane ponovčne žindre

and C_3S_2 (rankinite). Calcite, periclase and chromium spinel ($FeCr_3O_4$) were also observed.

Solid solutions of gehlenite and åkermanite are considered to be weakly hydraulic.²³ The presence of C_3S , C_2S and C_4AF endorses the cementitious properties of the steelmaking slags.⁵⁹ The presence of C_3A , $C_{12}A_7$, C_2S and C_3S implies that LS may serve as a binder supplement, or at least make a contribution to a short-term strength development. The fact that calcium aluminates react instantaneously with water implies that it is important to reconsider the method of slag handling, especially in terms of avoiding any exposure to weathering.³³ The spinel phase and iron oxide 2+, wüstite, do not exhibit hydraulic properties.⁸ As regards periclase, hydration and carbonation processes are expected in the presence of air moisture. The expansive hydration reaction from lime to calcite is obviously completed.

7 CONCLUDING REMARKS

According to the descriptions given in the literature, LS can develop cementitious hydraulic properties, so that it could have several benefits for the construction and civil-engineering applications.

A detailed analysis of LS from its ABS properties in terms of chemical, mineralogical and physical characterization should be performed to define its (latent) hydraulic properties. From the results of the performed SEM/EDS analysis it can be concluded that the investigated LS has a potential as a supplementary cementing material, but consideration should also be given to the quantity of the hydraulic mineral phases, as well as to the potential hydration and carbonation reactions of the expansive components.

8 REFERENCES

- ¹ The European slag association: Position Paper on the Status of Ferrous Slag complying with the Waste Framework Directive (Articles 5/6) and the REACH Regulation [online]. 2012, [cited 2012-11-27]. Available at: <http://goo.gl/3XEnB>
- ² R. Remus, M. A. Aguado-Monsonet, S. Roudier, L. Delgado Sancho, Best Available Techniques (BAT) Reference Document for Iron and Steel Production [online]. 2013, [cited 2013-01-16]. Available at: <http://goo.gl/EVZon>
- ³ Á. Rodríguez, J. M. Manso, Á. Aragón, J. J. González, Resources, conservation and recycling, 53 (2009), 645–651
- ⁴ J. M. Manso, Á. Rodríguez, Á. Aragón, J. J. González, Construction and Building Materials, (2011), 3508–3519
- ⁵ J. M. Manso, D. Hernández, M. M. Losáñez, J. J. González, ACI Materials Journal, 108 (2011), 673–681
- ⁶ J. A. Polanco, J. M. Manso, J. Setién, J. J. González, ACI Materials Journal, 108 (2011), 196–203
- ⁷ O. Bonetti, C. Mapelli, M. Guzzon, Recycling of ladle slag in the EAF: improvement of the foaming behaviour and increase of the environmental impact [online]. [cited 2012-11-16]. Available at: <http://goo.gl/SRdGZ>
- ⁸ J. Setién, D. Hernández, J. J. González, Construction and Building Materials, 23 (2009), 1788–1794
- ⁹ C. Shi, S. Hu, Cement and Concrete Research, 33 (2003), 1851–1856
- ¹⁰ EU Waste Framework Directive (2008/98/ES) [online]. 2008, [cited 2013-02-14]. Available at: <http://goo.gl/YSYSi>
- ¹¹ Technical University of Crete: PREWARC- Strategic Plan for the Prevention of Regional Water Resources contamination from Mining and Metallurgical Industries in Western Balkan Countries [online]. 2008, [cited 2012-09-18]. Available at: <http://goo.gl/tm8vq>
- ¹² D. Durinck, P. T. Jones, B. Blanpain, P. Wollants, Journal of American ceramic society, 91 (2008), 3342–3348
- ¹³ S. Fiore, M. C. Zanetti, B. Ruffino, American journal of applied sciences, 1 (2008), 512–518
- ¹⁴ B. Batchelor, Waste Management, 26 (2006), 689–698
- ¹⁵ Q. Y. Chen, M. Tyrer, C. D. Hills, X. M. Yang, P. Carey, Waste management, 29 (2009), 390–403
- ¹⁶ M. Guzzon, C. Mapelli, V. Sahajwalla, N. Saha-Chaudhury, F. Memoli, M. Pustorino, The behaviour of the secondary metallurgy slag into the EAF. How to create a good foamy slag with the appropriate basicity using a mix of lime and recycled ladle slag as EAF slag former [online]. 2011, [cited 2012-11-14]. Available at: <http://goo.gl/SurH5>
- ¹⁷ I. Papayianni, E. Anastasiou, Optimization of ladle furnace slag for use as a supplementary cementing material, In Measuring, Monitoring and Modeling Concrete Properties, Edited by M. S. Konsta-Gdoutos, Springer, Netherlands 2006, 411–417
- ¹⁸ P. L. Cavallotti, C. Mapelli, F. Memoli, M. Pustorino, La metallurgia Italiana, 99 (2007), 41–48
- ¹⁹ M. P. Luxán, R. Sotolongo, F. Dorrego, E. Herrero, Cement and concrete research, 30 (2000), 517–519
- ²⁰ I. Z. Yildirim, M. Prezzi, Chemical, Mineralogical, and Morphological Properties of Steel Slag. Advances in Civil Engineering [online]. 2011, 10pp [cited 2012-11-14]. Available at: <http://goo.gl/43LUQ>
- ²¹ I. Papayianni, E. Anastasiou, Cement and concrete composites, 34 (2012), 400–407
- ²² S. Monkman, Y. Shao, C. Shi, Journal of materials in civil engineering, 21 (2009), 657–665
- ²³ D. Adolfsson, E. Engström, R. Robinson, B. Björkman, Steel research international, 82 (2011), 398–403
- ²⁴ I. Herrmann, L. Andreas, S. Diener, L. Lind, Waste and management research, 28 (2010), 1114–1121
- ²⁵ I. Papayianni, E. Anastasiou, Construction and building materials, 24 (2010), 1412–1417
- ²⁶ J. M. Manso, M. Losáñez, J. A. Polanco, J. J. González, Journal of materials in civil engineering, 17 (2005), 513–518
- ²⁷ R. Dippenaar, Industrial uses of slag—The use and re-use of iron and steelmaking slags, VII International Conference on Molten Slags Fluxes and Salts [online]. 2004, 57–70 [cited 2012-08-26]. Available at: <http://goo.gl/1vsyg>
- ²⁸ T. S. Lee, I. S. Choi, W. Y. Song, Stahl und Eisen, 123 (2003), 113–117
- ²⁹ F. Memoli, M. Guzzon, Metallurgical plant and technology international, 3 (2006), 42–49
- ³⁰ A. Dahlin, Influence of Ladle-slag Additions on BOF-Process Parameters, Licentiate Thesis, Stockholm, 2011, 40
- ³¹ M. Shinkai, M. Tsuno, N. Ogawa, Denki Seiko (Electric Furnace Steel), 68 (1997), 295–299
- ³² M. Kojimori, K. Nemoto, T. Fukuokaya, S. Uchida, H. Matumoto, T. Mori, Denki Seiko (Electric Furnace Steel), 74 (2003), 55–59
- ³³ D. Adolfsson, R. Robinson, E. Engström, B. Björkman, Cement and concrete research, 41 (2011), 865–871
- ³⁴ H. Sasamoto, A. Tsubone, Y. Kamiya, K. Sano, Tetsu to Hagane, 89 (2003), 416–465
- ³⁵ N. Anagnostopoulos, K. K. Sideris, A. Georgiadis, Materials and structures, 42 (2009), 1393–1405
- ³⁶ C. Shi, Cement and concrete research, 32 (2002), 459–462
- ³⁷ S. Diener, L. Andreas, I. Herrmann, H. Ecke, A. Lagerkvist, Waste management, 30 (2010), 132–139

- ³⁸ S. Diener, L. Andreas, I. Herrmann, A. Lagerkvist, Mineral transformations in steel slag used as landfill cover liner material, Proc. of the Eleventh International Waste Management and Landfill Symposium, Sardinia, 2007, 9
- ³⁹ A. Kanagawa, T. Kuwayama, Denki Seiko (Electric Furnace Steel), 68 (1997), 261–267
- ⁴⁰ J. M. Montenegro, M. Celemín-Matachana, J. Cañizal, J. Setién-Marquín, Journal of Materials in Civil Engineering, 25 (2013) 8, 972–979
- ⁴¹ T. A. Branca, V. Colla, R. Valentini, Ironmaking and Steelmaking, 36 (2009), 597–602
- ⁴² M. C. Bignozzi, L. Barbieri, I. Lancelotti, Advances in Science and Technology, 69 (2010), 11–122
- ⁴³ S. C. Gahan, M. L. Cunha, A. Sandström, Hydrometallurgy, 95 (2009), 190–197
- ⁴⁴ D. D. Sun, J. H. Tay, H. K. Cheong, D. L. Leung, G. Quian, Journal of hazardous materials, 87 (2001), 213–23
- ⁴⁵ J. M. Manso, D. Hernández, J. M. Losáñez, J. A. González, ACI materials journal, 108 (2011), 673–681
- ⁴⁶ C. Shi, Journal of Materials in Civil Engineering, 16 (2004), 230–236
- ⁴⁷ M. Tossavainen, F. Engström, Q. Yang, N. Menad, M. Lidstrom, M. Larsson, B. Bjorkman, Waste Management, 27 (2007), 1335–1344
- ⁴⁸ Y. Yu, N. Wang, China's Refractories, 15 (2006), 25–28
- ⁴⁹ S. Böhmer, M. Gertraud, N. Christian, P. Milla, S. Elisabeth, T. Maria, W. Birgit, W. Brigitte, Aggregates case study, final report [online]. 2008, 282 pp [cited 2012-5-11]. Available at: <http://goo.gl/EwGPq>
- ⁵⁰ M. Guo, S. Parada, P. T. Jones, E. Boydens, J. Van Dyck, B. Blanpain, P. Wollants, Journal of the European ceramic society, 29 (2009), 1053–1060
- ⁵¹ W. Posch, H. Presslinger, H. Hiebler, Ironmaking & steelmaking, 29 (2002), 308–315
- ⁵² Ľ. Mihok, P. Demeter, D. Baricová, K. Seilerová, Metalurgija, 45 (2006), 163–168
- ⁵³ I. A. Altun, I. Yilmaz, Cement and concrete research, 32 (2002), 1247–1249
- ⁵⁴ W. Posch, H. Preblinger, M. Mayr, K. Klepp, H. Hiebler, Sulphur bonding in solidified ladle slags, Proc. of the VII International Conference on Molten Slags Fluxes and Salts, The South African Institute of Mining and Metallurgy, 2004, 249–254
- ⁵⁵ Q. Wang, P. Y. Yan, S. Han, Science China Technological Sciences, 54 (2011), 388–394
- ⁵⁶ D. Xu, H. Li, Journal of Wuhan University of Technology-Materials Science Edition, 24 (2009), 411–417
- ⁵⁷ F. Engström, D. Adolfsson, Q. Yang, C. Samuelsson, B. Björkman, Steel Research International, 81 (2010), 362–371
- ⁵⁸ C. Shi, J. Quian, Resources, Conservation and Recycling, 29 (2000), 195–207
- ⁵⁹ H. Alanyali, M. Çöl, M. Yilmaz, S. Kargöz, International journal of applied ceramics technology, 6 (2009), 736–748
- ⁶⁰ W. Xuequan, Z. Hong, H. Xinkai, L. Husen, Cement and Concrete Research, 29 (1999), 1103–1106
- ⁶¹ D. Durinck, P. T. Jones, S. Arnout, B. Blanpain, Stainless steel slag valorisation: on volume stability and disintegration, Proc. of the first international slag valorisation symposium, Leuven, 2009, 81–92
- ⁶² Y. Pontikes, L. Kriskova, X. Wang, D. Geysen, S. Arnout, E. Nagels, Ö. Cizer, T. Van Gerven, J. Elsen, M. Guo, P. T. Jones, B. Blanpain, Additions of industrial residues for hot stage engineering of stainless steel slags, Proc. of the second international slag valorisation symposium, Leuven, 2011, 313–326
- ⁶³ D. Durinck, S. Arnout, G. Mertens, E. Boydens, P. T. Jones, J. Elsen, B. Blanpain, P. Wollants, Journal of the American ceramic society, 91 (2008), 548–554

MODELLING OF THE LUBRICANT-LAYER THICKNESS ON A MANDREL DURING ROLLING SEAMLESS TUBINGS

MODELIRANJE DEBELINE PLASTI MAZIVA NA TRNU PRI VALJANJU BREŽŠIVNIH CEVI

Dušan Čurčija, Ilija Mamuzić

Croatian Metallurgical Society, Berislavićeva 6, Zagreb, Croatia
ilija.mamuzic@public.carnet.hr

Prejem rokopisa – received: 2012-07-03; sprejem za objavo – accepted for publication: 2013-02-26

AutoCAD-a 3D modelling and the programs of Mathematica, MATLAB and MathCAD Professional were used to calculate the approximate solutions of the Reynolds differential equations for lubrication. Excel Software and Monte-Carlo solutions are compared. The results indicate a fast decrease in the lubricant-layer thickness in the stands for the continuous rolling of tubes. At the start of the rolling, the conditions for stable hydrodynamic lubrication are fulfilled for the tube-diameter-reduction processes. Theoretical calculations indicate that, on the finishing stands, "lubricant pickling" may occur on the mandrel. An approximate calculation is performed for the rolling point M and verified with the numerical Monte-Carlo method.

Keywords: Reynolds equation, AutoCad camera viewing, lubricant, continuous rolling line, seamless tubes

Za izračun približnih rešitev Reynoldsovih diferencialnih enačb za mazanje so bili uporabljeni modeliranje AutoCAD-a 3D in programi Mathematica, MATLAB in MathCAD Professional. Primerjane so rešitve, dobljene s programom Excel in z numerično metodo Monte-Carlo. Rezultati kažejo hitro zmanjšanje debeline plasti maziva na ogrođjih za kontinuirno valjanje cevi. Na začetku valjanja, pri postopku zmanjševanja premera cevi, so izpolnjeni pogoji za stabilno hidrodinamsko mazanje. Teoretični izračuni kažejo, da lahko pri končnih ogrođjih na trnu pride do odsotnosti mazanja. Izvršen je približen izračun pri točki valjanja M, ki je bil preverjen z numerično metodo Monte-Carlo.

Ključne besede: Reynoldsova enačba, opazovanje z AutoCad-kamero, mazivo, kontinuirna valjarniška linija, brezšivne cevi

1 INTRODUCTION

Tube rolling with round calibres¹ is a variant of longitudinal rolling with a formation of a deformation zone and in **Figure 1** the rolls and a mandrel are shown. The tubes rolling on a long floating mandrel use rolling lines with 7 to 9 working stands. Before inserting the rolling stock between the rolls, a cylindrical mandrel is

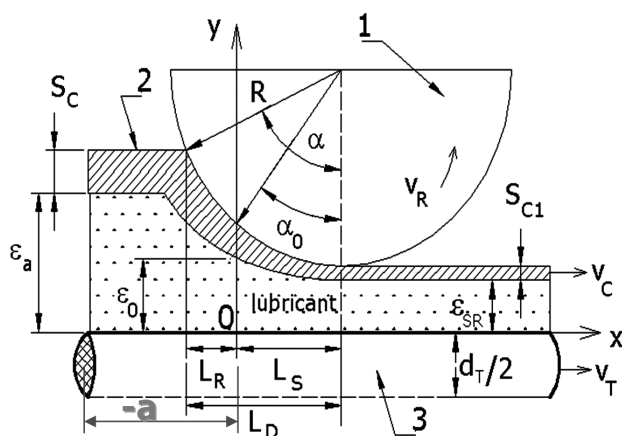


Figure 1: Scheme of rolling seamless tubes on a continuous rolling line

Slika 1: Shema valjanja brezšivnih cevi na kontinuirni valjarniški progi

put in, which then moves in the deformation zone jointly with the rolled tube. At the exit from the rolls, the mandrel speed is lower than that in the front tube part. The characteristic of the rolling is that the speeds of the tube and rolls are equal in the deformation zone only in two points of the roll groove. In recent years continuous rolling processes with a deformation of tubes with a stable, long, cylindrical cone mandrel or step-shaped mandrel were developed. The characteristic of this rolling is that there are two subzones of the reduction of the tube diameter and of the tube wall thickness, as shown in **Figure 1**. On the exterior contact of the tube and the rolls^{2,3} without a lubricant addition, friction occurs according to Kulon-Amonton laws, while in the tube interior, because of the lubricant presence, Newton's laws of fluid friction govern. The extent of the tangential stresses in the lubricant layer^{4,5} is calculated from equation (1):

$$\tau_x = \frac{\mu(v_c - v_T)}{\varepsilon(x)} - \frac{1}{2} \varepsilon(x) \frac{\partial p}{\partial x} \quad (1)$$

The change in the pressure in the lubricant layer⁴⁻⁷ is calculated from equation (2) and the volume of the lubricant used on the tube perimeter^{6,7} from equation (3):

$$\frac{dp}{dx} = \frac{6\mu(v_c + v_T)}{\varepsilon^2(x)} - \frac{12\mu Q}{\varepsilon^3(x)} \quad (2)$$

$$Q(x) = \int_0^{\varepsilon(x)} u dy = \frac{1}{12\mu} \frac{dp}{dx} \varepsilon^3(x) + \frac{(v_c + v_T)}{2} \varepsilon(x) \quad (3)$$

The geometry of the lubricant contact⁸⁻¹⁰ is calculated from equation (4) and the lubricant wedge length from equation (5):

$$\varepsilon(x) = \varepsilon_0 + R_0 \left[\cos \alpha_0 - \sqrt{1 - \left(\sin \alpha_0 - \frac{x}{R_0} \right)^2} \right] \quad (4)$$

$$a = R_0 \left[\sqrt{1 - \left(\cos \alpha_0 - \frac{\varepsilon_a}{R_0} + \frac{\varepsilon_0}{R_0} \right)^2} - \sin \alpha_0 \right] \quad (5)$$

$$\varepsilon(x) = \varepsilon_0 - \alpha_0 x + \frac{x^2}{2R_0} - \frac{\alpha_0 x^2}{2R_0^2} + \frac{x^4}{8R_0^3} \quad (6)$$

Relation (6) is an evolution¹¹⁻¹³ of equation (4) in a Maclaurin series. The lubricant characteristic for the theoretical investigation and the process geometry used are quoted from the references^{8,11} and are shown below.

The scheme of the tube-wall deformation geometry is shown in **Figure 2**. The cone shape of the tube is representative of the continuous rolling-line outset.

2 DISCUSSION, SOLUTIONS AND GRAPHIC INTERPRETATION

The equations for the approximate analytical solutions are listed in **Table 1**. The solution for the Ψ range is achieved using the gripping angle α from references^{11,14}, being the known solution of Grudev, Mazur and Kolmogorov¹⁴.

The solutions for the Ω range, M point and $\Phi\Sigma$ are derived in this work.

Figure 3 represents a comprehensive understanding of the solutions from **Table 1**. The M point is shown in a set of relations $\{\varepsilon_a^{1/3}/\Delta\varepsilon_0/\varepsilon_a\}$. For series 1, $\Delta\varepsilon_0$ is the difference from the pilot $\varepsilon_0^{1/3}$, i.e., the lubricant-layer thickness for every gripping α angle, minus the lubricant layer thickness for the pilot at 0.1 rad. Similarly, series 2

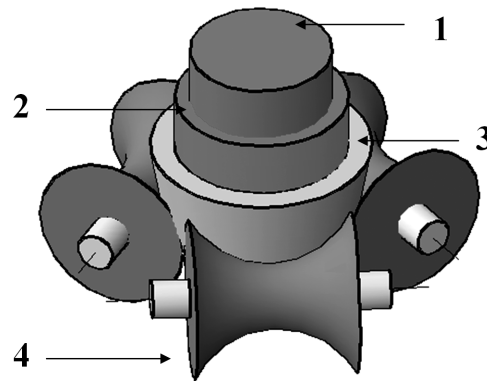


Figure 2: Stand with three rolls used in the analysis of tribomechanical systems: 1- mandrel, 2- lubricant, 3- tube, 4- roll

Slika 2: Ogradje s tremi valji, uporabljeno pri analizi tribomehanskih sistemov: 1- trn, 2- mazivo, 3- cev, 4- valj

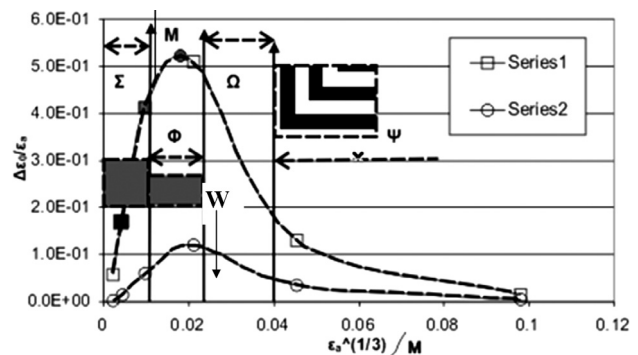


Figure 3: Distribution of the areas along the rolling line according to the solutions from **Table 1**

Slika 3: Porazdelitev področij po dolžini valjarniške proge skladno z rešitvami v tabeli 1

is calculated for $\varepsilon_0^1 - \varepsilon_0^*/\varepsilon_a$ and pilot ε_0^1 , with ε_0^* as the variable thickness of the lubricant layer.

Figure 4 shows a model of the lubricant layer on the mandrel calculated using the numerical Monte-Carlo method. At the entry (I) the lubricant is in surplus, while, at the exit of the continuous rolling line (II), the lubricant layer on the mandrel is picked because of the absence of fresh lubricant.

Table 1: Approximate solutions of equation (2)

Tabela 1: Približne rešitve enačbe (2)

Zone of Fig. 3	Approximate analytical solution
Ψ	$\varepsilon_0^* = 0.7726\varepsilon_0^1$ $\varepsilon_0^* = 0.5R_0(\alpha^*)^2$ $\alpha^* = \sqrt[3]{\frac{8}{15R_0A}}$ $\varepsilon_a \gg \varepsilon_0$
Ω	$\alpha^* = 2 \cdot \sqrt[3]{\frac{\varepsilon_a \sqrt{2R_0\varepsilon_a}}{10R_0^2 + 15R_0^2A\varepsilon_a \sqrt{2R_0\varepsilon_a}}}$ $\varepsilon_0^* = \frac{R_0(\alpha^*)^2}{2}$
M point	$\alpha_0^* = \left(\frac{2}{5}\right)^2 \frac{1}{A\varepsilon_{aMAX}}$ $\varepsilon_0^* = \frac{R_0(\alpha_0^*)^2}{2}$ $\varepsilon_{aMAX} = 0.28674 \cdot \sqrt[3]{\frac{R_0}{A^2}}$
$\Phi\Sigma$	$\varepsilon_0^1 = \varepsilon_a \left(1 - \frac{0.57348\varepsilon_a}{\varepsilon_{aMAX}}\right)$ $\varepsilon_{aMAX} = 0.28674 \cdot \sqrt[3]{\frac{R_0}{A^2}}$ $\varepsilon_a \rightarrow \varepsilon_0$

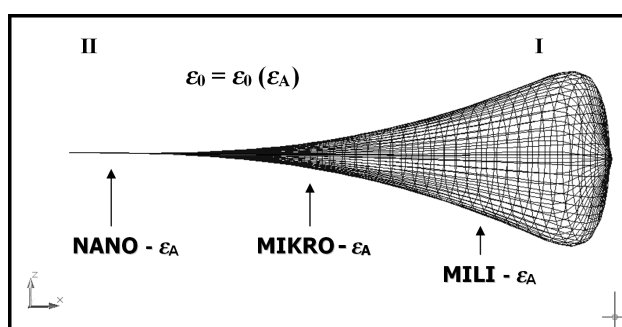


Figure 4: AutoCAD-modelled lubricant layer on the mandrel along the rolling line

Slika 4: AutoCAD modelirana plast maziva na trnu po dolžini valjarniške proge

In Figure 5 approximate analytical solutions and numerical calculations are compared. Series 1 relates to the Φ area; series 2 relates to the Σ area, the marker of square M is the solution for the M point from Table 1; series 3 is the Monte-Carlo solution and numbers 1, 2, 3 and 4 indicate the positions of the AutoCAD viewing

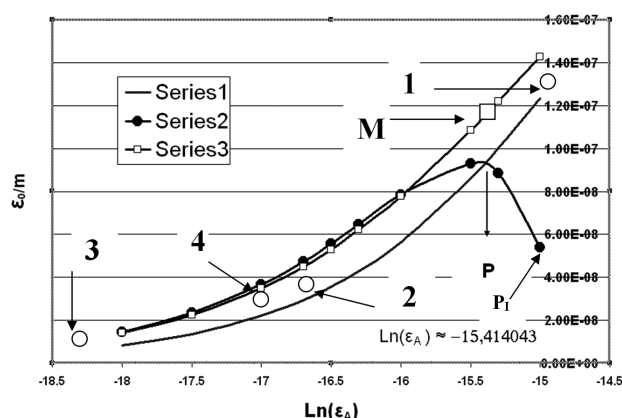


Figure 5: Comparison of the approximate analytical solutions from Table 1 and numerical Monte-Carlo solutions for the area between the approximate center of the rolling line and the exit stands

Slika 5: Primerjava približnih analitičnih rešitev iz tabele 1 in numeričnih rešitev Monte-Carlo za področje od približno sredine valjarniške proge do končnih ogradij

Table 2: 3D cameras for Figure 6, viewing left to W on Figure 5

Tabela 2: 3D-kamere za sliko 6, pogled levo od W na slici 5

Figure	Marking	Remark
Common markings		
Fig. 6 Fig. 7	Mark 1	Ω - area in Figure 3 and Table 1
	Mark 2	Σ - area in Figure 3 and Table 1
	Mark 3	Numerical Monte-Carlo method
	Mark 4	Point M in Figure 3, mark M in Figure 5, point M in Table 1
	$\text{Ln}(\varepsilon_A)$, $\text{Ln}(\varepsilon_0)$	Abscissa and ordinate in 2D, for the AutoCAD command Revsurf
Specific markings		
Figure	Marking	Remark
Fig. 6	Markers 1, 4	"Hat" obtained with the rotation of the arc P-P ₁ in Figure 5
Fig. 7	P	Drawing of pyramid for point P in Figure 3 (cross-section of Ω and Σ)

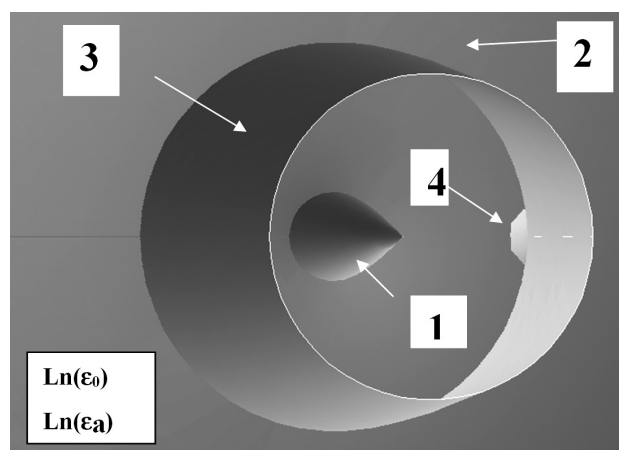


Figure 6: Viewing position 1 from Figure 5. The camera is covering the area between the center and the exit of the rolling line.

Slika 6: Pogled s pozicije 1 na slici 5. Kamera obsega področje od sredine do konca valjarniške proge.

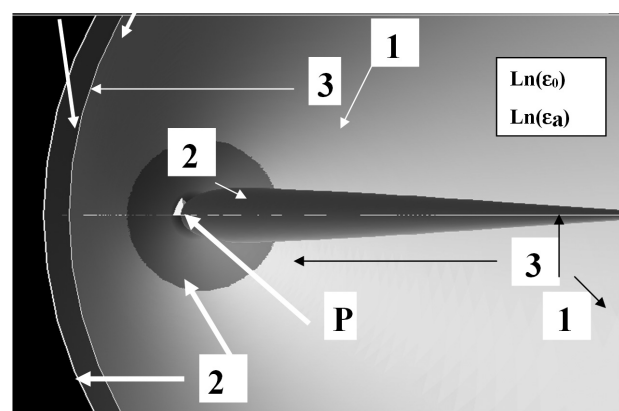


Figure 7: Viewing point 4 from Figure 5. The camera is directed to the approximate analytical solutions from Table 1.

Slika 7: Pogled s točke 4 na slici 5. Kamera je usmerjena k približnim analitičnim rešitvam v tabeli 1.

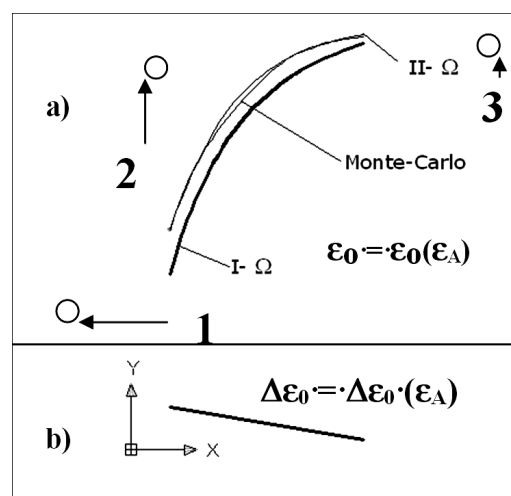


Figure 8: Comparison of the analytical and Monte-Carlo solutions for the area between the entering stands and the approximate center of the rolling line

Slika 8: Primerjava analitičnih rešitev in rešitev Monte-Carlo za področje od vhodnih ogradij do približno sredine valjarniške proge

Table 3: Explanations of the markers from **Figure 9****Tabela 3:** Pojasnila k markerjem na **sliki 9**

Marker	Link	Remark
Series 1	Monte-Carlo	Numerical calculations
Series 2	Ω - area in Table 1	
Series 3	Solution according to M point in Table 1	Control of Monte-Carlo
Series 4	Σ - area in Table 1 , left of point P	Graph agrees with Monte-Carlo
Point P	Equal significance as in Figure 7	Cross-section of solutions Ω and Σ
Ω -I	The transition area around the M point where Ω no longer agrees with Monte-Carlo and Σ formula is not yet in accord with the Monte-Carlo solution. Acceptable for interpolations of the polygonal method. ¹⁴ In the interval, the section point P is a polynomial of degree 12.	

Table 4: Comparison of the approximate analytical solutions from **Table 1** with the numerical Monte-Carlo solution from around the middle to the exit of the rolling line**Tabela 4:** Primerjava približnih analitičnih rešitev v **tabeli 1** z Monte-Carlo numerično metodo, od približno sredine valjarniške proge do izhodnih ogrođij

ε_a/m	Monte-Carlo ε_0^*/m	Zone Ω ε_0^*/m	M point ε_0^*/m	Zone Φ and Σ ε_0^I/m
9.420E-04	1.225E-05	1.225E-05	–	–
8.735E-05	1.136E-05	1.129E-05	–	–
1.069E-05	5.801E-06	–	5.801E-06	–
7.425E-06	4.618E-06	–	–	4.466E-06

cameras. According to solution Σ , $\ln(\varepsilon_A) \approx -15.414043$ for $\varepsilon_0 \rightarrow 0$.

The explanation of **Figures 6 and 7** is given in **Table 2**.

The numerical Monte-Carlo method and approximate analytical solutions for about half of the rolling line, according to references 7–9, are shown in **Figure 8**, where the calculated lubricant-layer thickness is shown for the area from the middle part to the exit of the rolling line. The linear correction of the Ω area was obtained with a solution in the M point according to **Table 1** and is also shown in **Figure 8b**.

An integral comparison for the whole continuous line is shown in **Figure 9** and, accordingly, for the abscissa as well in **Figure 5**. The markers are explained in **Table 3**.

An important characteristic of the M point is the control of the Monte-Carlo numerical method in this

point. The conditions from **Figure 9** are shown in **Table 4**.¹⁵

The solution for the M point has been confirmed. The numerical methods should be controlled in a narrow interval, at least in one initial point, with the approximate analytical solutions. In the case of the approximate analytical solutions with simplified mathematical solutions, the numerical methods are not reliable.

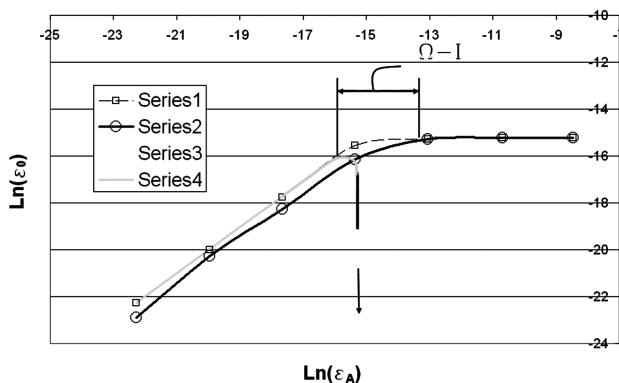
3 CONCLUSION

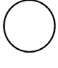
It is shown in several figures that the approximate analytical solutions of equation (2) from **Table 1** are in accordance with the numerical Monte-Carlo solutions. The representations in AutoCAD provide a refined understanding and a comparison, giving also realistic images of the lubricant on the mandrel for rolling the seamless tubes on a continuous line with several stands.

The solution developed for the M point^{15,16} is of special importance since it enables a linear correction of the lubricant layer in the area of the Ω formula and the correction can also be extended to the area Ω -I.

4 SYMBOLS

Symbol	Unit	Description
ε_0	m	Lubricant thickness in the entry section of the deformation zone (Figure 1)
ε_0^1	m	Lubricant thickness for the gripping angle α_0 tending to zero
$\varepsilon_0^{0.1}$	m	Lubricant-layer thickness for the gripping angle 0.1 rad, Figure 3 (series 1)

**Figure 9:** Comparison of the analytical solutions from **Table 1** with the numerical Monte-Carlo solutions for the whole rolling line**Slika 9:** Primerjava analitičnih rešitev iz **tabele 1** in numeričnih rešitev Monte-Carlo vzdolž cele valjarniške proge

ε^*_0	m	Characteristic lubricant thickness for the square trinomial in relation (6), with zero as a discriminant of the square equation
$\varepsilon(x)$	m	Lubricant-layer thickness in the range $[-a : 0]$, Figure 1 , equation (4)
ε_{SR}	m	Average mandrel-lubricant thickness after a pass
ε_a	m	Lubricant-layer thickness on the mandrel after the entry section of the deformation zone
ε_{aMAX}	m	Characteristic lubricant-layer thickness on the mandrel in point M
a	m	Length of the lubricant wedge (Figure 1), equation (5)
$\alpha - \alpha_0$	rad	Reduction-tube-diameter angle (Figure 1)
α_0	rad	Tube-wall deformation angle (Figure 1)
α^*_0	rad	Characteristic angle added to ε^*_0
v_R	m/s	Circumferential roll speed
v_C	m/s	Tube speed
v_T	m/s	Mandrel speed
$d_T/2$	m	Mandrel radius
R	m	Stand-roll radius
R_0	m	$R_0 = R + S_{CX}$
S_C	m	Tube-wall thickness on the mandrel after the deformation zone
S_{C1}	m	Rolled-tube wall thickness
L_R	m	Abscissa projection of the tube-diameter-reduction zone
L_S	m	Abscissa projection of the tube-wall-projection zone
L_D	m	$L_D = L_R + L_S$
τ_x	Pa	Tangential stress in the lubricant layer
	Pa s	Dynamic lubricant viscosity under rolling pressure
η_0	Pa s	Dynamic lubricant viscosity under atmospheric pressure
u	m/s	Lubricant speed along the abscissa
γ	Pa ⁻¹	Lubricant-viscosity piezocoefficient
p	Pa	Rolling pressure
Q	m ² /s	Lubricant use on the mandrel perimeter: one-dimensional model
dp/dx	Pa/m	Pressure gradient in the lubricant layer, equation (2)
$\partial p/\partial x$	Pa/m	Partial-pressure differential along the abscissa, equation (1)
$\sin \alpha \dots$ $\ln(\varepsilon_a)$	rad...	Symbol for the trigonometric functions and natural logarithm
		Symbols for the viewing locations of the AutoCAD cameras. After the approximate calculations according to Table 2 the obtained data are compared to the numerical Monte-Carlo solutions obtained with the mathematical programs and then modelled with AutoCAD, Figures 6 and 7 .
Ψ	m	Rolling-line zone described with the solutions from Table 1 and Figure 3 , according to ^{4,5} , for the lubricant surplus on the mandrel.
Ω	m	Rolling line after the Ψ zone where ε_a influences ε_0 and the solutions are presented, in this work, as the zone of tube-diameter reduction.

Σ	m	Part of the rolling line with the start and finish of intensive lubricant pickling on the mandrel and in the place where a tube-wall deformation takes place.
Φ	m	Area around point M from Figure 3 where interpolation polynomials can be used to connect the lubricant-layer calculations with the Ω and Σ equations from Table 1 .
$\Omega - I$	m	Larger area around point M, shown in Figure 9 and suitable for using the polygonal method ¹⁴
M-Point	m	Point of the approximate analytical solution from Table 1 controlling the numerical Monte-Carlo method, allowing a linear correction of the lubricant layer in Figure 8b . The effect is noticeable in Figures 3 and 5 .
W	–	Reference point in Figure 3 ; right of W – reduction of the tube diameter; left of W – deformation of the tube wall. It explains the topics and has no analytical expression.
$\gg, \approx, ^0, \rightarrow, ^\wedge, E$	–	Mathematical symbols for much greater, approximate, step mark, tending, mark for an exponent, base of number 10
A	m ⁻¹	Technological parameter: $A = [1 - \exp(-p)] / [6 \cdot (v_C + v_T)]$
\exp^{16}	–	Base of natural logarithm, a reference

5 REFERENCES

- I. Mamuzić, V. M. Drujan, Teorija, Materijali, Tehnologija Čeličnih cijevi, Hrvatsko Metalurško Društvo, Zagreb 1996, 137–275
- S. V. Mazur, Postanovka zadači i zakonomernosti tečenja smazki v očage deformacije pri prokatke trub, Sučasni problemi metalurgii, Nacionalna Metallurhičeskaja Akademia Ukraine, Dnepropetrovsk, Ukraine, 8 (2005), 447–452
- D. Čurčija, I. Mamuzić, Mater. Tehnol., 39 (2005) 3, 61–75
- O. P. Maksimenko, A. A. Semenča, Issledovanie kontaktno-gidrodinamičeskoj smazki pri prokatke, Sučasni problemi metalurgii, Nacionalna Metallurhičeskaja Akademia Ukraine, Dnepropetrovsk, Ukraine, 8 (2005), 99–103
- P. L. Klimenko, Kontaktnije naprjaženija pri prokatke s tehnologičeskoj smazkoj, Sučasni problemi metalurgii, Nacionalna Metallurhičeskaja Akademia Ukraine, Dnepropetrovsk, Ukraine, 8 (2005), 44–49
- D. Čurčija, Mater. Tehnol., 37 (2003) 5, 237–250
- D. Čurčija, I. Mamuzić, Metalurgija, 44 (2005), 221–226
- D. Čurčija, I. Mamuzić, Metalurgija, 44 (2005), 295–300
- D. Čurčija, I. Mamuzić, Lubricating film shape at band dressing, 38th Symposium Lubricants, Zagreb, Društvo za Goriva i Maziva, Rovinj, Croatia, 2005
- D. Čurčija, I. Mamuzić, Metalurgija, 43 (2004), 249
- D. Čurčija, I. Mamuzić, Goriva i Maziva, 46 (2007), 34–44
- D. Čurčija, I. Mamuzić, F. Vodopivec, Metalurgija, 45 (2006), 250
- D. Čurčija, I. Mamuzić, Mater. Tehnol., 41 (2007) 1, 21–27
- D. Čurčija, I. Mamuzić, Tehnika RGM, 34 (1983), 1075–1078
- D. Čurčija, I. Mamuzić, Estimation of lubricant film by pipe rolling in stands/mills, 40th Scientific Symposium Lubricants 2007, Pula, Croatia, 2007
- D. Čurčija, I. Mamuzić, Mater. Tehnol., 42 (2008) 2, 59–63

ALTERNATIVE UTILIZATION OF THE CORE SAND FOR A GREEN-SAND SYSTEM

ALTERNATIVNA UPORABA PESKA ZA JEDRA V SISTEMU PRIPRAVE LIVARSKEGA PESKA

Nikol Špirutová, Jaroslav Beňo, Vlasta Bednářová

VŠB-Technical University of Ostrava, Faculty of Metallurgy and Materials Engineering, Department of Metallurgy and Foundry, Ostrava,
Czech Republic
jaroslav.beno@vsb.cz

Prejem rokopisa – received: 2012-08-30; sprejem za objavo – accepted for publication: 2013-03-08

The foundry industry, like the other human activities, is associated with the production of various wastes. These secondary products of manufacturing are mainly composed of the moulding mixture, dust waste, fire-refractory materials and other wastes. A utilization of the waste moulding mixture, especially the core sand based on organic resins, as a replacement for new sand, can be a way of decreasing the portion of moulding-mixture waste, thus also decreasing its negative impact on the environment. Nowadays, the most preferred technology for manufacturing moulds is the green-sand system with clay (bentonite) as the binder.

The aim of this study is to determine the influence of a core-sand addition on the mechanical, physical, chemical and technological properties of the green-sand system.

Keywords: innovative foundry technologies and materials, green-sand system, organic binders, environment protection, active bentonite, waste management

Livarska industrija je kot vse človeške aktivnosti povezana z nastankom različnih odpadkov. Odpadki, ki nastajajo pri proizvodnji, so večinoma sestavljeni iz mešanice form, prahov, ognjevdržnih materialov in drugih odpadkov. Uporaba odpadnih mešanic iz form, kot nadomestilo za nov pesek, posebno mešanic za jedra, ki temeljijo na organskih vezivih, je lahko pot za zmanjšanje količine odpadnega peska, s čimer se lahko zmanjša negativni vpliv na okolje. Dandanes je najbolj priljubljena tehnologija za izdelavo form sistem z novim peskom in glino (bentonit) za vezivo. Namen te študije je ugotoviti vpliv dodatka peska jeder na mehanske, fizikalno-kemijske in tehnološke lastnosti peščene mešanice.

Ključne besede: inovativne livarske tehnologije in materiali, sistem priprave peska, organska veziva, varovanje okolja, aktivni bentonit, ravnanje z odpadki

1 INTRODUCTION

Industrial activity is associated with the waste production. A large part of these wastes is characterized as hazardous materials. The basic question of how we can use these wastes or how we can dispose of these wastes is the primary problem for today's society. The main reason for its disposal is the protection of human health. We have to establish environmentally friendly technology, but here the economic aspect also plays an important role. An elimination, or at least a minimization, of the amount of waste and/or recycling of the incurred wastes and/or a utilization of these wastes as raw materials in other technologies are possible ways of the solution.¹

The foundry industry generates about 0.6 t of waste per 1 t of castings.² Moulding mixtures represent the largest proportion of the wastes. Most of the attention is paid to the recycling of the sands. The regeneration and/or reusing of the mixtures have had a considerable progress in recent years. The mixtures should be used as a secondary material or be deposited. In this case the cost of a casting production is determined by the cost for

depositing the used sand mixtures, not by the cost of the raw materials.³

The most used technology for the mould production is the green-sand system (with bentonite as the binder)⁴ due to its low cost, easy recyclability and its environmentally friendly binder character. The cores, based on different types of organic resins, allow a faster curing and a production of thin-wall castings. The cores, cured with chemical and thermal processes, exhibit a high primary strength at low binder content and a good storability. Furthermore, a low adhesive strength of the binder to the sand grains allows a simple regeneration. A low temperature of the binder thermal destruction ensures an excellent collapsibility. However, a faster collapsibility of the cores is the main problem, because the core sand becomes a part of the green sand and then the properties of the moulding mixture can be affected and the casting defects such as scabs, defects of the gases and pinholes can occur.^{3,5} During a casting process the moulding and core mixtures are subjected to higher temperatures. The bentonite binding capacity is influenced by the physical and chemical changes that occur due to the heat exposition of the moulds. At elevated temperatures the bentonite behavior is not only affected

due to a degradation of its plastic properties, caused by dehydroxylation, but also due to the sorption of the liquid and gaseous products of carbonaceous additives and synthetic resin pyrolysis. The mixture is refreshed in order to keep the basic sand properties.

An addition of the treated cores to the green sand as a replacement for a new sand can be a way of a waste-core recycling, a form of hazardous waste utilization, and then the foundry produces no waste from the moulding sand and cores. However, the green-sand properties may be changed. In the theoretical studies in the literature there is no uniform opinion on the used cores' impact on the green-sand-system technology and re-bonding properties.⁵⁻⁸ Therefore, this study aims to experimentally determine the effect of a core addition on the green-sand technological system and re-bonding properties and it considers different opinions on these problems. The problem was solved by determining:

- the properties of the green-sand system (GGS) standard,
- the influence of the cores on the GGS properties,
- the degree of the bentonite passivation.

2 MATERIALS AND METHODS

In order to simulate the core-sand influence on the GGS properties, four kinds of the most common technology for the core production were used:

1. ASHLAND COLD – BOX (CB) based on phenolic polyurethane resins Askocure EP3929 300 and polyisocyanate component Askocure 600 FW 3 with catalyst 704.
2. HOT – BOX (HB) based on phenolic resins Thermophen 1002 with hardener Härter HP.
3. Croning method (CR) using phenolic resin Plasti-sable 42B 630X.
4. The method of Resol cores (RE) using Novanol phenolic resin 180 hardened by CO₂ gas.

Additions of a core concentration, ranging from 10 % to 50 %, were studied and compared to the GGS standard prepared from the Czech-foundry soda-activated bentonites without any additives.

The samples of the green-sand systems (the standard ones or the samples with cores) were prepared with a 6 min homogenization of the mixture of the studied bentonite with the silica sand in the constant weight ratio of 8 : 100 and an appropriate amount of water, which provided for a constant compactibility of (45 ± 3) % using a MK 00 sand mill. The prepared mixtures were shaped into the standard cylinders (diameter of 50 mm, the height of 50 mm) to obtain the samples for determining the technological parameters.

Technological parameters of active bentonite (8 parts by weight), compactibility (moisture of the mixture) and preparation (mixing) time were kept at the constant values, as they can significantly affect the mechanical properties of GGS.

The following general parameters (**Table 1**), commonly used for characterizing GGS, were determined:

- a) moisture under a temperature of 105 °C up to the constant weight,
- b) pH and conductivity of water suspension (1 : 10 ratio),
- c) loss of ignition of dried samples (105 °C up to the constant weight) at 900 °C/2 h.

Strength parameters of the GGS samples including the green compression strength and splitting strength were measured using a testing machine WADAP, the LRU-1 type; wet tensile strength was measured using a testing machine +GF+ (the SPNF type). Wear (the loss in weight after 1 min) was also determined using an NS1-12RH from the Bodine Electric Company.

Experiments were carried out in two temperature regimes. At first the core influence on the GGS properties was studied at laboratory temperature (25 °C) and then the moulding mixture was annealed at the temperature of 350 °C and the samples were prepared in order to simulate a realistic condition in a mould when a decomposition of the resins occurs and bentonite dehydroxylation (a loss of the binding properties and a destruction of the crystalline structure) does not start and the "burnt-out" bentonite is not formed.⁹ This working temperature resulted from the thermal DTA/TG analysis of the used bentonite binder, conducted on the laboratory samples at 15 °C/min under oxidizing atmosphere using the NETZSCH GmbH equipment, according to the details from the literature.¹⁰

Table 1: General parameters of the GGS-standard

Tabela 1: Glavni parametri GGS-standarda

Property		STD
compactibility	(%)	44–45
wet tensile strength	(kPa)	3.04–4.95
green compression strength	(kPa)	139.0–151.8
splitting strength	(kPa)	35.20–48.34
wear	(%)	2.85–5.69
moisture	(%)	2.15–2.26
pH	(–)	10.1–10.5
conductivity	($\mu\text{S cm}^{-1}$)	239–504
active bentonite	(%)	7.65–8
loss of ignition	(%)	0.52–0.97

3 EXPERIMENTAL RESULTS AND DISCUSSION

The influence of a core, based on organic resins in the range of 10–50 % at laboratory temperature, on the technological properties of the GGS standard is shown in **Figures 1 to 4**.

From these figures it is evident that no significant change has been achieved for the CB and/or HB cores over the whole concentration range. Only the addition of the CB cores caused a slight increase in the green compression strength (about 14 %). This effect was also documented in some other sources.^{6,8} A presence of the

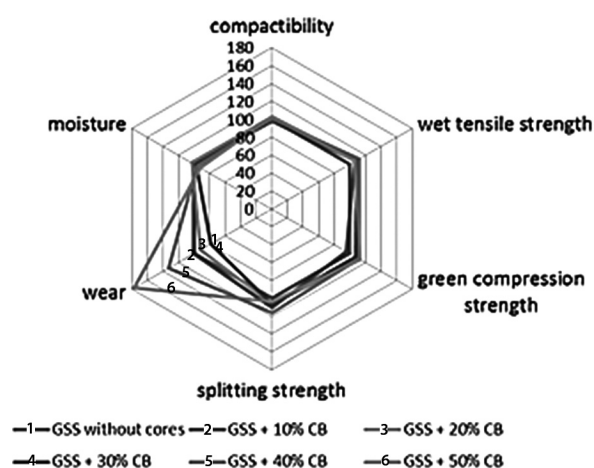


Figure 1: Properties of the moulding mixture with CB-cores (10–50 %)

Slika 1: Lastnosti formarske mešanice z dodatkom CB-jeder (10–50 %)

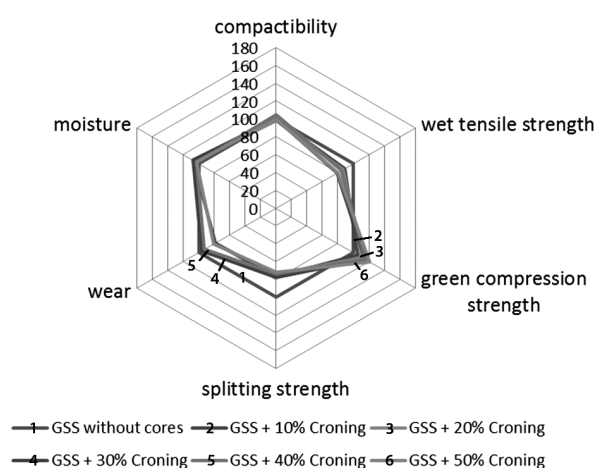


Figure 3: Properties of the moulding mixture with CR-cores (10–50 %)

Slika 3: Lastnosti formarske mešanice z dodatkom CR-jeder (10–50 %)

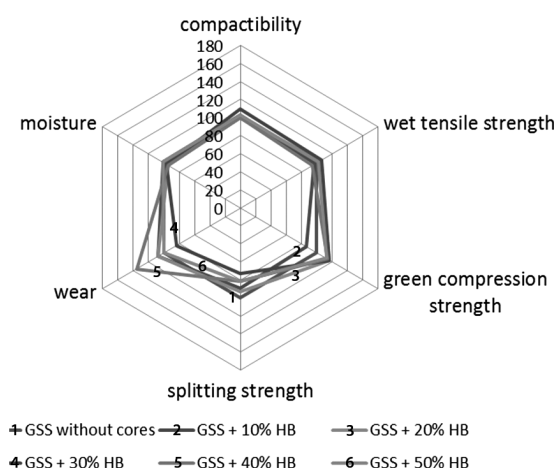


Figure 2: Properties of the moulding mixture with HB cores (10–50 %)

Slika 2: Lastnosti formarske mešanice z dodatkom HB jeder (10–50 %)

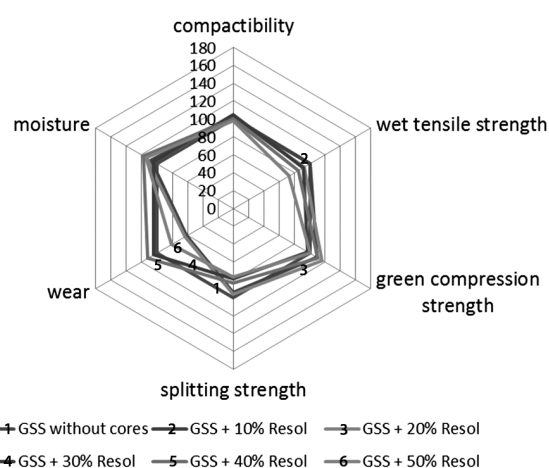


Figure 4: Properties of the moulding mixture with HB-cores (10–50 %)

Slika 4: Lastnosti formarske mešanice z dodatkom HB-jeder (10–50 %)

core in GGS causes an increase in the wear of the mixture, especially for the GGS–CB system cores, increasing up to 44 %. This can lead to a greater risk of a mould damage during its manipulation and composition, thus the possibility of an erosion of the molten metal increased as well.

The addition of the CR cores showed growing trends in the values of the green compression strength in comparison with the standard. The splitting strength and wet tensile strength show a gradual reduction in the mechanical properties due to the increasing content of the CR cores. An increase in the RE-core content shows a gradual decrease in the strength values. Both can be caused by a deactivation of the bentonite plastic properties due to various ions, salt and other formations of the organic resins and their additives (as catalysts, etc.).

Further experiments were conducted with a study of the interaction between GGS and the core sand under

annealed temperature (350 °C) in order to partially simulate the conditions in the moulds after the heat stress. At this temperature it can be assumed that the start of a thermal decomposition of the resin and the binding-capacity bentonite may be influenced by the pyrolysis products (passivation of the active bentonite), which will be reflected in the changes of the mixture properties.

Therefore, with the scanning electron microscope (JEOL JSM-6490LV) and the quantitative analysis with an energy dispersive analyzer Inca EDS X-ACT, an analysis of the selected samples was employed and the theoretical assumptions were confirmed. On the surface layer of the grains pyrolysis products (PC) were detected and, according to its chemical composition, it can be assumed that this layer corresponds to the pyrolysis carbon layer. For example, an analysis of the surface layer of the grains with a mixture of GGS and CB is shown in **Figure 5**.

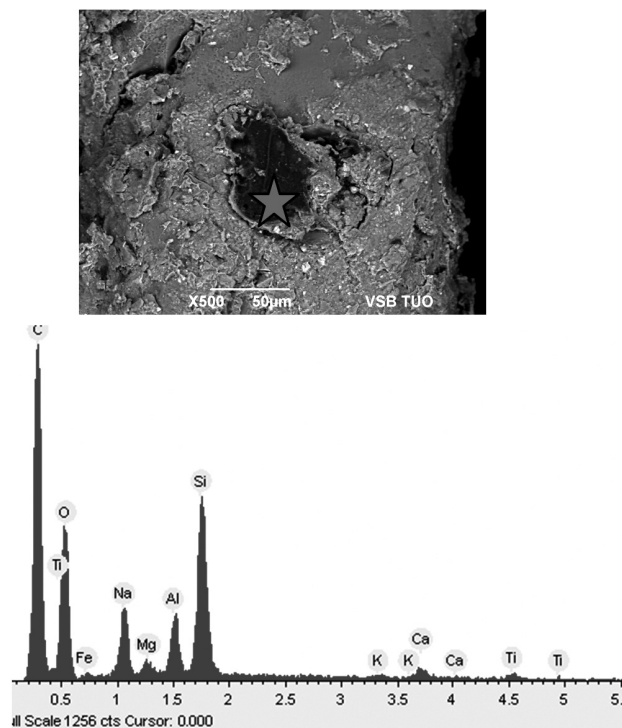


Figure 5: Detail of the grain surface with the locally excluded PC
Slika 5: Detajl površine zrna z lokalno odsotnostjo PC

These experiments were carried out only for the 50 % addition of the cores. The preparation (mixing) time of the mixture was also changed (from 6 min to 12 min) in order to study the mechanism of the bentonite passivation (a kind of sorption). The results of these experiments are shown in **Figures 6 to 9**.

As a result of the core addition (50 %) there is a marked decrease in the active bentonite, probably due to its deactivation caused by the pyrolysis products generated during the heat exposure of the cores. Therefore, this fact has an influence on the mechanical properties of

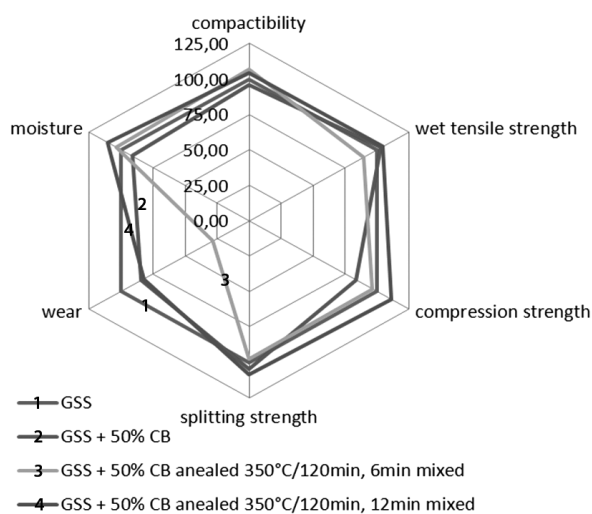


Figure 6: Properties of the moulding mixture with CB-cores (50 %)
Slika 6: Lastnosti formarske mešanice z dodatkom CB-jeder (50 %)

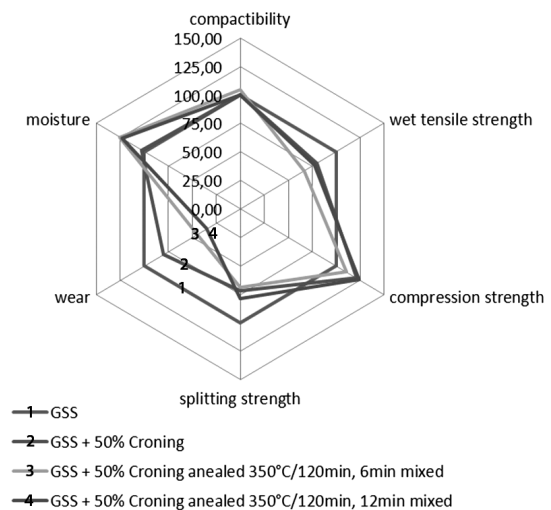


Figure 7: Properties of the moulding mixture with CR-cores (50 %)
Slika 7: Lastnosti formarske mešanice z dodatkom CR-jeder (50 %)

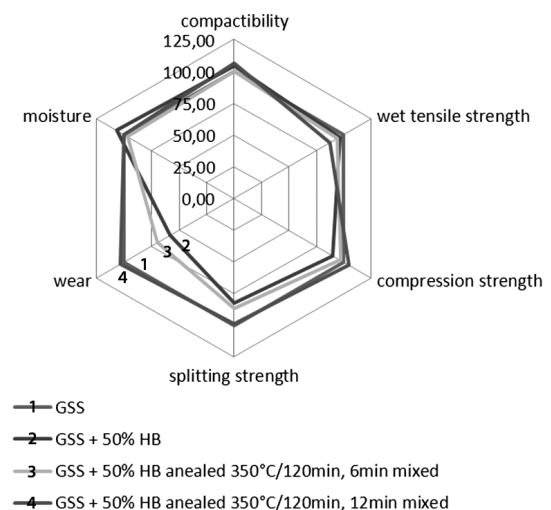


Figure 8: Properties of the moulding mixture with HB-cores (50 %)
Slika 8: Lastnosti formarske mešanice z dodatkom HB-jeder (50 %)

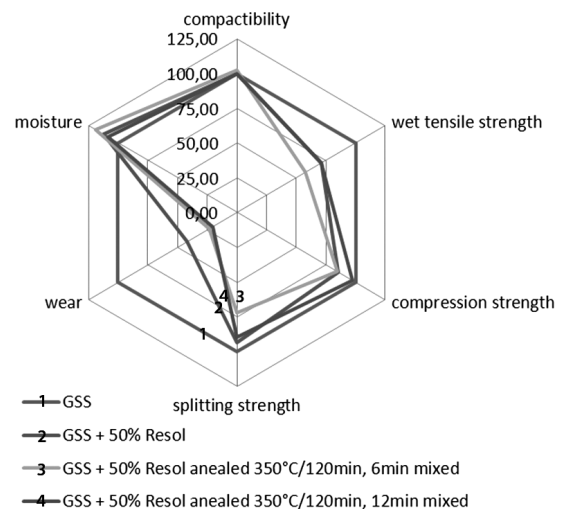


Figure 9: Properties of the moulding mixture with HB-cores (50 %)
Slika 9: Lastnosti formarske mešanice z dodatkom HB-jeder (50 %)

the mixture, and the strengths have been decreased, on average, by 20 % to 40 %. The deterioration of the mechanical properties is higher for the CB cores. Boenisch¹¹ reached the same conclusions and maintained that CB is a binder system with the greatest influence on the deactivation of bentonite in comparison with HB and/or CR. However, this view is not unanimously confirmed by the other authors.⁶ In this research, an active bentonite deactivation was confirmed due to the developed films of pyrolytic carbon, found on the grain surface and determined with an EDX analysis.

An extension of the sample preparation time (from 6 min to 12 min) caused an increase in the mixture mechanical properties (strengths). This probably happened due to the activation of the passive bentonite. We can probably conclude that the mechanism of the bentonite passivation is a physical sorption (reversible changes).

4 CONCLUSIONS

Utilization of the sand waste in a circulation system of a foundry moulding sand is one of the many ways of reducing wastes of a foundry production. There is a very significant problem as to how this waste can affect the technological properties of a foundry moulding mixture (green-sand system) during its circulation.

The aim of this contribution is to determine the impact of the selected core systems (COLD-BOX, HOT-BOX, CRONING, CO₂ – RESOL) on the bentonite moulding-sand properties. For the purpose of this research an "uncirculated" moulding mixture was used.

At laboratory temperature, a slight increase in certain strength (e.g., the green compression strength after an addition of the CB cores) was obtained. On the other hand, an addition of the CRONING and RESOL cores caused a decrease in the sand mechanical strengths. The core addition exhibits a negative impact on the wear, especially for the GGS system with the CB cores.

After a thermal exposure a significant decrease in the sand properties was observed. It was probably caused by a formation of the pyrolytic-carbon films on the grain

surfaces (a deactivation of the bentonite); this assumption was confirmed with an EDX analysis of the sand samples. An extension of the sample preparation time (from 6 min to 12 min) caused an increase in the mixture mechanical properties (strengths), probably due to an activation of the passive bentonite. This paper is the first in a series of articles on this topic.

Acknowledgement

The research was realized with the financial support within the specific-research project at VŠB-TU Ostrava, SP 2012/23, "Studium přípravy a vlastností materiálů na bázi litých kovových pěn".

5 REFERENCES

- ¹ A. Pribulová, P. Gengel, Complex treatment of dust from cast iron casting cleaning, *Przeglad odlewnictwa*, (2009) 3, 150–153
- ² L. Rimoux, Valorisation des déchets de fonderie, *Fonderie-Fondeur d'aujourd'hui*, 257 (2006), 43–55
- ³ J. Beňo et. al., Alternative use of core mixtures in bentonite mixtures, *Slévárenství*, LIX., 9–10 (2011), 309–313
- ⁴ I. Vasková et. al., Physical and chemical clay binder characteristics from various locality and their influence on some technological properties of bentonite moulding mixtures, *Archives of foundry engineering*, 10 (2010) 1, 211–216
- ⁵ D. Boenisch, Effect of Coldbox, Hotbox and Corning Cores on the Properties of Bentonite Bonded Molding Sands, RWTH Aachen University, Germany, 1977
- ⁶ R. L. Naro, Influence of Chemical Binder Core Sand Contamination on Green Sand Molding Properties – 25 Years of Controversy, *AFS Trans.*, 112 (2004), paper 04-001(04).pdf
- ⁷ M. Holtzer et. al., The influence of reclaim on properties of molding sand with furan resin, *Archives of Foundry Engineering*, 10 (2010) 2, 61–64
- ⁸ M. J. Granlund, How Green Sand Systems are impacted by Core Sand Dilution, *Modern Casting*, (1999) 3, 35–37
- ⁹ V. Š. Fajnor, K. Jesenák, Diferential Thermal Analysis of Montmorillonite, *Journal of Thermal Analysis*, 46 (1996), 489–493
- ¹⁰ J. Beňo, et. al., Alternativní využití jádrových směsí, část II.: CO₂ – Resol, Croning, *Slévárenství*, 55 (2012) 3–4, 90–94
- ¹¹ D. Boenisch, N. Ruhland, Über den Einfluss von Cold-Box, Hot-Box und Croning-Kernen auf die Eigenschaften bentonit-gebundener Formsande, *Giesserei*, 75 (1988) 4, 69–76

MICRO-ABRASION WEAR TESTING OF MULTILAYER NANOCOMPOSITE TiAlSiN/TiSiN/TiAlN HARD COATINGS DEPOSITED ON THE AISI H11 STEEL

MIKROABRAZIJSKO PREIZKUŠANJE OBRABE VEČPLASTNE NANOKOMPOZITNE TRDE PREVLEKE TiAlSiN/TiSiN/TiAlN NA JEKLU AISI H11

Halil Çalışkan¹, Azmi Erdoğan¹, Peter Panjan², Mustafa Sabri Gök¹, Abdullah Cahit Karaoğlu¹

¹Bartın University, Faculty of Engineering, 74100 Bartın, Turkey

²Jožef Stefan Institute, Jamova 39, 1000 Ljubljana, Slovenia
halilcaliskan06@yahoo.com, hcaliskan@bartin.edu.tr

Prejem rokopisa – received: 2012-08-31; sprejem za objavo – accepted for publication: 2013-01-09

Nanostructured hard coatings are widely used to improve the wear resistance of tool steels in tribological applications. These coatings generally work under abrasive conditions and, therefore, a determination of their abrasive wear resistance has great importance. In this study, the free-ball micro-scale abrasion test, based on the ball-crater technique, has been used to evaluate the wear resistance of a multilayer nanocomposite nc-TiAlSiN/TiSiN/TiAlN hard coating. The coating was deposited on the AISI H11 cold-work tool steel using the industrial magnetron sputtering system. The microhardness and adhesion of the coating to the substrate were measured with the nanoindentation and scratch tests, respectively. The wear tests have been performed using SiC abrasive slurry on ball-cratering equipment. The crater-wear volumes have been evaluated using an optical microscope (OM). An analysis of the worn craters was conducted with a scanning electron microscope (SEM). It was found that the nc-TiAlSiN/TiSiN/TiAlN hard coating has a better adhesion to the AISI H11 steel substrate and a higher abrasive wear resistance than a conventional TiN coating. A two-fold increase in the sliding speed resulted in an approximately two-fold increase in the removed-wear volume. Three different wear mechanisms, i.e., micro-scratch, lateral fracture and plastic deformation, took place on the craters formed on the nc-TiAlSiN/TiSiN/TiAlN coated steel.

Keywords: nanocomposite hard coating, TiAlSiN/TiSiN/TiAlN, micro-scale abrasion wear, scratch test, tool steel

Nanostrukturirane trde prevleke se uporabljajo za izboljšanje obrabne odpornosti orodnih jekel za tribološko uporabo. Te prevleke navadno delujejo v razmerah abrazijske obrabe in je zato pomembno ugotavljanje njihove odpornosti proti abrazijski obrabi. V tej študiji je bil uporabljen mikroabrazijski preizkus s prosto kroglico, ki temelji na tehniki kraterja kroglice, za preizkus obrabne odpornosti trde prevleke iz večplastnega nanokompozita nc-TiAlSiN/TiSiN/TiAlN. Prevleka je bila nanosena na orodno jeklo za delo v hladnem AISI H11 z uporabo industrijskega magnetronskega sistema za naprščevanje. Mikrotredota in oprijemljivost na podlago sta bili izmerjeni z nanomerilnikom trdote in s preizkusom razenja. Preizkus obrabe je bil narejen z uporabo abrazijske suspenzije s SiC na napravi s kroglico. Volumen kraterja pri obrabi je bil ocenjen z uporabo svetlobnega mikroskopa (OM). Analiza kraterjev pri obrabi je bila narejena z vrstičnim elektronskim mikroskopom (SEM). Ugotovljeno je bilo, da ima trda prevleka nc-TiAlSiN/TiSiN/TiAlN boljšo oprijemljivost na podlagi iz jekla AISI H11 in boljšo odpornost proti obrabi kot navadna TiN-prevleka. Dvakratno povečanje hitrosti drsenja je povzročilo dvakratno povečanje volumna obrabe. Na kraterjih, ki so nastali na jeklu, prevlečenem z nc-TiAlSiN/TiSiN/TiAlN, so bili vidni trije mehanizmi obrabe: mikrorazenje, bočno drobljenje in plastična deformacija.

Ključne besede: nanokompozitna trda prevleka, TiAlSiN/TiSiN/TiAlN, abrazijska obraba na mikropodročju, preizkus razenja, orodno jeklo

1 INTRODUCTION

The AISI H11 hot-work tool steel is widely used in the production of mandrels, punches, dies, moulds, knives and rollers. Despite the fact that different types of wear mechanisms such as fatigue and adhesive wear take place on these components, abrasion is one of the most important wear types. The friction occurring under working conditions necessitates the components to have a high hardness and wear resistance.¹ Therefore, thin film coatings of different materials (TiN, TiAlN, TiAlSiN, etc) have been developed and deposited on these steel components in order to prolong their lifetime in industry. The most important properties of these coatings are their much higher hardness and abrasive wear resistance compared to the uncoated substrates.²⁻⁶

The newly developed nc-TiAlSiN/TiSiN/TiAlN multi-layer nanocomposite hard coating was found to be smooth and chemically stable, and it has low residual stresses and the maximum application temperature of 1100 °C.⁷ Therefore, the coating has a wide application area in industry. In order to improve the performance of the nc-TiAlSiN/TiSiN/TiAlN coating and to select the coating which is suitable for the applications mentioned above, a determination of its abrasive wear resistance is important.

The micro-abrasion wear test, introduced by Kassman et al.,⁸ is a widely used method for determining the abrasive wear resistance of thin hard coatings.^{2,9-11} In the test, a hardened ball is rotated on a sample under a certain load, with an addition of an abrasive slurry into the contact zone. Then, the crater track formed is

evaluated using profilometry and microscopy, and the wear characteristics are determined.¹² The test is easy to perform and very effective with respect to the wear resistance of the materials, and it needs only a small area of a sample. Therefore, in this study, the effect of the nc-TiAlSiN/TiSiN/TiAlN coating on the wear resistance of the AISI H11 steel was investigated using the micro-abrasion test. The adhesion of the coating on the substrate was determined and the wear behavior of the coating and the substrate was evaluated.

2 EXPERIMENTAL WORK

2.1 Substrate and the coating material

The test plates made of the AISI H11 tool steel with the diameter of 23 mm and the thickness of 1 mm were used as a substrate for the characterization and wear tests. The AISI H11 steel was quenched at 1150 °C and tempered at 560 °C to its final hardness of 931 HV. The heat treatment was performed in a vacuum furnace.

The industrial magnetron sputtering system CC800/9 sinOx ML (CemeCon) was used for depositing the nc-TiAlSiN/TiSiN/TiAlN coatings onto the test plates. The deposition system has four unbalanced magnetron sources placed on the corners of a rectangle. Two segmental TiSi and two segmental TiAl targets were used for depositing the nc-TiAlSiN/TiSiN/TiAlN coatings. The samples were moved in a two-fold rotation to obtain the nanoscale structures and also to ensure a constant film-thickness distribution on the substrates. The conventional TiN coating was also deposited on the H11 steel to make a comparison between the micro-abrasion

wear tests. The layer structures and thickness data for the coatings are shown in **Figure 1**. The thickness of the coatings was calculated from the craters formed with the ball-cratering technique (Calotest). It is seen that both coatings have a similar thickness (5.4 µm for the nc-TiAlSiN/TiSiN/TiAlN and 6.2 µm for the TiN coating).

2.2 Laboratory tests

The microhardness of the coatings on the AISI H11 substrates was measured with a Fisherscope H100C nanoindenter using a Vickers indenter at room temperature. The load increased stepwise and then decreased. From the loading/unloading curves, the indentation modulus $E^* = E/(1 - \nu^2)$ (where E and ν are Young's modulus and Poisson ratio, respectively)¹³ and hardness H of the coatings were calculated. The microhardness measurements were made at the maximum load of 50 mN for the coatings and at the maximum load of 1000 mN for the substrate. For a better reliability of the results, the measurements deviating significantly from the general trend in the load-displacement graph were deleted. The mean of the remaining values (typically around twenty) were determined as the hardness of the coatings.

The adhesion of the coatings to the substrates was investigated using a CSM Revetest scratch tester where a moving diamond stylus pressed along a sample surface with a progressive load. The radius of the diamond indenter used in the scratch test was 200 µm. The test parameters were selected as follows: the scratch length of 3 mm, the maximum load of 150 N, the loading rate of 200 N/min and the stylus speed of 4 mm/min. The load, which caused the chipping without an exposure of the substrate (the cohesive failure) at the track edges, was considered as the critical load of L_{C1} . The critical load of L_{C2} was determined with a complete removal of the coating in the scratch track. The critical load for the beginning of the coating chipping (L_{C1}) was determined with optical observation and acoustic emission. For the critical load of L_{C2} , friction-force recording was additionally used.

2.3 Micro-abrasion wear tests

The micro-abrasion wear tests were carried out using a free-ball cratering device in order to compare the abrasive wear resistance of the nc-TiAlSiN/TiSiN/TiAlN and conventional TiN coatings and the uncoated AISI H11 steel (**Figure 2**). The abrasive slurry composed of 25 g of SiC (1200 mesh) in 75 ml of water and a polished ball of AISI 52100 steel with the diameter of 25.4 mm were used. The ball rotation speeds were selected as 73.7 r/min and 147.4 r/min (corresponding to 0.099 m/s and 0.198 m/s, respectively). All the tests were performed within the duration of (300, 360 and 420) s, and they were repeated three times. The crater-wear

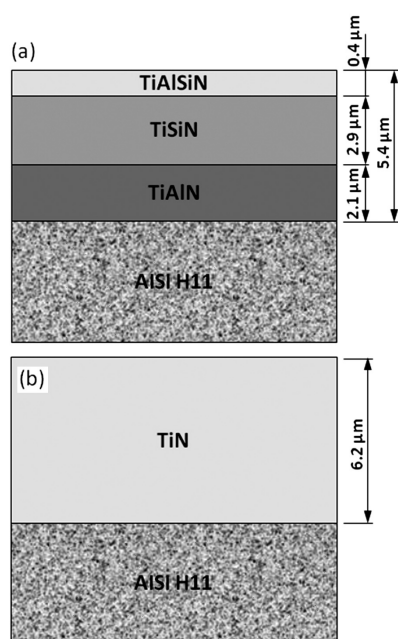


Figure 1: Layer structure and thickness data for: a) nc-TiAlSiN/TiSiN/TiAlN and b) TiN coating

Slika 1: Struktura plasti in podatki o debelini: a) nc-TiAlSiN/TiSiN/TiAlN in b) prevleka TiN

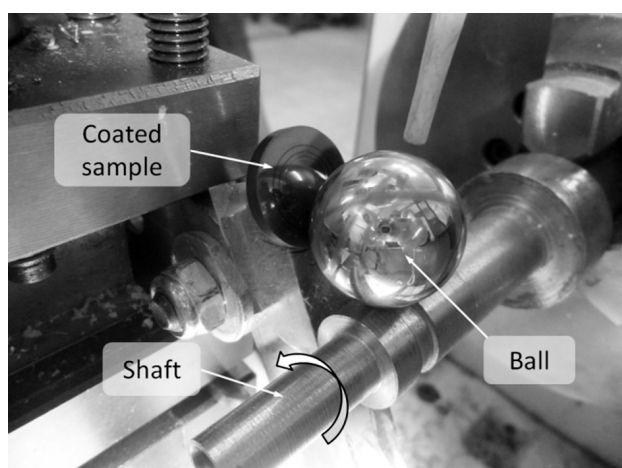


Figure 2: Free-ball micro-abrasion test device

Slika 2: Naprava za mikroabrazijski preizkus s prosto kroglico

volumes have been evaluated using an optical microscope and calculated using the equations from^{14,15}. The analysis of the worn craters was conducted with SEM.

3 RESULTS

3.1 Mechanical analysis

A comparison of the hardness and indentation modulus of the coatings and the substrate is given in

Table 1. The microhardness of the nc-TiAlSiN/TiSiN/TiAlN coating is 1.26 times higher than that of the TiN coating and 4.16 times higher than that of the substrate.

Table 1: Hardness and indentation modulus of the coatings and substrate

Tabela 1: Trdota in modul vtiskavanja prevlek in podlage

Material	H/HV	E^*/GPa
nc-TiAlSiN/TiSiN/TiAlN	3869 ± 387	361 ± 21
TiN	3072 ± 216	398 ± 18
AISI H11	931 ± 2	245 ± 2

During the progressive scratch tests of the coatings, chipping, spalling, conformal cracking and buckling failures were observed.¹⁶ **Figure 3** shows images of the scratch tracks at L_{C1} and L_{C2} that occurred in the nc-TiAlSiN/TiSiN/TiAlN coating deposited onto the AISI H11 steel. The failures on the coating started with the angular cracks outside the tracks. The chippings formed at the edges of the tracks. Delamination of the TiAlSiN top layer or TiSiN layer was observed. The critical loads of L_{C1} and L_{C2} were measured as 41 N and 145 N, respectively. Thus, the nc-TiAlSiN/TiSiN/TiAlN coating exhibited a much better adhesion than the conventional single-layer TiN coating ($L_{C1} = 40$ N and $L_{C2} = 85$ N).

3.2 Micro-abrasion wear tests

The wear-coefficient graphs for the coated and uncoated samples obtained at the ball rotation speed of 147.4 r/min are given in **Figure 4**. Using the equations from^{14,15}, two different wear coefficients were calculated for the substrate and substrate + coating. The graph shows that the wear resistance of the AISI H11 steel was drastically improved by both the nc-TiAlSiN/TiSiN/TiAlN and TiN coatings, and the lowest wear coefficient was obtained with the nc-TiAlSiN/TiSiN/TiAlN coating. As seen from the graph, the wear coefficient of the nc-TiAlSiN/TiSiN/TiAlN coated sample slightly decreases with the sliding distance, while that of the TiN

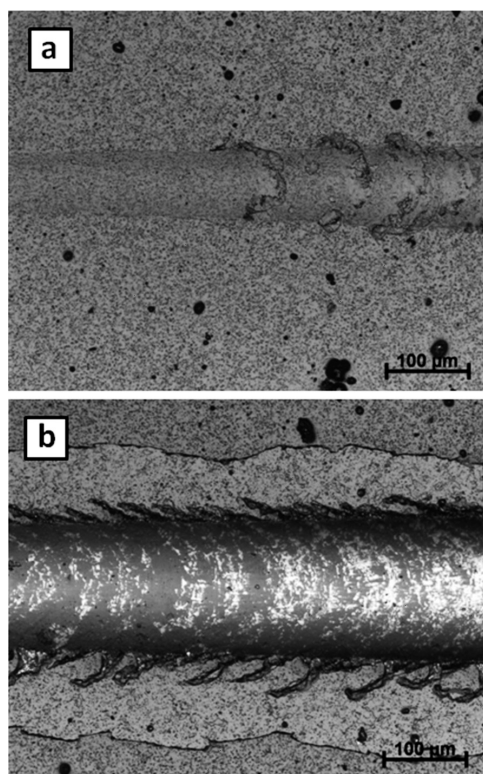


Figure 3: Scratch images of the nc-TiAlSiN/TiSiN/TiAlN coating on the AISI H11 substrate at the critical loads of: a) L_{C1} and b) L_{C2}

Slika 3: Slika raze na prevleki nc-TiAlSiN/TiSiN/TiAlN na podlagi AISI H11 pri kritičnih obremenitvah: a) L_{C1} in b) L_{C2}

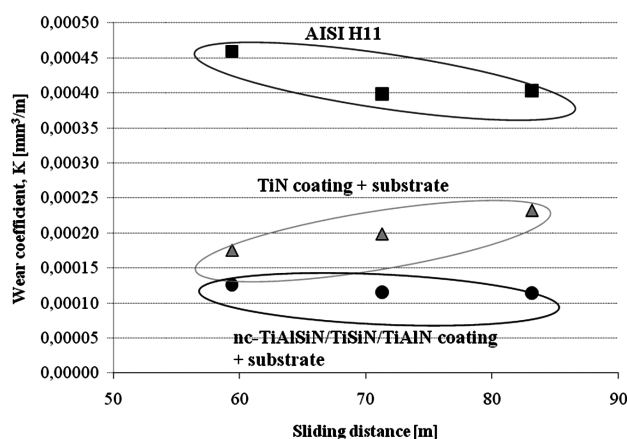


Figure 4: Wear coefficient as a function of sliding distance
Slika 4: Koeficient obrabe v odvisnosti od dolžine drsenja

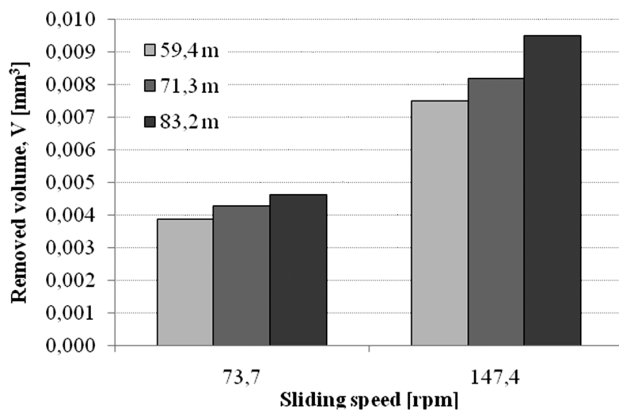


Figure 5: Effect of the sliding speed on the wear
Slika 5: Vpliv hitrosti drsenja na obrabo

coated one increases. This situation can be explained by concluding that at the beginning of the wear testing of both coatings the pressure applied on the abrasive SiC particles, and thus on the coated sample, is high (due to the point contact) causing a high wear rate. However, the pressure on the sample decreases with the increasing contact area during the sliding as a result of the wear. Owing to the high hardness and adhesion of the nc-TiAlSiN/TiSiN/TiAlN coating, a slight decrease in the wear coefficient was observed. On the other hand, in the case of the TiN coating, the coating was detached from the substrate due to the abrasion wear and a lower adhesion of the TiN coating to the AISI H11 steel and, therefore, the wear coefficient increased with the sliding distance.

In **Figure 5** the effect of the ball sliding speed on the removed volume is shown. Here, the tests were repeated at 73.7 r/min for the same sliding distance with the nc-TiAlSiN/TiSiN/TiAlN coating. A two-fold increase in the sliding speed resulted in an approximately two-fold increase in the removed wear volume. An increase in the ball rotation speed increased the peripheral speed of the SiC particles moved by the ball surface. Accordingly, more energy was applied onto the sample surface and more particles were removed from the coating and the substrate.

The image of the crater formed on the nc-TiAlSiN/TiSiN/TiAlN coating of the AISI H11 steel after the sliding distance of 83.2 m at the ball rotation speed of 147.4 r/min is shown in **Figure 6a**. It is seen that the crater has a well-defined circular shape that is the same for all the craters obtained. As seen from **Figures 6b** and **d**, the coating has shown quite a good adhesion to the substrate. It is possible to divide the wear on the crater into three different zones. The first one is the tearing that occurred at the top side of the crater (**Figure 6b**). Observing the SEM image, it can be concluded that it was caused by a plastic deformation of the coating material due to the cutting effect of the abrasive particles. The second wear is the rupture of the coating and the substrate material resulting from a locally exceeded plastic deformation of these materials in front of the abrasive SiC particles (**Figure 6c**). On the surface, the lateral-fracture wear mechanism was observed depending on a very small size of the abrasive particles. The third wear is the regularly spaced, parallel grooves that occurred at the bottom side of the crater where the abrasive slurry leaves the wear zone, as observed by

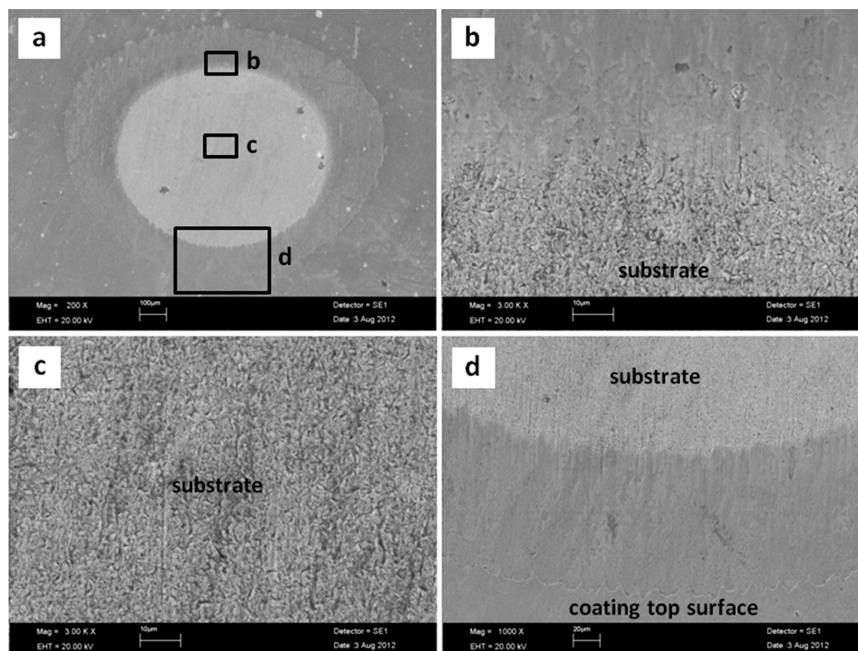


Figure 6: SEM images of a micro-abrasion crater on the nc-TiAlSiN/TiSiN/TiAlN coating after the sliding distance of 83.2 m
Slika 6: SEM-posnetki kraterja pri mikroabraziji na prevleki nc-TiAlSiN/TiSiN/TiAlN po 83,2 m drsenja

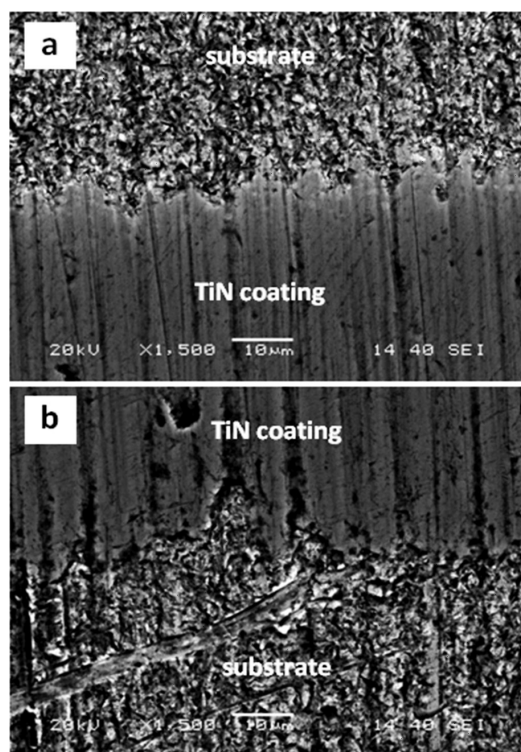


Figure 7: SEM images of the: a) bottom and b) top side of the micro-abrasion crater on the single-layer TiN coating after the sliding distance of 83.2 m

Slika 7: SEM-posnetka: a) dna in b) vrha kraterja pri mikroabraziji na enoplastnem sloju TiN po 83,2 m drsenja

Martinho et al.¹⁷ (**Figure 6d**). The difference between the wear mechanisms at the top and bottom sides of the crater can be due to the initial particle distribution in the contact inlet area. At the bottom side, the first grooves are drawn by the first particles embedded in the ball surface due to the two-body micro-abrasion wear mechanism, and the following particles follow the same trajectory.⁹ However, at the top side of the crater, the abrasive-slurry supply destroys the groove trajectory of the previous particles due to the three-body wear mechanism.

The images of the crater formed on the single-layer TiN coating of the AISI H11 steel after the sliding distance of 83.2 m at the ball rotation speed of 147.4 r/min are shown in **Figure 7**. It is clearly seen from the wear image that the regularly spaced, parallel, deep grooves form on the TiN coating and AISI H11 steel as a result of the sliding of the harder SiC particles due to a two-body micro-abrasion wear mechanism. Differently from the nc-TiAlSiN/TiSiN/TiAlN coating, these grooves exist at both the bottom (**Figure 7a**) and top sides (**Figure 7b**) of the crater on the TiN coating. The wear mechanisms at the top side of the crater on the nc-TiAlSiN/TiSiN/TiAlN coating were explained beforehand (**Figure 6b**). The reason for the difference in the wear mechanisms at the top sides of the craters on the compared coatings is probably that the micro-hardness of the TiN coating (3072 HV) is lower than that

of the nc-TiAlSiN/TiSiN/TiAlN coating (3869 HV). The TiN coating is easily worn by hard SiC particles and the forming grooves are deepened quickly. In addition, the lower adhesion of the TiN coating, compared to the nc-TiAlSiN/TiSiN/TiAlN coating, resulted in the detachments of the coating along the substrate-coating boundary and even in the wearing of the inner part of the coating. The wear mechanism on the AISI H11 steel is similar to that on the TiN coating due to the same reasons explained above (**Figures 7a** and **b**).

4 CONCLUSIONS

In the study, the effect of the nc-TiAlSiN/TiSiN/TiAlN hard coating on the abrasive-wear resistance of the AISI H11 steel was investigated using the free-ball abrasive-wear test and the following results were drawn:

The nc-TiAlSiN/TiSiN/TiAlN hard coating has a better adhesion to the AISI H11 steel substrate and a higher abrasive-wear resistance than the conventional TiN coating. The nc-TiAlSiN/TiSiN/TiAlN hard coating provides three times more micro-abrasive wear resistance than the uncoated AISI H11 substrate under the test conditions. A two-fold increase in the sliding speed results in an approximately two-fold increase in the removed-wear volume. Three different wear mechanisms – micro-scratch, lateral fracture and plastic deformation – take place on the craters formed on the nc-TiAlSiN/TiSiN/TiAlN coated AISI H11 steel.

5 REFERENCES

- ¹ M. B. Karamış, K. Yıldızlı, G. Çarkıt Aydın, Sliding/rolling wear performance of plasma nitrided H11 hot working steel, *Tribology International*, 51 (2012), 18–24
- ² X. Z. Ding, C. T. Bui, X. T. Zeng, Abrasive wear resistance of Ti1-xAlxN hard coatings deposited by a vacuum arc system with lateral rotating cathodes, *Surface and Coatings Technology*, 203 (2008) 5–7, 680–684
- ³ J. Richter, Micro-scale abrasion testing of PVD TiN coatings on conventional and nonledeburitic high-speed steels, *Wear*, 257 (2004) 3–4, 304–310
- ⁴ H. Çalışkan, C. Kurbanoglu, P. Panjan, D. Kramar, Investigation of the performance of carbide cutting tools with hard coatings in hard milling based on the response surface methodology, *The International Journal of Advanced Manufacturing Technology*, 66 (2013), 5–8, 883–893
- ⁵ M. G. Faga, G. Gautier, R. Calzavarini, M. Perucca, E. A. Boot, F. Cartasegna, L. Settineri, AlSiTiN nanocomposite coatings developed via Arc Cathodic PVD: Evaluation of wear resistance via tribological analysis and high speed machining operations, *Wear*, 263 (2007) 7–12, 1306–1314
- ⁶ H. Çalışkan, C. Kurbanoglu, D. Kramar, P. Panjan, J. Kopač, Hard milling operation of AISI O2 cold work tool steel by carbide tools protected with different hard coatings, *Engineering Science and Technology: An International Journal (JESTECH)*, 15 (2012) 1, 21–26
- ⁷ F. Klocke, F. Quito, K. Arntz, A. A. Souza, C. Ader, Investigation of tool geometry, coating and coolant in micro milling of single crystal Nickel-based superalloy René N5, in: 3rd CIRP International Conference on High Performance Cutting, Dublin-Ireland, 2008, 561–574

- ⁸ Å. Kassman, S. Jacobson, L. Erickson, P. Hedenqvist, M. Olsson, A new test method for the intrinsic abrasion resistance of thin coatings, *Surface and Coatings Technology*, 50 (1991) 1, 75–84
- ⁹ M. F. C. Andrade, R. P. Martinho, F. J. G. Silva, R. J. D. Alexandre, A. P. M. Baptista, Influence of the abrasive particles size in the micro-abrasion wear tests of TiAlSiN thin coatings, *Wear*, 267 (2009) 1–4, 12–18
- ¹⁰ J. C. A. Batista, C. Godoy, A. Matthews, Micro-scale abrasive wear testing of duplex and non-duplex (single-layered) PVD (Ti,Al)N, TiN and Cr–N coatings, *Tribology International*, 35 (2002) 6, 363–372
- ¹¹ D. N. Allsopp, I. M. Hutchings, Micro-scale abrasion and scratch response of PVD coatings at elevated temperatures, *Wear*, 251 (2001) 1–12, 1308–1314
- ¹² M. J. Ibáñez, J. Gilabert, M. Vicent, P. Gómez, D. Muñoz, Determination of the wear resistance of traditional ceramic materials by means of micro-abrasion technique, *Wear*, 267 (2009) 11, 2048–2054
- ¹³ W. C. Oliver, G. M. Pharr, An improved technique for determining hardness and elastic modulus using load and displacement sensing indentation experiments, *Journal of Materials Research*, 7 (1992), 1564–1583
- ¹⁴ K. I. Schiffmann, R. Bethke, N. Kristen, Analysis of perforating and non-perforating micro-scale abrasion tests on coated substrates, *Surface and Coatings Technology*, 200 (2005) 7, 2348–2357
- ¹⁵ I. M. Hutchings, Abrasive and erosive wear tests for thin coatings: a unified approach, *Tribology International*, 31 (1998) 1–3, 5–15
- ¹⁶ S. J. Bull, Failure mode maps in the thin film scratch adhesion test, *Tribology International*, 30 (1997) 7, 491–498
- ¹⁷ R. P. Martinho, M. F. C. Andrade, F. J. G. Silva, R. J. D. Alexandre, A. P. M. Baptista, Micro-abrasion wear behaviour of TiAlCrSiN nanostructured coatings, *Wear*, 267 (2009) 5–8, 1160–1165

DETERMINATION OF THE SOLIDUS AND LIQUIDUS TEMPERATURES OF THE REAL-STEEL GRADES WITH DYNAMIC THERMAL-ANALYSIS METHODS

DOLOČANJE SOLIDUSNIH IN LIKVIDUSNIH TEMPERATUR REALNIH JEKEL Z METODAMI DINAMIČNE ANALIZE

Karel Gryc¹, Bedřich Smetana², Monika Žaludová², Karel Michalek¹, Petr Klus¹,
Markéta Tkadlečková¹, Ladislav Socha¹, Jana Dobrovská², Pavel Machovčák³,
Ladislav Válek⁴, Radim Pachlopník⁴, Bohuslav Chmiel⁵

¹VŠB-Technical University of Ostrava, Faculty of Metallurgy and Materials Engineering, Department of Metallurgy and Foundry, and Regional Materials Science and Technology Centre, 17. listopadu 15, 708 33 Ostrava-Poruba, Czech Republic

²VŠB-Technical University of Ostrava, Faculty of Metallurgy and Materials Engineering, Department of Physical Chemistry and Theory of Technological Processes, and Regional Materials Science and Technology Centre, 17. listopadu 15, 708 33 Ostrava-Poruba, Czech Republic

³Vítkovice Heavy Machinery a. s., Ruská 2887/101, 706 02 Ostrava-Vítkovice, Czech Republic

⁴AccelorMittal Ostrava a.s., Research, Vratimovská 689, 707 02 Ostrava-Kunčice, Czech Republic

⁵Třinecké Železářny a.s., Průmyslová 1000, 73970 Třinec-Staré Město, Czech Republic
karel.gryc@vsb.cz

Prejem rokopisa – received: 2012-10-10; sprejem za objavo – accepted for publication: 2013-02-22

The knowledge of the solidus and liquidus temperatures of the real-steel grades is one of the most important technological factors – especially when dealing with the processes of casting and solidification. These temperatures are critical parameters for proper settings of the models (physical or numerical) or in the final stage of an applied research of a real process. A correct setting of a production technology is significantly affecting the final quality of the as-cast steel (billets or ingots). Therefore, this paper is devoted to discussing the findings obtained during a utilization of dynamic thermal-analysis methods to identify the solidus and liquidus temperatures applicable to commercially produced steels. The results obtained with a differential thermal analysis (DTA) for three steel grades and with 3D differential scanning calorimetry (3D DSC) for two steel grades are compared with the results of the selected equations commonly used for liquidus and/or solidus temperature calculations. The calculations obtained with the Computherm SW for the discussed steels were also realized.

It can be stated that the equilibrium liquidus and solidus temperatures obtained with the above-mentioned methods for each steel grade differ. The differences between the calculated results, the thermodynamic calculations and thermal-analysis results are very unpredictable and vary individually for different steels. These differences are not marginal (tens of Celsius degrees). So, it is sometimes suitable to combine several methods for a proper determination of the liquidus and solidus temperatures for a correct setting of a steel-making process or its modelling. The best solution for a technological process is to obtain the liquidus and solidus temperatures for a concrete-steel grade from a given steelmaking practice – a thermal analysis of a concrete-steel grade is a possible way.

Keywords: steel, solidus temperature, liquidus temperature, thermal analysis, thermodynamic database, calculation

Poznavanje solidusnih in likvidusnih temperatur realnih jekel je med najpomembnejšimi tehnološkimi dejavniki – še posebno pri obravnavi procesov med ulivanjem in strjevanjem. Te temperature so kritični parametri za pravilno postavitev modela (fizikalnega ali numeričnega) ali pri končni stopnji raziskav realnega procesa. Pravilna postavitev proizvodne tehnologije pomembno vpliva na končno kvaliteto ulitega jekla (gredic in ingotov). Zato je ta članek namenjen razpravi o ugotovitvah, dobljenih med uporabo metod dinamične termične analize za ugotavljanje solidusne in likvidusne temperature pri komercialno proizvedenih jeklih. Rezultati, dobljeni z diferenčno termično analizo (DTA) za 3 jekla in s 3D diferenčno vrstično kalorimetrijo (3D DSC) za 2 vrsti jekel, so bili primerjani z rezultati iz izbranih enačb, ki se navadno uporabljajo za izračun temperature solidusa in likvidusa. Za obravnavana jekla so bili tudi izdelani izračuni s Computherm SW.

Ugotovljeno je bilo, da se ravnotežne likvidusne in solidusne temperature, dobljene z omenjenimi metodami, razlikujejo. Razlike med izračunanimi rezultati, termodinamičnimi izračuni in rezultati termične analize so nepredvidljivi in se različno spreminjajo pri različnih jeklih. Te razlike niso nepomembne (desetine stopinj Celzija). Zato je včasih pomembno kombinirati več metod za pravilno določitev likvidusne in solidusne temperature pri procesu proizvodnje jekla ali njegovem modeliranju. Najboljša rešitev za tehnološki proces je ugotavljanje likvidusne in solidusne temperature pri konkretnem jeklu iz dane jeklarske prakse – mogoča pot pa je tudi s termično analizo konkretnega jekla.

Ključne besede: jeklo, temperatura solidusa, temperatura likvidusa, termična analiza, termodinamični podatki, izračun

1 INTRODUCTION

A better control of the entire steel production cycle – from the selection of quality raw materials to a proper control of primary and secondary metallurgy processes and, finally, an optimum setting of the casting and solidification conditions, is necessary for a modern, competitive steel-making company. In the refining processes, optimizing the slag regimes,^{1,2} thermal and chemical

homogenization of the melt³ or filtration of the steel⁴ are very important stages. With respect to the casting and solidification of the examined steel, important steps toward optimizing the process of solidification of heavy forged ingots⁵ are currently being implemented.

It is not simple^{6–11} to experimentally determine the phase transformation temperatures, especially the solidus and liquidus temperatures of the complex multicom-

ponent systems (steels), and at the level above 1000 °C. There are only a few methods that are suitable to provide these results. A comparison between them is shown in the literature.¹² Generally, these methods (briefly described below) are based on a detection of the temperature or a dimensional change induced due to a heat-treated process (an on-going phase transformation).

The direct thermal-analysis method^{13–15} is based on a direct measurement of the temperature of the sample during its continuous linear heating/cooling. The result is a heating/cooling curve. There is a deviation from the otherwise linear curve progression during the phase transformation in the samples. It is possible to obtain the temperatures of a phase transformation based on the curve deviations (e.g., liquidus and/or solidus temperatures).

The differential thermal analysis (DTA) and/or the differential scanning calorimetry (DSC)^{13–15} are the methods based on the same principle. The principle of these methods is a measurement of the temperature difference (heat-flow difference) between the measured sample and the reference. The reference can be an empty reference crucible or a reference crucible with a standard material. The sample and reference are subjected to the same setting of the temperature program of the continuous linear heating/cooling. The result is a DTA curve (a DSC curve) expressing the dependence of the temperature difference (the heat-flux difference) between the measured sample and the reference. If there is an on-going phase transformation in the sample, there is also a deflection from the baseline (a peak is formed). It is possible to obtain the temperatures of phase transformations by interpreting such peaks for given experimental conditions.

Dilatometry^{13–15} is a method based on monitoring the dimensional changes of a sample when it is exposed to a controlled temperature regime, most often to linear heating or cooling. The method is used mainly for the study of the phase transformation temperatures and dimensional changes of the samples in the solid phase. The measurement result is a curve, expressing the dimensional change of a sample in dependence on the

time or the temperature, respectively. The breaks on this curve (a significant deviation from the linear shape) indicate an on-going phase transformation. The temperatures detected with the phase transformations, under the conditions of the experiment, can be obtained by interpreting these deviations.

Apart from the above-mentioned dynamic methods of the thermal analysis, it is also possible to obtain the temperatures of the solidus and liquidus of steel using the broadly known and used equations (1–11).^{16–22} Different kinds of thermodynamic databases integrated into the software packages that are on the market, such as IDS or Computherm, can be used, too.

2 METHODS FOR DETERMINING THE LIQUIDUS AND SOLIDUS TEMPERATURES

Our study of the phase transformations in a high-temperature area was realized with the dynamic methods of the thermal analysis (TA), with the below-described equations and the thermodynamic software Computherm, in the new Laboratory for Modelling the Processes in the Liquid and Solid Phases. This laboratory was set up for the project establishing the Regional Materials Science and Technology Centre at the VŠB – Technical University of Ostrava, Faculty of Metallurgy and Materials Engineering in the Czech Republic. The liquidus and solidus temperatures were determined for the industrially produced steel grades taken from the production cycles in the companies represented by the above-mentioned coauthors.

2.1 High-temperature dynamic thermal analysis

It is possible to use three different laboratory devices for the thermal analysis in the conditions of the new laboratory: Netzsch STA 449 F3 Jupiter (STA-Simultaneous Thermal Analyser), Setaram SETSYS 18_{TM} and Setaram MHTC (Multi High Temperature Calorimeter) (Table 1).

Table 1 shows the characteristic features of our experiment. It is possible to study thermophysical

Table 1: Experimental parameters of the used analytical systems

Tabela 1: Eksperimentalni parametri pri uporabljenih analitičnih sistemih

Parameter	Netzsch STA 449 F3 Jupiter	Setaram SETSYS 18 _{TM}	Setaram MHTC
Experimental method	c-DTA – "calculated curve"; TG/DTA; TG/DSC; TG	TG/DTA; TG/DSC; TG; TMA	HF DSC; DROP; DSC
Temperature range	20 °C to 2000 °C	20 °C to 1750 °C	20 °C to 1600 °C
Heating/cooling rate	0.01–50 K min ^{–1}	0.01–100 K min ^{–1}	0.001–50 K min ^{–1}
Temperature programme	Linear heating/cooling; isothermal holding; cycling		
Sample mass	Up to 30 g (35 g)	Up to 500 mg	HF DSC up to 2.5 g DROP up to 30 g
Atmosphere	Vacuum; inert; reactive		
Sensor type	Flat DSC sensor, S-type	DTA-tricouple sensor, S-type	HF 3D DSC sensor, B-type

Note: STA (Simultaneous Thermal Analysis), TG (Thermogravimetry), MHTC (Multi-High Temperature Calorimeter), DSC (Differential Scanning Calorimetry), HF (Heat Flux), TMA (Thermomechanical Analysis), DROP Calorimetry (a method based on throwing a sample to a pre-heated furnace at a defined temperature after measuring the heat absorbed, also known as the "throwing calorimetry" method)

properties, e.g., the liquidus and solidus temperatures of the steel grades under various experimental conditions: different sample masses, different heating/cooling rates, and different methods.

The measurements carried out in the laboratory are focused not only on determining the temperatures close to the equilibrium temperatures, or almost the equilibrium, but also on determining the phase-transformation temperatures depending on the cooling process and the subsequent thermomechanical treatment of the steels in the steel plants. The obtained temperatures can differ from the equilibrium, or close-to-equilibrium, temperatures, but can be also very important for an optimal setting of a real steelmaking technology. An example of such a solution was already presented²³.

To achieve the equilibrium state of a sample is, in some cases, very difficult. The equilibrium means that the structure and phases of the samples are at equilibrium. Moreover, an achievement of an equilibrium state during DTA (or DSC) is, due to the principle of these methods, not possible. For this reason the temperatures are set close to equilibrium, being almost equilibrium. Possible approximations to the equilibrium state, with respect to DTA or DSC, can be found, e.g., in^{9,24,25}.

Table 2: Studied steel grades, used devices, methods and sample mass
Tabela 2: Preučevane vrste jekel, uporabljene naprave, metode in masa vzorcev

Steel grade	Chemical composition, selected elements, w/%	Device, method	Sample mass, g
A	0.6 C; 5 Cr; 2 Ni + V	SETSYS; DTA	0.2
B	0.5 C; 8 Cr; 2 Ni + V		
C	0.04 C; 3 Si		
D	0.35 C; 0.08 Si; 1.3 Mn; 0.25 Cr; 0.2 Ni	MHTC; 3D DSC	2.6
E	0.25 C; 0.25 Si; 1.4 Mn; 0.1 Cr; 0.75 Ni		

Note: The publication of the chemical compositions of the steels was limited due to the requirements of the industrial partners

This paper is devoted to determining the liquidus and solidus temperatures for the selected real-steel grades (**Table 2**).

The content of carbon was determined with the combustion-infrared detection technique (LECO devices). The contents of the other selected elements were determined with the optical emission spectrometers. The steel samples were taken from different steel semi-products, depending on the used technologies in individual steel-works. For the sake of the heterogeneity of the steel samples, they were always obtained with the internal methods used to verify the crucial mechanical and other properties of the studied steel grades. In this way the possibility of the non-standard structural and chemical heterogeneity in the taken samples was minimized. The Setaram SETSYS 18_{TM} and Setaram MHTC devices were used.

The DTA method and the S-type measuring thermocouple (Pt/PtRh 10 %) was used to obtain the temperatures of the phase transformations with the SETSYS 18_{TM} equipment for the samples of the A, B and C steel grades. The samples were analysed in alumina (Al₂O₃) crucibles with a capacity of 0.10 mL. The weight of the analysed steel samples was approximately 200 mg. The experiments were performed at a linear heating rate of 10 °C min⁻¹ and 15 °C min⁻¹ using also a reference crucible – without the standard material. A constant dynamic atmosphere – inert argon with the purity of >99.9999 % – was maintained during the measurement. Such a high-purity gas is obtained by using a gas filtering device (a Getter gas purifier).

The DSC method was used for analysing the D and E steel-grade samples. The HF 3D DSC sensor (B-type thermocouple: PtRh 6 %/PtRh 30 %) was used with the MHTC equipment. The samples were analysed in alumina crucibles (Al₂O₃) with a capacity of 0.7 mL. The weight of the analysed samples was approximately 2.6 g. A stable, dynamic atmosphere (helium, 6 N) and a linear

Table 3: Conditions and results of the thermoanalytical measurements; standard deviations and mean values of T_S and T_L

Tabela 3: Pogoji in rezultati termoanalitskih meritev, standardni odmik in glavne vrednosti T_S in T_L

Steel grade	Method	Sample mass/mg	Heating rate/ °C min ⁻¹	Determined temperature		Std. deviation		Mean value	
				<i>T_S</i> /°C	<i>T_L</i> */°C	<i>T_S</i> /°C	<i>T_L</i> /°C	<i>T_S</i> /°C	<i>T_L</i> /°C
A	DTA	210.1	10	1341.0	1464.4	0.6	0.6	1341	1465
		204.8	15	1340.1	1465.2				
B		190.1	10	1340.0	1458.5	2.8	1.0	1338	1458
		222.3	15	1336.0	1457.1				
C		198.3	10	1480.8	1495.5	0.3	1.3	1481	1497
		206.4		1481.1	1495.9				
		205.6		1481.0	1498.5				
		207.9		1480.5	1496.4				
D	DSC	2721.5	1	1437.7	1499.8	0.4	0.9	1437	1500
		2589.5	2	1437.2	1501.1				
E		2758.7	1	1454.2	1505.4	2.1	0.1	1456	1505
		2709.2		1457.2	1505.5				

Note: * T_L recalculated for the "zero" heating rate and "zero" mass of the sample

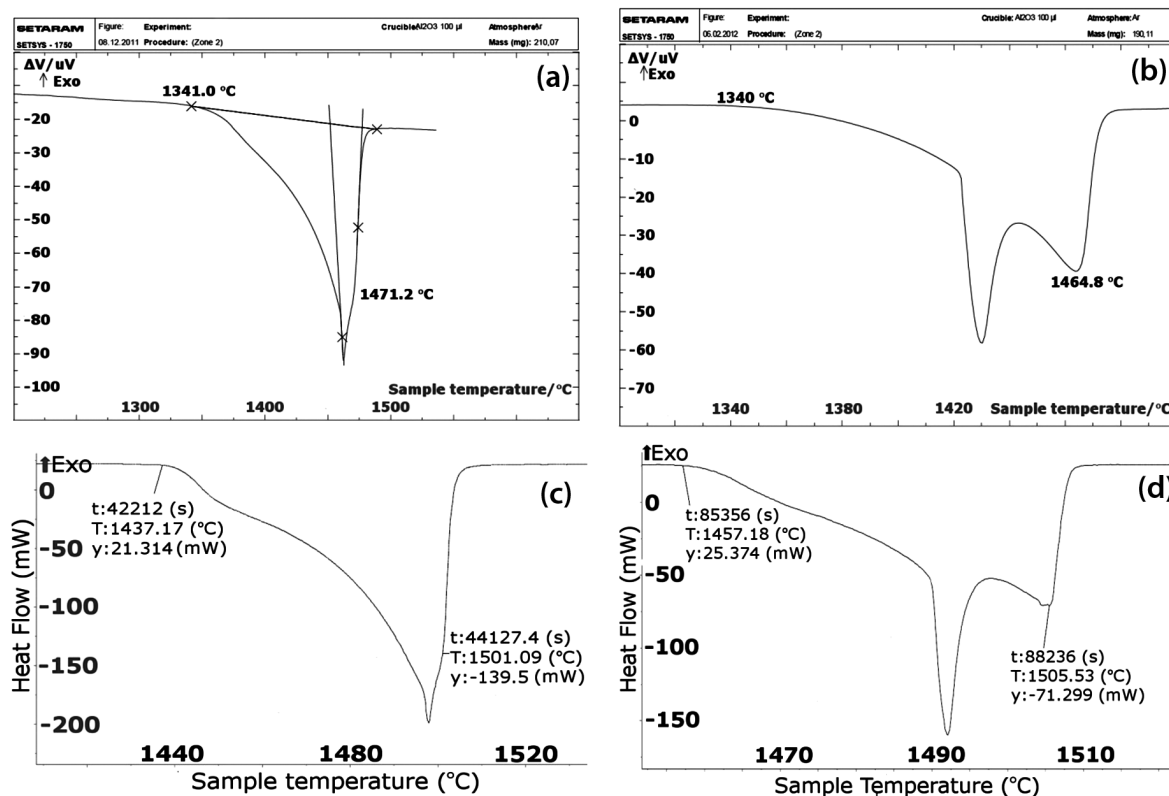


Figure 1: Examples of the selected DTA and DSC curves obtained with the measurements of the real-steel grades, liquidus and solidus temperatures: a) DTA curve, the heating rate of $10\text{ }^{\circ}\text{C min}^{-1}$, A steel grade, b) DTA curve, the heating rate of $10\text{ }^{\circ}\text{C min}^{-1}$, B steel grade, c) DSC curve, the heating rate of $2\text{ }^{\circ}\text{C min}^{-1}$, D steel grade, d) DSC curve, the heating rate of $1\text{ }^{\circ}\text{C min}^{-1}$, E steel grade

Slika 1: Primeri izbranih DTA in DSC krivulj, dobljenih med meritvami realnega jekla, likvidus in solidus temperature: a) DTA-krivulja, hitrost ogrevanja $10\text{ }^{\circ}\text{C min}^{-1}$, jeklo A, b) DTA-krivulja, hitrost ogrevanja $10\text{ }^{\circ}\text{C min}^{-1}$, jeklo B, c) DSC-krivulja, hitrost ogrevanja $2\text{ }^{\circ}\text{C min}^{-1}$, jeklo D, d) DSC-krivulja, hitrost ogrevanja $1\text{ }^{\circ}\text{C min}^{-1}$, jeklo E

heating rate of $1\text{ }^{\circ}\text{C min}^{-1}$ and $2\text{ }^{\circ}\text{C min}^{-1}$ were maintained during the analyses.

Each grade of steel was analysed two or four times at identical or almost identical conditions (the samples selected for DTA and the samples selected for DSC were treated separately). The final values of T_L and T_S were calculated as the mean values of the two or four experimentally obtained values (Table 3). The maximum standard deviation from the two or four measurements of the individual steel grades was $2.8\text{ }^{\circ}\text{C}$ for T_S of the B steel grade.

The examples of the DTA and DSC curves for the studied steel grades are shown in Figure 1. The temperature of solidus was evaluated as the onset point of the first peak and the temperature of liquidus as the peak top (the last peak of the three observed peaks, e.g., 1501.09 for sample D – Figure 1c). Three thermal events (endothermic effects) were observed during the whole melting process, which demonstrated the melting of the steel (the melting region). The peak top, in comparison with the peak start (onset) temperature, is strongly dependent on the sample mass^{9,13–15,26} and heating rate.^{9,13–15,26} The correction with respect to the sample mass and heating rate (the experimental parameters) was undertaken.^{9,26} The temperature of liquidus was recalculated to the "zero"

heating rate and to the "zero" mass of the sample.^{13–15} The temperature calibration was also performed with the high-purity Ni and Pd (5N).

2.2 Calculation of the liquidus and solidus temperatures

The below-described equations and the Computherm software were used for calculating the liquidus (T_L) and solidus (T_S) temperatures of the above-mentioned steel grades.

The equations (1⁷, 2¹⁸, 3¹⁹, 4¹⁹, 5²⁰, 6²¹, 7²², 8¹⁹, 9¹⁹, 10²³, 11²³) are based on the effect of the contents of the selected elements (mass fraction (%)) of an element in the steel on the final liquidus/solidus temperatures. Only Computherm SW and equation (11) were used for the solidus-temperature calculations.

$$T_L = 1535 - 73(\%C) - 3(\%Mn) - 12(\%Si) - 28(\%P) - 30(\%S) - 7(\%Cu) - 1(\%Cr) - 3.5(\%Ni) - 3(\%Al) - 1(\%Sn) - 2(\%Mo) - 18(\%Ti) - 2(\%V) - 1.8(\%Co) \quad (1)$$

$$T_L = 1534 - [80(\%C) + 4(\%Mn) + 14(\%Si) + 35(\%P) + 1.4(\%Cr) + 2.6(\%Ni) - 1.2(\%Mo) + 3.4(\%Al)] \quad (2)$$

$$T_L = 1537.7 - 100.3(\%C) + 22.1(\%C)^2 - 13.55(\%Si) + 0.64(\%Si)^2 - 5.82(\%Mn) - 0.3(\%Mn)^2 - 4.18(\%Ni) -$$

$$- 0.01(\%Ni)^2 - 4.1(\%Cu) - 1.59(\%Cr) + 0.07(\%Cr)^2 - 3(\%Mo) \quad (3)$$

$$T_L = 1535.6 - 88(\%C) - 8(\%Si) - 5(\%Cu) - 1.5(\%Cr) - 4(\%Ni) - 2(\%Mo) - 18(\%Ti) \quad (4)$$

$$T_L = 1535 - 66.73(\%C) - 7.8(\%Si) - 5(\%Mn) - 30(\%P) - 25(\%S) - 5(\%Cu) - 1.5(\%Cr) - 4(\%Ni) - 2(\%V) \quad (5)$$

$$T_L = 1535 - 80(\%C) - 14(\%Si) - 4(\%Mn) - 35(\%P) - 35(\%S) - 1.4(\%Cr) - 2.6(\%Ni) - 3.4(\%Al) \quad (6)$$

$$T_L = 1539 - K(\%C) - 8(\%Si) - 5(\%Mn) - 30(\%P) - 25(\%S) - 5(\%Cu) - 1.5(\%Cr) - 4(\%Ni) - 2(\%Mo) - 2(\%V) - 1(\%W) - 14(\%As) - 10(\%Sn) - 1300(\%H) - 90(\%N) - 80(\%O) \quad (7)$$

where the K coefficient varies with respect to different contents of carbon:

$$C \leq 1\%; \quad K = 65$$

$$C > 1\%; \quad K = 70$$

$$C > 2\%; \quad K = 75$$

$$C > 2.5\%; \quad K = 80$$

$$T_L = 1536.6 - K(\%C) - 8.1(\%Si) - 5.05(\%Mn) - 31(\%P) - 25.5(\%S) - 1.5(\%Cr) - 4(\%Ni) - 2(\%Mo) \quad (8)$$

where the K coefficient varies with respect to different contents of carbon:

$$T_L = 1536 - K(\%C) - 8(\%Si) - 5(\%Mn) - 30(\%P) - 25(\%S) - 1.7(\%Al) - 5(\%Cu) - 1.5(\%Cr) - 4(\%Ni) - 2(\%V) - 1(\%W) - 1.7(\%Co) - 12.8(\%Zr) - 7(\%Nb) - 3(\%Ta) - 14(\%Ti) \quad (9)$$

where the K coefficient varies with respect to different contents of carbon:

$$C \leq 2\%; \quad K = 65$$

$$C \in (0.2; 0.5)\%; \quad K = 88$$

$$T_L = 1536 - 8(\%C) - 7.6(\%Si) - 3.9(\%Mn) - 33.4(\%P) - 38(\%S) - 3.7(\%Cu) - 3.1(\%Ni) - 1.3(\%Cr) - 3.6(\%Al) \quad (10)$$

$$T_L = 1536 - 251(\%C) - 12.3(\%Si) - 6.8(\%Mn) - 123.4(\%P) - 183.9(\%S) - 3.3(\%Ni) - 1.4(\%Cr) - 3.1(\%Cu) - 3.6(\%Al) \quad (11)$$

It can be seen from the equations (1–10) that there are different elements and their multiples are taken into account in individual calculations. Some equations only include the effects of certain elements; on the other hand, other equations include a higher number of the elements. This fact can, in some cases, lead to substantially different calculated values of T_s and T_L . A discussion about the limitations of the mentioned and generally used equations is out of range of this paper.

Computherm SW is able to calculate both studied temperatures. It is possible to choose two microsegregation models (Scheil or Lever). In the case of Lever, the Lever rule has been applied, corresponding to a complete mixing of the solute in the solid (i.e., a very good diffusion in the solid). On the other hand, the Scheil model corresponds to a no-diffusion model for the solid phase (both models consider a complete mixing of an infinite diffusion in the liquid). The Back-Diffusion model allows for some diffusion in the solid and corresponds thus to the situation in between the Lever rule and Scheil. When the Back-Diffusion model is used, the average cooling rate (corresponding to the representative cooling rate of the casting to be modelled) should be specified in order to determine the amount of back diffusion. For iron and carbon steel, the Lever rule is still recommended.²⁷

The Computherm Fe-rich-alloy database has defined the limitations of the chemical composition and recommended composition limits for them.²⁸ The Lever rule was selected (without the Pb, Sn, As, Zr, Bi, Ca, Sb, B, N contents) for determining T_L and/or T_s in the frame of this paper.

Table 4: Liquidus temperatures for the studied steel grades determined with the equations, Computherm and thermoanalytical methods

Tabela 4: Likvidusne temperature preučevanih jekel, določene z enačbami, s Computherm in termoanalitičnimi metodami

Method	Liquidus temperatures for steel grades, $T_L/^\circ\text{C}$					Deviations of calculated T_L against TA results for steels/ $^\circ\text{C}$				
	A	B	C	D	E	A	B	C	D	E
(1)	1471	1471	1491	1499	1503	6	13	-6	-1	-2
(2)	1464	1465	1486	1495	1502	-1	7	-11	-5	-3
(3)	1461	1459	1495	1490	1495	-4	1	-2	-10	-10
(4)	1463	1465	1504	1492	1498	-2	7	7	-8	-7
(5)	1476	1476	1504	1499	1504	11	18	7	-1	-1
(6)	1465	1466	1487	1496	1502	0	8	-10	-4	-3
(7)	1479	1478	1508	1504	1508	14	20	11	4	3
(8)	1463	1465	1506	1493	1499	-2	7	9	-7	-6
(9)	1478	1477	1505	1501	1505	13	19	8	1	0
(10)	1473	1475	1509	1498	1504	8	17	12	-2	-1
SW	1467	1465	1492	1497	1503	2	7	-5	-3	-2
TA	1465*	1458*	1497*	1500**	1505**	0	0	0	0	0

Note: *DTA results; **DSC results

3 RESULTS AND DISCUSSION

Based on the above-described methods of the thermal analysis, the equations and calculations realized in Computherm SW, the liquidus temperatures for the selected, industrially produced steels were determined (**Table 4**).

It can be seen that certain variability between the obtained T_L values exists. Since the T_L values obtained with the thermal analysis (TA) – DTA/DSC measurement – were determined from the real-steel samples on the basis of the standardized methodology, it can be stated that the thermal-analysis results are the closest to the real T_L of the studied industrially produced steels. So, the thermal-analysis results are used as the core values for the next comparison.

The data based on the equations differs from the thermal-analysis results by 0 °C to 20 °C. It is not possible to identify the best equation for the T_L determination for all the analysed steel grades. The overall best agreement of the T_L calculated using equations (1–10) with the thermal-analysis results was achieved as the "zero" deviation for steel grade A if equation (6) was used. While calculating the T_L for steel grade A using equation (7), the calculated value is by 14 °C higher than the experimentally obtained T_L . However, the best agreement between the measured and the calculated results for steel grade B is reached using equation (3) – the calculated T_L is only 1 °C above the measured temperature. The overall poorest deviation for all the steels was obtained for steel grade B when comparing the value calculated with equation (7) with the TA measurements – this calculation is 20 °C above the thermal-analysis results. For the C steel grade, the T_L closest to the measurements (2 °C lower) was calculated with equation (3). The poorest value (12 °C above TA) was determined with equation (10). For the D steel, the TA measured T_L differs by 1 °C from the calculations made with the equations (1, 5 and 9). The poorest agreement between the equations and the TA results obtained with the DSC method was found for the D and E steels (this T_L is 10 °C lower than in the case of TA). The T_L value obtained with equation (9) fits the temperature found with the TA measurements.

Thus, the reason for this variability of the results can mainly be found in different contents of the alloying elements of individually studied steel grades. Moreover, the steel grades studied are such that they cannot be labelled as the common Fe-C systems.

If the Computherm calculation (SW line in **Table 4**) is compared with the thermal-analysis data, the difference in T_L is from 2 °C to 7 °C, and the mean difference value for all five steel grades is 3.8 °C. Focused on a comparison between the T_L computed with Computherm or calculated with equations (1–10) and the T_L measured with the DTA or 3D DSC methods, it can be postulated that the results achieved with Computherm are very close (unlike equations) to the thermal-analysis core measurements for the studied steel.

The solidus temperatures for the studied steel grades were obtained with only one equation (11), with the Computherm thermodynamic calculation (SW) and with the thermal-analysis methods (DTA or 3D DSC) – the results and their comparison are in **Table 5**.

Opposed to the liquidus temperatures, **Table 5** shows that there are big differences between the T_S values calculated with equation (11) or with Computherm SW, and the thermal-analysis results, ranging from 1 °C to 50 °C. The T_S determination for the B steel grade shows that the value calculated with equation (11) is 42 °C higher than the results of the TA experiments. This equation (11) was designed for the steels with low contents of alloying elements. On the other hand, the T_S obtained with this equation was only 1 °C higher for the C steel grade. The best fit of the SW prediction was obtained for the B steel grade (4 °C) and the poorest one for the C steel grade (50 °C). The reasons for such great differences can be connected with the limitations defined in the User Guide²⁶ in terms of a very specific (high) content of Si in this steel.

4 CONCLUSIONS

The aim of this paper was to present the current possibilities of determining the liquidus and solidus temperatures for the real-steel grades with a specific alloying-element content using the thermal-analysis methods, and their comparison with the calculated values obtained with the commonly used equations and the values obtained with the thermodynamic calculations performed with Computherm SW.

The thermal-analysis results were used as the core values for the comparison.

It is possible to conclude the following results:

1. The values of the liquidus (T_L) temperatures calculated with equations (1–10) differ from the experimentally obtained data by up to 20 °C.

Table 5: Solidus temperatures for the studied steel grades determined with the equations, Computherm and thermoanalytical methods

Tabela 5: Solidus temperature preučevanih jekel, določene z enačbami, s Computherm in termoanalitičnimi metodami

Method	Solidus temperatures for steel grades, T_S /°C					Deviations of calculated T_S against TA results for steels/°C				
	A	B	C	D	E	A	B	C	D	E
(11)	1360	1380	1482	1425	1451	19	42	1	–12	–5
SW	1358	1342	1431	1429	1444	17	4	–50	–8	–12
TA	1341*	1338*	1481*	1437**	1456**	0	0	0	0	0

Note: *DTA results; **DSC results

2. A better conformity was observed between the experimentally obtained liquidus temperatures and the liquidus temperatures obtained with the Computherm calculations (differences between 2 to 7 °C).
3. Solidus temperatures (T_s) were also obtained on the basis of a DTA (DSC) curve evaluation. The experimental solidus temperatures differ significantly, in some cases, from the values obtained on the basis of the performed calculations; they differ by up to 50 °C from the Computherm SW results and by up to 42 °C from the calculated values, see equation (11).
4. Generally, it may be stated that the variability of the calculated values, in comparison with the thermal analysis of the real-steel samples, is due to the specific contents of the alloying elements in the studied specific steel grades.
5. The calculated values should be verified against the experimental results. The calculation equations and SWs have some limitations with respect to the composition, i.e., the composition ranges of the alloyed and admixed elements. We should not include the influence of the phases presented in the steel and the segregation of the elements. SW calculations also have limitations in the implemented calculation methods.

The best possible way of optimising the metallurgical process of steel casting is to obtain the theoretical values of the crucial parameters such as the liquidus and solidus temperatures and to verify them using experimental measurements, followed by simulations and an implementation into the real casting process.

Acknowledgements

This paper was created in the frame of the following projects:

- No. CZ.1.05/2.1.00/01.0040 "Regional Materials Science and Technology Centre" within the frame of the operation programme "Research and Development for Innovations" financed by the Structural Funds and by the state budget of the Czech Republic;
- FR-TI3/373 "Research and Development of New Subledeburitic Steels for Wood Working with Improved Performance";
- TIP programme, project No. FR-TI3/053 "Improvement of magnetic and quality properties of strips from grain oriented electrical steels";
- No. P107/11/1566 of the Czech Science Foundation;
- SGS (student's university project) project No. 2012/10.

5 REFERENCES

- ¹ K. Michalek, L. Čamek, K. Grys et al., *Mater. Technol.*, 46 (2012) 3, 297–303
- ² L. Socha, J. Bažan, K. Grys et al., *Proc. of the 20th Int. Conf. on Met. and Mat.*, Metal 2011, Brno, 2011, 163–169
- ³ K. Michalek, K. Grys, J. Moravka, *Metalurgija*, 48 (2009), 215–218
- ⁴ K. Janiszewski, *Archives of Metallurgy and Materials*, 57 (2012), 135–143
- ⁵ M. Tkadlečková, P. Machovčák, K. Grys, et al., *Mater. Technol.*, 46 (2012) 4, 399–402
- ⁶ D. A. Porter et al., *Phase Transformations in Metals and Alloys*, 3rd ed., CRC Press, Boca Raton 2009, 500
- ⁷ J. Miettinen, *Metallurgical and Materials Transactions B*, 28B (1997), 281–297
- ⁸ B. Smetana, S. Zlá, M. Žaludová et al., *Metalurgija*, 51 (2012) 1, 121–124
- ⁹ M. Žaludová, B. Smetana, S. Zlá et al., *Journal of thermal analysis and calorimetry*, 111 (2013) 2, 1203–1210
- ¹⁰ J. C. Zhao, *Methods for Phase Diagram Determination*, Elsevier, Oxford 2007, 505
- ¹¹ W. Banda et. al., *Journal of Alloys and Compounds*, 461 (2008), 178–182
- ¹² S. Rusz, B. Smetana, I. Schindler et al., *Hutnické listy*, 64 (2011) 4, 66–69
- ¹³ P. K. Gallagher, *Handbook of Thermal Analysis and Calorimetry: Principles and Practice*, Vol. 1, 1st ed. 1998, 2nd impress., Elsevier Science B.V., Amsterdam 2003, 722
- ¹⁴ J. Šesták, *Měření termofyzikálních vlastností pevných látek [Measurement of thermophysical properties of solids]*, 1st edition, Academia, Prague 1982, 294 (in Czech)
- ¹⁵ A. Blažek, *Termická analýza [Thermal analysis]*, 1st ed., SNTL, Prague 1972, 132 (in Czech)
- ¹⁶ T. Myslivec, *Fyzikálně chemické základy ocelářství [Physico-chemical fundamentals of steelmaking]*, 2nd ed., SNTL, Prague 1971, 445 (in Czech)
- ¹⁷ L. Šmrha, *Tuhnutí a krystalizace ocelových ingotů [Solidification and crystallization of steel ingots]*, SNTL, Prague 1983, 305 (in Czech)
- ¹⁸ Unpublished information from the industrial partners, 2008–2011
- ¹⁹ W. Dubowick, *Thermal Arrest Measurements and their application in the investment casting*, *Proc. of the 2nd Foundry Congress*, Dusseldorf, 1960
- ²⁰ J. P. Aymard, P. Detrey, *Industrial method for determining liquidus temperatures of steels – evaluation of solidification intervals*, *Fonderie*, 29 (1974) 330, 14
- ²¹ W. Roeser, H. T. Wensel, *Stahl und Eisen*, (1951) 8
- ²² J. Štětina, *Dynamický model teplotního pole plynule odlévané bramy [Dynamic model of temperature field of continuously cast slabs]*, Ph.D. thesis, VŠB-TU Ostrava, 2007 [cited 2012-08-30], Available from World Wide Web: <http://ottp.fme.vutbr.cz/users/stetina/disertace/index.htm> (in Czech)
- ²³ K. Grys, B. Smetana, M. Žaludová et al., *Proc. of the 21st Int. Conf. on Met. and Mat.*, Metal 2012, Brno, 2012, 6
- ²⁴ B. Smetana, S. Zlá, A. Kroupa et al., *Journal of Thermal Analysis and Calorimetry*, 110 (2012) 1, 369–378
- ²⁵ M. Žaludová, B. Smetana, S. Zlá et al., *Journal of thermal analysis and calorimetry*, 112 (2013) 1, 465–471
- ²⁶ M. Žaludová, B. Smetana, S. Zlá et al., *Proc. of the 21st Int. Conf. on Met. and Mat.*, Metal 2012, Brno, 2012, (CD ROM)
- ²⁷ ProCast 2009.0, User's manual (released: Feb-09), ESI Group, 2009, 163
- ²⁸ ProCast 2009.0, User's manual (released: Feb-09). ESI Group, 2009, 175

SYNTHESIS OF Au NANOPARTICLES PREPARED WITH ULTRASONIC SPRAY PYROLYSIS AND HYDROGEN REDUCTION

SINTEZA Au-NANODELCEV, PRIPRAVLJENIH Z ULTRAZVOČNO RAZPRŠILNO PIROLIZO IN REDUKCIJO Z VODIKOM

**Srečko Stopić¹, Rebeka Rudolf^{2,3}, Jelena Bogović¹, Peter Majerič²,
Miodrag Čolić⁴, Sergej Tomić⁴, Monika Jenko⁵, Bernd Friedrich¹**

¹IME Process Metallurgy and Metal Recycling, RWTH University Aachen, Germany

²University of Maribor, Faculty of Mechanical Engineering, Maribor, Slovenia

³Zlatarna Celje d.d., Celje, Slovenia

⁴Military Medical Academy, Institute of Medical Research, Belgrade, Serbia

⁵Institute of Metals and Technology, Ljubljana, Slovenia
rebeka.rudolf@um.si

Prejem rokopisa – received: 2012-10-12; sprejem za objavo – accepted for publication: 2013-03-04

Golden nanoparticles of different sizes and shapes (spherical, cylindrical, triangular and round) were prepared during a synthesis of gold with ultrasonic spray pyrolysis (USP) and hydrogen reduction. The experimental investigations of the USP method were performed with an ultrasonic source of 0.8 MHz and 2.5 MHz, acting on the water solution of HAuCl_4 forming aerosols with micron-sized and nanosized droplets. The results of the investigation show that the final shape and size of the Au particles depend on the characteristics of the solution and the frequency of the ultrasound. The second step of synthesizing the Au nanoparticles includes the subsequent thermal decomposition of the aerosol droplets in a hydrogen atmosphere between 260 °C and 500 °C. The investigations showed that the Au nanoparticles prepared in this way are smaller and more homogeneous.

Keywords: gold, ultrasonic spray pyrolysis, reduction, nanoparticles

Zlate nanodelce različnih velikosti in oblik (sferični, cilindrični, trikotni in okrogli) smo pripravili s sintezo zlata z uporabo ultrazvočne razpršilne pirolize (USP) in redukcije. Eksperimentalne raziskave USP-metode so bile izvedene z ultrazvočnim izvirom s frekvenco med 0,8 MHz in 2,5 MHz z delovanjem na vodno raztopino HAuCl_4 , kjer je prišlo do formiranja aerosolov z mikro- in nanovelikostjo kapljic. Rezultati preiskav kažejo, da je oblika in velikost nastalih Au-delcev odvisna od karakteristik raztopine in od frekvence ultrazvoka. Drugi proces sinteze Au-nanodelcev je vključeval kasnejšo toplotno dekompozicijo kapljic aerosola. Izveden je bil v vodikovi atmosferi med 260 °C in 500 °C. Preiskave so pokazale, da so tako izdelani Au-delci bolj homogeni in manjši.

Ključne besede: zlato, ultrazvočna razpršilna piroliza, redukcija, nanodelci

1 INTRODUCTION

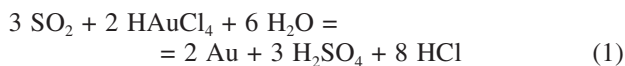
Gold as a noble metal has a resistance to corrosion and it is used mostly in many engineering applications (contacts in microelectronics), medicine (dental alloys, implants) and also in jewellery and currency. When gold is broken into nanoparticles, this form could be highly useful for a wide range of processes, including general nanotechnology, electronics manufacturing and the synthesizing of different functional materials. Schmid and Corain¹ have studied the synthesis, structures, electronics and reactivity of gold nanoparticles. Their main conclusion is that a decrease in the sizes of gold nanoparticles has dramatic consequences on their physical and chemical properties.

Gold nanoparticles can have a better effect than micron-sized ones, because they accelerate the oxidation processes² easily. Successful examples of such practice are the published results, and, especially, the patents granted before 1978 (Bond²) revealing frequent observations of the potential of gold as a catalyst. Qi³ reported on the production of propylene oxide over nanosized

gold catalysts in the presence of hydrogen and oxygen. Polte et al.⁴ reported on the mechanism of gold-nanoparticle formation in the classical citrate-synthesis method derived from a coupled in-situ XANES (X-ray absorption near-edge spectroscopy) and SAXS (small-angle X-ray scattering) evaluation. The efficient recovery of scraps and wastes in the gold-jewellery manufacturing is a vital component of a profitable manufacturing business, irrespective of whether it is a large factory or small, traditional workshop⁵. From the literature it is known that available techniques for gold purification include: 1) the cupellation, 2) the Miller chlorination process, 3) the Wohlwill electrolytic process, 4) the Fizzer cell, 5) the solvent extraction, 6) the aqua regia process and 7) the pyrometallurgical process. On the other hand, the process for recovering gold from a chloride solution is presented in the US Patent 4131454 by Piret et al.⁶ It involves adding finely divided, activated carbon to the solution for the reduction of gold metal and its subsequent absorption by the carbon.

Prior⁷ reported on successful hydrometallurgical refining of gold from the HAuCl_4 using the SO_2 gas as

the selective gold-precipitating agent. A gold sponge was produced with a chemical composition better than mass fraction 99.99 % and a uniform particle size. Using an efficient mass transfer, gold precipitation was realized with an injection of the SO₂ gas, based on the following reaction equation:



The interactions between the gold nanoparticles and biological species found in an aqueous solution are being used as the basis for developing biosensors⁸. Many preparation methods for nanometallic particles have been proposed, such as photo reduction, chemical reduction in an aqueous medium with sodium citrate, chemical reduction in reverse micelles, or thermal decomposition in organic solvents. Aihara et al.⁹ have reported on the preparation and characterization of gold and silver nanoparticles in the layered laponite suspensions.

The development of the colloid chemistry route continues to be essential for the synthesis and manipulation of anisotropic gold nanoparticles, with the major requirements already demonstrated by Treguer-Delapierre¹⁰, such as the control of the nuclei shape and the growth on specific facets. A key feature of the non-spherical nanoparticles is that their optical properties vary dramatically with their physical dimensions. In contrast to the spherical gold nanoparticles, their resonance frequency is tuneable over a wide range from blue to near infrared and enables one to set the surface plasmon resonance to the wavelength or the spectral region specific to a particular application.

The most commonly used methods for synthesizing the gold powder are presented in **Table 1**.

In our previous research¹¹ spherical, round and cylindrical nanosized particles of gold were synthesized with the ultrasonic atomization of chloride-nitrate solutions based on the gold from a jeweller's scrap and an alloying element (Cu, Ag, Zn, In and Ni). A subsequent decomposition of the obtained solution at the temperatures of 300 °C and 800 °C in hydrogen and nitrogen atmospheres was performed. The aerosol produced by the resulting frequencies of 2.5 MHz and 0.8 MHz was

transported by a carrier, mostly a reduction gas, into a hot reactor, where the aerosol droplets underwent drying, droplet shrinkage, solute precipitation, thermolysis and sintering to form the particles with different forms.

This study provides the latest information regarding the synthesis of different gold nanoparticles from a chloroauric acid using the USP method and the subsequent hydrogen reduction. Our main aim was to identify the influence of the reaction parameters on the particle size in order to obtain a better control of the particle nanosize and its morphology.

2 EXPERIMENTAL PROCEDURES

2.1 Ultrasonic spray pyrolysis method and hydrogen reduction

Tetrachloroauric acid HAuCl₄ (Johnson Matthey Company, Germany) was used as the precursor for the synthesis of gold nanoparticles with ultrasonic spray pyrolysis using the equipment developed at the IME, RWTH Aachen University.¹² The precursor was dissolved in water in order to prepare the solution for the aerosol production in an ultrasonic atomizer. The most

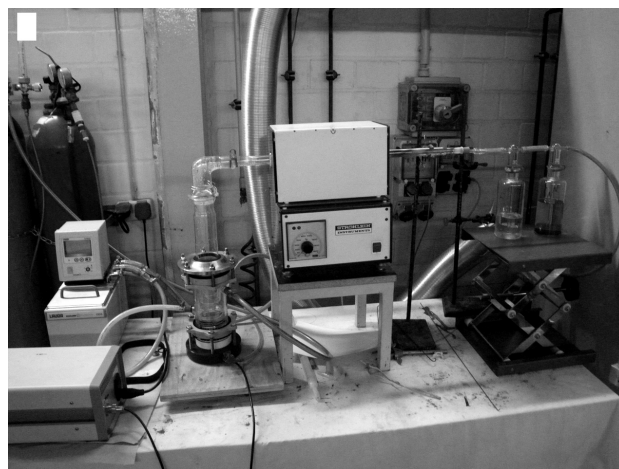


Figure 1: USP device
Slika 1: USP-naprava

Table 1: Methods for producing Au nanoparticles

Tabela 1: Metode izdelave Au-nanodelcev

Author	Method	Precursor	Reducing agent	Form and particle size (nm)
Schmid ¹	Reduction	HAuCl ₄	Phosphor	Spherical
Polte ⁴	Reduction	HAuCl ₄	Na ₃ C ₆ H ₅ O ₇	Spherical, below 100 nm
Piret ⁶	Reduction, precipitation	Precious metal containing chloride leach	Zn, Fe	Above 1000 nm
Prior ⁷	Reduction	HAuCl ₄	SO ₂	No information about the particle form (above 1000 nm)
M. Treguer-Delapierre ¹⁰	Reduction	HAuCl ₄	NaBH ₄	Non-spherical, below 100 nm
Rudolf ¹¹	Ultrasonic spray pyrolysis/reduction	Water solution after a dissolution of jewellery scrap in HNO ₃ /HCl	H ₂	Spherical, cylindrical, triangular, below 100 nm

important part of the set up contains the following (**Figure 1**): an ultrasonic atomizer, a small reactor with a quartz tube, a thermostat, two bottles with water and alcohol for the nanoparticle collection. The atomization of the obtained solution based on a water solution of gold chloride took place in an ultrasonic atomizer (Gapusol 9001, RBI/ France) with one transducer to create the aerosol. With regard to our previous results, the resonant frequency was selected to be between 0.8 MHz and 2.5 MHz.

Nitrogen was first flushed from the bottle to remove the air from the system. Under the spray-pyrolysis conditions hydrogen was passed continuously through the quartz tube ($l = 1.0$ m, $b = 20$ mm) at a flow rate of 1 L/min. Then, the atomized droplets of the solution based on gold were transported further by hydrogen to the furnace for the subsequent reduction of gold chloride at a different reaction temperature. After the completed reduction process, the obtained gold nanopowder was collected in the reaction tube and in two bottles with ethanol and water. In order to stabilize the collected gold nanoparticles, different solutions were used in the bottles. The performed experiments are shown in **Table 2**.

Table 2: Experimental conditions for the preparation of nanosized Au powder in hydrogen atmosphere, flow rate of 1 L/min, solution concentration of Au 2.5 g/L

Tabela 2: Eksperimentalni pogoji za pripravo Au-prahu nanovelikosti v vodikovi atmosferi; pretok 1 L/min, koncentracija raztopine Au 2,5 g/L

Exp.	Temperature, $T/^{\circ}\text{C}$	Time, t/h	Solution	Ultrasonic frequency, f/MHz
1	260	5	Ethanol/Water	0.8
2	300	5	Ethanol/Water	0.8
3	280	5	Ethanol/Ethanol	0.8
4	400	5	Water/Water	0.8
5	500	6	Ethanol/Ethanol	0.8
6	300	5	Ethanol/Ethanol	2.5
7	260	5	Ethanol/Ethanol	2.5
8	280	6	Ethanol/Ethanol	2.5
9	260	4	Ethanol/Ethanol	2.5
10	260	4	Ethanol/Water	2.5

The obtained colours of the solutions were compared with the ones reported for the commercial gold nanoparticles (STREM Chemicals, Inc.).

Scanning electron (SEM) and high-resolution transmission (HR-TEM) electron microscopy with the connected energy-dispersive-spectroscopy (EDS) analysis were used for characterizing the nanoparticles. The SEM and TEM images have shown the surface morphologies of the particles formed at different parameter sets.

2.2 Formation of Au nanoparticles with hydrogen reduction in an ultrasonic generator

During the aerosol formation, the gold nanoparticles appeared in the ultrasonic generator, which was not

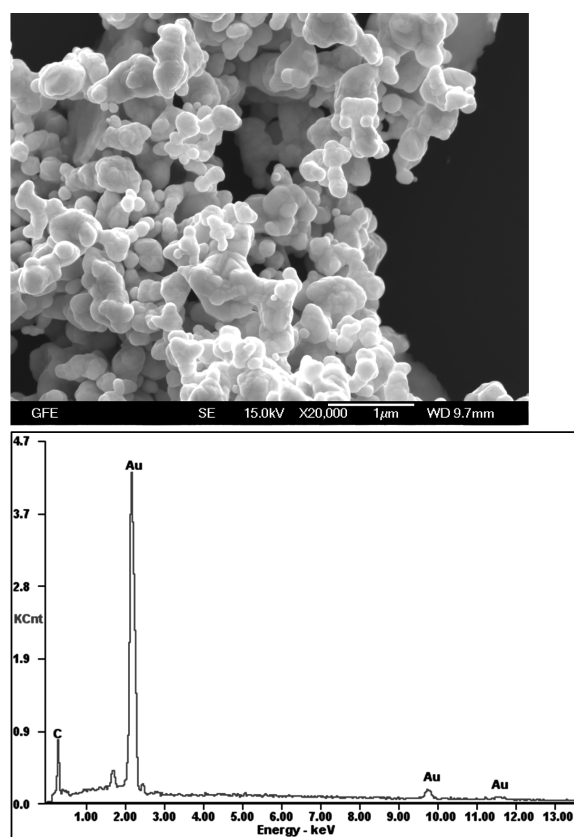


Figure 2: SEM image and EDS analysis of the Au nanoparticles obtained in an ultrasonic generator

Slika 2: SEM-posnetek in EDS-analiza Au-nanodelcev, izdelanih v ultrazvočnem generatorju

expected. The formed particles were agglomerated and round, as shown in **Figure 2**. This phenomenon has to be investigated further and discussed in order to find the optimum parameters for the synthesis (ultrasonic frequency, hydrogen flow rate, concentration of the solution). We hope that the ultrasonic frequency (0.8 MHz and 2.5 MHz) can initiate the formation of nanosized gold particles at room temperature. In the absence of hydrogen the formation of gold nanoparticles was not seen. After the experiments, the gold nanoparticles were separated with the filtration. The collected gold nanopowders from the ultrasonic generator were analysed with SEM and EDS (**Figure 2**).

3 RESULTS AND DISCUSSION

3.1 Characterisation of the obtained gold nanoparticles

A different morphology of the nanoparticles was obtained with the USP method at 260 $^{\circ}\text{C}$ using an ultrasonic frequency of 0.8 MHz (**Figure 3**). The presence of triangular, rounded and irregular particles revealed that a synthesis of gold nanoparticles is possible at low temperatures, but this structure is different from the ideally spherical metallic nanoparticles (copper, cobalt, nickel)

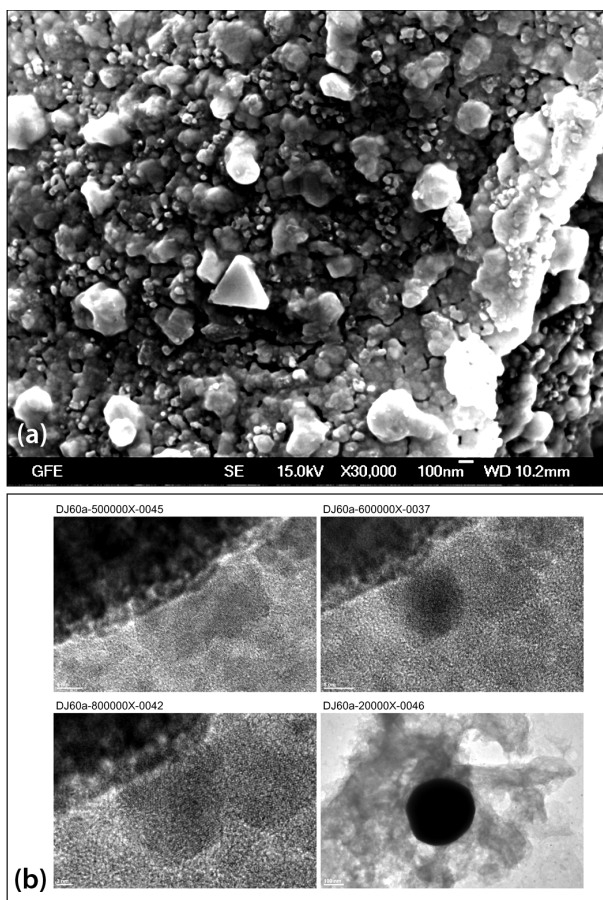


Figure 3: a) SEM image of Au nanoparticles (synthesis parameters: 260 °C, $f = 0.8$ MHz), b) TEM image of Au nanoparticles (synthesis parameters: 260 °C, $f = 0.8$ MHz)

Slika 3: a) SEM-posnetek Au-nanodelcev (parametri sinteze: 260 °C, $f = 0.8$ MHz), b) TEM-posnetek Au-nanodelcev (parametri sinteze: 260 °C, $f = 0.8$ MHz)

prepared during our previous research¹². The presence of a similar, triangular and rounded, morphology was only reported for the synthesis of silver nanoparticles from silver nitrate at 300 °C in our previous work.

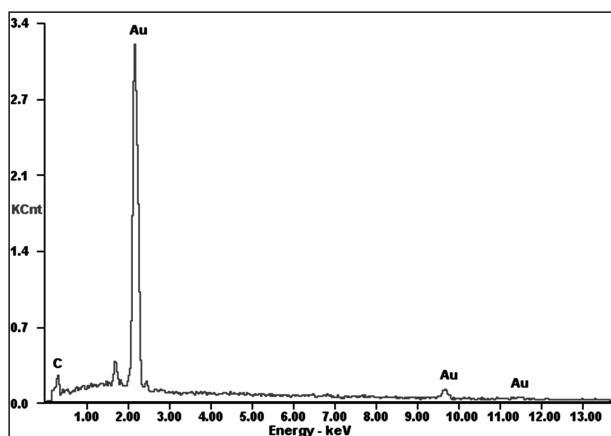


Figure 4: EDS analysis spectrum of the Au nanoparticles from the experiment (1)

Slika 4: EDS analizni spekter Au-nanodelcev iz eksperimenta (1)

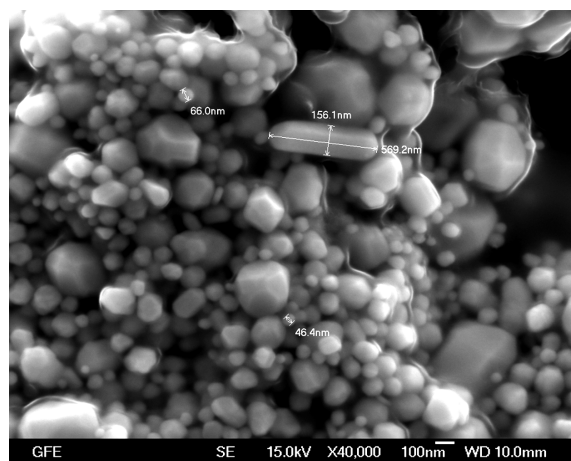


Figure 5: SEM image of Au nanoparticles (synthesis parameters: 280 °C, 2.5 MHz)

Slika 5: SEM-posnetek Au-nanodelcev (parametri sinteze: 280 °C, 2,5 MHz)

The Au particles produced during the USP experiment are of high purity as seen also from the spectrum on **Figure 4**.

The increase in the temperature to 280 °C revealed a presence of cylindrical particles (**Figure 5**). In addition, the proportion of the rounded particles is larger at 280 °C than at 260 °C. It seems that the nanoparticles grow together.

The presence of the triangular, rounded and irregular particles revealed that a synthesis of gold nanoparticles is possible at low temperatures, but their structure is different from the ideally spherical metallic particles (silver, nickel) prepared during our previous research.^{12,13} The increase in the temperature from 260 °C to 280 °C revealed a presence of cylindrical particles. Also, the proportion of the rounded particles is more prevalent at higher temperatures. It seems that nanoparticles grow together. The particle size of the finally obtained Au powder especially depends on the droplet diameter and the initial concentration of the solution. The increase in the ultrasonic frequency from 0.8 MHz to 2.5 MHz, at a constant precursor concentration, leads to a decrease in the droplet size and, finally, to a higher amount of smaller nanoparticles in the final product.

The experiments showed that the increase in the reaction temperature to 500 °C, at the same frequency, leads to a different form of the particles and an increased agglomeration of the particles.

Based on the capillary theory, the diameter of nanoparticles was predicted from equation (2), formed by combining the Kelvin equation and the equation reported by Messing et al.¹⁴:

$$D_{Au} = 0.34 \cdot \left(\frac{8\pi\gamma}{\rho_{sol} f^2} \right)^{\frac{1}{3}} \cdot \left(\frac{C_{sol} M_{Au}}{\rho_{Au} M_{sol}} \right)^{\frac{1}{3}} \quad (2)$$

where D_{Au} is the diameter of a nanoparticle (m), γ is the surface tension (N/m), f is the ultrasonic frequency (s^{-1}),

C_{sol} is the concentration of the starting solution (g/cm^3), M_{sol} is the molar mass of the starting solution of HAuCl_4 (g/mol), M_{Au} is the molar mass of gold (g/mol), ρ_{sol} is the density of the atomized solution and ρ_{Au} is the density of gold (g/cm^3).

Assuming that the characteristics of water are close to those of the used diluted precursor solution, the parameters of our experiments amounted to: $\gamma = 72.9 \times 10^{-3} \text{ N/m}$, $\rho = 1.0 \text{ g}/\text{cm}^3$, $f = 0.8 \times 10^6 \text{ s}^{-1}$ leading to the calculated value of the ultrasonically dispersed droplet diameter of $D = 4.79 \times 10^{-6} \text{ m}$. An increase in the operating frequency from $f = 0.8 \times 10^6 \text{ s}^{-1}$ to $f = 2.5 \times 10^6 \text{ s}^{-1}$ decreased the aerosol droplet size from $D = 4.79 \times 10^{-6} \text{ m}$ to $2.26 \times 10^{-6} \text{ m}$.

The expected mean diameter of a particle in the finally obtained Au-powder, after the hydrogen reduction, depends, especially, on the droplet diameter and the initial concentration of the solution. Assuming that each droplet is transformed into one particle and that during the atomization no coalescence occurs, the final particle diameter can be calculated using equation (2).

Using the parameters of our experiments – the droplet mean diameter $D = 4.79 \mu\text{m}$, $M_{Au} = 196.97 \text{ g}/\text{mol}$, $M_{\text{HAuCl}_4} = 339.8 \text{ g}/\text{mol}$, $\rho_{Au} = 19.3 \text{ g}/\text{cm}^3$, the concentration of gold between $1 \text{ g}/\text{dm}^3$ and $10 \text{ g}/\text{dm}^3$ – the calculated mean particle diameter of gold amounts to between 60 nm and 150 nm. Under the same conditions and for the frequency of $f = 2.5 \times 10^6 \text{ s}^{-1}$ the calculated mean particle diameter of gold amounted to between 150 nm and 300 nm (Figure 6). The particle size of gold was decreased as a result of the reaction in a smaller droplet with the same concentration. In contrast to the water solution, the stabilization of gold nanoparticles was performed successfully using ethanol in the second bottle in order to prevent a possible agglomeration.

The present differences between the calculated and experimentally obtained values of gold particles may be due to the approximate values used for the surface tension and density of the aqueous solution, the microporosity of the particles and, especially, due to the coale-

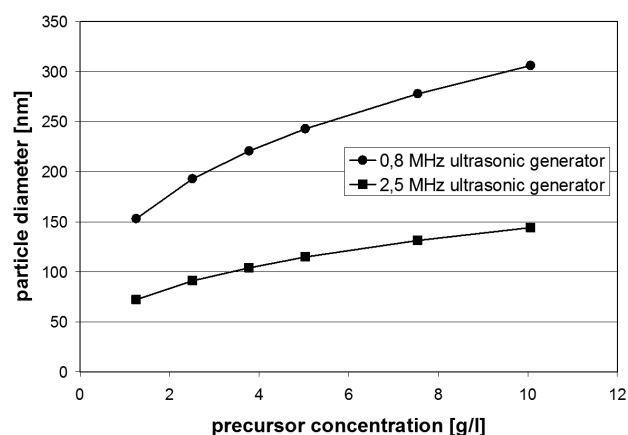


Figure 6: Calculated size of Au nanoparticles

Slika 6: Izračunana velikost Au-nanodelcev

scence/agglomeration of the aerosol droplets at a high flow rate of the carrier gas (the turbulence effects). Also, in equation (2), based on the assumption of one particle per one droplet, the influence of the temperature on the mean particle size was not taken into account. In order to decrease this difference between the calculated and experimentally obtained values of gold nanoparticles, the aerosol droplet size obtained from the gold-based solution should be measured precisely with the laser diffraction and used in the above-mentioned calculations (Table 3). Additionally, in contrast to our previously prepared spherical particles of Cu, Co and Ni, the presence of rods and discs in the gold structure represents news of interest for an application.

Table 3: Comparison of the experimental and calculated particle diameters

Tabela 3: Primerjava eksperimentalno dobljenih ter izračunanih vrednosti premera delcev

Concentration of Au in HAuCl_4 : 2.5 (g/L)	Particle size (nm)	
	$f = 0.8 \text{ MHz}$	$f = 2.5 \text{ MHz}$
Experimental	38–200	10–250
Calculated	193	91

3.2 Influence of different parameters

The influence of the reaction temperature and type of the carrier gas on the size and shape was studied. Because of the very fast kinetics of the thermal decomposition of HAuCl_4 and a short retention time of the aerosol in the reactor, causing a fast particle formation and growth of gold nanoparticles, it is very difficult to separately obtain only one ideal form of the nanoparticles (a sphere or a triangle) by changing different reaction parameters (Figure 7).

Treguer-Delapierre et al.¹⁰ maintained that further efforts should focus on a better understanding of the growth mechanism to find the best shape.

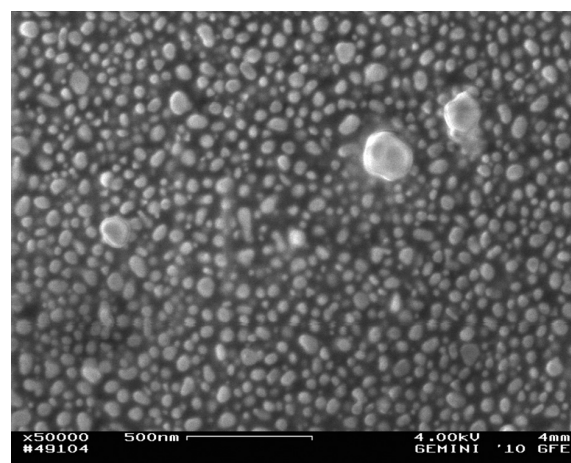
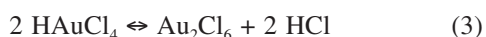


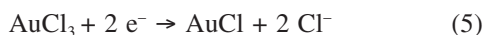
Figure 7: SEM image of Au nanoparticles (synthesis parameters: 260 °C, 2.5 MHz)

Slika 7: SEM-slika Au-nanodelcev (parametri sinteze: 260 °C, 2,5 MHz)

A thermal-gravimetric analysis was used by Sawada and Ando¹⁵ in order to explain the decomposition of HAuCl_4 in a neutral atmosphere. They reported that the formation of the first peak below 120 °C was caused by the evaporation of the crystal water and the decomposition of HAuCl_4 into AuCl_3 , because the residual weight between 260 °C and 750 °C (75 %) was close to the weight of AuCl_3 (77 %). The subsequent decomposition began at 750 °C and did not stop at 900 °C. This indicates that HAuCl_4 was not reduced to gold by the thermal treatment below 900 °C in a neutral atmosphere. The gold formation from HAuCl_4 takes place in two steps:



As shown in **Figure 8**, an increase in the temperature up to 800 °C increases the changes in the Gibbs-free energies ΔG between -527 kJ and -872 kJ for the hydrogen reduction and between 251 kJ and -54 kJ for the thermal decomposition of HAuCl_4 . In contrast to the thermal decomposition (positive values of ΔG), up to 600 °C the hydrogen reduction of gold chloride was always characterized with negative values, which suggests that there is a high possibility that this reaction happens. The thermal decomposition of HAuCl_4 is reported by Kumar¹⁶ for a reduction of a tetrachloroauric acid with trisodium citrate. Trisodiumcitrate is both the reducing agent and the stabilizer. In this multiple-step process, the most important steps are:



The disproportionation step requires three aurous species to gold atoms.

The positive value of ΔG for the thermal decomposition of HAuCl_4 suggests a small possibility for a formation of gold chloride, although the reported theoretical decomposition temperature of HAuCl_4 amounts to 258 °C.

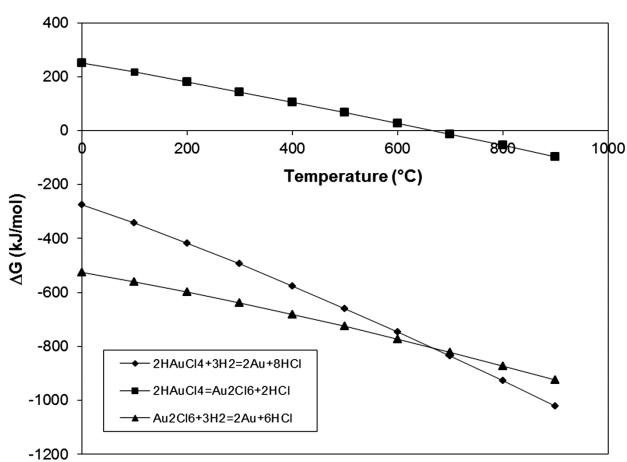


Figure 8: Thermochemical calculation for a decomposition of HAuCl_4 and hydrogen reduction

Slika 8: Termokemijski izračun za razgradnjo HAuCl_4 z redukcijo v vodiku

Also, our previous TGA analysis¹³ confirmed that the thermal decomposition of HAuCl_4 takes place between 260 °C and 750 °C.

4 CONCLUSIONS

Gold nanoparticles were prepared with USP and the subsequent hydrogen reduction between 260 °C and 500 °C. Using the ultrasonic frequencies between 0.8 MHz and 2.5 MHz, the formed aerosols with constant droplet sizes between 2.2 μm and 4.8 μm were thermally decomposed in a hydrogen atmosphere in a reactor. The SEM and EDS analyses confirmed the presence of gold with different morphological forms (spherical, cylindrical and triangular), which is of great importance for some medical applications. It was very difficult to separately prepare only one ideal form of nanoparticles (a sphere or a triangle) by changing different reaction parameters during the USP synthesis and the subsequent hydrogen reduction. The controlled morphology of the gold nanoparticles prepared with USP and other methods (precipitation, reduction in autoclave) will be studied in our future research investigating the influence of the other important reaction parameters (reducing agent, gas flow rate, pressure).

Acknowledgment

We would like to thank the Federal State of North Rhine-Westphalia and Programme "NanoMikro+Werkstoffe.NER" covered by the Ziel 2-Programm 2007-2013 (EFRE) for the financial support on the project "Electromechanic components with new nanoparticle-modified noble-metal surface" – NanoGold. The research leading to these results was carried out within the framework of the research project "Production technology of Au nanoparticles" (L2-4212) that was funded by the Slovenian Research Agency (ARRS).

5 REFERENCES

- G. Schmid, B. Corain, Nanoparticulated Gold: Syntheses, electronics, and reactivities, *Eur. J. Inorg. Chemistry*, 17 (2003), 3081–3098
- G. Bond, The early history of catalysis by gold, *Gold Bulletin*, 41 (2008) 3, 235–241
- C. Qi, The production of propylene oxide over Au catalysts in presence of hydrogen and oxygen, *Gold Bulletin*, 41 (2008) 3, 224–234
- J. Polte, T. Ahner, F. Delissen, S. Sokolov, F. Emmerling, A. Thünenman, R. Kraehnert, Mechanism of gold nanoparticle formation in the classical citrate synthesis method derived from coupled in situ XANES and SAXS Evaluation, *J. Am. Chem. Soc.*, 132 (2010), 1296–1301
- C. Corti, Recovery and refining of gold jewellery scraps and wastes, The Santa Fe Symposium on Jewellery Manufacturing Technology, 2002, 1–20
- N. Piret, Process for recovering Au and Ag from chloride solutions, US Patent 4131454, 1977
- N. Prior, Surface effect gassing technology (SEGTEC)-Advanced in 4N Gold precipitation, EMC Conference, Precious metals, 2011, 1087–1102

- ⁸ S. Carabineiro, Gold highlights at NanoSpain Conference in Praga, Gold Bulletin 41 (2008) 3, 265–268
- ⁹ N. Aihara, K. Torigoe, K. Esumi, Preparation and characterization of gold and silver nanoparticles in layered laponite suspensions, Langmuir, American Chemical Society, 14 (1998), 4945–4949
- ¹⁰ M. Treguer-Delapierre, J. Majimel, S. Mornet, E. Duguet, S. Ravaine, Synthesis of non-spherical gold-nanoparticles, Gold Bulletin, 41 (2008) 2, 195–207
- ¹¹ R. Rudolf, B. Friedrich, S. Stopic, I. Anzel, S. Tomic, M. Čolić, Cytotoxicity of gold nanoparticles prepared by ultrasonic spray pyrolysis, Journal of Biomaterials Applications, 26 (2012) 5, 595–612
- ¹² S. Stopic, B. Friedrich, T. Volkov-Husovic, K. Raic, Mechanism and kinetics of nano silver formation by ultrasonic spray pyrolysis-Progress report after a successful up-scaling - First part, Metall, 10 (2010), 419–426
- ¹³ S. Stopić, I. Ilić, D. Uskoković, Structural and morphological transformations during NiO and Ni particles generations from chloride precursor by ultrasonic spray pyrolysis, Materials Letters, 24 (1995), 369–376
- ¹⁴ G. Messing, S. Zhang, G. Jayanthi, Ceramic powder synthesis by spray pyrolysis, Journal of American Ceramic Society, 76 (1993) 11, 2707–2026
- ¹⁵ T. Sawada, S. Ando, Synthesis, characterization, and optical properties of metal-containing fluorinated polyimide films, Chem. Mater., 10 (1998), 3368–3378
- ¹⁶ S. Kumar, K. Gandhi, R. Kumar, Modelling of formation of gold nanoparticles by citrate method, Ind. Eng. Chem. Res., 46 (2007), 3128–3136

EFFECT OF HEAT TREATMENT ON THE MICROSTRUCTURE AND MECHANICAL PROPERTIES OF PISTON ALLOYS

VPLIV TOPLOTNE OBDELAVE NA MIKROSTRUKTURO IN MEHANSKE LASTNOSTI ZLITIN ZA BATE

**Srećko Manasijević¹, Srdjan Marković², Zagorka Acimović - Pavlović²,
Karlo Raić², Radomir Radiša¹**

¹LOLA Institute, Kneza Viseslava 70a, 11000 Belgrade, Serbia

²Faculty of Technology and Metallurgy, University of Belgrade, Karnegijeva 4, 11000 Belgrade, Serbia
srecko.manasijevic@li.rs

Prejem rokopisa – received: 2012-12-10; sprejem za objavo – accepted for publication: 2013-02-19

This research paper presents the results of the effects of heat treatment on the microstructure and mechanical properties of aluminum piston alloys. Four piston alloys of different chemical compositions were experimentally investigated. Different temperatures and times (480 °C to 515 °C for 1 h to 60 h) of the solution heat treatment were investigated. Additionally, the influence of the aging time and temperature (140–200 °C for 1 h to 30 h) on the hardness was studied. The results have shown that it is necessary to find the optimum combinations of the temperature and the time of heat treatment in order to achieve the required performance and economic savings.

Keywords: piston, aluminum alloys, heat treatment

V članku so predstavljeni rezultati vpliva toplotne obdelave na mikrostrukturo in mehanske lastnosti aluminijevih zlitin za bate. Eksperimentalno so bile preiskane štiri zlitine za bate z različno kemijsko sestavo. Preiskovane so bile pri različnih temperaturah in časih (480–515 °C od 1 h do 60 h) raztopnega žarjenja. Dodatno je bil preučevan vpliv časa in temperature (140–200 °C od 1 h do 30 h) staranja na trdoto. Rezultati so pokazali, da je za zagotavljanje lastnosti in ekonomičnosti potrebno poiskati optimalno kombinacijo temperature in časa toplotne obdelave.

Ključne besede: bat, aluminijeve zlitine, toplotna obdelava

1 INTRODUCTION

Aluminum piston alloys are a special group of industrial aluminum alloys^{1–5} that have good mechanical properties at elevated temperatures (approximately up to 400 °C).^{1–5} At the same time, these alloys are resistant to sudden temperature changes.^{1–19} Due to this, in the design of this type of alloys, their mechanical and thermal strains have to be critically considered without neglecting the aggressive environments, to which they are exposed during exploitation.^{1,2,4,5} In order to accomplish such a set of requirements, aluminum alloys assigned for piston production need to have an appropriate microstructure. Together with their chemical composition, the process parameters and heat treatment affect their microstructure, which is an important parameter that has a significant impact on the mechanical properties of cast parts.^{3,5,7,10,12,13,18}

Different grades of piston alloys have different contents of the major and minor alloying elements. The usual ranges for some of the alloying elements used by the world famous manufacturer of the KS pistons, Mahle, and the Serbian Concern PDM Mladenovac are in mass fractions: 11–23 % Si; 0.5–3 % Ni; 0.5–5.5 % Cu; 0.6–1.3 % Mg; up to 1.0 % Fe and up to 1 % Mn.^{5–8} Typical aluminum piston alloys are very complex with

respect to their chemical compositions and the obtained structures. There are at least six major alloying elements, Al, Si, Cu, Ni, Mg and Fe, which have a significant impact on the solidification path of these alloys.^{1–5,8,9} Interactions among them create different phases and intermetallics, the shape and distribution of which, in the as-cast and heat-treated alloys, depend on the corresponding process parameters.^{1,5,6,12,15,18,19}

The zones subjected to greater strains during the exploitation (the pin support and the zone of the piston rings) require a greater resistance to plastic deformation. This requires a fine grain structure in these zones as fine grain structures can accumulate larger quantities of energy.^{2,4,5} The size of the primary silicon crystals in these zones ranges from 21–29 µm.^{2,4,5} In the zone subjected to higher temperatures (the piston head, i.e., the combustion chamber) but lower mechanical strains, coarse grains are required. The size of the primary silicon crystals in this zone ranges from 50–75 µm.^{2,4,5} Given that higher temperatures can stress out thermally actuated processes (diffusion), the material has a potential to compensate deformations that were formed during a temperature decrease. Likewise, an increase in the grain size results in a slower expansion of deformation. Thus, the structure of a material directly affects the physical and mechanical properties of the cast.^{2,4,5}

Al–Si alloys should have a high strength at elevated temperatures. In order to increase the mechanical properties of such alloys at elevated temperatures (approximately around 350 °C), it is necessary to introduce, into the solidified structure, new thermally stable intermetallics formed through complex eutectic or peritectic reactions.^{1,4,5} At elevated temperatures, thermally stable intermetallics should prevent or retard the movement of dislocations and thus increase the mechanical properties of an alloy at elevated temperatures. The strengthening effect of such intermetallics depends on their stability at elevated temperatures. More thermally stable intermetallics achieve a better strengthening effect.^{1,3,5,10,11,14}

The formatted intermetallic phases in piston alloys can be soluble or insoluble. Soluble particles are formed by the atoms of magnesium or copper, in the presence or absence of aluminum.^{1,5} Copper forms a θ -(CuAl₂) intermetallic phase with aluminum,^{1,3,5,7–9,12,14} while Mg reacts with Si and produces a complex intermetallic and the β -(Mg₂Si) intermetallic mainly affects the strength of the alloy at ambient temperature.^{5,7–10,12,14,15} The main characteristics of the Mg₂Si intermetallic phase are high strength and hardness.^{5,10} Therefore, this intermetallic has been used as a strengthener in pistons produced using a series of Al–Si alloys. The good mechanical properties of Al–Si piston alloys have been further improved by choosing the optimum heat-treatment procedure.^{5,6,12,15} The presence of copper and magnesium as additional alloying elements in pistons alloys leads to a formation two additional intermetallic phases: Al₂CuMg, the so-called *S*-phase, and the more complex Al_xMg₅Cu₄Si₄ (*W*-phase).^{5,7,12}

Heat treatment is the final process of treating castings in the Al–Si alloy piston production stage. Heat treatment includes the processes of heating the castings to the critical temperatures, holding them at these temperatures for a certain time and then cooling them in a certain way and at a certain rate. This is an unavoidable way of improving the properties of piston alloys in the production process, where the phase and structural changes primarily take place in the solid state. The process of heat treatment of piston castings, which are very sensitive to the conditions of the treatment, requires a very precise process control. First, it is necessary to accurately define the mode of heat treatment on the basis of the initial properties of the casting and desired thermomechanical properties that a piston should achieve. Bearing in mind that the phase and structural changes depend on the time

and temperature, it is therefore necessary to precisely define the optimum temperature and time of holding. Otherwise, the set goals cannot be achieved.

The most common modes of heat treatment applied to piston alloys are solution heat treatment, aging and stabilization.⁵ The essence of solution heat treatment comprises heating the piston castings to the maximum allowable temperature, which is very close to the eutectic melting temperature, the period of holding them at this temperature and the cooling rate. The heating temperature depends on the nature of an alloy and the reinforcing phase dissolution, and its determination is based on the equilibrium diagram. The length of maintaining this temperature depends on the nature of the alloy sheet structure and the heating conditions, i.e., the dissolution of the strengthening component.^{5,15} In addition, the duration of the holding time has a significant influence on the wall thickness and configuration as well as on the casting process.⁵ Aging is often the final technological operation of heat treatment. The aging temperature and time depend on the size of the saturated solid solution.^{6,12,15,18,19} Moreover, a stabilization process is performed to remove residual stresses.

The aim of the experimental investigations of this study was to analyze the influence of heat treatment on the microstructure and mechanical properties of aluminum piston alloys. In addition, the aim was to find an optimum combination of the time and temperature of a heat treatment of piston castings in order to optimize the processes and enable economic savings as the key issue of the considered process and to determine the technical and economic parameters.

2 EXPERIMENTAL PROCEDURE

Four different piston alloys (**Table 1**) of approximately eutectic composition were used to analyze the influence of heat treatment on the microstructure. The mass content of the alloying elements varied between 11.20–13.12 % Si, 1.11–5.41 % Cu, 0.89–1.91 % Ni, 0.53–1.02 % Mg and 0.37–0.59 % Fe, to ensure a separation of the dominant phase in each of the test structures. In the real case, there is a change in the mean concentrations of alloying elements due to a redistribution of the rich or depleted melt, which can lead to a change in the mean concentrations being significantly above or below the nominal value and to the creation of the conditions for a formation of new phases. Any chan-

Table 1: Nominal chemical compositions of the experimental alloys in mass fractions

Tabela 1: Kemijska sestava preizkusnih zlitin v masnih deležih

Alloys	Chemical composition (w/%)										
	Si	Cu	Ni	Mg	Fe	Mn	Cr	Ti	Zr	V	Al
A	13.12	1.11	0.89	0.85	0.59	0.18	0.09	0.07	≈0.03	≈0.01	residue
B	13.05	3.58	1.01	0.90	0.52	0.19	0.09	0.07			
C	12.95	3.91	1.91	1.02	0.42	0.18	0.09	0.07			
D	11.20	5.41	1.90	0.53	0.37	0.25	0.09	0.07			

ge during the entire curing process (primary, secondary and tertiary) of piston alloys has a significant impact on the concentration profiles of the alloying elements in the solid phase.⁵ Therefore, several alloys with different ratios of the main alloying elements were investigated.

The Al–Si piston-alloy testing was performed on a Φ 89 mm piston used for an OM604 diesel engine with a turbocharger. The mass of the tested piston cast with a pouring system and feeder is 1275 g and the mass of the cast is 868 g. Taking into account that the structure of the material has a direct impact on the physical and mechanical properties of the cast, it is therefore necessary to define and describe its macrostructure and microstructure (Figure 1).

All the investigated alloys of the required elemental contents were prepared under industrial conditions in the Petar Drapsin Company, Mladenovac, Serbia with the standard procedure for the melting and preparation of piston alloys prescribed by the manufacturer.

This study investigated different conditions of heat treatment of cast pistons. The alloy constituents were introduced to the solution at a temperature of 480–515 °C for various time intervals of 1–60 h in one cycle, or a combination of two or three temperatures for different time intervals. After completing the solution heat treatment, water quenching to 30 °C was performed. Then the casts were aged at various temperatures. All the castings were marked in order to monitor the changes in the results.

The piston castings were packed in a steel lattice basket with the whole ear turned down. The space between the rows of pistons was 5–10 mm. The layout and dimensions of the basket were defined by the internal standard of the Petar Drapsin Company, Mladenovac. The batch size of the thermal set was the usable capacity of the furnace. The samples of cast pistons were solution heat treated in a furnace chamber with electric heating, type KPA 16/32 CER Čačak, with the fans for the hot-air recirculation. The capacity of this furnace is 500 kg/h and the consumption is 212 kW h. The piston castings were automatically quenched by pulling the furnace

floor out and lowering the metal basket with the pistons directly from the furnace into a water tank. For the aging and stabilization, a CER Čačak EPC 200/300 furnace with a capacity of 3000 kg/h and consumption of 180 kW h was employed. The temperature in the furnace was maintained within the prescribed narrow limits (± 5 °C) with a good atmosphere control.

A 38532-type device (Karl Frank GmbH) was used to measure the hardness of the pistons. The measurements were performed using a Brinell JUS.C.A4103 (5/250/30) 5 mm ball and a 250 N load for 30 s. An optical microscope (Leica DMI 5000M) was employed for a visualization of the microstructure formed with the aim of collecting data for determining the internal construction, i.e., the structure of the material. A further characterization of the structure was performed with a reflection electron microscope (REM) with a magnification of up to 1000-times.

3 RESULTS AND DISCUSSION

3.1 Analysis of the effects of heat treatment on the microstructure

The solidification of the investigated piston alloys (Table 1) starts with a separation of the primary silicon crystals ($L \rightarrow (Si)$).^{1,5,6,8} Further growth of the formed silicon crystals reduces the surrounding space and creates the conditions for a development of the secondary or eutectic reaction ($L \rightarrow (Al)+(Si)$).^{1,5,6,8} Further, depending on the chemical composition and the conditions of solidification, one of the following three reactions takes place: $L \rightarrow (Al)+(Si)+Y$ and $L+Y \rightarrow (Al)+(Si)+Y$, where $Y(\epsilon, \theta, M, \delta, \gamma, T, \beta, \pi$ and $Q)$.^{5,6,8} After the completion of the solidification process, there are different intermetallic phases in the microstructure in addition to the primary silicon crystals (Si) and $\alpha(Al)$ of the solid solution. Their shape, size and distribution depend on the nominal chemical composition of the alloy and the cooling conditions. Therefore, four Al–Si

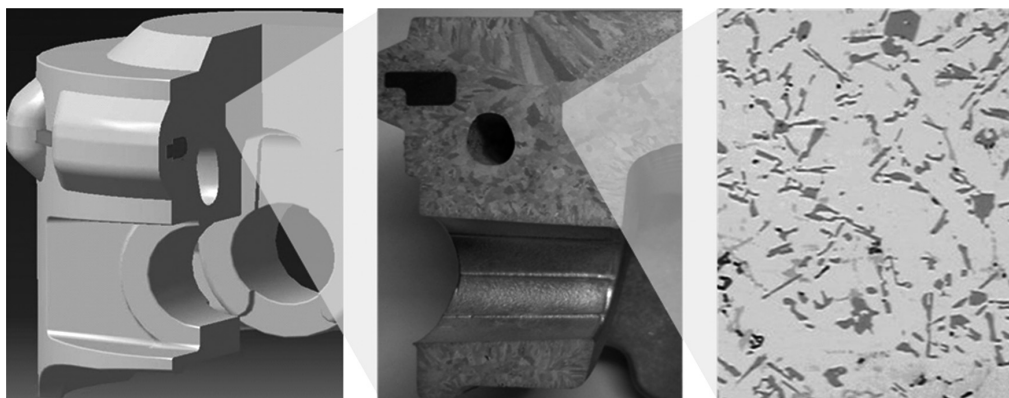


Figure 1: Macrostructure and microstructure of the piston cast of alloy A
Slika 1: Makrostruktura in mikrostruktura bata, ulitega iz zlitine A

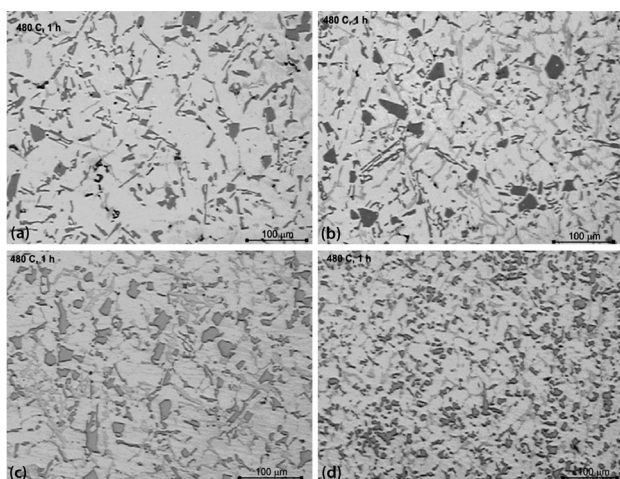


Figure 2: Shape of the primary Si crystals at a temperature of 480 °C and with the holding time of 1 h: a) alloy A, b) alloy B, c) alloy C and d) alloy D

Slika 2: Oblika primarnih kristalov Si po zadržanju 1 h na temperaturi 480 °C: a) zlitina A, b) zlitina B, c) zlitina C in d) zlitina D

piston alloys that have different initial microstructures were selected for the heat treatment.

As stated in the introduction, the last stage in the piston casting process, where the changes in the structure and physicochemical and mechanical properties can be made, is the heat treatment. These changes are analyzed in the following section of the paper. The microstructures of the cast pistons heat treated for 1 h at a temperature of 480 °C are shown in **Figure 2**, (alloy A (**Figure 2a**), alloy B (**Figure 2b**), alloy C (**Figure 2c**) and alloy D (**Figure 2d**)).

The microstructure of the cast pistons (alloy C) heat treated for 4 h at the temperatures of 480 °C and 490 °C are shown in **Figure 3**. The uneven distribution of the primary Si crystals can be seen in all the alloys, which means that the time and temperature of the solution heat

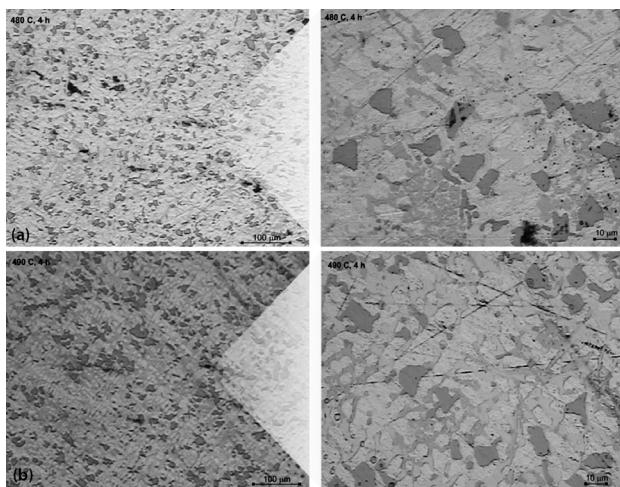


Figure 3: Shape of the primary Si crystals at the temperatures of 480 °C and 490 °C and with the holding time of 4 h, alloy C

Slika 3: Oblika primarnih kristalov Si v zlitini C, po zadržanju 4 h na temperaturah 480 °C in 490 °C

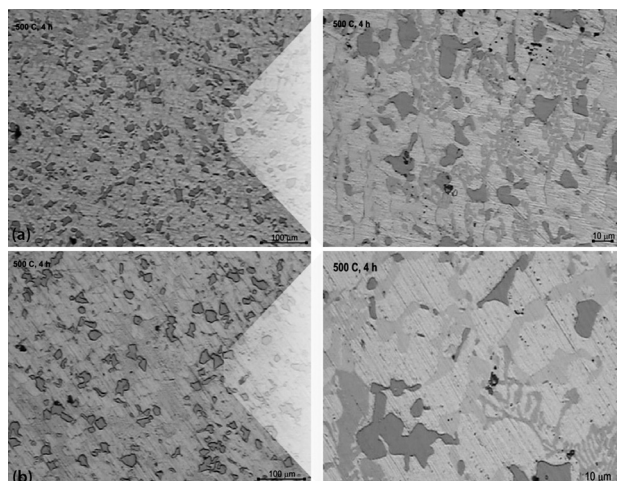


Figure 4: Morphologies of the alloys solution heat treated for 4 h at 500 °C: a) alloy C and b) alloy D

Slika 4: Morfologija zlitine, raztopno žarjene 4 h na 500 °C: a) zlitina C in b) zlitina D

treatment were not satisfactory. This form and distribution of the primary Si crystals and intermetallic phases in the microstructure of a cast piston reduce the mechanical properties of the investigated piston alloys.

The microstructure of the piston alloy C after the solution heat treatment at 500 °C for a period of 4 hours is shown in **Figure 4a**. The microstructure of the piston alloy D after solution heat treatment at a temperature of 500 °C for a period of 4 h is shown in **Figure 4b**. Based on the obtained results, it can be concluded that the process was better than the previous solution heat treatments (**Figures 2** and **3**), but that the time of the solution heat treatment was not long enough. A better distribution of the primary Si crystals, a homogeneous distribution of the precipitated Al_2Cu in the matrix and a dissolution of the metastable phases are visible.

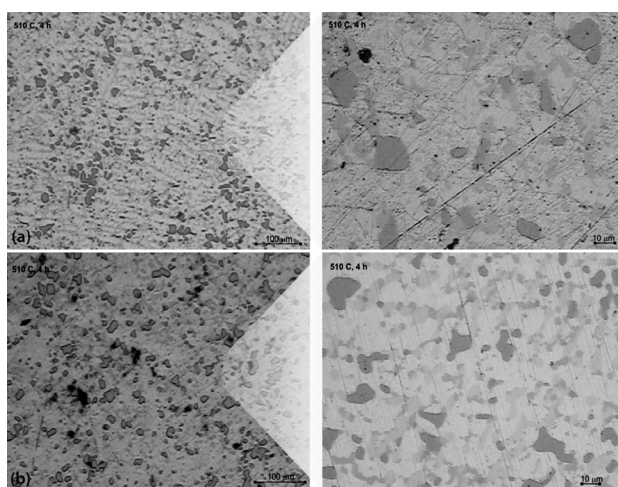


Figure 5: Morphologies of the alloys solution heat treated for 4 h at 510 °C: a) alloy C and b) alloy D

Slika 5: Morfologija zlitine, raztopno žarjene 4 h na 510 °C: a) zlitina C in b) zlitina D

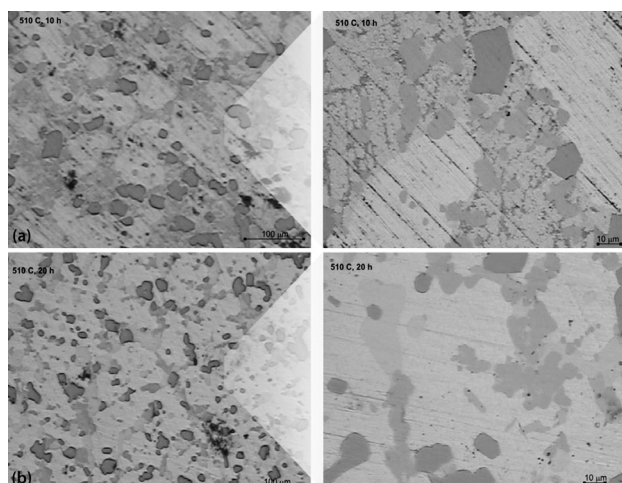


Figure 6: Morphology of alloy D, solution heat treated at 510 °C: a) 10 h, b) 20 h

Slika 6: Morfologija zlitine D, raztopno žarjene na 510 °C: a) 10 h, b) 20 h

Figure 5 shows that increasing the duration of the solution heat treatment at the temperature of 510 °C to 4 h gave better results, i.e., a homogeneous distribution of the primary Si crystals with a rounded shape of the tiles, a homogeneous distribution of the precipitates and dissolution of the metastable phases.

By increasing the solution heat-treatment time (alloy D) at the temperature of 510 °C from 4 h to 10 h, better results were obtained (**Figure 6a**). The results of the microstructural changes obtained when the solution heat-treatment time was extended to 20 h are shown in **Figure 6b**.

In this part of the obtained results, the microstructural changes after the major increases in the time of the solution heat treatment at the temperatures of 500 °C, 510 °C and 515 °C are presented. The results of the combined solution heat treatment of the investigated

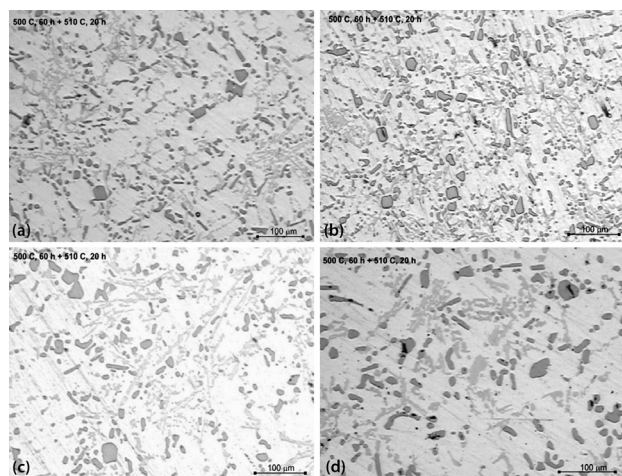


Figure 7: Solution heat treatment for 60 h at 500 °C + 20 h at 510 °C: a) alloy A, b) alloy B, c) alloy C and d) alloy D

Slika 7: Raztopno žarjeno 60 h na 500 °C + 20 h na 510 °C: a) zlitina A, b) zlitina B, c) zlitina C in d) zlitina D

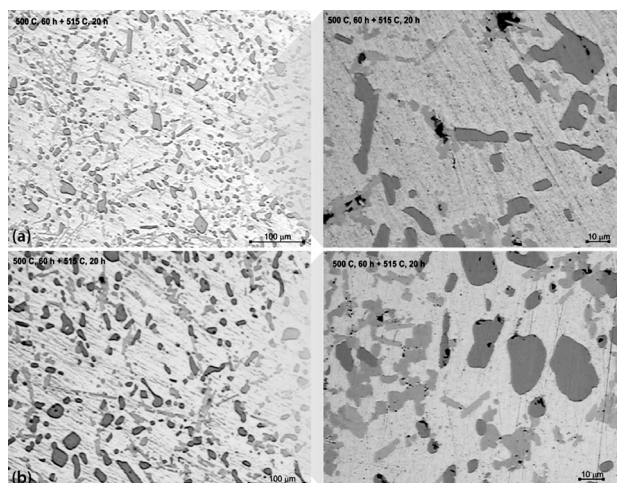


Figure 8: Solution heat treatment for 60 h at 500 °C + 20 h at 515 °C: a) alloy B and b) alloy D

Slika 8: Raztopno žarjeno 60 h na 500 °C + 20 h na 515 °C: a) zlitina B, b) zlitina D

piston alloys A, B, C and D (**Table 1**) at the temperature of 500 °C for 60 h and for a further period of 20 h at 510 °C are presented in **Figure 7**.

Figure 8 shows the combined solution temperatures of 500 °C for 60 h and 515 °C for 20 h. From the obtained results, a rounding of the primary silicon crystals and a dissolution of the metastable phases can be seen in all the alloys. The non-dissolved metastable phases remained in the piston alloys, for which the percentages of the alloying elements are greater than the percentages of their maximum solubility.

The results shown in **Figures 2 to 8** show that heat treatment leads to an interruption of the dendritic structure, a reduction in the segregation of the alloying elements, a rounding of the silicon crystals and an improvement of the links between the particles of the other phases and the aluminum matrix. In the previous research,^{5,16} it was shown that an improved distribution and slow rounding of the silicon crystals affected the crack propagation, to which the improved wear resistance is attributed.^{1,7}

Based on the results shown, it may be concluded that the homogenization time is too long, because, despite the long homogenization time, a complete dissolution of the metastable phases is not possible due to the supersaturation of the solid solution. High temperatures stimulate diffusion and have a positive impact. In order to benefit from deposition annealing, the alloying elements have to be dissolved in the aluminum matrix. However, the results of the boundary dissolution of the alloying elements and the temperature diffusion depend on the heat-treatment temperature. Increasing the temperature of the solution increases both of these parameters and, in this way, also the effect of annealing and, consequently, it improves the mechanical properties and wear resistance of the alloy.⁵

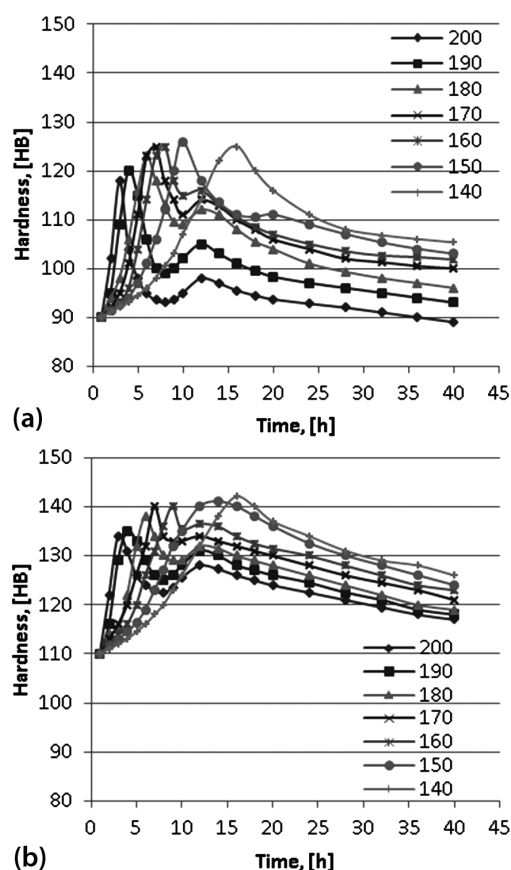


Figure 9: Hardness curves after aging at different temperatures and times: a) alloy A and b) alloy C

Slika 9: Krivulje trdote po staranju pri različnih temperaturah in časih: A) zlitina A in b) zlitina C

3.2 Analysis of the impact of heat treatment on hardness

The process of solution heat treatment at the temperatures below the eutectic temperature and quenching in water down to 20–30 °C results in oversaturated solid solutions. It is then necessary that the obtained supersaturated solid solutions undergo an aging process in order to improve their mechanical properties. The strength curves for alloys A and C (**Table 1**) depending on the temperature and time of aging are shown in **Figure 9**. On both curves, there are two peaks of increasing hardness. The first increase in the hardness is due to a formation of the GP zones. The decrease in the

hardness after the first peak results from a transformation of the GP zones into an intermediate metastable phase, which increases the hardness after a certain time and leads to the second peak.^{5,12} Bearing in mind that the initial composition of these two piston alloys was different, the proportion and arrangement of the formed metastable phases are therefore different, resulting in the samples having different mechanical properties.

3.3 Analysis of economic indicators of heat treatment

In establishing the price of the finished product sample, an important segment is the price of the heat treatment of the castings. An increase in the cost of heat treatment increases the total cost per unit. Bearing in mind that the market economy and increased competition have led to a better quality and lower costs, it is necessary to analyze and optimize the cost of each segment of the piston-fabrication process. The results of the analysis of the economic parameters of the piston heat-treatment process are presented in **Table 2**. Electricity consumption is given in kW h/t. The price of industrial electricity in Serbia is 0.058 €/kW h).

4 CONCLUSIONS

Based on the analysis of the results of the experimental tests presented in this paper, it can be concluded that:

- The choice of heat treatment of alloys depends on the nature of an alloy and the demand. Obtaining the final properties of piston alloys depends on the heat treatment. A combination of heating, the temperature, at which the alloy is being heated, the holding time at this temperature and the cooling rate defines the properties of the obtained material.
- A very long time of solution heat treatment gives excellent results but is certainly not economically viable. About 172 kW h/t of electricity is consumed for every hour of a solution heat treatment in these conditions, or about 180 kW h/t for a 10 °C increase in the treatment temperature.
- It turned out that the optimum modes for the investigated piston casting are the solution heat treatment at 510 °C for 4 h and aging at 180 °C for 6 h.

Table 2: Consumption of electricity

Tabela 2: Poraba električne energije

Process	Consumption of electricity (kW h/t)								
Solution heat treatment	4 h at 480 °C	4 h at 500 °C	1 h at 510 °C	4 h at 510 °C	10 h at 510 °C	15 h at 500 °C	15 h at 510 °C	60 h at 500 °C	60 h at 510 °C
	1090.4	1139.4	628.0	1165.4	2240.0	44265	3135.5	11037.9	11195.4
Aging	4 h at 150 °C	4 h at 160 °C	4 h at 180 °C	7 h at 150 °C	7 h at 160 °C	7 h at 180 °C	7 h at 200 °C	15 h at 200 °C	30 h at 200 °C
	658.7	678.8	720.6	1019.5	1048.7	1108.4	1170.3	2252.1	4280.4

- Therefore, we recommend a determination of the optimum time and temperature of solution heat treatment necessary to achieve a satisfactory structure and obtain the required mechanical properties of castings.

5 REFERENCES

- ¹ S. Manasijevic, R. Radisa, S. Markovic, K. Raic, Z. Acimovic-Pavlovic, Implementation of the infrared thermography for thermo-mechanical analysis of the Al-Si cast piston, *Practical Metallography*, 46 (2009), 565–579
- ² S. Manasijevic, R. Radisa, S. Markovic, Z. Acimovic-Pavlovic, K. Raic, Thermal analysis and microscopic characterization of the piston alloy AlSi13Cu4Ni2Mg, *Intermetallics*, 19 (2011), 486–492
- ³ E. R. Wang, X. D. Hui, G. L. Chen, Eutectic Al-Si-Cu-Fe-Mn alloys with enhanced mechanical properties at room and elevated temperature, *Materials and Design*, 32 (2011), 4333–4340
- ⁴ S. Manasijevic, Z. Acimovic-Pavlovic, K. Raic, R. Radisa, V. Kvrđic, Optimization of cast pistons made of Al-Si piston alloy, *International Journal of Cast Metals Research*, 26 (2013) 5, 255–261
- ⁵ S. Manasijevic, Aluminum piston alloys, LOLA Institute, Belgrade 2012
- ⁶ M. Zeren, The effect of heat treatment on aluminum-based piston alloys, *Materials and Design*, 28 (2007), 2511–2517
- ⁷ R. Gholizadeh, S. G. Shabestar, Investigation of the effects of Ni, Fe and Mn on the formation of complex intermetallic compounds in Al-Si-Cu-Mg-Ni alloys, *Metallurgical and Materials Transactions A*, 42 (2011), 3447–3458
- ⁸ N. A. Belov, D. G. Eskin, N. N. Avxentieva, Constituent phase diagrams of the Al-Cu-Fe-Mg-Ni-Si system and their application to the analysis of aluminum piston alloys, *Acta Materialia*, 53 (2005) 17, 4709–4722
- ⁹ R. C. Hernández, J. H. Sokolowski, Thermal analysis and microscopical characterization of Al-Si hypereutectic alloys, *Journal of Alloys and Compounds*, 419 (2006), 180–190
- ¹⁰ Z. Qian, X. Liu, D. Zhao, G. Zhang, Effects of trace Mn additional on the elevated temperature tensile strength and microstructure of a low-iron Al-Si piston alloy, *Materials Letters*, 62 (2008), 2146–2149
- ¹¹ C. L. Chena, R. C. Thomson, The combined use of EBSD and EDX analyses for the identification of complex intermetallic phases in multi-component Al-Si piston alloys, *Journal of Alloys and Compounds*, 490 (2010), 293–300
- ¹² R. X. Li, R. D. Li, L. Z. He, C. X. Li, H. R. Gruan, Z. Q. Hu, Age-hardening behavior of cast Al-Si base alloy, *Materials Letters*, 58 (2004), 2096–2101
- ¹³ Y. Yang, Y. Li, W. Wu, D. Zhao, X. Liu, Effect of existing form of alloying elements on the microhardness of Al-Si-Cu-Ni-Mg piston alloy, *Materials Science and Engineering A*, 528 (2011), 5723–5728
- ¹⁴ Y. Yang, K. Yu, Y. Li, D. Zhao, X. Liu, Evolution of nickel-rich phases in Al-Si-Cu-Ni-Mg piston alloys with different Cu additions, *Materials and Design*, 33 (2012), 220–225
- ¹⁵ R. Sharma, D. K. Dwivedi, Solutionizing temperature and abrasive wear behavior of cast Al-Si-Mg alloys, *Materials and Design*, 28 (2007), 1975–1981
- ¹⁶ A. Humbertjean, T. Beck, Effect of the casting process on microstructure and lifetime of the Al piston alloy AlSi12Cu4Ni3 under thermo-mechanical fatigue with superimposed high-cycle fatigue loading, *International Journal of Fatigue*, 53 (2013), 67–74
- ¹⁷ R. Taghiabadi, H. M. Ghasemi, S. G. Shabestari, Effect of iron-rich intermetallics on the sliding wear behavior of Al-Si alloys, *Materials Science and Engineering A*, 490 (2008), 162–170
- ¹⁸ M. A. Azmah Hanim, S. Chang Chung, O. Khang Chuan, Effect of a two-step solution heat treatment on the microstructure and mechanical properties of 332 aluminum silicon cast alloy, *Materials and Design*, 32 (2011), 2334–2338
- ¹⁹ Í. Özbek, A study on the re-solution heat treatment of AA 2618 aluminum alloy, *Materials Characterization*, 58 (2007), 312–317

EFFECT OF THE BONDING TIME ON THE MICROSTRUCTURE AND MECHANICAL PROPERTIES OF A TRANSIENT-LIQUID-PHASE BONDED IN718 USING A Ni-Cr-B FILLER ALLOY

VPLIV ČASA SPAJANJA NA MIKROSTRUKTURO IN MEHANSKE LASTNOSTI SPOJA S PREHODNO TEKOČO FAZO PRI SPAJANJU IN718 Z UPORABO ZLITINE Ni-Cr-B ZA SPAJANJE

Majid Pouranvari, Ali Ekrami, Amir Hossein Kokabi

Department of Materials Science and Engineering, Sharif University of Technology, 11365-11155 Tehran, Iran
mpouranvari@yahoo.com, mpouranvari@mehr.sharif.ir

Prejem rokopisa – received: 2012-12-14; sprejem za objavo – accepted for publication: 2013-01-10

The paper aims at addressing the effect of the bonding time on the metallurgical and mechanical properties of a transient-liquid-phase (TLP) bonded IN718 nickel-based superalloy using an Ni-15.2Cr-4B (%) amorphous filler alloy. The results showed that after a partial isothermal solidification, the residual liquid in the joint centerline transformed, during the cooling, to non-equilibrium eutectic-type microconstituents composed of Ni-rich boride, Cr-rich boride and eutectic γ -solid solution phase. The complete isothermal solidification which resulted in a formation of an intermetallic-free joint centerline occurred after a holding period 40 min at the bonding temperature of 1100 °C. An increase in the bonding time improved the joint shear strength due to a decrease in the width of the eutectic-type microconstituents in the joint centerline.

Keywords: transient-liquid-phase bonding, superalloy, solidification, mechanical properties

Članek obravnava vpliv časa spajanja na metalurške in mehanske lastnosti nikljeve superzlitine IN718, spojene s prehodno tekočo fazo (TLP) in z uporabo Ni-15,2Cr-4B (%) amorfnega polnila. Rezultati kažejo, da se po delnem izotermnem strjevanju preostala talina v sredini spoja pretvori pri ohlajanju v neravnotežno sestavino evtektičnega tipa, ki jo sestavljajo z Ni bogati boridi, s Cr bogati boridi in evtektična γ -trdna raztopina. Popolno izotermno strjevanje je bilo doseženo po 40 min zadrževanja pri 1100 °C, pri čemer je nastala sredica spoja brez intermetalnih zlitin. Podaljšanje časa spajanja je izboljšalo strižno trdnost spoja zaradi zmanjšanja širine sestavine evtektičnega tipa v sredini spoja.

Ključne besede: spajanje s prehodno tekočo fazo, superzlitina, strjevanje, mehanske lastnosti

1 INTRODUCTION

Nickel-based superalloys are extensively used in the modern industry due to their excellent high-temperature tensile strength, stress rupture and creep properties, fatigue strength, oxidation and corrosion resistance, and microstructural stability at elevated temperatures.¹⁻³ The superalloy IN718 is one of the workhorse materials being extensively used in critical aero-engines and space applications for high-temperature, creep-resistant applications, nuclear power plants and petrochemical industry.⁴ The strength of IN718 is governed by both the solid-solution and precipitation-hardening mechanisms. While both ordered face-centered-cubic (FCC) γ' -Ni₃(Al,Ti) and metastable ordered body-centered-tetragonal (BCT) γ'' -Ni₃Nb precipitates are formed during an aging cycle of the alloy, the predominant contribution to the precipitation hardening is provided by the latter.⁵

Fusion welding and brazing are two main repairing/joining techniques for superalloys that have been commonly applied in industry.⁶ Conventionally, high temperature brazing, using nickel-based filler alloys, is extensively used as a standard repair/regeneration tech-

nique for superalloy components.^{7,8} In order to lower the liquidus temperature of nickel-based superalloys and increase the fluidity of the braze, melting point depressants (MPD) and modifiers such as phosphorus, silicon and boron are added to the braze alloy. However, these elements are incorporated into the intermetallic phases such as borides, silicides and phosphides during a non-equilibrium eutectic-type solidification of the liquid phase during the cooling stage of the brazing process.^{9,10} The presence of the intermetallic phases in a brazed joint's centerline is known to detrimentally affect the performance of the joint in several ways:

1. Reducing the mechanical properties.¹¹⁻¹⁴
2. Lowering the re-melting temperature and service temperature of a brazed component due to the segregation of the melting-point depressants into a low melting-point eutectic.¹⁵
3. Reducing the corrosion and oxidation resistance of the brazed component.¹⁵

While the sluggish kinetics of the γ'' precipitation makes the IN718 welds free of strain-age cracking,¹⁶ the welding of IN718 suffers from certain problems including:

1. Microfissuring and liquation cracking in the HAZ.^{4,17}

2. The segregation of Nb during the non-equilibrium solidification of the fusion zone and the consequent formation of the Nb-rich Laves phase.^{4,18,19}

Transient-liquid-phase bonding or diffusion brazing is considered to be the preferred repairing/joining process for the nickel-based superalloys,^{6,15,20–24} which is a hybrid process, combining beneficial features of the liquid-phase bonding and the solid-state bonding. In general, it is considered that there are three distinct stages during the diffusion brazing, namely: the base-metal dissolution, the isothermal solidification and the solid-state homogenization.²¹ Combining isothermal solidification with the subsequent solid-state homogenization treatment, offers a possibility of producing the bonds that are chemically almost identical to the parent material and have no discernable microstructural discontinuity at the bond line.^{15,21}

Despite an extensive application of IN718 in various industries, there is only a limited number of published works¹² on the diffusion brazing of this superalloy. There have been some modeling efforts regarding the isothermal solidification time for the TLP bonding of a wrought IN718 alloy using a Ni-Cr-Si-Fe-B filler alloy.¹² In addition, there is only limited information regarding the microstructure development and mechanical properties during a TLP bonding of this superalloy. Therefore, this paper aims at investigating the metallurgy of diffusion brazing of a cast IN718 nickel-based superalloy using a Ni-Cr-B filler alloy.

2 EXPERIMENTAL PROCEDURE

A cast IN718 nickel-based superalloy was used as the base metal in this investigation. A 50 μm thick amorphous Ni-Cr-B (MBF80) filler alloy was used as the interlayer for the TLP bonding. The chemical composition of the base metal and the filler metal is given in **Table 1**.

10 mm \times 5 mm \times 5 mm coupons were sectioned from the base metal using an electro-discharge machine. Thereafter, in order to remove the oxide layer, the contacting surfaces were grounded using 600-grade SiC paper and then ultrasonically cleaned in an acetone bath. The interlayer was then inserted between two base-metal coupons. A Cr-Mo steel fixture was used to fix the coupons in order to hold the sandwich assembly and reduce the metal flow during the TLP operation. No external pressure was applied at the bond line. The bonding operation was carried out in a vacuum furnace under a vacuum of approximately 1.33×10^{-5} mbar. The bonding temperature was selected as 1100 °C. The bonding time was varied from 10 min to 40 min.

The bonded specimens were sectioned perpendicularly to the bond and then microstructural observations were made on the cross-sections of the specimens using an optical microscope and a field emission scanning electron microscope (FESEM). For the microstructural examinations, specimens were etched using 10 mL of HNO_3 , 10 mL of $\text{C}_2\text{H}_4\text{O}_2$, and 15 mL of HCl . Semi-quantitative chemical analyses of the phases formed in the centerline of the bond region and adjacent to the base metal were conducted using a JEOL 5900 FESEM equipped with an ultra-thin-window Oxford Energy Dispersive X-ray Spectrometer (EDS). The element distribution across the joint region was analyzed using a JEOL JXA-8900R electron probe X-ray microanalyzer equipped with line-scan Wavelength-Dispersive Spectrometry (WDS).

A microhardness test was used to determine the joint-region hardness profile. The test was conducted on the sample cross-sections using a 10 g load on a Buehler microhardness tester. To evaluate the mechanical strength of the TLP bonds, the shear test was used instead of the tensile test. The tensile test is not strict to the bond line. Indeed, a minimum amount of the bond line is oriented on the plane experiencing the maximum resolved shear stress (i.e., the plane is oriented at 45° to

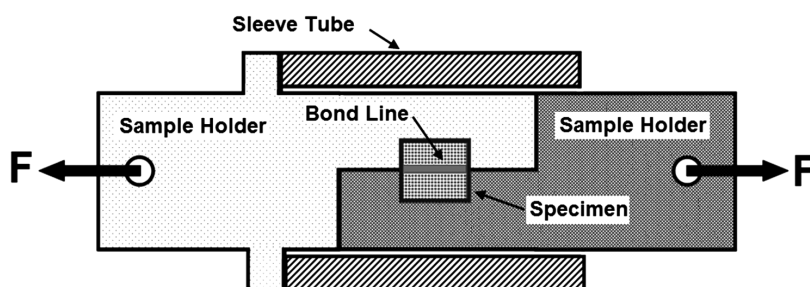


Figure 1: Schematic diagram of a shear-test fixture

Slika 1: Shematski prikaz pritrditve pri strižnem preizkusu

Table 1: Chemical compositions (amount fraction, $\varphi/\%$) of the base metal and interlayer

Tabela 1: Kemijska sestava (množinski delež, $\varphi/\%$) osnovne kovine in vmesnega sloja

	Ni	Cr	Fe	Nb	Mo	Ti	Al	B
IN718	Balance	20.07	18.56	2.75	1.99	1.11	0.86	0.037
Interlayer	Balance	14.34	–	–	–	–	–	18.15

the tensile axis).²⁵ Therefore, it can be deduced that a tensile testing of a TLP bond with a thin interlayer (i.e., 50 μm) does not effectively test the bond line. Therefore, a fixture was designed for the shear testing (**Figure 1**). The designed fixture subjects a sample to a pure shear stress at the bond line. A room-temperature shear test was performed employing an Instron tensile machine with a cross-head speed of 2 mm/min. The edge effects were eliminated by machining before the shear test.

3 RESULTS AND DISCUSSION

3.1 Microstructure and hardness characteristics in a partially isothermal solidified bond

Figures 2a and **b** show optical microscopy images of the bonds made at 1100 °C for 10 min indicating three distinct microstructural zones in the bond region:

(i) Isothermally solidified zone (ISZ):

This zone is formed due to an interdiffusion-induced compositional change.²⁰ A typical compositional analysis of ISZ is given in **Table 2**. The microstructure of this zone consisted of a proeutectic Ni-rich γ solid-solution phase and it is free of the intermetallic phase. According to **Table 2**, this zone contains certain amounts of Nb, Mo, Al and Ti that were not present in the initial composition of the filler alloy. This indicates a dissolution of the base metal during the bonding process. The diffusion of boron (B) from the liquid phase into the base metal increases the liquidus temperature of the liquid phase. Once the liquidus temperature reaches the bonding temperature, the liquid re-solidifies during the holding time at the bonding temperature (i.e., the isothermal solidification starts). Due to the absence of the solute rejection at the solid/liquid interface during the isothermal solidification under equilibrium condition, the only solid phase that forms is the solid-solution phase and the formation of the other phases is basically prevented.¹⁴

(ii) Athermally solidified zone (ASZ):

This zone is formed due to an insufficient time for the completion of isothermal solidification. The microstructure of ASZ consists of the microconstituents with a eutectic-like morphology and is made up of three distinct phases (**Figures 2c, e, f**). The phases in ASZ are marked as X, Y and Z. Their SEM-EDS spectra are shown in

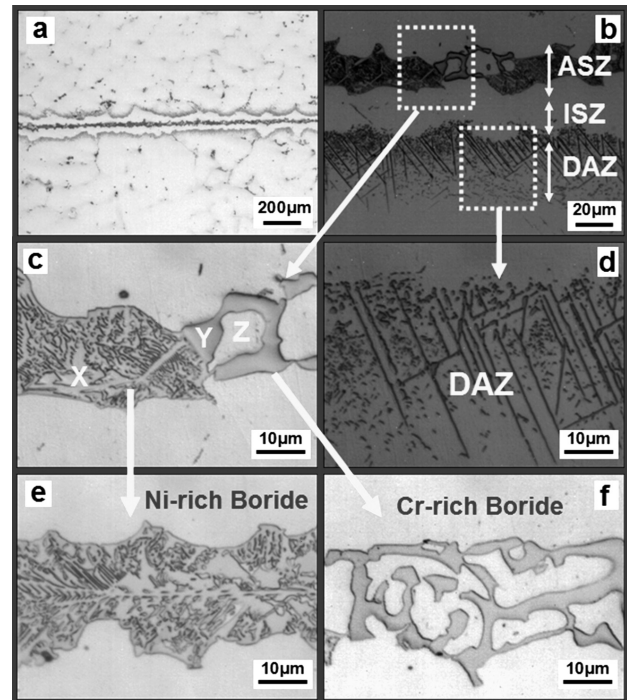


Figure 2: Microstructure of TLP bonded IN718 at 1100 °C for 10 min: a) and b) overview of the joint region indicating three distinct microstructural zones including athermal solidification zone (ASZ), isothermal solidification zone (ISZ) and diffusion affected zone (DAZ); c) a magnified micrograph of eutectic microconstituents in ASZ; d) secondary precipitates in DAZ; e) a magnified view of Ni-rich boride; f) a magnified view of Cr-rich boride

Slika 2: Mikrostruktura TLP-spoja IN718 pri 1100 °C, 10 min: a) in b) pregled območja spoja, ki kaže tri ločena področja, vključno z atermičnim področjem strjevanja (ASZ), področje izotermičnega strjevanja (ISZ) in difuzijsko vplivanega področja (DAZ), c) povečan posnetek evtektika v ASZ, d) sekundarni izločki v DAZ, e) povečan posnetek z Ni bogatih boridov, f) povečan posnetek s Cr bogatih boridov

Figure 3. Typical compositional analyses of the X, Y and Z are given in **Table 2**. The EDS analyses suggest that X is Ni-rich boride (**Figure 2e**). **Figure 4** shows an X-ray elemental map of the phase marked as Y. According to **Figures 3b** and **4**, this intermetallic phase is Cr-rich boride (**Figure 2f**) which is also rich in Mo and Nb. The phase marked as Z is a Ni-rich solid solution formed as a part of the eutectic reaction.

Indeed, the presence of an intermetallic phase in the joint centerline indicates that the bonding time of 10 min

Table 2: Chemical compositions (amount fraction, $\phi/\%$) of different metallic constituents for various phases observed in the brazed affected zone
Tabela 2: Kemijska sestava (množinski delež, $\phi/\%$) različnih kovinskih sestavin različnih faz, opaženih v območju vpliva spajkanja

		Ni	Cr	Fe	Mo	Nb	Al	Ti
ASZ	Ni-rich boride*	74.93	13.19	3.12	–	6.70	–	2.06
	Cr-rich boride*	6.71	55.64	3.29	12.87	20.71	–	0.78
	γ eutectic	68.54	17.49	5.5	0.45	6.31	0.38	1.33
DAZ	Needle-like precipitates*	56.44	22.34	11.67	4.82	2.98	0.92	0.83
	Adjacent γ matrix	66.54	13.43	15.54	1.74	1.32	0.71	0.72
ISZ	Solid solution	74.53	18.22	4.57	0.69	0.88	0.60	0.51

*Boron could be detected with EDS in this phase, but light elements could not be quantified due to the inability of the EDS system

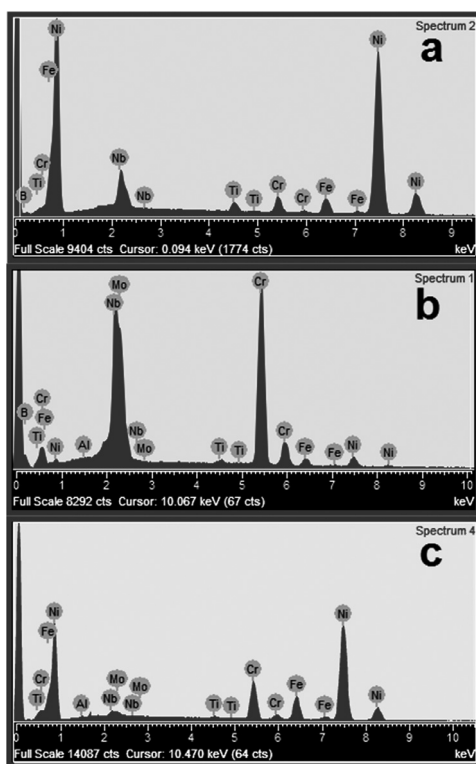


Figure 3: SEM-EDS spectra of: a) Ni-rich boride, b) Cr-rich boride and c) eutectic γ solution

Slika 3: SEM-EDS-spektri: a) z Ni bogati boridi, b) s Cr bogati boridi in c) evtektična γ -raztopina

is not sufficient for the completion of isothermal solidification. This suggests that there was an amount of the residual liquid in the joint gap after holding the sample at 1100 °C for 10 min. Therefore, the solidification of the residual liquid occurred during the cooling. The segregation of the solute elements is the key feature of the athermal solidification. A very low solubility of B in Ni (amount fractions: 0.3 % according to the binary Ni-B equilibrium phase diagram²⁶) and a very low partition coefficient of B in Ni (≈ 0.008 according to the Ni-B binary phase diagram²⁶) lead to a rejection of B into the adjacent melt. A continuous solute enrichment of the liquid could make B exceed the solubility limit of the solute in the γ phase. Then, the secondary solidification constituents (i.e., intermetallic phases) are formed. Ohsasa et al.²⁷ modeled the solidification behavior of the residual liquid phase during the TLP bonding of Ni/Ni-Cr-B/Ni using the Scheil simulation. They reported that the solidification of the liquid phase started with a formation of the Ni-rich γ solid solution as the primary phase, followed by a eutectic reaction of Ni_3B and the γ solid solution at 1042 °C. The solidification process is terminated by a formation of the ternary eutectic-reaction microconstituents of the γ solid solution, Ni_3B and CrB at 997 °C. Therefore, it can be concluded that the centerline eutectic-like microconstituents observed in the present work, consisting of γ , Bi-rich boride and Cr-rich

boride, are formed by the eutectic-type solidification reactions during the cooling, due to an insufficient holding time for a complete isothermal solidification during the bonding.

(iii) Diffusion affected zone (DAZ):

This zone consists of the second-phase particles with two different morphologies: the particles with a blocky morphology and the particles with a needle-like morphology (**Figure 2d**). **Table 2** presents the compositional analyses of the precipitates and the adjacent γ matrix. **Figure 5** shows an X-ray line-scan across some needle-like precipitates in DAZ indicating a partitioning tendency of various elements that are present in the particles compared to that of the adjacent austenitic γ matrix. According to **Table 2** and **Figure 5**, the precipitates are enriched with Cr, Mo, Nb, and B, while they are lean in Fe and Ni. Therefore, this confirms that these secondary phases are Cr-Mo-Nb-based borides.

The morphology of these precipitates suggests that they are not formed during the solidification. The formation of boride precipitates in DAZ is directly associated with the B diffusion out of the liquid into the base metal during the bonding process. Considering the fact that the isothermal solidification is controlled by the diffusion of B into BM, a formation of boride precipitates in DAZ is possible. Due to the diffusion of B into BM, a B-containing alloy is formed in a narrow region in the substrate zone adjacent to ISZ. The solubility of B in this alloy is

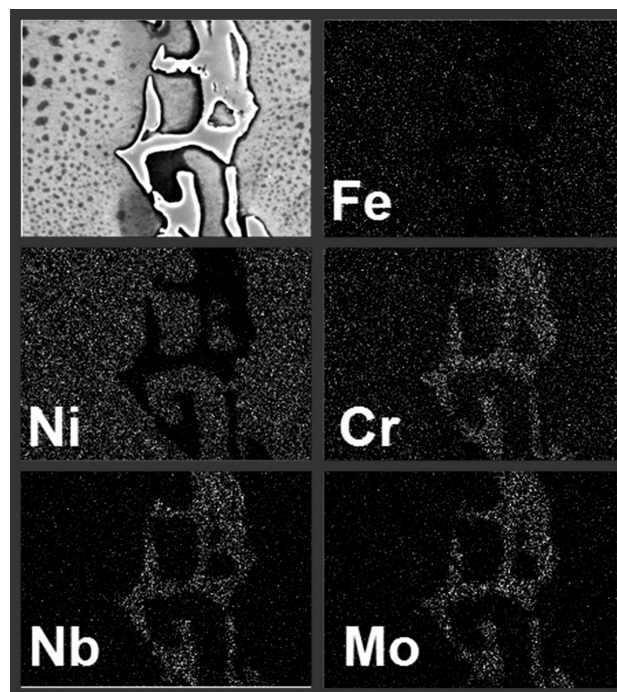


Figure 4: X-ray elemental map of Cr-rich boride in ASZ showing that the intermetallic phase is rich in Cr, Mo and Nb and lean in Fe and Ni compared to the surrounding γ solid-solution matrix

Slika 4: Rentgenski posnetek razporeditve s Cr bogatih boridov v ASZ kaže, da so intermetalne faze obogatene s Cr, Mo in Nb, ni pa Fe in Ni v primerjavi z γ -trdno raztopino osnove

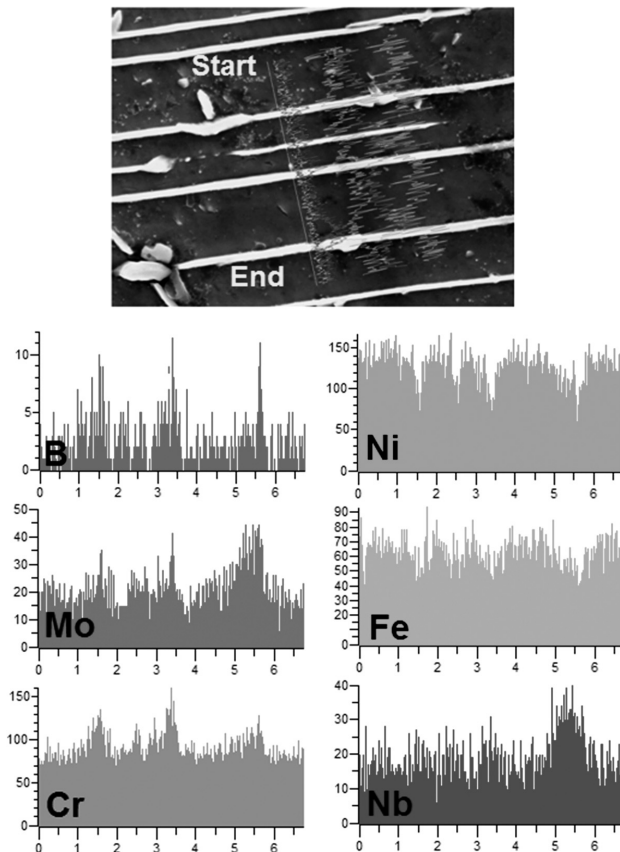


Figure 5: X-ray line scan across the DAZ precipitates showing the partitioning tendency of the elements between the precipitates and the matrix

Slika 5: Rentgenska linijska analiza preko izločkov v DAZ, ki kaže tendenco različnega razporejanja elementov med izločki in osnovo

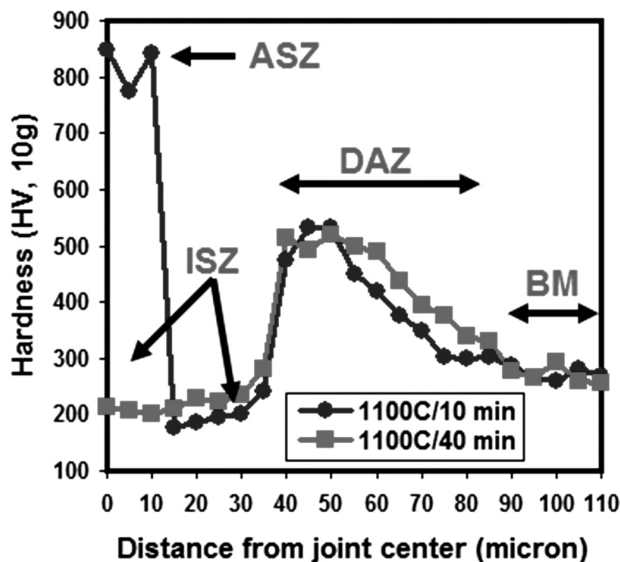
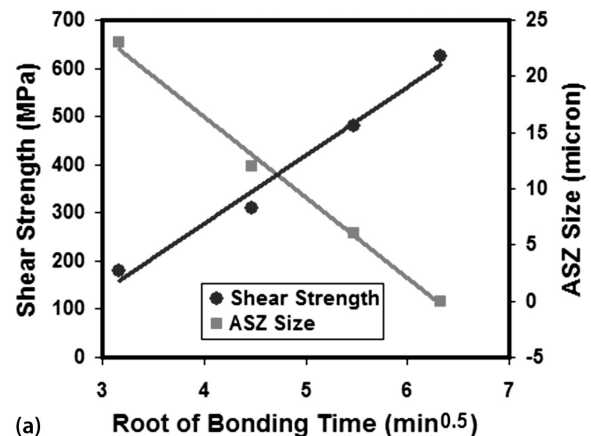


Figure 6: Hardness distribution across the bond region after a partial isothermal solidification at 1100 °C for 10 min and after a complete isothermal solidification at 1100 °C for 40 min

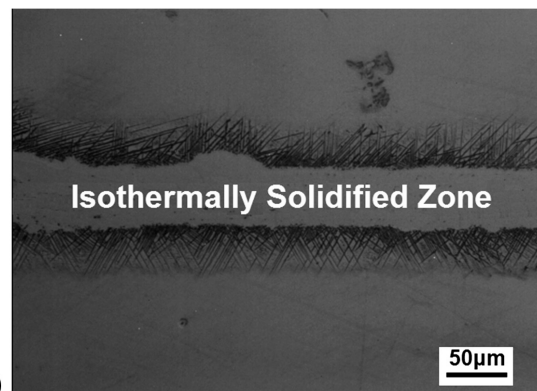
Slika 6: Potek trdote preko spoja po delnem izotermnem strjevanju pri 1100 °C po 10 min ter po popolnem izotermnem strjevanju pri 1100 °C po 40 min

limited. This fact coupled with the presence of Cr, Mo and Nb in the matrix, which are strong boride formers, can explain the formation of the Cr-Mo-Nb-rich precipitates. Gale and Wallach²⁸ provided the some evidence confirming that these precipitates are formed at the bonding temperature not during the cooling.

The hardness profile across the joint region is a quantitative measurement of the mechanical properties of different zones in the joint region. The hardness profile is a good indicator of the bond microstructure and can be used to assess the effect of the secondary-phase precipitates on mechanical properties.¹³ **Figure 6** shows the hardness profile of this bond indicating four distinct zones: Region I corresponds to ASZ. The average hardness of ASZ is about 820 HV. According to the microstructure of ASZ, the peak hardness in this zone is due to the fact that the eutectic-type structure contains hard brittle nickel boride. Region II corresponds to ISZ. The average hardness of ISZ is 200 HV, which is lower than for BM. The interdiffusion of the alloying elements between the joint region and the base metal determines the hardness of ISZ. The low hardness of ISZ can be attributed to an insufficient diffusion of the alloying



(a) Root of Bonding Time ($\text{min}^{0.5}$)



(b)

Figure 7: a) ASZ size and shear strength versus square root of bonding time, b) microstructure of the joint region after the completion of isothermal solidification at 1100 °C for 40 min

Slika 7: a) Velikost ASZ in strižna sila v odvisnosti od kvadratnega korena časa vezanja, b) mikrostruktura področja spoja po končanem izotermnem strjevanju pri 1100 °C in času 40 min

elements such as Nb, Mo, Cr, Al and Ti. The amounts of Nb, Mo, Cr, Al and Ti in ISZ (**Table 2**) are lower than those found in BM (**Table 1**). Region III corresponds to DAZ. The average hardness of DAZ is 420 HV, which can be related to boride precipitates. Region IV corresponds to the base metal.

3.2 Effect of the bonding time on the microstructure and hardness characteristics

A joint microstructure depends on the elemental interdiffusion between the base metal and the joint region, which in turn is governed by the bonding time. The average ASZ size was measured and plotted against the square root of the bonding time (**Figure 7a**). As can be seen, there is a linear relation between the ASZ size and the square root of the bonding time. According to Fick's second law,²⁹ the implication is that the formation of a gamma solid solution is a diffusion-controlled process. Indeed, in the case of the diffusion brazing of IN718/Ni-Cr-B/IN718, the isothermal solidification process is controlled by the formation and growth of the γ -solid solution, which is governed by the B diffusion in the base metal. An increase in the bonding time reduces the volume fraction of the eutectic-type microconstituent in the joint centerline. When the bonding time increased to 40 min, no eutectic microconstituent was observed in the bond region (**Figure 7b**). Therefore, it is concluded that the holding time of 40 min at 1100 °C is sufficient for an isothermal solidification completion.

The effect of isothermal solidification on the hardness profile is also superimposed in **Figure 6**. Since the isothermal solidification eliminates the eutectic-type microconstituent, it is not surprising that the peak hardness in the joint centerline is not present. However, the completion of isothermal solidification does not influence the peak hardness in DAZ. This is due to the fact that boride precipitates in DAZ are still stable even after the isothermal-solidification completion.

3.3 Effect of the bonding time on the shear strength

The effect of the bonding time on the shear strength of the TLP joints is shown in **Figure 7a**. It can be seen that an increase in the bonding time increases the joint shear strength. As can be seen, the shear strength of the bonds made at 1100 °C for 10 min is the lowest. According to **Figure 7a** there is an inverse relation between the joint shear strength and the ASZ size. When the bonding time is increased up to 20 min, the joint shear strength increases to 310 MPa. With a further increase in the bonding time up to 30 min, the joint shear strength increases to 480 MPa. This can be related to the decrease in the ASZ size. Therefore, it can be deduced that in the bonding condition, in which the isothermal solidification is not completed, the extent of the eutectic constituent (ASZ) is the controlling factor of the joint strength. A high hardness of the eutectic products (**Figure 6**) is

coupled with the fact that the boride phases form the interlinked network provide a metallurgical notch, which significantly decreases the load-carrying capacity of the joint. Therefore, it is necessary to eliminate the eutectic products in order to improve the strength of the joints. In the bonding time of 40 min at 1100 °C, when the eutectic products are completely removed, the bonds with the shear strength of 625 MPa were achieved.

4 CONCLUSIONS

The joining of the as-cast IN718 nickel-based superalloy was conducted through the TLP bonding using Ni-15.2Cr-4B (in mass fractions, %) at the bonding temperature of 1100 °C. The following conclusions can be drawn from this study:

1. The solidification mechanism of the liquid phase is controlled with the bonding time. When the bonding time is lower than the critical value (40 min for the present system), isothermal solidification is not completed at the bonding temperature and the remaining liquid is transformed into a eutectic-type microconstituent made up of Ni-rich boride, Cr-rich boride and a eutectic-gamma solid solution.
2. A complete isothermal solidification which resulted in the formation of an intermetallic-free joint centerline occurred after the holding time of 40 min at the bonding temperature of 1100 °C.
3. Extensive Cr-Mo-Nb-based boride precipitates were observed in DAZ. These precipitates were stable even after the completion of isothermal solidification.
4. It has been shown that the bonding time has a significant impact on the joint mechanical properties in terms of hardness distribution and shear strength. An increase in the bonding time increased the shear strength of the joint due to a decrease in the width of the eutectic-type microconstituents.
5. It was found that there is an inverse relation between the width of a eutectic-type microconstituent (i.e., ASZ) and the shear strength of the TLP bonded IN718.

Acknowledgement

One of the authors (MP) gratefully acknowledges the support provided during his sabbatical at the Department of Materials Science & Engineering, Seoul National University (SNU). The support from Professor H. N. Han (SNU) is greatly acknowledged.

5 REFERENCES

- ¹ A. Milosavljevic, S. Petronic, S. Polic-Radovanovic, J. Babic, D. Bajic, The influence of the heat treatment regime on a fracture surface of nickel-based superalloys, *Mater. Tehnol.*, 46 (2012) 4, 411–417
- ² R. Sunulahpašić, M. Oruč, M. Hadžalić, M. Rimac, Optimization of the mechanical properties of the superalloy Nimonic 80A, *Mater. Tehnol.*, 46 (2012) 3, 263–267

- ³ A. Semenov, S. Semenov, A. Nazarenko, L. Getsov, Computer simulation of fatigue, creep and thermal-fatigue cracks propagation in gas-turbine blades, *Mater. Tehnol.*, 46 (2012) 3, 197–203
- ⁴ B. Rivaux, X. Cao, M. Jahazi, J. Cuddy, A. Birur, Effect of pre- and post-weld heat treatment on metallurgical and tensile properties of Inconel 718 alloy butt joints welded using 4 kW Nd:YAG laser, *J. Mater. Sci.*, 44 (2009), 4557–4571
- ⁵ A. C. Yeh, K. W. Lu, C. M. Kuo, H. Y. Bor, C. N. Wei, Effect of serrated grain boundaries on the creep property of Inconel 718 superalloy, *Mater. Sci. Eng. A*, 530 (2011), 525–529
- ⁶ M. Pouranvari, A. Ekrami, A. H. Ekrami, Microstructure development during transient liquid phase bonding of GTD-111 nickel-based superalloy, *J. Alloys Comp.*, 461 (2008), 641–647
- ⁷ J. H. G. Matthij, Role of brazing in repair of superalloy components—advantages and limitations, *Mater. Sci. Technol.*, 1 (1985), 608–612
- ⁸ A. Rabinkin, Brazing with (NiCoCr)-B-Si amorphous brazing filler metals: Alloys, processing, joint structure, properties, applications, *Sci. Technol. Weld. Joining*, 9 (2004), 181–199
- ⁹ S. K. Tung, L. C. Lim, M. O. Lai, Solidification phenomena in nickel base brazes containing boron and silicon, *Scripta Mater.*, 34 (1996), 125–133
- ¹⁰ N. R. Philips, C. G. Levi, A. G. Evans, Mechanisms of Microstructure Evolution in an Austenitic Stainless Steel Bond Generated Using a Quaternary Braze Alloy, *Metall. Mater. Trans. A*, 39 (2008), 142–9
- ¹¹ A. Sakamoto, C. Fujiwara, T. Hattori, S. Sakai, Optimizing processing variables in high-temperature brazing with nickel-based filler metals, *Weld. J.*, 68 (1989), 63–71
- ¹² M. A. Arafin, M. Medraj, D. P. Turner, P. Bocher, Transient liquid phase bonding of Inconel 718 and Inconel 625 with BNi-2: Modeling and experimental investigations, *Mater. Sci. Eng. A*, 447 (2007), 125–133
- ¹³ M. Pouranvari, A. Ekrami, A. H. Kokabi, Microstructure-properties relationship of TLP-bonded GTD-111 nickel-base superalloy, *Mater. Sci. Eng. A*, 490 (2008), 229–234
- ¹⁴ O. A. Ojo, N. L. Richards, M. C. Chaturvedi, Effect of gap size and process parameters on diffusion brazing of Inconel 738, *Sci. Technol. Weld. Joining*, 9 (2004), 209–220
- ¹⁵ D. S. Duvall, W. A. Owczarski, D. F. Paulonis, TLP Bonding: A new method for joining heat resistant alloys, *Weld. J.*, 53 (1974), 203–214
- ¹⁶ R. Thambury, W. Wallace, J. A. Goldak, Post weld heat treatment cracking in superalloys, *Int. Met. Rev.*, 28 (1983), 1–22
- ¹⁷ N. L. Richards, X. Huang, M. C. Chaturvedi, Heat affected zone cracking in cast inconel 718, *Mater. Charact.*, 28 (1992), 179–87
- ¹⁸ C. H. Radhakrishna, K. P. Rao, The formation and control of Laves phase in superalloy 718 welds, *J. Mater. Sci.*, 32 (1997), 1977–1984
- ¹⁹ G. D. J. Ram, A. V. Reddy, K. P. Rao, G. M. Reddy, Control of Laves phase in Inconel 718 GTA welds with current pulsing, *Sci. Technol. Weld. Joining*, 9 (2004), 390–398
- ²⁰ M. Pouranvari, A. Ekrami, A. H. Kokabi, Effect of bonding temperature on microstructure development during TLP bonding of a nickel base superalloy, *J. Alloys Comp.*, 469 (2009), 270–275
- ²¹ W. F. Gale, D. A. Butts, Transient liquid phase bonding, *Sci. Technol. Weld. Joining*, 9 (2004), 283–300
- ²² O. A. Idowu, N. L. Richards, M. C. Chaturvedi, Effect of bonding temperature on isothermal solidification rate during transient liquid phase bonding of Inconel 738LC superalloy, *Mater. Sci. Eng. A*, 397 (2005), 98–112
- ²³ F. Jalilian, M. Jahazi, R. A. L. Drew, Microstructural evolution during transient liquid phase bonding of Inconel 617 using Ni-Si-B filler metal, *Mater. Sci. Eng. A*, 447 (2007), 125–33
- ²⁴ M. Pouranvari, A. Ekrami, A. H. Kokabi, Microstructure-properties relationship of TLP-bonded GTD-111 nickel-base superalloy, *Materials Science and Engineering A*, 490 (2008), 229–34
- ²⁵ D. A. Butts, Transient liquid phase bonding of a third generation gamma-titanium aluminium alloy-Gamma Met PX, PhD thesis, Auburn University, 2005
- ²⁶ T. B. Massalski (ed.), Binary alloy phase diagrams, ASM, Metals Park, OH 1986
- ²⁷ K. Ohsasa, T. Shinmura, T. Narita, Isothermal solidification behavior during the transient liquid phase bonding process of nickel using binary filler metals, *J. Phase Equil.*, 20 (1999), 199–206
- ²⁸ W. F. Gale, E. R. Wallach, Microstructural development in transient liquid-phase bonding, *Metall. Trans. A*, 22 (1991), 2451–2457
- ²⁹ J. Crank, The Mathematics of Diffusion, 2nd ed., Oxford University Press, Oxford, United Kingdom 1975

ELECTRO-CODEPOSITED Cr-SiC COMPOSITE COATINGS: EFFECT OF THE PULSE-CURRENT FREQUENCY ON MORPHOLOGY AND HARDNESS

KOMPOZITNA PREVLEKA IZ ELEKTRONANESENEGA Cr-SiC: VPLIV FREKVENCE PULZIRAJOČEGA TOKA NA MORFOLOGIJO IN TRDOTO

Orkut Sancakoğlu^{1,2,3}, Mustafa Erol^{1,2,3}, Bahattin Agaday^{2,4}, Erdal Çelik^{1,2}

¹Dokuz Eylül University, Dept. of Metallurgical and Materials Engineering, Buca, 35160 Izmir, Turkey

²Dokuz Eylül University, Center for Production and Applications of Electronic Materials (EMUM), Buca, 35160 Izmir, Turkey

³Dokuz Eylül University, Graduate School of Natural and Applied Sciences, Buca, 35160 Izmir, Turkey

⁴Dokuz Eylül University, Izmir Vocational School of Higher Education, Department of Technical Programs, Buca, 35160 Izmir, Turkey
orkut.sancakoglu@deu.edu.tr

Prejem rokopisa – received: 2012-12-18; sprejem za objavo – accepted for publication: 2013-01-31

In this research, submicrometer silicon-carbide (SiC) ($APS = 200$ nm) ceramic particles were co-deposited with chromium metal (Cr) via an electrodeposition system to fabricate Cr-SiC metal-matrix composite films. Phase identifications of the fabricated composite coatings were performed with an X-ray diffractometer (XRD) and surface morphologies were investigated using a scanning electron microscope (SEM) with an energy dispersive X-ray spectroscopy (EDS) system attachment. Mechanical properties of the coatings such as hardness were determined under an applied load of 980.7 mN using a micro-hardness tester. It was concluded that SiC ceramic particles were physically adsorbed on the cathode surface forming a composite film structure with Cr metal and that a co-deposition of the sub-micron-sized ceramic particles with metals via an electrodeposition system was successful. In addition, in comparison with the reference coatings, the hardness of the SiC-reinforced composite coatings was increased by up to 50 %. The frequency, being a parameter of pulse current, is determined as an effective parameter in a co-deposition of ceramic particles with metals.

Keywords: co-deposition technique, pulse current (PC), composite coatings, micro-hardness

V tej raziskavi so bili za izdelavo kompozitne tanke plasti Cr-SiC s kovinsko matrico sonaneseni mikrometrski keramični delci silicijevega karbida (SiC) ($APS = 200$ nm) z elektronanosom kovinskega kroma (Cr). Identifikacija faz v izdelani kompozitni prevleki je bila narejena z rentgenskim difraktometrom (XRD), morfologija površine pa je bila preiskana z vrstičnim elektronskim mikroskopom (SEM) z dodano energijsko disperzijsko spektroskopijo (EDS). Mehanske lastnosti prevleke, kot je trdota, so bile ugotovljene z merilnikom mikro-trdote z obtežbo 980,7 mN. Ugotovljeno je bilo, da so keramični delci SiC fizikalno adsorbirani na površini katode in da je z elektronanosom mogoč uspešen nastanek kompozitne plasti s strukturo iz kovinskega Cr in sonanosom keramičnih delcev, manjših od mikrometra. Glede na referenčno prevleko s SiC ojačena kompozitna prevleka izkazuje do 50-odstotno povečanje velikosti trdote. Ugotovljeno je, da je frekvenca kot parameter pulzirajočega toka učinkovit parameter pri sonašanju keramičnih delcev in kovin.

Gljučne besede: tehnika sonašanja, pulzirajoč tok (PC), kompozitna prevleka, mikrotrdota

1 INTRODUCTION

Electrodeposition is a surface finishing technique that has been used to improve the properties such as hardness, wear and corrosion resistance compared to the parent (substrate) metals for decades. This technique involves only pure metal^{1,2} or alloy³⁻⁵ depositions on the substrates. However, a promising technique called the co-deposition (electrolytic co-deposition) involves a deposition of fine ceramic particles with metals on the metal substrates. There are not many alternatives to obtaining the materials with both improved corrosive and mechanical properties. It is known that "combining the best properties of two different materials to obtain one material with excellent properties" is the main idea of fabricating composites. Based on this idea, several research groups focused on the co-deposition of metal-ceramic pairs such as: Ni-SiC,⁶⁻⁸ Zn-Al₂O₃,⁹⁻¹¹ Ni-Al₂O₃,^{10,11} Cr-Al₂O₃,^{12,13} to improve the mechanical

and/or corrosive properties of the coatings. Within this scope, a production of less studied Cr-SiC composite films^{12,14} was performed, new systems were designed replacing the traditional electrodeposition cells, and coatings were fabricated within these systems using different electrodeposition parameters such as the pulse current (PC) and its sub-parameters (pulse-current frequency) that directly affect the co-deposition.

2 EXPERIMENTAL DETAILS

In the present study, we draw attention to the micro-structural and mechanical properties of the composite coatings formed on steel substrates with an electro-codeposition process. Low-carbon steel cylinders with 13 mm diameters were used as the cathode and a Pb-7 % Sn alloy was used as the anode. Prior to electroplating, the substrates were mechanically ground with SiC abrasive paper to achieve the final surface quality of

2400 grit and then ultrasonically cleaned in trichloroethylene for 10 min to remove the contamination. After that, etching at 20–30 A/dm² in a volume fraction 60 % H₂SO₄ solution was performed for 1–2 min.

For the experimental studies two different electrolytes (baths) were prepared: a bath without SiC and a bath with a 4g/(100 ml) SiC (*APS* = 200 nm) addition defined as Bath-Ref and Bath-S, respectively. The composition of Bath-Ref and electrodeposition conditions for all the processes are listed in **Table 1**. The bath codes relating to their ceramic contents and the sample codes derived for different deposition parameters are given in **Table 2**. To avoid a precipitation of the ceramic content in the electrolyte, the baths were circulated with both a magnetic stirrer and air ventilators during the process.

Table 1: Composition of the electrolytes and electrodeposition conditions

Tabela 1: Sestava elektrolita in parametri elektronanašanja

Bath composition:	
Chromium oxide (CrO ₃)	300 g/L
Catalyst*	30 g/L
Sulfuric acid (H ₂ SO ₄)	2.18 ml/L
Gas-reducer additive**	6.5 ml/L
Bath conditions:	
Temperature	40–50 °C
Current density	60 A/dm ²
Agitation type	Magnetic stirring & air ventilation

Catalyst* (AK 3651 D AKROM) and gas-reducer additive** (AK 3301 FS) are the registered trademarks of ATILIM CHEMICALS COMPANY, ISTANBUL

Table 2: Bath codes and sample codes (R, S1, S2, and S3) according to their ceramic contents and pulse-frequency conditions

Tabela 2: Oznaka kopeli in vzorcev (R, S1, S2 in S3) glede na vsebnost keramike in frekvenco pulza

Bath codes (Electrolyte codes)	Ceramic-particle content and type (g/(100 ml))	Pulse-frequency conditions of the samples (Hz)		
		10	25	50
Bath-Ref.	–	–	R	–
Bath-S	4-SiC	S1	S2	S3

Table 3: Pulse-current parameters for the electrodeposition

Tabela 3: Parametri pulza toka pri elektronanašanju

Frequency (Hz)	Pulse-base time (ms)			Current density (A/dm ²)	
	<i>T</i> _{on}	<i>T</i> _{off}		Peak (<i>I</i> _p)	Average (<i>I</i> _{avr.})
10	80	20	0.80	75	60
25	20	20	0.50	120	60
50	15	5	0.75	80	60

Using some of the optimization sets reported in our previous study,¹⁴ the optimum parameters were found to be 60 A/dm², simultaneous air ventilation and magnetic stirring, and PC (pulse current) for the current density, agitation type and current type, respectively. In addition to this, a set of samples was fabricated for three different frequency conditions in the pulse current to compare the

current type and pulse-frequency effect on the properties. These parameters applied to all the sets are given in **Table 3**.

In order to determine the acidic and basic characteristics of electrolytes, the pH values of the prepared solutions were measured using a standard pH meter with a Mettler Toledo electrode. X-ray diffraction (XRD) patterns of the electrodeposited composite coatings were determined by means of a multipurpose RIGAKU-D/Max-2200/PC model diffractometer with a Cu-K_α radiation using a multipurpose thin-film attachment. The surface morphologies of the coatings were examined with a scanning electron microscope (JEOL-JSM 6060 SEM) with an energy-dispersive x-ray spectroscopy (IXRF System EDS) system attachment. An accelerating voltage of 20 kV was used for SEM imaging and SEM/EDX analyses. Weight percentage distributions and an elemental mapping of the elements were determined with EDS. A SHIMADZU-HMV-2 model micro-hardness tester was used for the hardness tests. In this study, all the hardness tests were handled under an applied load of 980.7 mN (HV_{0.1}).

3 RESULTS AND DISCUSSION

The anti-corrosion coatings fabricated with the electrodeposition have been widely investigated in the literature.^{15,16} With the development of nanoceramic particles, the nanocomposite electrodeposition has attracted more attention due to its potential applications in improving the corrosion resistance.^{17–19} Benea et al.¹⁷ reported that SiC nanoparticles in a Ni-SiC composite coating decreased both the electrochemical corrosion and the wear corrosion, compared with the pure-nickel coating. Zn-Ni alloys have been widely applied as highly corrosion-resistant coatings, especially in the automobile industry.^{20,21} Al₂O₃/SiC/WC possesses an excellent

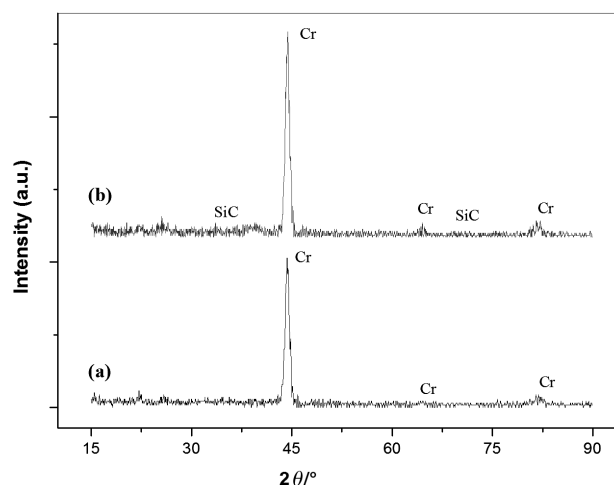


Figure 1: XRD patterns of: a) pure-Cr and b) SiC-reinforced composite coatings produced with the electrodeposition system

Slika 1: Rentgenska posnetka: a) čisti Cr in b) s SiC ojačana kompozitna prevleka, izdelana z elektronanosom

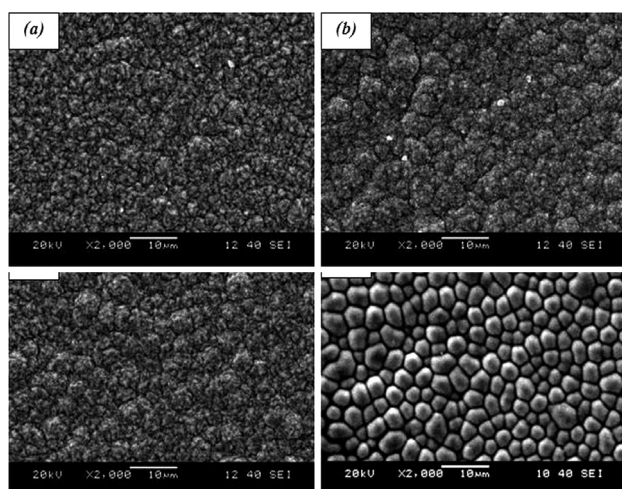


Figure 2: SEM images of: a) R1, b) S1, c) S2 and d) S3 samples (embedded and metal-coated agglomerates of the ceramic particles at 2000x magnification)

Slika 2: SEM-posnetki, ki pripadajo vzorcem z oznakami: a) R1, b) S1, c) S2 in d) S3 (vloženi keramični delci in aglomerat prevleke pri 2000-kratni povečavi)

chemical stability and good mechanical properties, such as high microhardness and wear resistance. It has been used extensively in the metal-matrix composite coatings.^{22–25} In our present work, the method of fabricating hard, wear-resistant Cr-SiC coatings has been determined. The objective of the present study is to reveal the coating process, analyze the co-deposited products and investigate the mechanical behavior.

The phase identifications of the coatings were performed with the XRD technique for all the Cr-matrix

composite coatings. **Figure 1** denotes the XRD patterns of the pure Cr coating and the samples chosen from the SiC-reinforced composite coatings.

As it is seen in **Figure 1a**, the coating fabricated in the reference chromium bath contains only the metallic Cr-phase structure. On the other hand, from the patterns belonging to the coatings fabricated in the SiC (containing) bath, it is clear that the co-deposition process was successful having no chemical interaction (alloying, intermetallic-phase formation, etc.) between the electrolyte and the particles (**Figure 1b** for details).

SEM images are part of a systematic study being interpreted on the basis of the particle addition and pulse-frequency effect on the coating structures. **Figure 2** presents the SEM images according to the increased frequency values (10, 25 and 50) Hz. Once the images are compared with each other, a small decrease in the grain size with an increased frequency is observed. As known theoretically, a decrease in the grain size gives the material advanced mechanical properties such as high hardness.

The X-ray mapping results in **Figure 3** indicate that the sub-micron-sized SiC ceramic particles were successfully co-deposited with chromium metal. Even though it was thought that the surface morphologies were homogenous, when all the coated surfaces were inspected, it became clear from the mapping results that there are also non-homogenous local parts on the surfaces.

Micro-Vickers hardness tests were performed for the Cr-matrix composite coatings. But as seen from the figures, the ceramic-reinforced composite coatings,

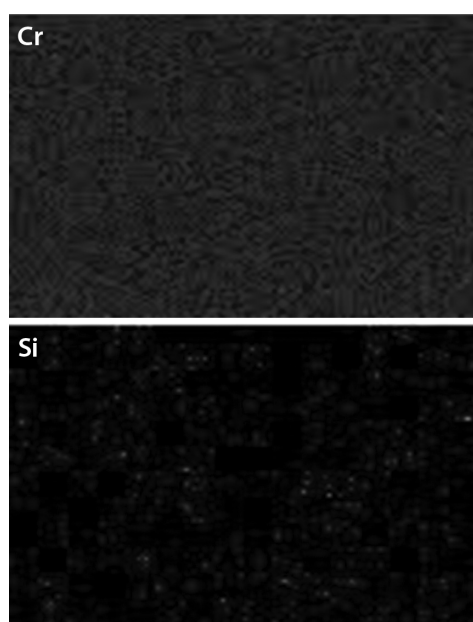


Figure 3: X-ray mapping results for the SiC-reinforced Cr-composite coatings

Slika 3: Rentgenski posnetek razporeditve elementov v kompozitni Cr-prevleki, ojačeni s SiC

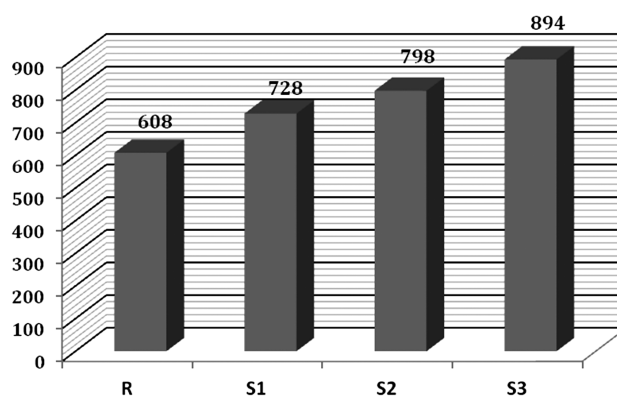


Figure 4: Comparable hardness results for the R- and S-coded samples

Slika 4: Primerjava trdote vzorcev z oznako R in S

Table 4: Hardness (HV_{0.1}); results of the R- and S-coded samples

Tabela 4: Trdota (HV_{0.1}); rezultati za vzorce z oznako R in S

	R1	S1	S2	S3
1. indentation	561	680	739	785
2. indentation	592	693	745	937
3. indentation	672	811	910	961
Average value	608	728	798	894

whose grains were coarser than those of the reference sample, showed better performances during the micro-Vickers tests. The main reason for this result is thought to be the effect of the ceramic particles with high hardness values embedded into the metal matrix. In other words, it was proven that the SiC-addition characteristics dominated over the grain-size effect. The obtained hardness results given in **Table 4** and **Figure 4** schematically show an increase in the hardness values for the composite coatings with the ceramic additions depending on an increase in the pulse frequency.

4 CONCLUSIONS

In summary, a co-deposition of the sub-micron-sized SiC ceramic particles with Cr metal via an electrodeposition system was successfully carried out. The general results obtained during this process are as follows:

It was seen that the pulse current is an alternative and optimum method for co-depositing the metals with ceramic particles such as Cr-SiC pairs. The obtained phase results proved that the SiC particles were physically adsorbed on the cathode surface and made a composite structure with Cr metal. For the sets containing the sub-micron-sized ceramic particles, the obtained mapping results show particle-dense regions; however, they generally show homogenous behavior. The extreme hardness results obtained for these sets are thought to be the hardness results for these dense regions. However, the mapping results support the XRD analysis. When the coatings were compared (the coatings with no reinforcement and the SiC-reinforced ones), it was seen that the hardness values for the ceramic-particle-reinforced composite coatings were increased. With respect to the reference coatings, the performance of the SiC-composite coatings is increased by up to 50 %. Frequency, being a parameter of the pulse current, is determined as a parameter affecting the co-deposition of the ceramic particles with metals, and when the frequency increases the co-deposition performance increases as well.

Acknowledgement

The present study was supported by The Turkish Ministry of Science, Industry and Technology under the project code 0099-STZ-2007-1.

5 REFERENCES

- R. C. M. Salles, G. C. G. de Oliveira, S. L. Díaz, O. E. Barcia, O. R. Mattos, Electrodeposition of Zn in acid sulphate solutions: pH effects, *Electrochimica Acta*, 56 (2011), 7931–7939
- R. Inguanta, S. Piazza, C. Sunseri, Influence of electrodeposition techniques on Ni nanostructures, *Electrochimica Acta*, 53 (2008), 5766–5773
- V. D. Jovi, B. M. Jovi, M. G. Pavlovi, Electrodeposition of Ni, Co and Ni-Co alloy powders, *Electrochimica Acta*, 51 (2006), 5468–5477
- F. Hu, K. C. Chan, Equivalent circuit modelling of Ni-SiC electro-deposition under ramp-up and ramp-down waveforms, *Materials Chemistry and Physics*, 99 (2006), 424–430
- V. C. Kieling, Parameters influencing the electrodeposition of Ni-Fe alloys, *Surface and Coatings Technology*, 96 (1997), 135–139
- Z. Wu, L. Liu, B. Shen, C. Zhong, W. Hu, Effect of α - Al_2O_3 coatings on the mechanical properties of Ni/SiC composites prepared by electrodeposition, *Materials Science & Engineering*, 556 (2012), 767–774
- Y. Yao, S. Yao, L. Zhang, H. Wang, Electrodeposition and mechanical and corrosion resistance properties of Ni-W/SiC nanocomposite coatings, *Materials Letters*, 61 (2007), 67–70
- M. R. Vaezi, S. K. Sadrnezhad, L. Nikzad, Electrodeposition of Ni-SiC nano-composite coatings and evaluation of wear and corrosion resistance and electroplating characteristics, *Colloids and Surfaces A: Physicochem. Eng. Aspects*, 315 (2008), 176–182
- O. Sancakoglu, O. Culha, M. Toparli, B. Agaday, E. Celik, Co-deposited Zn-submicron sized Al_2O_3 composite coatings: Production, characterization and micromechanical properties, *Materials and Design*, 32 (2011), 4054–4061
- H. Zheng, M. An, Electrodeposition of Zn-Ni- Al_2O_3 nanocomposite coatings under ultrasound conditions, *Journal of Alloys and Compounds*, 459 (2008), 548–552
- H. Zheng, M. An, J. Feng, Surface characterization of the Zn-Ni- Al_2O_3 nanocomposite coating fabricated under ultrasound condition, *Applied Surface Science*, 254 (2008), 1644–1650
- J. Gao, J. Suo, Preparation and characterization of the electrodeposited Cr- Al_2O_3 /SiC composite coating, *Applied Surface Science*, 257 (2011), 9643–9648
- Y. Zhou, H. Chen, H. Zhang, Y. Wang, Oxidation of Al_2O_3 -dispersion chromizing coating by pack-cementation at 800 °C, *Trans. Non-ferrous Met. Soc. China*, 18 (2008), 598–602
- O. Sancakoglu, Co-deposition of metal films with ceramic nanoparticles on metallic substrates by electrodeposition system, MSc thesis, University of Dokuz Eylul, 2009
- O. Hammami, L. Dhoubi, E. Triki, Influence of Zn-Ni alloy electrodeposition techniques on the coating corrosion behaviour in chloride solution, *Surface & Coatings Technology*, 203 (2009), 2863–2870
- A. Vaskevich, F. Sinapi, Z. Mekhalif, Underpotential deposition of nickel on {111}-textured gold electrodes in dimethyl sulfoxide, *J. Electrochem. Soc.*, 152 (2005), 744
- L. Benea, Composite Electrodeposition-Theory and Practice, Porto-Franco, 1998
- Y. Yao, S. Yao, L. Zhang, H. Wang, Electrodeposition and mechanical and corrosion resistance properties of Ni-W/SiC nanocomposite coatings, *Materials Letters*, 61 (2007), 67–70
- X. Zhu, C. Cai, G. Zheng, Z. Zhang, J. Li, Electrodeposition and corrosion behavior of nanostructured Ni-TiN composite films, *Trans. of Nonferrous Met. Soc. of China*, 21 (2011), 2216–2224
- M. Gavrila, J. P. Millet, H. Mazille, Corrosion behaviour of zinc-nickel coatings electrodeposited on steel, *Surf. Coat. Technol.*, 123 (2000), 2–3
- E. B. Lehman, P. Ozga, Z. Swiatek, Electrodeposition of Zn-Ni protective coatings from sulfate-acetate baths, *Surf. Coat. Technol.*, 1 (2002), 151–152
- G. Wu, N. Li, D. Zhou, Electrodeposited Co-Ni- Al_2O_3 composite coatings, *Surf. Coat. Technol.*, 176 (2004), 157
- S. Alirezai, S. M. Monirvaghefi, M. Salehi, Effect of alumina content on surface morphology and hardness of Ni-P- Al_2O_3 electroless composite coatings, *Surf. Coat. Technol.*, 184 (2004), 170
- C. Lee, C. Wan, A study of the composite electrodeposition of copper with alumina powder, *Electrochem. Soc.*, 135 (1988), 1930
- N. K. Shrestha, D. B. Hamal, T. Saji, Composite plating of Ni-P- Al_2O_3 in two steps and its anti-wear performance, *Surf. Coat. Technol.*, 183 (2004), 247–253

EFFECT OF SHEET THICKNESS ON THE ANISOTROPY AND THICKNESS DISTRIBUTION FOR AA2024-T4

VPLIV DEBELINE PLOČEVINE NA ANIZOTROPIJO IN RAZPOREDITEV DEBELINE PRI AA2024-T4

Murat Dilmec¹, Huseyin Selcuk Halkaci², Fahrettin Ozturk^{3,4}, Mevlut Turkoz²

¹Department of Mechanical Engineering, Necmettin Erbakan University, Konya, Turkey

²Department of Mechanical Engineering, Selcuk University, Konya, Turkey

³Department of Mechanical Engineering, Nigde University, Nigde, Turkey

⁴Department of Mechanical Engineering, The Petroleum Institute, Abu Dhabi, United Arab Emirates
muratdilmec@konya.edu.tr

Prejem rokopisa – received: 2012-12-18; sprejem za objavo – accepted for publication: 2013-02-19

In this study, the effect of sheet thickness on the anisotropy and thickness distribution at room temperature (RT) was investigated for AA2024-T4 sheets. The anisotropy was determined using automated strain measurement with a grid analysis and profile-projector methods. The results indicate that the effects of the thicknesses of 0.8 mm, 1 mm, and 2 mm on the anisotropy were insignificant. In addition to the anisotropy measurement, the thickness variation of the specimens was also monitored. Besides the anisotropy values, no significant differences were observed between various thicknesses and directions.

Keywords: planar anisotropy, automated strain-measurement method, sheet thickness, AA2024

V tem delu je bil preiskovan vpliv debeline pločevine AA2024-T4 na anizotropijo in razporeditev debeline pri sobni temperaturi (RT). Anizotropija je bila ugotovljena z avtomatskim merjenjem raztezka z analizo mreže in metodo projiciranja profila. Rezultati kažejo, da je vpliv debeline 0,8 mm, 1 mm in 2 mm na anizotropijo zanemarljiv. Dodatno z meritvami anizotropije je bilo tudi spremljano spreminjanje debeline vzorcev. V primerjavi z vrednostmi anizotropije ni bilo opažene pomembne razlike pri različnih debelinah in smereh.

Ključne besede: ravninska anizotropija, avtomatizirana metoda merjenja deformacije, debelina pločevine, AA2024

1 INTRODUCTION

Normal anisotropy r is an indication of resistance to the thinning of a material and is defined as the ratio of transverse strain to thickness strain at the uniform elongation region. In sheet materials, material properties usually change with rolling directions.¹ If the r value is equal to 1, the material is considered to be isotropic otherwise it is anisotropic. Planar anisotropy Δr is an indication of a variation in the r value depending on the direction. Mechanical properties of sheet materials become very different depending on the crystallography and rolling process.^{1,2} In a sheet-forming operation, the orientation of a sheet is quite important in order to produce the desired shape with a high accuracy. It is well known that an earing is usually seen on the upper edges of the cups formed with deep drawing. In other words, the upper edge of a cup takes a wavy shape instead of being smooth.³ Earing behavior occurs due to the fact that the drawing ratios are different at different directions in deep drawing. In this case, the orientation of a sheet helps produce the desired geometry.⁴

Mechanical properties of sheet metals are the most important factors that affect sheet-metal formability. The chemical composition of a material, production methods and various treatments applied to the material during the production are among the main factors that change the mechanical properties of sheet metals.⁵ Beside strength

and strain, the strain-hardening exponent n , normal anisotropy r , and strain-rate sensitivity exponent m are the other factors that affect the mechanical characteristics of sheet formability.^{6,7}

Hospers⁸ and Banabic et al.⁹ stated that the r and n values affect the formability significantly. Raghavan¹⁰ specifies that the r value has a great influence on deep drawing, increasing the drawability. However, it has a relatively low effect on the stretching process. For an optimum drawability, it is desired that the materials have a high r value and a low Δr value.⁸ If the r value is high, deeper cups can be drawn and if the Δr value is low, the earing behavior is suppressed. Deep drawability of aluminum alloys is good when $0.6 \leq r \leq 0.85$ and not adequate when $r \leq 0.6$.

Hatipoglu¹¹ looked at the effect of the rolling direction on the flow curve for AA2024-T3. The planar anisotropy of a 1 mm sheet was determined as -0.13 . Therefore, he assumed the material was isotropic.

As described in the above studies, the effect of sheet thickness on the anisotropy is not studied for AA2024-T4. However, it is necessary to study this area when dealing with an alloy important for the aerospace industry.

In this study, the effect of sheet thickness on the anisotropy of AA2024-T4 was thoroughly investigated. The study was performed at RT for the rolling (0°),

diagonal (45°) and transverse (90°) directions. Two different measurement methods were used to measure the anisotropy. These methods are the automated strain-measurement method with grid marking and the measurement with a profile projector. The thickness changes in the 0.8 and 2 mm Nakajima test specimens were also monitored.

2 EXPERIMENTAL PROCEDURE

In this research, AA2024-T4 with the thicknesses of 0.8 mm, 1 and 2 mm was studied. The chemical composition of the alloy is given in **Table 1**. First, the tensile and anisotropy test specimens were cut in the directions of 0°, 45°, and 90° according to the ASTM E 8M-04 and ASTM E 517¹² standards, respectively, for all the thicknesses. Then they were solution heat treated or solutionized at 493 °C for 30 min, quenched in cold water and allowed to age naturally at RT for at least 7 d. The mechanical properties of the materials changed within 7 d. After 7 d, a substantially stable condition, which is the T4 temper, is achieved. In order to see the variations in the mechanical properties of AA2024 with respect to time, tensile tests were conducted for the 1st h, 4th, 5th, 10th, and 30th d of the aging of the material with the thickness of 1 mm. The edges of the specimens were ground to eliminate the notch effect.

2.1 Determination of mechanical properties

The tensile-stress and strain curves were obtained by conducting the tensile tests according to the ASTM E 8M-04 standard for all the thicknesses and the directions of 0°, 45°, and 90°. The tensile tests were conducted using a Shimadzu AG-IS testing machine with a capability of 100 kN. Since the yield point was not clearly detected for any of the samples due to the brittle nature of AA2024-T4, this value was determined with the 0.2 % strain offset method.

2.2 Determination of anisotropy

The ASTM E-517 standard was used to determine anisotropy for all the thicknesses. A 2.5 mm × 2.5 mm grid pattern was applied to a specimen surface with the serigraphy method shown in **Figure 1**. The size of the pattern was applied after the heat treatment, being 50 mm long, along the overall width. This method is one of the most convenient and easy applications for grid marking.¹³ The details of the serigraphy method were explained in the authors' earlier study.¹⁴ The grid patterns

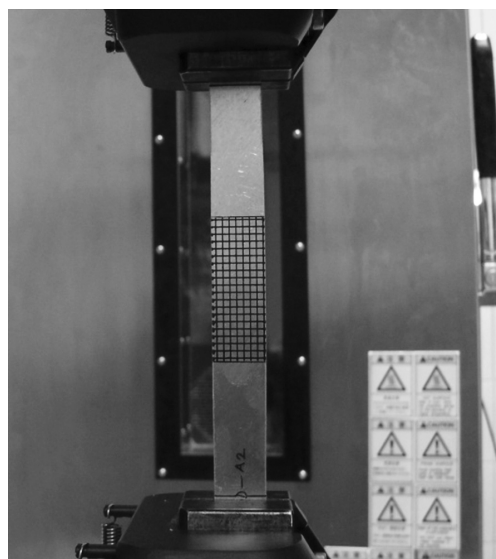


Figure 1: Photograph of an anisotropy specimen during the tensile test

Slika 1: Posnetek vzorca za anizotropijo med nateznim preizkusom

have high accuracies and resolutions. The patterns were resistant to deformation and operating processes such as friction and lubrication. In their earlier study, the authors found, with the serigraphy method and the Automated Strain Analysis and Measurement Environment (ASAME) software, that the total accuracy and repeatability of the grid pattern were 0.011 and 0.0062, respectively, in the range of 95 % confidence.¹⁴ It is a reasonable assumption that this method may be adequate for the measurements.

The patterned specimens were elongated or pulled by up to 10 % of the strain value at the speed of 25 mm/min using a tensile testing machine. The automated strain measurement with a grid analysis and the profile projector method were used to determine the anisotropy coefficients.

2.2.1 Automated strain-measurement method

The grid-analysis method is a method which requires a long time to determine the strain values of a specimen. The measurements can be performed manually or with a computer. In this study, the strain measurements were made using the ASAME software. The grid marking is an extremely important process for accurate measurements.

For many materials, the anisotropy value generally remains constant until the ultimate tensile strength is reached. For this reason, the measurements are usually

Table 1: Chemical composition of AA2024 sheets with various thicknesses (w/%)

Tabela 1: Kemijska sestava pločevine AA2024 z različno debelino (w/%)

Sheet thickness (mm)	Cu	Mg	Mn	Fe	Si	Zn	Ti	Other	Al
0.8–2	4.34–4.44	1.23–1.34	0.62–0.63	0.12–0.17	0.058–0.068	0.077–0.092	0.024–0.029	0.035–0.070	93.29–93.39
ASTM B 209M-07	3.8–4.9	1.2–1.8	0.3–0.9	0.5	0.5	0.25	0.15	0.15	90.85–93

performed at the 10 % strain to determine the r value. When the anisotropy data is provided, it must be specified which elongation r value is obtained.

In the automated strain-analysis method the photographs of the grid pattern were taken before the deformation and used as reference. Then the photographs of the grid patterns of the specimens were taken at the 10 % strain during the tensile test. Moreover, the photographs were also taken for (5, 6, 7 and 9) % elongation values during the process in order to see whether the anisotropy values of the materials with various thicknesses change with different elongation values. A professional Single Lens Reflex camera with a 12 MP resolution was used to record the deformed grids. Then the longitudinal strain ε_l and width strain ε_w were calculated from the measured data on the photographs by the ASAME system. The thickness strain ε_t can be measured directly, but it is a difficult task and its error rate is high. Therefore, ε_t cannot be measured accurately for a thin sheet.¹⁵ In this research, the strain in the thickness direction was calculated using the assumption of a constant volume as follows:

$$\varepsilon_l + \varepsilon_w + \varepsilon_t = 0 \quad (1)$$

Using equation (1), ε_t was calculated and then the anisotropy coefficient was calculated using equation (2):

$$r = \varepsilon_w / \varepsilon_t \quad (2)$$

2.2.2 Profile-projector method

In order to validate the ASAME measurements, the ε_l and ε_w values were also calculated using the profile-projector data with a 0.001 mm precision. Although the dimensions of the grids are 2.5 mm \times 2.5 mm having a high precision, the dimensions of at least 6 and 15 grids were measured for length on each specimen. The initial gage length l_0 and width w_0 were determined. After the specimens were elongated up to the 10 % strain value, the final gage length l and width w were measured using the profile projector and the strain values were calculated with equations (3) and (4). Then ε_t was calculated from equation (1). The plastic anisotropy values for each direction were obtained from equation (2):

$$\varepsilon_w = \ln \left(\frac{w}{w_0} \right) \quad (3)$$

$$\varepsilon_l = \ln \left(\frac{l}{l_0} \right) \quad (4)$$

These measurements were conducted for three different regions in order to increase the accuracy and the obtained values were averaged. So the r values were determined for the 0°, 45°, and 90° directions using both methods.

The average of the obtained values is called the normal anisotropy r_m and it was calculated with the following equation:

$$r = \frac{r_0 + 2r_{45} + r_{90}}{4} \quad (5)$$

where r_0 , r_{45} , and r_{90} are the anisotropy values for the 0°, 45°, and 90° directions, respectively. The planar-anisotropy values were calculated with equation (6):^{2,16}

$$\Delta r = \frac{r_0 - 2r_{45} + r_{90}}{2} \quad (6)$$

All the tests were repeated at least three times in order to check the repeatability. The results were obtained with a 99 % confidence.

2.3 Monitoring the thickness distribution

The thickness distributions on the deformed Nakajima specimens with a width of 100 mm (**Figure 2**) for the thicknesses of 0.8 mm and 2 mm in the directions of 0°, 45°, and 90° were measured in order to verify whether the obtained anisotropy values change with respect to the sheet thickness for AA2024-T4. Initially, the specimens were cut using a fret saw, making the shape in the most critical section, from at the apex of the dome perpendicularly to the fracture; then the thickness distributions were measured with a profile projector at the intervals of 1 mm with a 0.002 mm accuracy and a 20X scale factor.

All the tests in this study were also conducted at least three times in order to check the repeatability.

3 RESULTS AND DISCUSSION

3.1 Mechanical properties of the materials

The yield curves obtained on different days of the natural aging are given in **Figure 3** for AA2024 with a 1 mm thickness. As shown in the figure, the mechanical properties became stable after the 5th d. For this reason, the experiments were conducted after 7 d.

The measured mechanical properties for the materials with various thicknesses are given in **Table 2**. The mechanical properties obtained are compatible with those in the literature.^{11,17-19} The variations in the flow curves according to the rolling directions for the 0.8 mm and 2 mm thicknesses are given in **Figure 4**.

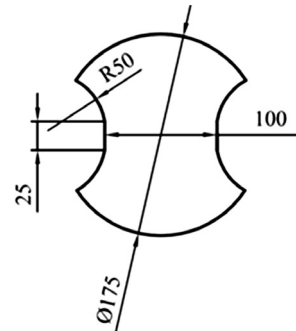


Figure 2: Nakajima specimen with the width of 100 mm
Slika 2: Vzorec Nakajima s širino 100 mm

Table 2: Mechanical properties of AA2024-T4 with various thicknesses**Tabela 2:** Mehanske lastnosti pločevine AA2024-T4 z različno debelino

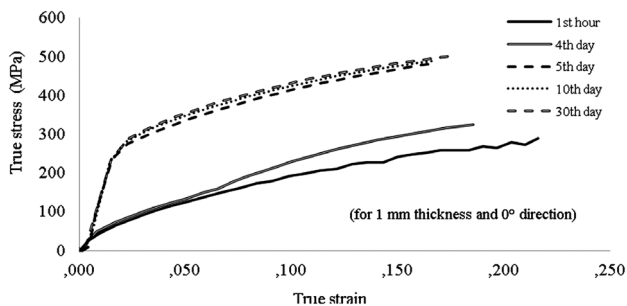
Sheet thickness (mm)	Direction	True yield strength σ_a /MPa	True tensile strength σ_u /MPa	Total true strain ϵ	Strain hardening coefficient n	Strength coefficient K /MPa
0.8	0°	263 ± 5	497 ± 4	0.1685 ± 0.007	0.20 ± 0.004	762 ± 3
	45°	249 ± 4	473 ± 5	0.1815 ± 0.027	0.20 ± 0.004	738 ± 2
	90°	264 ± 3	502 ± 6	0.1713 ± 0.020	0.21 ± 0.004	719 ± 3
1	0°	271 ± 4	499 ± 4	0.1640 ± 0.008	0.21 ± 0.006	724 ± 6
	45°	263 ± 5	500 ± 8	0.1797 ± 0.027	0.22 ± 0.012	686 ± 6
	90°	270 ± 2	495 ± 5	0.1745 ± 0.007	0.21 ± 0.004	714 ± 10
1.2	0°	270 ± 1	512 ± 4	0.1773 ± 0.015	0.22 ± 0.003	764 ± 3
	45°	266 ± 1	536 ± 2	0.1741 ± 0.017	0.21 ± 0.005	749 ± 5
	90°	263 ± 2	518 ± 3	0.1721 ± 0.006	0.22 ± 0.004	751 ± 7
2	0°	308 ± 3	546 ± 10	0.1796 ± 0.007	0.22 ± 0.027	753 ± 7
	45°	262 ± 4	537 ± 5	0.1823 ± 0.019	0.23 ± 0.001	718 ± 5
	90°	271 ± 5	499 ± 6	0.1803 ± 0.006	0.23 ± 0.010	730 ± 8
ASTM B 209M-07 (0.5–1.6 mm)	–	Min. 245	Min. 400	0.15	0.17–0.22	676–690

3.2 Anisotropy coefficient

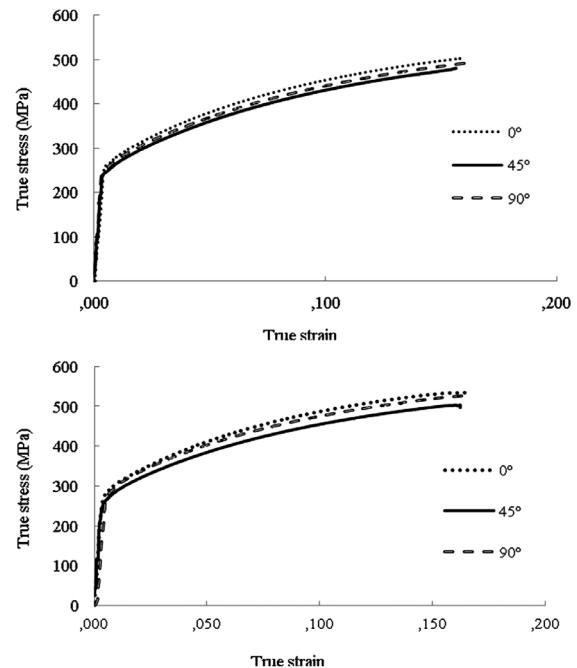
A sample strain distribution on a deformed specimen measured by using the grid-analysis method is given in **Figure 5**. Uniform strain distributions were obtained for all the tests as shown in the figure.

The obtained anisotropy values are given in **Table 3** for the (5, 6, 7 and 9) % elongation values during the process. The variation in the anisotropy values depend-

ing on the percent elongation are visually displayed in **Figure 6** averaging the results of three repeats for each percent elongation. It is seen that the anisotropy values do not significantly change depending on the elongation in the specified range for each direction. The obtained anisotropy values at 10 % for AA2024-T4 and AA5754-O with a 1 mm thickness by using the automated strain-measurement and profile-projector methods are given in **Table 4**. Since the results are close to each other with the maximum 15 % error, the reliability of the automated strain-measurement method is presented. Therefore, the anisotropy values for the other thicknesses

**Figure 3:** Mechanical properties of AA2024-T4 for various natural-aging times**Slika 3:** Mehanske lastnosti AA2024-T4 pri različnih časih naravnega staranja**Table 3:** Anisotropy values for various percent elongations for a 1 mm thickness, $r = \epsilon_w/\epsilon_t$ **Tabela 3:** Vrednosti anizotropije pri različnih deležih raztezka pri debelini 1 mm, $r = \epsilon_w/\epsilon_t$

Direction	Repeat	5 %	6 %	7 %	8 %	9 %	10 %	Mean
0°	1.	0.73	0.75	0.75	0.74	0.70	0.74	0.74
	2.	0.64	0.66	0.64	0.65	0.63	0.69	0.69
	3.	0.71	0.70	0.74	0.78	0.77	0.77	0.76
45°	1.	0.92	0.93	0.96	0.91	0.92	0.91	0.92
	2.	0.89	0.96	0.95	0.95	0.98	1.02	0.96
	3.	0.85	0.87	0.96	0.93	0.95	0.97	0.96
90°	1.	0.85	0.87	0.84	0.86	0.81	0.80	0.84
	2.	0.84	0.86	0.83	0.81	0.81	0.81	0.83
	3.	0.72	0.75	0.77	0.77	0.81	0.82	0.78

**Figure 4:** Variations in the flow curves with respect to the rolling directions for: a) 0.8 mm and b) 2 mm thicknesses**Slika 4:** Spreminjanje krivulj tečenja glede na smeri valjanja za debeline: a) 0,8 mm in b) 2 mm

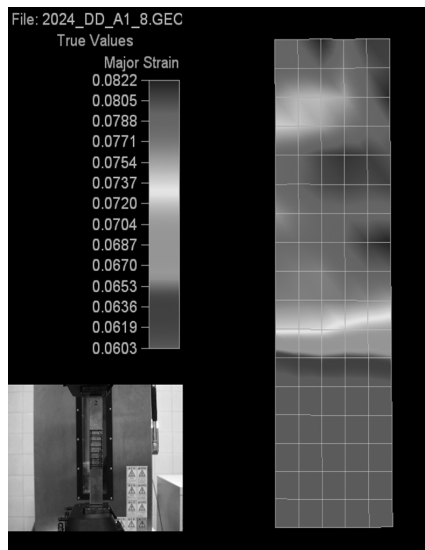


Figure 5: Uniform strain distribution on the deformed anisotropy sample

Slika 5: Enakomerna razporeditev raztezka na deformiranem anizotropijskem vzorcu

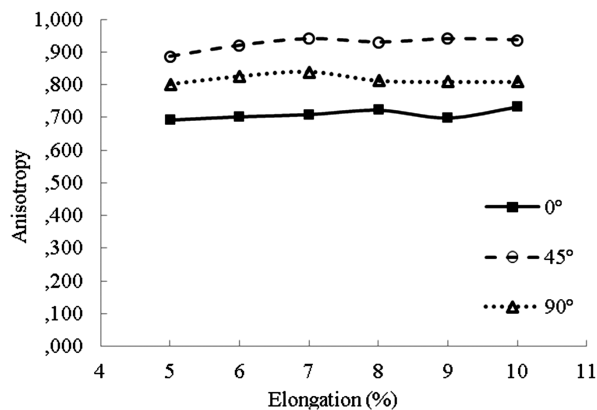


Figure 6: Variations in the anisotropy values for various percent elongations

Slika 6: Spreminjanje vrednosti anizotropije pri različnih deležih raztezkov

of AA2024 were determined by ASAME. The obtained normal and planar anisotropy values at 10 % for the (0.8, 1 and 2) mm thicknesses calculated by ASAME are given in **Table 5**.

Table 4: Anisotropy values obtained with the automated strain-measurement and profile-projector methods for the 10 % elongation for AA2024 and AA5754

Tabela 4: Vrednosti anizotropije, dobljene z avtomatizirano metodo merjenja deformacije in z metodo projiciranja profila pri raztezu 10 % za AA2024 in AA5754

Material	Direction	Profile projector			Automated strain measurement		
		r	r_m	Δr	r	r_m	Δr
AA2024-T4	0°	0.72 ± 0.03	0.87	-0.20	0.71 ± 0.04	0.88	-0.22
	45°	0.96 ± 0.03			0.99 ± 0.02		
	90°	0.82 ± 0.03			0.82 ± 0.03		
AA5754-O	0°	0.76 ± 0.02	0.71	0.087	0.72 ± 0.02	0.72	0.11
	45°	0.67 ± 0.04			0.67 ± 0.03		
	90°	0.75 ± 0.03			0.85 ± 0.04		

Table 5: Anisotropy values for various percent elongations for different thicknesses, $r = \varepsilon_w/\varepsilon_t$

Tabela 5: Vrednosti anizotropije pri različnih deležih raztezka pri različnih debelinah, $r = \varepsilon_w/\varepsilon_t$

Sheet thickness (mm)	Direction	r	r_m	Δr
0.8	0°	0.79 ± 0.06	0.75	-0.14
	45°	0.82 ± 0.02		
	90°	0.57 ± 0.05		
1	0°	0.72 ± 0.04	0.88	-0.22
	45°	0.99 ± 0.02		
	90°	0.82 ± 0.03		
2	0°	0.75 ± 0.01	0.83	-0.17
	45°	0.90 ± 0.07		
	90°	0.75 ± 0.04		
Hursman ¹⁷ for 0.8 mm				-0.11

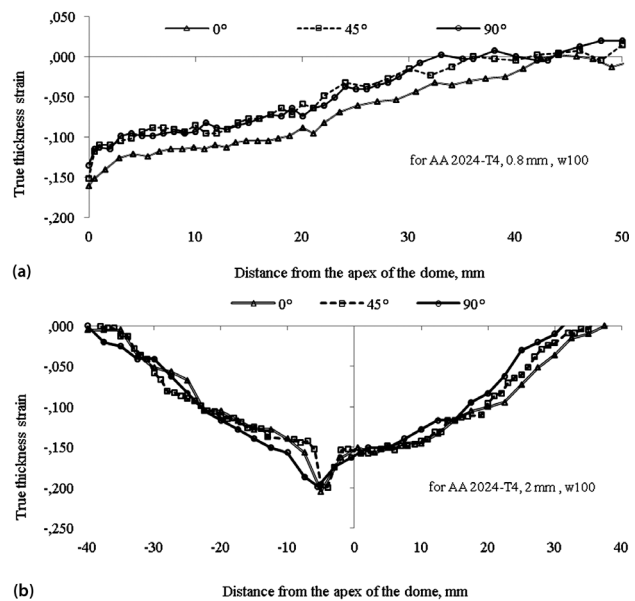


Figure 7: Variations in the thickness-strain distributions with respect to the rolling directions

Slika 7: Spreminjanje razporeditve debeline pri deformaciji glede na smer valjanja

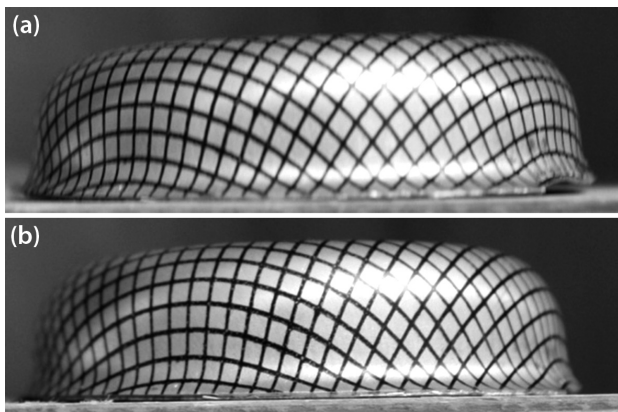


Figure 8: Earing tendency for deep-drawn parts from AA2024-T4 with: a) 1 mm and b) 2 mm thicknesses

Slika 8: Nagnjenost k ušesenju pri delih za globoki vlek iz AA2024-T4 z debelino: a) 1 mm in b) 2 mm

Hursman¹⁷ obtained the planar anisotropy value of AA2024-T3 as -0.11. For this reason it is said that the obtained results in the current study are in accord with the literature. The Δr values for all the thicknesses of AA2024-T4 and AA5754-O with a 1 mm thickness can be acceptably small so that they do not generate the earing behavior. Thus, the materials with different thicknesses may be assumed as isotropic for AA2024-T4.

The variations in the thickness-strain distributions of the Nakajima specimens depending on the rolling direction are given in **Figure 7** for a width of 100 mm and for the 0.8 mm and 2 mm thicknesses. The figure reveals that the thickness distributions do not change considerably with respect to the rolling directions for the formed specimens with the 0.8 mm and 2 mm thicknesses in the directions of 0°, 45°, and 90°. The earing tendency was not observed for the deep-drawn parts of AA2024-T4 as shown in **Figure 8**. So it is verified that the obtained anisotropy values for various thicknesses are consistent with the measured thickness distributions.

4 CONCLUSIONS

In this study, the effect of sheet thickness on the anisotropy and the thickness distribution was investigated at RT for AA2024-T4 sheets. For the anisotropy measurements, automated strain-measurement and profile-projector methods were used and compared. The following results were obtained:

The maximum error range between the automated strain-measurement method and the profile projector is about 15 %. These results indicate that the automated strain-measurement method can be easily used for the anisotropy measurement.

The values of anisotropy were not significantly changed with respect to elongation up to the 10 % strain range for AA2024-T4.

No significant change was found with respect to the rolling directions for AA2024-T4 and AA5754-O. The

planar anisotropy values are small and do not change significantly with respect to the sheet thickness of AA2024-T4. Therefore, the effect of the planar anisotropy may be ignored for AA2024-T4 with various thicknesses.

The thickness distributions do not change considerably with respect to the rolling directions.

Acknowledgements

This work was supported by the Research Project Units (BAP) of the Necmettin Erbakan and Selcuk Universities. The Research Project Offices and the Metal Forming Laboratory at the Nigde University are profoundly acknowledged.

5 REFERENCES

- Z. Marciniak, S. J. Hu, J. L. Duncan, *Mechanics of Sheet Metal Forming*, Butterworth-Heinemann, London 2002
- S. Kohara, *Metallurgical and Materials Transactions A*, 36A (2005), 1033–1037
- M. A. Khaleel, K. I. Johnson, M. T. Smith, *Materials Science Forum*, 243–245 (1997), 739–744
- D. W. A. Rees, *Journal of Materials Processing Technology*, 118 (2001), 1–8
- G. E. Dieter, *Mechanical Metallurgy*, McGraw Hill Book Company, London 1988
- K. Nakajima, T. Kikuma, K. Hasuka, *Yawata Tech. Rep.*, 284 (1968), 678–680
- C. Svensson, *The Influence of Sheet Thickness on the Forming Limit Curves for Austenitic Stainless Steel*, Master Thesis, Örebro University, Sweden, 2004
- F. Hospers, Report LR-242A, Netherlands, 1977
- D. Banabic, H. J. Bünge, K. Pöhlandt, A. E. Tekkaya, *Formability of Metallic Materials*, Springer-Verlag, Germany 2000
- K. S. Raghavan, *Metallurgical and Materials Transactions A*, 26A (1995), 2075–2084
- H. A. Hatipoglu, *Experimental and Numerical Investigation of Sheet Metal Hydroforming (Flexforming) Process*, Master Sci. Thesis, Middle East Technical University, Ankara, 2007
- Standard Test Method for Plastic Strain Ratio r for Sheet Metal, ASTM International, Designation: E 517–98
- K. Siegert, S. Wagner, *Formability Characteristics of Aluminium Sheet*, Training in Aluminium Application Technologies (TALAT), 1994
- F. Ozturk, M. Dilmec, M. Turkoz, R. E. Ece, H. S. Halkaci, *Grid Marking and Measurement Methods for Sheet Metal Formability*, The 5th International Conference and Exhibition on Design and Production of Machines and Dies/Molds, Turkey, 2009, 41–49
- G. Richard, *Advanced Materials & Processes*, (2002), 33–36
- G. E. Dieter, *Mechanical Behavior under Tensile and Compressive Loads*, ASM Handbook, volume 8, Mechanical Testing and Evaluation, ASM International, 2000
- T. L. Hursman, *Development of Forming Limit Curves for Aerospace Aluminum Alloys*, In B. A. Niemeler, A. K. Schmieder, J. R. Newby, Eds., *Formability Topics-Metallic Materials*, ASTM STP 647, American Society for Testing and Materials, 1978, 122–149
- R. Gedney, *Sheet Metal Formability*, *Advanced Materials & Processes*, (2002), 33–36
- G. Hussain, N. Hayat, L. Gao, *International Journal of Machine Tools & Manufacture*, 48 (2008), 1170–1178

EFFECT OF A Mo ADDITION ON THE PROPERTIES OF HIGH-Mn STEEL

VPLIV DODATKA Mo NA LASTNOSTI VISOKOVSEBNOSTNEGA Mn-JEKLA

Gholam Reza Razavi, Mohsen Saboktakin Rizi, Hossein Monajati Zadeh

Department of Materials Engineering, Najafabad Branch, Islamic Azad University, Isfahan, P.O.Box 517, Iran
reza.razavi64@gmail.com

Prejem rokopisa – received: 2012-12-31; sprejem za objavo – accepted for publication: 2013-01-10

TWIP steels are a family of high-Mn austenitic steels having both high strength and high ductility used as automotive-body steels. In the present paper, the effect of an addition of Mo on the improvement of the mechanical properties of a TWIP steel (Fe-33Mn-3Si-2Al) is investigated. Different amounts of Mo were added to the chemical composition of the steel and the resulted mechanical properties, microstructure and crystallographic phases were examined after the casting, hot rolling and annealing. The results showed that an addition of Mo enhances the mechanical properties; however, the optimum strength was obtained with an addition of 1.3 % Mo. This resulted in an increase in the ultimate strength and elongation of the steel.

Keywords: molybdenum, TWIP steels, hot rolling, Mo carbide

TWIP-jekla so skupina avstenitnih jekel z visoko vsebnostjo Mn, ki imajo visoko trdnost in dobro preoblikovalnost ter se uvrščajo med jekla za avtomobilsko pločevino. V tem članku smo preiskovali vpliv dodatka Mo na izboljšanje mehanskih lastnosti TWIP-jekla (Fe-33Mn-3Si-2Al). Dodane so bile različne količine Mo v jeklo in preiskovane so bile mehanske lastnosti, mikrostruktura in kristalografske faze po ulivanju, vročem valjanju in žarjenju. Rezultati so pokazali, da dodatek Mo izboljšuje mehanske lastnosti, vendar pa je bila največja trdnost dosežena pri dodatku 1,3 % Mo. To se je izrazilo v povečanju natezne trdnosti in raztezku jekel.

Ključne besede: molibden, TWIP-jekla, vroče valjanje, Mo-karbid

1 INTRODUCTION

In recent decades, various kinds of steels have been developed for the automotive industry. These steels significantly enhanced various properties like safety, fuel consumption, impact resistance and other properties. But the safety issues and the necessity of welfare increment require the use of the accessories that are in contrast with the principle of down-weighting of cars.¹

TRIP, transformation-induced plasticity, steels are known as the steels combining high-strength and high-ductility properties, attracting the attention of the automotive industry. The phenomenon of the transformation-induced plasticity includes the formation of martensite from the remaining austenite phase under the effects of strain and deformation, which leads to an increase in the strength and ductility.² In TRIP steels, ϵ (HCP) and α (BCC) martensites are formed in the γ (FCC) lattice due to internal and external stresses.²

TWIP steels are high-manganese steels ($w(\text{Mn}) = 17\text{--}35\%$) whose microstructure remains austenite even at room temperature. For this reason, these steels are deformed through the twins within the grains. The formation of twins and its rate depend on the hardening rate of steels. A greater hardening rate will lead to a finer microstructure. Therefore, twin boundaries will act similarly to grain boundaries which, in turn, will lead to a higher strength of the steel.³ The formation of twins, or the occurrence of a phase transformation, depends on the

value of SFE^3 of the austenite phase (γ_{fcc}). A higher rate of SFE ($80 > \gamma_{fcc} > 20 \text{ mJ/m}^2$) stimulates the formation of twins and its lower rate causes austenite to transform to ϵ martensite and then to a martensite.³

Although there are no comprehensive studies on the influence of the alloy elements on the SFE phase of the Fe-Mn austenite phase, it was defined, with the researches carried out, that Cu and Al significantly increase the value of SFE of an austenite phase, while Cr decreases SFE of steel.⁴ In this research, we study the influence of Mo on the mechanical properties of a group of TWIP steels.

2 EXPERIMENTAL PROCEDURE

Two heats with the chemical compositions shown in **Table 1** were prepared in an induction furnace under argon atmosphere and then cast. The homogenization treatment was conducted for an hour at a temperature of 1200 °C to remove any segregation of the alloying elements during the solidification. Hot rolling in five successive passes up to a total strain of 70 % was applied thereafter and the specimens were cooled in air (with the finishing rolling temperature of 900 °C). The treatment continued with a full annealing of the samples for 10 min at 1100 °C followed by air cooling. Uniaxial tensile tests were performed at ambient temperature and the strain rate of 10^{-3} s^{-1} , according to the ASTM E8M standard

using an Instron 4486 tensile machine. Phase analyses of the samples were carried out at ambient temperature with the X-ray diffraction method using a Bruker device at the angles ranging from 35° to 100° as well as Cu-K α x-rays and a nickel filter.

Table 1: Chemical compositions of the investigated steels (w/%)

Tabela 1: Kemijska sestava preiskovanih jekel (w/%)

S	Fe	Mo	Al	Si	Mn	C
<0.006	Ball	–	2	3	32.9	0.13
<0.006	Ball	1.3	2	3	33	0.13

3 RESULTS AND DISCUSSION

3.1 Phase studies

Figure 1 shows a phase analysis of the sample without molybdenum before and after the tensile test. We can see in this figure that after the tensile test, there is no phase change in the sample without the molybdenum alloy and it remains austenitic. In the case of the sample with 1.3 % molybdenum, after the tensile test, the microstructure consists of austenite and α martensite with a bcc structure.

Figure 1b shows this phase. As the microstructure of this steel consists of austenite and martensite, the governing deformation mechanism is the TRIP transformation occurring in the high-manganese steels with $SFE < 20$ mJ/m 2 . This deformation is based on the following transformation:

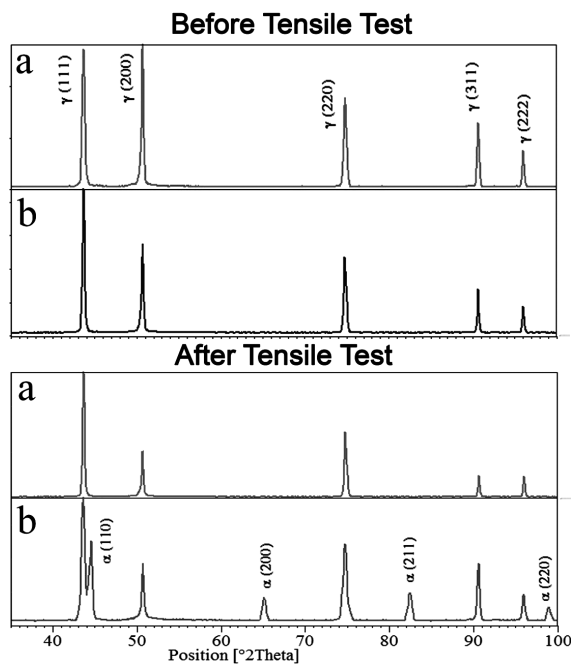


Figure 1: Phase analysis of the samples before and after the tensile test: a) sample without Mo, b) sample with 1.3 % Mo

Slika 1: Fazna analiza vzorcev pred nateznim preizkusom in po njem: a) vzorec brez Mo, b) vzorec z 1,3 % Mo

This transformation is stimulated by increasing the percentage of molybdenum, which lowers the value of SFE below 20 mJ/m 2 , while in the sample without molybdenum the decrease rate of SFE is not sufficient to change the deformation mechanism from the twinning of austenite to a martensite transformation.⁵

3.2 Microstructure

Figure 2a shows the microstructure of the sample without molybdenum before and after the tensile test. In this sample, the annealing twins are apparent in the microstructure. Also, after the tensile test, the mechanical twins were formed in the microstructure due to the deformation process. As mentioned above, this phenomenon occurs due to the SFE level of this steel. Also, in **Figure 2b** we see that the grain size in this sample, before and after the tensile test, is smaller than in the sample without molybdenum. It has been argued that as molybdenum is a carbide-generating element, it generates carbide in a microstructure.⁶ When molybdenum is added to steel, molybdenum carbide forms at the grain boundaries.^{7,8} The carbide on the grain boundaries prevents the grain growth.⁹ It has been shown that the formed carbide at the grain boundaries is $(\text{Fe},\text{Mo})_3\text{C}$ carbide.^{6,10}

We found no mechanical twins and slip bands in the microstructures of the samples after the tensile test. This indicates an occurrence of transformation in this steel through a transformation of austenite to martensite.

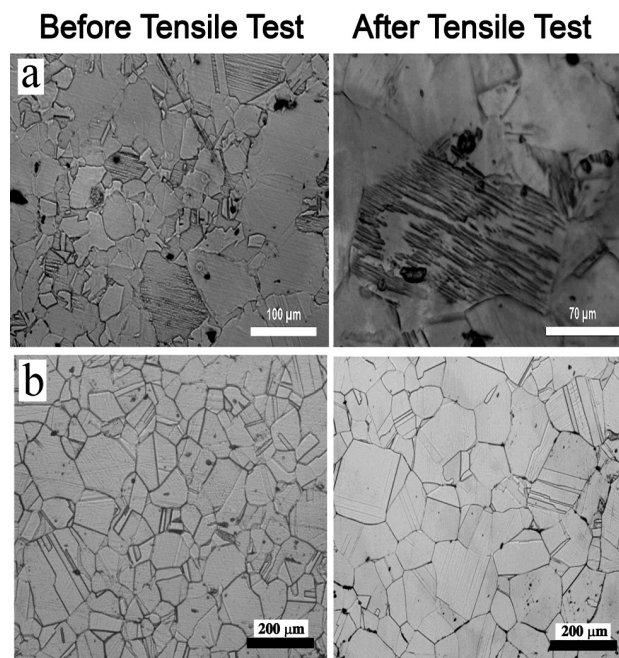


Figure 2: Microstructures of the samples before and after the tensile test: a) without Mo and b) with 1.3 % Mo

Slika 2: Mikrostruktura vzorcev pred nateznim preizkusom in po njem: a) brez Mo in b) z 1,3 % Mo

3.3 Estimating the results of the tensile test

Figure 3 shows the tensile-test curves at ambient temperature. It is apparent that the sample containing molybdenum shows a higher strength and ductility compared with the sample containing no molybdenum. As mentioned above, the reason for this is the formation of molybdenum carbides. Also, it has been found that the sample containing molybdenum shows a higher ductility due to the carbides between the grain boundaries. This prevents a disintegration of the grain boundaries and increases the ductility.

Figure 4 shows images of the microstructures of the samples after the tensile test obtained with the SEM microscope and also the results of a surface analysis of the dispersion of carbon and molybdenum. The contents of molybdenum and carbon near the grain boundaries in the sample containing 1.3 % molybdenum are increased. This increase indicates a formation of molybdenum carbide, which increases the stability of the grain boundaries. From the point analysis of the carbide

precipitates in **Figure 5** the type of carbide may be recognized as $(\text{Fe},\text{Mo})_3\text{C}$.

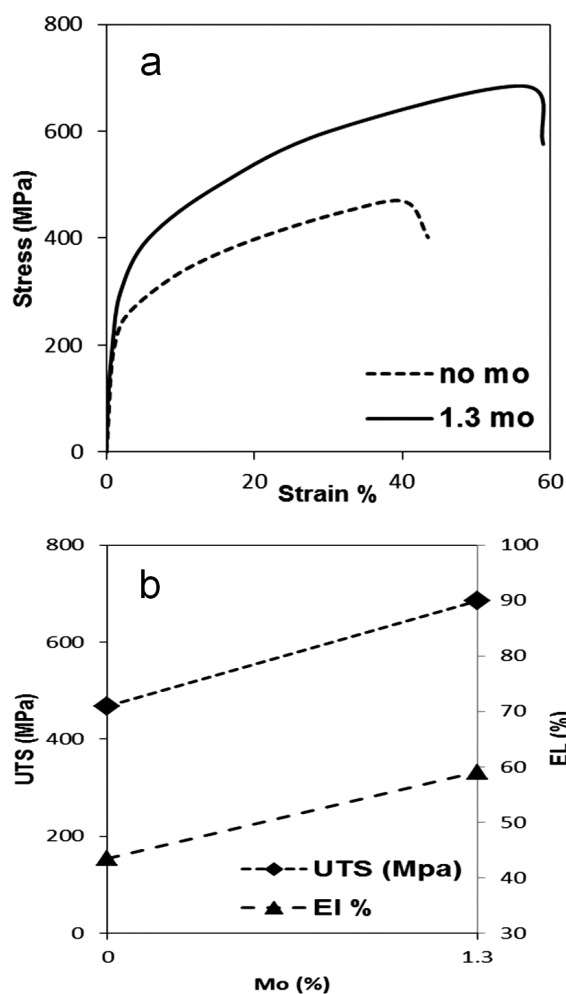


Figure 3: a) Engineering stress-strain curve, b) results obtained from the engineering stress-strain curve

Slika 3: a) Inženirska krivulja napetost – raztezek, b) rezultati, dobijeni iz inženirske krivulje napetost – raztezek

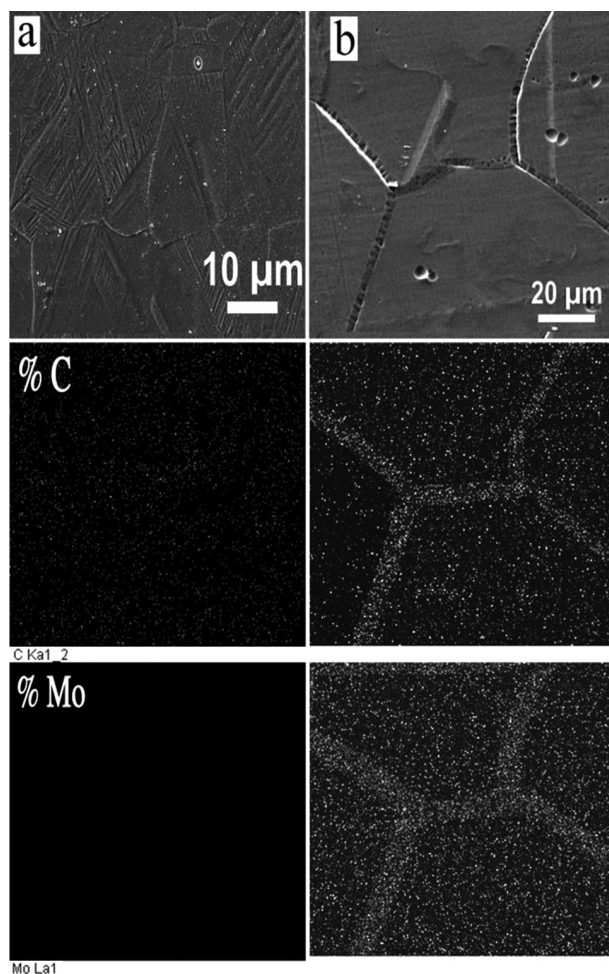


Figure 4: Images obtained with the SEM microscope and a surface analysis: a) sample without Mo, b) sample containing 1.3 % Mo

Slika 4: SEM-posnetki in analiza površine: a) vzorec brez Mo, b) vzorec z 1,3 % Mo

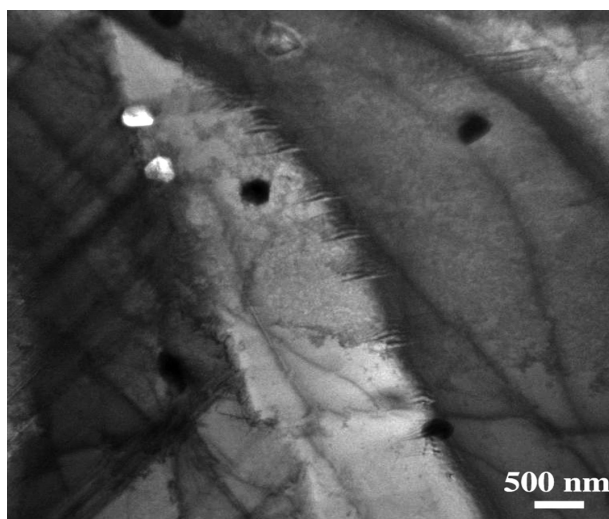


Figure 5: Microstructure of the sample with 1.3 % Mo and carbides
Slika 5: Mikrostruktura vzorca z 1,3 % Mo in karbidi

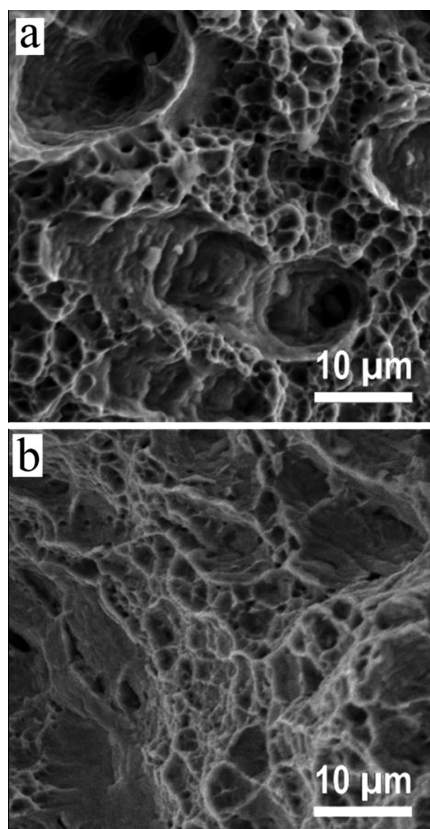


Figure 6: Fracture cross-sections of the estimated samples: a) sample without Mo, b) sample containing 1.3 % Mo

Slika 6: Prelom ocenjenih vzorcev: a) vzorec brez Mo, b) vzorec z 1,3 % Mo

3.4 Estimating fracture surface

Figure 6 shows the fracture surface after the tensile test. In the sample containing 1.3 % Mo, the size of dimples is decreased. As in the FCC metals, no brittle fracture was observed and after thorough studies we found out that these regions had been created due to the martensite generated during the transformation.¹⁰

4 CONCLUSIONS

1. Adding 1.3 % Mo increases the ultimate strength of the Fe-33Mn-3Si-2Al-0.13C steel.
2. Adding Mo to the Fe-33Mn-3Si-2Al steel up to 1.3 % decreases the grain size.
3. Adding 1.3 % Mo lowers *SFE* of the austenite phase, which prevents an occurrence of the TWIP mechanism and encourages the TRIP mechanism.

5 REFERENCES

- ¹ H. Hoffmann, D. Mattissen, T. W. Schaumann, Advanced cold rolled steels for automotive applications, *Material Wissenschaft und Werkstofftechnik*, 37 (2006), 716–723
- ² O. Grassel, L. Kruger, G. Frommeyer, L. W. Meyer, High strength Fe-Mn-(Al, Si) TRIP/TWIP steels development – properties – application, *International Journal of Plasticity*, 16 (2000) 10, 1391–1409
- ³ S. Vercammen, B. Blanpain, B. C. De Cooman, Cold rolling behaviour of an austenitic Fe–30Mn 3Al–3Si TWIP-steel: the importance of deformation twinning, *Acta Materialia*, 52 (2004) 7, 2005–2012
- ⁴ R. E. Schramm, R. P. Reed, Stacking fault energies of seven commercial Austenitic stainless steels, *Material Trans. A*, 6 (1974), 1975–1345
- ⁵ S. Allain, J. P. Chateau, O. Bouaziz Migot, N. Guelton, High manganese austenitic twinning induced plasticity steels: A review of the microstructure properties relationships, *Materials Science and Engineering A*, 15 (2011) 4, 141–168
- ⁶ H. O. Pierson, *Handbook of refractory carbides and nitrides*, Noyes Co, New Jersey 1996
- ⁷ H. Luo, P. Zhao, Effect of molybdenum and temperature reduction on hot ductility of 0.2C–Mn steels, *Iron making and Steel making*, 28 (2001) 6, 439–443
- ⁸ H. Mohrbacher, Principal Effects of Mo in HSLA steels and Cross Effects with MicroAlloying elements, *International seminar on applications of Mo in steels*, Beijing, China, 2010, 74–96
- ⁹ X. Sun, The roles and application of molybdenum element in low alloy steels, *International seminar on applications of Mo in steels*, Beijing, China, 2010, 60–74
- ¹⁰ P. Arnaud, On the interactions between strain-induced phase transformations and mechanical properties in Mn-Si-Al steels and Ni-Cr austenitic stainless steels, *Department of Materials Science and Process*, Louvain University, 2006, 236–267

INFLUENCE OF THE MATRIX TYPE ON THE TEMPERATURE RESPONSIVENESS OF A POLY-NIPAAm/CHITOSAN MICROGEL FUNCTIONALIZED PES FABRIC

VPLIV VRSTE MATRICE NA TEMPERATURNO ODZIVNOST POLI-NIPAAm/HITOZAN MIKROGELA NA PES-TKANINI

Brigita Tomšič¹, Pavla Križman Lavrič², Barbara Simončič¹, Dragan Jocić³

¹Department of Textiles, Faculty of Natural Sciences and Engineering, University of Ljubljana, Aškerčeva 12, 1000 Ljubljana, Slovenia

²TenCate, Almelo, The Netherlands

³Textile Engineering Department, Faculty of Technology and Metallurgy, University of Belgrade, Karnegijeva 4, 11120 Belgrade, Serbia
drjoc@tmf.bg.ac.rs; draganes@yahoo.es; brigita.tomsic@ntf.uni-lj.si

Prejem rokopisa – received: 2013-01-07; sprejem za objavo – accepted for publication: 2013-01-29

In this paper, the temperature responsiveness (swelling/de-swelling) of the poly-NiPAAm/chitosan (PNCS) microgel applied to a PES fabric in combination with two different matrixes, i.e., 1,2,3,4-butanetetracarboxylic acid (BTCA) or vinyltrimethoxysilane (VTMS) with hydrophilic fumed-silica nanoparticles (SiO₂) was studied. While a BTCA-based matrix enables chemical bonding of the PNCS microgel particles, resulting in a formation of a rigid surface-modified system, a VTMS/SiO₂ polysiloxane matrix has the ability to physically entrap the PNCS microgel particles and stimulate, due to its elasticity, a formation of a more flexible coating on the surface of PES fibres. Morphological and chemical properties of differently finished samples were studied with the SEM and XPS analyses. To determine the swelling/de-swelling ability of the PNCS microgel, the moisture contents of the samples, before and after five repetitive washings, were obtained for the samples conditioned at two different temperatures, i.e., at 25 °C and 40 °C, when the PNCS hydrogel was in its swollen or collapsed phase. The results showed that the rigid structure of the BTCA-based matrix restricted the swelling ability of the microgel particles, resulting in a 12 % lower moisture content of the corresponding sample in comparison to the moisture content determined for the sample with the PNCS microgel particles physically entrapped within the polysiloxane matrix. Due to its elasticity, the polysiloxane matrix enables the microgel particles to fully expand, which is the consequence of a partial removal of the PNCS microparticles during the washing procedure.

Keywords: hydrogel, microgel, poly-NiPAAm/chitosan, 1,2,3,4-butanetetracarboxylic acid, vinyltrimethoxysilane, responsiveness

V prispevku je preučevana temperaturna odzivnost (nabrekanje/skrčenje) poli-NiPAAm/hitozan (PNCS) hidrogela, nanesenega na PES-tkanino v kombinaciji z dvema različnima matricama, in sicer z 1,2,3,4-butanetrakarboksilno kislino (BTCA) ter viniltrimetoksi silanom (VTMS) s hidrofilnimi nanodelci silicijevega dioksida (SiO₂). Medtem ko je BTCA-matrica omogočila kemijsko vezanje PNCS-mikrogela ter nastanek bolj togega apreturnega filma na površini vlaken, so se delci PNCS-mikrogela v VTMS/SiO₂-matrico vezali fizikalno, pri čemer se je zaradi prožnosti in raztegljivosti matrice na površini vlaken tvoril elastičen apreturni film. Morfološke in kemijske lastnosti apretiranih vzorcev so bile preučevane s SEM- in XPS-analizama. Sposobnost nabrekanja/krčenja PNCS-mikrogela je bila določena z meritvami vsebnosti vlage nepranih in 5-krat pranih apretiranih vzorcev, klimatiziranih pri 25 °C in 40 °C, ko se je PNCS-hidrogel nahajal v nabrekli oziroma skrčenem stanju. Rezultati so pokazali, da je toga struktura BTCA-matrice vplivala na zmanjšano sposobnost nabrekanja delcev mikrogela, saj je bila vsebnost vlage teh vzorcev za 12 % nižja od vsebnosti vlage, določene pri vzorcih, na katere je bil PNCS-mikrogel fizikalno vezan v polisiloksansko matrico. Slednja je zaradi svoje elastičnosti omogočila neovirano nabrekanje delcev mikrogela, kar se je bolj izrazilo pri pranih vzorcih. Med pranjem je namreč prišlo do delne odstranitve PNCS-mikrogela iz vlaken, zaradi česar so imeli delci mikrogela, ki so ostali na vlaknu, več prostora za polno nabrekanje.

Ključne besede: hidrogel, mikrogel, poli-NiPAAm/hitozan, 1,2,3,4-butanetrakarboksilna kislina, viniltrimetoksi silan, odzivnost

1 INTRODUCTION

In the production of textiles special attention is devoted to the creation of the apparel with specific properties that could be activated "on demand" by sensing and reacting to the stimuli in the immediate environment. The creation of such textiles involves, among other methods, an application of hydrogels, where a hydrogel based on chitosan and poly-(N-isopropylacrylamide) (poly-NiPAAm) is of great importance since it ensures a dual pH and temperature responsiveness.¹⁻³ Namely, due to weakly basic moieties (primary amines that have the *pKa* values of about 6.3) chitosan can respond to the changes in the pH of the surrounding medium with a

protonation/de-protonation of the amino groups.⁴ A pH-induced phase transition of chitosan results in the varying dimensions (swelling and de-swelling) of the hydrogel made of it. Poly-NiPAAm exhibits a reversible temperature-sensitive phase transition in aqueous solutions at a lower critical-solution temperature (LCST) of 32 °C. At the temperatures below the LCST, poly-NiPAAm is water-soluble, i.e., hydrophilic, so the hydrogel made of it exists in the swollen phase. At the temperatures above the LCST, poly-NiPAAm becomes hydrophobic and, consequently, the hydrogel collapses.^{5,6} Therefore, after combining the swelling and shrinking effects, applied to textile materials, a poly-NiPAAm/chitosan (PNCS) hydrogel is expected to provide com-

fort to the wearer due to its moisture-management and liquid-management properties, as well as the thermo-regulating ability.

An advanced approach to the textile-material functionalization is based on micro-sized and nano-sized hydrogels because their polymeric form has an increased surface area per unit mass, significantly improving the response times. When creating a stimuli-responsive textile, the main challenge is to apply the microgel onto the textile fibres in such a way as to create a sufficient durability while still retaining the effectiveness of the hydrogel. In our previous research a PNCS hydrogel was successfully applied to cotton in combination with the crosslinking agent 1,2,3,4-butanetetracarboxylic acid (BTCA).⁷⁻⁹ During the curing process, the chemical bonding of the PNCS microgel was obtained. Namely, the carboxylic groups of BTCA reacted with the hydroxyl groups from both cotton and chitosan by forming stable ester bonds, possibly reacting also with the free amino groups of chitosan via a formation of an amide.^{10,11} Even though good moisture-management properties of the functionalized cotton were obtained, the question arose whether these chemical bonds formed between the cotton, BTCA and PNCS hydrogel, resulting in the formation of a rigid, surface-modified system, restricted the expansion ability of a microgel particle in such a way that it could not swell as fully as a free particle. Therefore, in the continuation of the research, a PNCS microgel was applied to a PES fabric with the sol-gel technique, using the vinyltrimethoxysilane (VTMS) and hydrophilic fumed-silica nanoparticles (SiO_2) as the precursors.¹² In the application process, VTMS formed a continuous network on the surface of the fibres, enabling a physical entrapment of the PNCS microgel. Besides, SiO_2 nanoparticles acted as possible anchoring sites for the PNCS microgel particles, thus enabling their enhanced incorporation into the surface of the PES fibres. Since the polysiloxane precursors are known by their ability to form an elastic film on a solid surface of only ≈ 10 nm thickness,¹³ it was found out that the presence of a VTMS/ SiO_2 matrix did not influence the responsiveness of the PNCS microgel particles.¹²

The aim of this work was to study the influence of the chemical structure and composition of the matrix on the performance of the PNCS microgel particles. For this purpose the PNCS microgel was first applied in combination with a matrix based on the crosslinking agent (BTCA), which enabled a covalent bonding of the microgel particles and, later, in combination with a VTMS/ SiO_2 polysiloxane matrix, where a physical embedment of the microgel particles was obtained. The thermal responsiveness (i.e., the swelling/de-swelling ability) of the PNCS microgel particles was studied using the moisture-content determination. For this reason, a PES woven fabric was chosen as the substrate due to its non-polarity and a low moisture regain in order to avoid any interference with the results of the moisture-content determination of the studied samples. In the application process, a simple pad-dry-cure procedure was used since

it is especially interesting for an application in industrial conditions.

2 EXPERIMENTAL WORK

A 100 % woven (plain weave) PES fabric with a mass per unit area of 153 g/m^2 , supplied by Ten Cate Advanced Textiles (The Netherlands) was used throughout the experiment. The surface of the PES fibres was chemically activated using the UV grafting of the acrylic acid AA (Sigma-Aldrich) in the presence of benzophenone BP (Sigma-Aldrich) as the initiator, according to the procedure of Song et al.¹⁴ In this way the pre-treated fabric was referred to as the activated PES (PES-AA) and was used as the starting material for all the subsequent experiments.

The PNCS microgel was prepared according to the slightly modified¹⁵ procedure of Lee et al.¹⁶ For its application with the matrix based on the crosslinking agent (BTCA), the finishing bath was prepared by adding 1,2,3,4-butanetetracarboxylic acid BTCA (Sigma-Aldrich) and sodium hypophosphite SHP (Sigma-Aldrich) (as a catalyst) into the PNCS dispersion (23.7 g/l). The ratios used were PNCS : BTCA = $3.75 : 1$ and BTCA : SHP = $2 : 1$. The finishing bath was applied with the pad (60 % WPU) – dry (105°C , 5 min) – cure (160°C , 3 min) method. The PES sample treated in this manner is henceforth referred to as BTCA-PNCS.

To apply the PNCS microgel in combination with a polysiloxane matrix, vinyltrimethoxysilane VTMS (Sigma-Aldrich) was acid-catalysed. The finishing bath was prepared by adding 0.1 % fumed-silica nanoparticles (SiO_2) (Aerosil 2000, Evonik, Germany) and 10 % benzophenone BP – photoinitiator (Sigma-Aldrich) into a 4 % VTMS solution in ethanol. The prepared finishing bath was applied by the pad (60 % WPU) – dry (105°C , 5 min) method. Subsequently, the PNCS microgel (23.7 g/l) was applied (60 % WPU) and the samples were UV treated for 40 s using a UV lamp (HQV, Osram). Afterwards, the samples were dried (105°C , 5 min) and cured (160°C , 3 min). This PES sample is referred to as Si-PNCS.

The washing fastness of the BTCA-PNCS and Si-PNCS finished samples was determined after five repetitive washings in Atlas Linitester according to the ISO 105-C01:1989(E) standard method. The washing was carried out in a solution of the SDC standard detergent with a concentration of 5 g/l , previously heated to 40°C , at a liquor ratio of $50 : 1$. The duration of a washing cycle was 30 min. After each washing cycle the samples were thoroughly rinsed in cold running tap water.

A microscopic evaluation of the morphological changes occurring after the finishing and washing of the PES samples was carried out using a SEM 1550 HRSEM (Zeiss, Germany), operating at 5 kV. Before SEM images were taken, the samples were dried in a vacuum.

An X-ray photoelectron spectroscopy (XPS) analysis was carried out using a PHI Quantera Scanning ESCA Microprobe spectrometer (Physical Electronics, USA) with monochromatic Al K α radiation (1486.6 eV) at 25 W. The quantification of the surface composition was obtained from the XPS peak intensities measured on five different spots of a sample, taking into account the relative sensitivity factors provided by the instrument manufacturer.

In order to study the thermal responsiveness of the PNCS microgel, the moisture content (MC) was determined. The method was performed on the samples pre-conditioned at 80 % relative humidity, at 25 °C and 40 °C (i.e., the temperatures below and above the transition temperature of poly-NiPAAm) during a period of 24 h. MC was measured thermogravimetrically with a moisture analyser (MS-70 Moisture Analyser equipped with the WinCT-Moisture software, A&D, Japan) by drying the samples at 105 °C until a constant mass was obtained. The measurements were done on the finished samples and five-times washed samples. The final moisture content (MC) was calculated as follows:

$$MC = \frac{W_0 - W_f}{W_0} \cdot 100 (\%) \quad (1)$$

where W_0 is the mass of a sample before drying (g) and W_f is the mass of a completely dried sample (g).

In order to determine the share of the measured MC, which can be attributed to the responsiveness of the PNCS surface-modified system only, the swelling ability (SA) parameter was introduced. By using the results of the moisture content determined for the samples pre-conditioned at 25 °C and 40 °C, the swelling ability of the PNCS microgel particles was calculated as follows:

$$SA = \frac{MC_{(BTCA-PNCS; Si-PNCS)} - MC_{(PES-AA)}}{MC_{(PES-AA)}} \cdot 100 (\%) \quad (2)$$

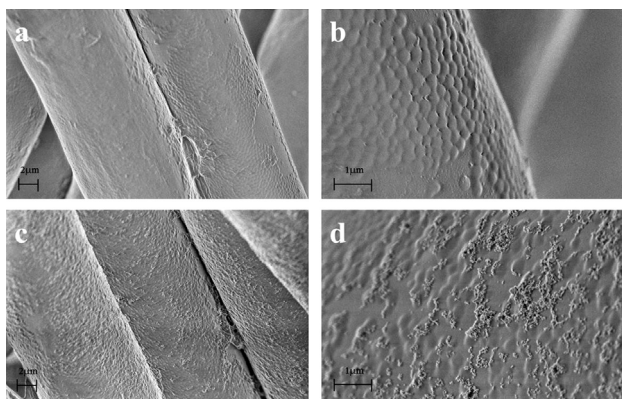


Figure 1: SEM images of: a), b) BTCA-PNCS and c), d) Si-PNCS functionalized PES samples taken at a lower (10000x) and higher (45000x) magnification

Slika 1: SEM-posnetki: a), b) BTCA-PNCS ter c), d) Si-PNCS funkcionaliziranih vzorcev PES-tkanine, posnetih pri manjši (10000-kratni) in večji (45000-kratni) povečavi

where $MC_{(BTCA-PNCS; Si-PNCS)}$ is the moisture content of the functionalized PES samples (BTCA-PNCS or Si-PNCS) and $MC_{(PES-AA)}$ is the moisture content of the activated PES (PES-AA).

With such a calculation, the contribution of the PES substrate to the measured MC can be avoided and the response efficiency of the PNCS surface-modified system can be easily assessed.

3 RESULTS AND DISCUSSION

To be able to prove that the incorporation of the PNCS hydrogel in a combination with BTCA and VTMS/SiO₂ took place, the SEM images of the functionalized PES samples were taken. On **Figure 1** the spherically shaped microgel particles with an estimated size of up to 200 nm could be clearly seen on the surface of the BTCA-PNCS and Si-PNCS finished PES, thus indicating a successful deposition of the PNCS microgel particles, regardless of the matrix used (BTCA or VTMS/SiO₂). A detailed assessment of the SEM images of the Si-PNCS finished sample also revealed that the SiO₂ nanoparticles agglomerated and distributed on the top of the coating (**Figures 1c** and **1d**). However, after five consecutive washings the SiO₂ agglomerates were rinsed away, as evident in **Figure 2b**. Moreover, the clearly present PNCS microgel particles became smoothened, while their shape change could be observed on the surface of the washed BTCA-PNCS sample (**Figure 2a**). This could be a consequence of the volume transition (swelling/de-swelling) of the microgel particles during the washing procedure. While the VTMS/SiO₂ matrix, due to its elastic properties, allowed such transition

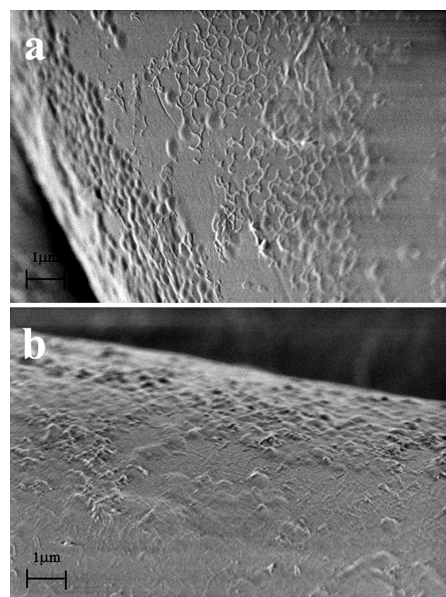


Figure 2: SEM images of: a) five-times washed BTCA-PNCS and b) Si-PNCS functionalized PES samples

Slika 2: SEM-posnetki: a) 5-krat prani BTCA-PNCS in b) Si-PNCS funkcionaliziranih vzorcev PES-tkanine

behaviour of the PNCS microgel, the rigid structure of the BTCA-based matrix might have been the reason for the PNCS-particle rupture on certain parts of the BTCA-PNCS finished fibres.

Further evidence of a successful deposition of the PNCS hydrogel was obtained with the XPS analysis (**Figure 3**). While only two bands were obtained in the XPS spectrum of the activated PES (PES-AA), ascribed to carbon (C1s) (285 eV) and oxygen (O1s) (533 eV), the XPS spectra of both finished samples also displayed a band ascribed to nitrogen (N1s) (400 eV), while in the case of the Si-PNCS sample, a band belonging to silicon (Si2p) was observed as well. It can be seen from **Figure 3** that the application of the PNCS microgel in combination with BTCA resulted in an increase in the carbon concentration and a decrease in the oxygen concentration, indicating an efficient crosslinking of the BTCA agent. On the other hand, a simultaneous decrease in the carbon and oxygen concentrations occurred in the XPS spectrum of the Si-PNCS sample, indicating a formation of a continuous polysiloxane matrix. Nevertheless, an effective incorporation of the PNCS microgel particles could be confirmed by detecting nitrogen, which was present in both poly-NiPAAm and chitosan. In the XPS spectra a higher concentration of nitrogen was detected for the Si-PNCS sample, which decreased after the washing, indicating a partial removal of the PNCS microgel. This was expected, since the PNCS microgel particles were mostly physically entrapped into the VTMS/SiO₂ matrix. On the other hand, in the XPS spectra of the unwashed and five-times washed BTCA-PNCS samples, the concentrations of nitrogen were almost unchanged, proving that, in the application process, a covalent bonding of PNCS to BTCA took place. In any case, comparable concentrations of nitrogen were determined for both the finished samples and washed samples, showing that each time approximately the same concentration of the PNCS microgel particles remained on the fibres.

The influence of the type of the bonds formed between the microgel particles and the BTCA crosslinking agent or the VTMS/SiO₂ polysiloxane matrix on the swelling/de-swelling ability was studied by determining the moisture content (MC). It can be seen from **Figure 4**

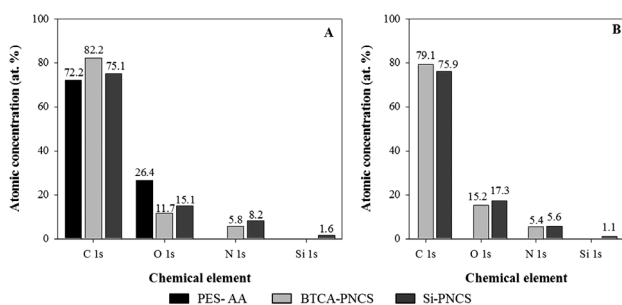


Figure 3: Surface chemical compositions of the studied PES samples: a) before and b) after five consecutive washings

Slika 3: Kemijska sestava površine preučevanih vzorcev PES-tkanine: a) pred 5-kratnim zaporednim pranjem in b) po njem

that the comparable temperature responsiveness of the PNCS microgel for BTCA-PNCS and the VTMS/SiO₂-PNCS finished samples was observed. Namely, irrespective of which type of matrix was used, the hydrophilic character of the PNCS microgel was observed (**Figure 4a**). With the samples preconditioned at 25 °C, the PNCS microgel particles were in their highly swollen state, resulting in a significantly higher moisture content of both finished samples in comparison to the bare activated PES (PES-AA). As expected, after the conditioning at 40 °C the hydrophobic character of poly-NiPAAm in the PNCS hydrogel predominated. The PNCS microgel particles were in their collapsed phase, causing water expulsion from the PNCS hydrogel, which resulted in a general decrease in the moisture content. After five consecutive washings the same trend could be observed for both sample types (**Figure 4b**). However, it can be seen that for the samples conditioned at ambient temperature (25 °C) a 12 % higher moisture content of Si-PNCS was obtained in comparison to the BTCA-PNCS sample, even though the results of the XPS analysis showed the same concentration of the PNCS microgel after the washing. This indicated that the PNCS microgel particles applied with BTCA absorbed less water under ambient conditions, which could occur due to a mechanical rupture of the PNCS microgel particles during the washing procedure as seen on the SEM images (**Figure 2a**).

The hindered responsiveness of the PNCS microgel particles due to the rigidity of the BTCA matrix became more expressed with a calculation of the swelling ability (SA). From the results shown in **Figure 5** it can be seen that the difference in SA obtained by subtracting the SA determined at 40 °C from the SA determined at 25 °C, which could be the measure for the amount of expelled water, was approximately the same for both unwashed samples, i.e., 20 % and 22 %. However, after the washing the difference in the amount of the expelled water between differently finished samples became more pronounced being 14 % for the BTCA-PNCS sample and 30 % for the Si-PNCS sample. This undoubtedly proved that, due to its rigidity, the BTCA matrix did not allow a

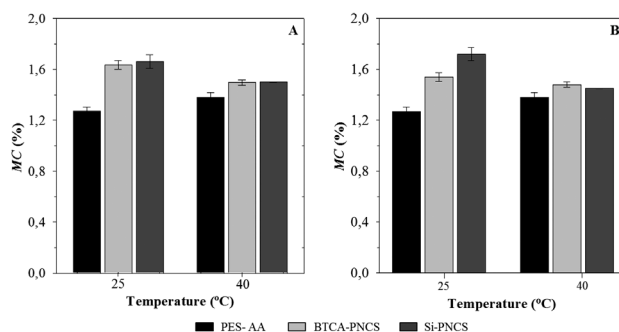


Figure 4: Final moisture content, MC, of the studied PES samples determined: a) before and b) after five consecutive washings

Slika 4: Vsebnost vlage MC preučevanih vzorcev PES-tkanine, določena: a) pred 5-kratnim zaporednim pranjem in b) po njem

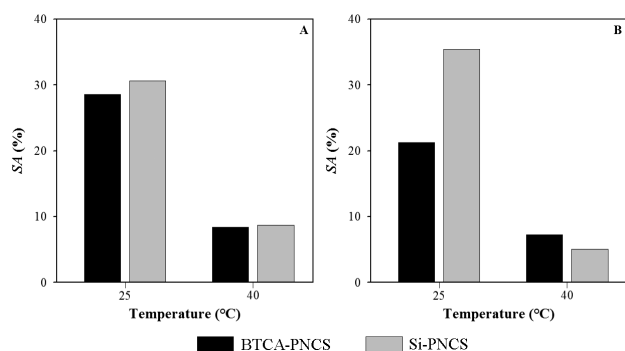


Figure 5: Swelling ability, SA, of the PNCS microgel particles, determined: a) before and b) after five consecutive washings of the samples
Slika 5: Zmožnost nabrekanja SA delcev PNCS-mikrogela, določena: a) pred 5-kratnim zaporednim pranjem vzorcev in b) po njem

flexible volume transition of the PNCS microgel particles during the washing process performed at 40 °C (the microgel particles were in their collapsed phase) and the rinsing of the samples in cold running tap water (the microgel particles were in their swollen phase). On the contrary, in the case of the Si-PNCS sample, the amount of expelled water increased after the washing. The most reasonable explanation would be a partial removal of the PNCS microgel particles, giving the microgel particles remaining on the fibres more space for expansion at the conditions below the transition temperature, which was reflected in a higher amount of expelled water at 40 °C. In this case, the physical entrapment of the PNCS hydrogel acted beneficially on the response efficiency. Namely, as it was pointed out before, for better results not more than 50 % of the fibre surface should be covered with the microgel.¹⁷ This means that with the physical incorporation of the PNCS microgel particles into the VTMS/SiO₂ polysiloxane matrix, a gradual leaching of the microgel with every washing cycle could occur, giving the remaining microgel particles on the fibre surface more space to fully swell at ambient temperature. At this point, it also has to be taken into account that after a certain number of washings the concentration of the PNCS microgel particles falls under the limit necessary to retain the response efficiency.

4 CONCLUSIONS

From the results obtained it can be concluded that the use of the matrix based on an BTCA crosslinking agent, results in a decreased swelling ability of the PNCS microgel particles, which consequently leads to a reduced capacity of water absorption under ambient conditions (25 °C) and thus less water can be expelled at 40 °C. This behaviour is attributed to the formation of chemical

bonds between the PNCS hydrogel and BTCA, creating a rigid surface-modified system on the PES fibres. The rigid nature of this matrix hindered the volume transition (swelling/de-swelling) of the PNCS microgel particles during the washing procedure, resulting in a shape change of the microgel particles. Consequently, after five washings, a 12 % smaller moisture content of the BTCA-PNCS sample, preconditioned at ambient temperature, was obtained in comparison to the corresponding Si-PNCS sample. On the other hand, when being physically entrapped into the VTMS/SiO₂ matrix, the PNCS microgel particles can expand quite freely. After five washings their swelling ability became even more pronounced, due to a partial removal of the microgel particles, giving the remaining ones more space on the fibre surface to fully expand at ambient conditions.

5 REFERENCES

- A. S. Carreira, F. A. M. M. Gonçalves, P. V. Mendonça, M. H. Gil, J. F. J. Coelho, *Carbohydrate Polymers*, 80 (2010), 618–630
- M. Prabakaran, J. F. Mano, *Macromolecular Bioscience*, 6 (2006), 991–1008
- M. A. C. Stuart, W. T. S. Huck, J. Genzer, M. Muller, C. Ober, M. Stamm, G. B. Sukhorukov, I. Szleifer, W. Tsukruk, M. Urban, F. Winnik, S. Zauscher, I. Luzinov, S. Minko, *Nature Materials*, 9 (2010), 101–113
- K. M. Vårum, M. H. Ottøy, O. Smidsrød, *Carbohydrate Polymers*, 25 (1994), 65–70
- H. G. Schild, *Progress in Polymer Science*, 17 (1992), 163–249
- R. P. Dumitriu, R. G. Mitchell, C. Vasile, *Polymer International*, 60 (2011), 222–233
- A. Kulkarni, A. Tourrette, M. M. C. G. Warmoeskerken, D. Jocić, *Carbohydrate Polymers*, 82 (2010), 1306–1314
- P. Križman Lavrič, B. Tomšič, B. Simončič, M. M. C. G. Warmoeskerken, D. Jocić, *Cellulose*, 19 (2012) 1, 257–271
- P. Križman Lavrič, B. Tomšič, B. Simončič, M. M. C. G. Warmoeskerken, D. Jocić, *Cellulose*, 19 (2012) 1, 273–287
- O. Sauperl, K. Stana-Kleinschek, V. Ribitsch, *Textile Research Journal*, 79 (2009), 780–791
- K. F. El-tahlawy, M. A. El-bendary, A. G. Elhendawy, S. M. Hudson, *Carbohydrate Polymers*, 60 (2005), 421–430
- B. Tomšič, P. Križman Lavrič, B. Simončič, B. Orel, D. Jocić, *Journal of Sol-Gel Science and Technology*, 61 (2012) 3, 463–476
- C. J. Brinker, G. W. Scherer, *Sol-Gel Science: The Physics and Chemistry of Sol-Gel Processing*, Academic Press, Boston 1990, 908
- Y. W. Song, H. S. Do, H. S. Joo, D. H. Lim, S. Kim, H. J. Kim, *Journal of Adhesion Science and Technology*, 20 (2006), 1357–1365
- A. Tourrette, N. De Geyter, D. Jocić, R. Morent, M. M. C. G. Warmoeskerken, C. Leys, *Colloids and Surfaces A: Physicochemical and Engineering Aspects*, 352 (2009), 126–135
- C. F. Lee, C. J. Wen, W. Y. Chiu, *Journal of Polymer Science Part A: Polymer Chemistry*, 41 (2003), 2053–2063
- D. Jocić, P. Križman Lavrič, M. M. C. G. Warmoeskerken, *Stimuli-responsive cotton by functional finishing with chitosan/poly-NiPAAm microgel*, International Conference on Intelligent Textiles (ICIT2010), Seoul, Korea, 2010, 15–16

APPLICATION OF INFINITE-ELEMENT CALCULATIONS FOR CONSOLIDATING A RAILWAY FOUNDATION OF BLOWING SAND RECLAMATION

UPORABA IZRAČUNA Z NESKONČNIMI ELEMENTI ZA UTRDITEV PODLAGE ŽELEZNIŠKE PROGE Z DROBNIM PESKOM

Kai-zhong Xie^{1,2}, Ying-zhong Pan³, Hao Ni¹, Hong-wei Wang¹

¹Dept. Civil & Architecture Engineering of Guangxi University, Nanning, Guangxi, China

²Guangxi Key Laboratory of Disaster Prevention and Engineering Safety, Guangxi University, Guangxi, China

³Guangxi Railway Investment Group CO., LTD, Nanning, Guangxi, China
zhiwen54321@126.com

Prejem rokopisa – received: 2013-01-27; sprejem za objavo – accepted for publication: 2013-02-19

The dynamic-compaction method was adopted for consolidating a railway foundation of blowing sand reclamation in the North Bay of Guangxi, China. Based on the physical characteristics of the sands, the parameters of the infinite-finite elements for an extended Drucker-Prager model were obtained with the soil tests. This model was used to analyze the area of dynamic compaction and the mechanical behaviors of the sands under dynamic compactions with a dynamic explicit analysis. By comparing the test results, we demonstrated that dynamic compaction was an effective method for a railway foundation of blowing sand reclamation, and the numerical-analysis model based on the infinite-element method was a very powerful tool used in the actual conditions, having no boundary reflection under dynamic compactions.

Keywords: infinite element, dynamic compaction, blowing sand reclamation, explicit analysis, railway foundation

Za utrditev podlage železniške proge v North Bay, Guangxi, Kitajska, je bila uporabljena dinamična metoda kompaktiranja. Na podlagi fizikalnih lastnosti peskov in preizkusov tal so bili dobljeni parametri neskončno-končnih elementov za razširjeni Drucker-Pragerjev model. Tak model in dinamična eksplicitna analiza sta bila uporabljena za analizo področja dinamičnega kompaktiranja in mehanskih lastnosti peska pri dinamičnem kompaktiranju. S primerjavo rezultatov preizkusov smo pokazali, da je dinamično kompaktiranje peska učinkovita metoda za utrjevanje podlage železniške proge. Model za numerično analizo, ki temelji na metodi končnih elementov, je močno orodje brez omejitev v realnih razmerah dinamičnega kompaktiranja.

Ključne besede: neskončni element, dinamično kompaktiranje, droben pesek, eksplicitna analiza, podlaga železniške proge

1 INTRODUCTION

To construct highways and railways in the coastal region, in many sections blowing sand reclamation is used for constructing the foundation of the roads. The key problem of this kind of engineering is how to construct, economically and efficiently, large volumes of blowing-sand-reclamation foundations. There are many methods for consolidating a foundation of blowing sand reclamation, such as vibro-replacement stone pile, dynamic compaction, water-soil whip pile, and filler-vibration impact. For an estimation of the main construction parameters (the effective strengthening depth and radius) in the foundation treatment with the dynamic-compaction method, Li¹ built a three-dimensional finite-element model with LS-DYNA to get a numerical calculation of the single-point poulder strike of the kinetics process (a dynamic-compaction-method estimation based on a three-dimensional soil-dynamics numerical simulation). Li et al.² developed an estimation method and a formula for a dynamic-compaction foundation settlement in collapsible loess areas with a dynamic-compaction foundation-settlement-theory deduction, error analysis and mea-

sured-data verification. Mostafa³ developed two-dimensional and three-dimensional finite-element models to study the dynamic compaction in cohesive soils.

In order to analyze the effect of the dynamic-compaction method, which is applied in the blowing-sand-reclamation projects in the coastal regions, we built an infinite-finite-element coupling model of the blowing-sand-reclamation foundation by introducing the infinite-element method providing the boundaries of the three-dimensional numerical model.

2 SPATIAL INFINITE-ELEMENT METHOD

Infinite elements are used for the boundary-value problems defined in unbounded domains or the problems, in which the region of interest is small in size, compared to the surrounding medium, and are usually used in conjunction with finite elements.

The static behavior of the infinite elements is based on modeling the basic solution variable u (in the stress analysis u is a displacement component) with respect to the spatial distance r measured from a "pole" of the solution, so that $u \rightarrow 0$ as $r \rightarrow \infty$, and $u \rightarrow \infty$ as $r \rightarrow 0$. The

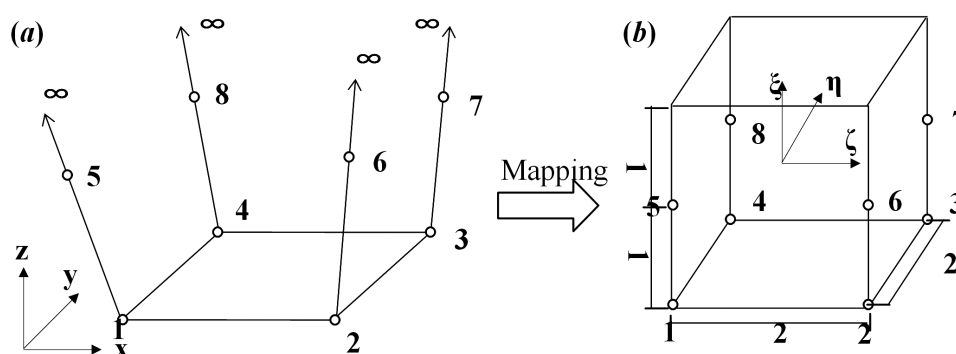


Figure 1: Node spatial mapping of an infinite element: a) practical element, b) parent element

Slika 1: Prostorska razporeditev vozlišč neskončnega elementa: a) praktični element, b) osnovni element

interpolation provides the terms of order $1/r$, $1/r^2$ and, when the solution variable is a stress-like variable (such as the pore liquid pressure in an analysis of the flow through a porous medium), also $1/r^3$. The far-field behavior in many common cases, such as a point load on a half-space, is thereby included. This modeling is achieved by using the standard cubic interpolation for $u(s)$ in $-1 \leq r \leq 1$, where s is a mapped coordinate that is chosen so that the mapping causes $r(s)$. We obtained a three-dimensional model of domains reaching infinity by combining this interpolation in the s -direction of a product form with the standard linear or quadratic interpolation in orthogonal directions in the mapped space.

Three-dimensional infinite elements only map the infinite domain along one direction, as shown on **Figure 1**, where the elements along the x and y directions are finite, while the z direction is infinite. After using a coordinate transformation, we can map the practical element of the xyz coordinates in a spatial cube element where the length of each side is 2.

The conversion relationship between the whole coordinates $x - y - z$ and the local coordinate is:

$$x = \sum_{i=1}^n M_i x_i \quad y = \sum_{i=1}^n M_i y_i \quad z = \sum_{i=1}^n M_i z_i \quad (1)$$

in which n is the node number, M_i is the mapping function, and x_i, y_i, z_i are the nodal coordinates:

$$\begin{aligned} M_1 &= \frac{(1-\xi)(1-\eta)(-\zeta)}{2(1-\zeta)} & M_2 &= \frac{(1+\xi)(1-\eta)(-\zeta)}{2(1-\zeta)} \\ M_3 &= \frac{(1+\xi)(1+\eta)(-\zeta)}{2(1-\zeta)} & M_4 &= \frac{(1-\xi)(1+\eta)(-\zeta)}{2(1-\zeta)} \\ M_5 &= \frac{(1-\xi)(1-\eta)(1+\zeta)}{4(1-\zeta)} & M_6 &= \frac{(1+\xi)(1-\eta)(1+\zeta)}{4(1-\zeta)} \\ M_7 &= \frac{(1+\xi)(1+\eta)(1+\zeta)}{4(1-\zeta)} & M_8 &= \frac{(1-\xi)(1+\eta)(1+\zeta)}{4(1-\zeta)} \end{aligned} \quad (2)$$

When practical elements are mapped to be parent elements, we can analyze the characteristics of the parent elements. If we assume that the parent elements use the same shape function as the 8-node spatial elements, they

can couple with the 8-node spatial finite elements. The selection of a displacement model is as follows:

$$u = \sum_{i=0}^n N_i u_i \quad v = \sum_{i=0}^n N_i v_i \quad w = \sum_{i=0}^n N_i w_i \quad (3)$$

where n is the node number, N_i is the mapping function and u_i, v_i, w_i are the nodal displacements:

$$\begin{aligned} N_1 &= 0.125(1-\xi)(1-\eta)(\zeta^2 - \zeta) \\ N_2 &= 0.125(1+\xi)(1-\eta)(\zeta^2 - \zeta) \\ N_3 &= 0.125(1+\xi)(1+\eta)(\zeta^2 - \zeta) \\ N_4 &= 0.125(1-\xi)(1+\eta)(\zeta^2 - \zeta) \\ N_5 &= 0.25(1-\xi)(1-\eta)(1-\zeta^2) \\ N_6 &= 0.25(1+\xi)(1-\eta)(1-\zeta^2) \\ N_7 &= 0.25(1+\xi)(1+\eta)(1-\zeta^2) \\ N_8 &= 0.25(1-\xi)(1+\eta)(1-\zeta^2) \end{aligned} \quad (4)$$

3 CONSTITUTIVE MODEL OF THE SAND SOILS

For a non-metal particle material such as soil and rock, we can adopt a D-P model that can simulate a non-metal material, extending its function on the basis of an ideal elastic-plastic model.

The Drucker-Prager ideal elastic-plastic model is one of the earliest constitutive models for elastic-plastic geotechnical materials; its parameters are few and the calculation is simple.^{4,5} Its yield-criterion expression is shown in equation (5):

$$F(\sigma_{ij}) = \sqrt{J_2} - \alpha I_1 - K = 0 \quad (5)$$

where J_2 is the second invariant of the stress-deviation tensors, I_1 is the first invariant of the stress deviation tensors and α, K are the material constants. As Drucker and Prager derived the relations between α, K and the material constants C, φ of the Mohr-Coulomb criterion is shown in equation (6):

$$K = \frac{\sqrt{3} \cos \varphi}{\sqrt{3 + \sin^2 \varphi}} \quad \alpha = \frac{\sin \varphi}{\sqrt{3} \sqrt{3 + \sin^2 \varphi}} \quad (6)$$

Drucker and Prager (1952) proposed a yield condition, according to which the yield surface is a cone in the

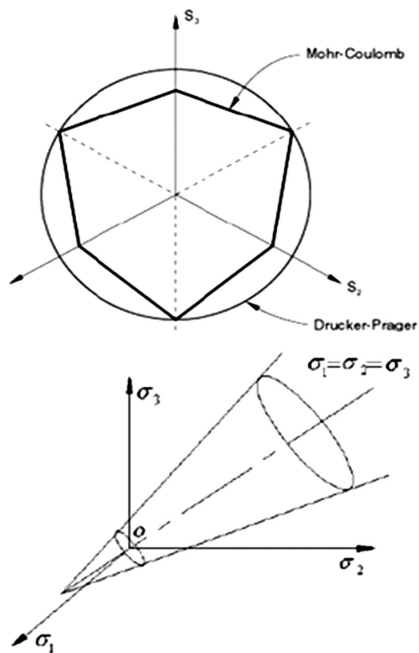


Figure 2: Generalized von Mises yield surface

Slika 2: Posplošena površina meje plastičnosti po von Misesu

stress space, as seen on **Figure 2**, on the π -plane, while its yield curve is a circle that is inscribed in the Mohr-Coulomb yield curve; in the stress space, its yield surface is a cone, while the center axis and the isocline are coincident.

The D-P model considers that when the material is in its elastic phase ($F < 0$) or unloading phase ($F = 0$, and $\delta F < 0$), the stress-strain relation shown in equation (7) applies:

$$\sigma_{ij} = K\epsilon_{KK}\delta_{ij} + 2G\delta\epsilon_{ij} \quad (7)$$

If $F = 0$ and the loading is ($\delta F > 0$), the stress-strain relation shown in equation (8) applies:

$$\delta\sigma_{ij} = K\delta\epsilon_{KK}\delta_{ij} + 2G\delta\epsilon_{ij} - d\lambda(-3K\alpha)\delta_{ij} + \frac{G\sigma_{ij}}{\sqrt{J_2}} \quad (8)$$

$$\text{where } d\lambda = \frac{-3K\alpha\delta\epsilon_{KK} + \frac{G}{\sqrt{J_2}}\sigma_{mn}\epsilon_{mn}}{9K\alpha^2 + G};$$

δ_{ij} is the Kronecher sign; when $i = j$, $\delta_{ij} = 1$; when $i \neq j$, $\delta_{ij} = 0$; σ_{ij} indicates the stress tensors, ϵ_{ij} indicates the strain tensors; K is the volume-elastic modulus; G is the shear-elastic modulus.

4 LINEAR DRUCKER-PRAGER MODEL

The linear model is written in terms of all three stress invariants. It provides for a possible noncircular yield surface in the deviatoric plane matching different yield values of the triaxial tension and compression, the associated inelastic flow in the deviatoric plane, the separate dilation and friction angles.

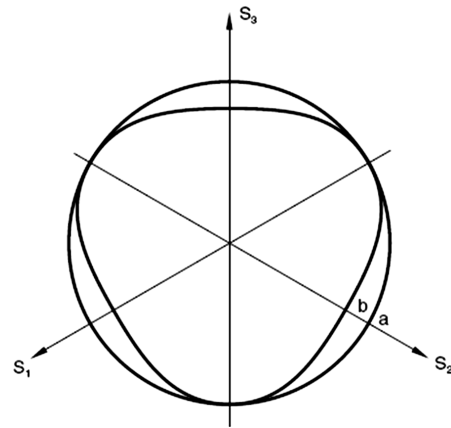


Figure 3: Typical yield/flow surfaces

Slika 3: Značilna mejna površina plastičnosti

(1) Yield criterion

The linear Drucker-Prager criterion is written as:

$$F = t - p \tan \beta - d = 0 \quad (9)$$

$$\text{where: } t = \frac{1}{2} \theta \left[1 + \frac{1}{K} - \left(1 - \frac{1}{K} \right) \left(\frac{r}{\theta} \right)^3 \right] \quad (10)$$

$\beta(\theta, f_i)$ is the slope of the linear yield surface in the $p - t$ stress plane and is commonly referred to as the friction angle of the material; d is the cohesion of the material; $K(\theta, f_i)$ is the ratio of the yield stress in the triaxial tension to the yield stress in the triaxial compression, thus, controlling the dependence of the yield surface on the value of the intermediate principal stress (as seen in **Figure 3**). θ is the temperature, $f_i (i = 1, 2, \dots)$ refers to the other predefined field variables.

The cohesion d of the material is related to the input data as:

$$d = \left(1 - \frac{1}{3} \tan \beta \right) \sigma_c = \left(\frac{1}{K} + \frac{1}{3} \tan \beta \right) \sigma_t \quad (11)$$

$$\sigma_t = \frac{\sqrt{3}}{2} \tau \left(1 + \frac{1}{K} \right)$$

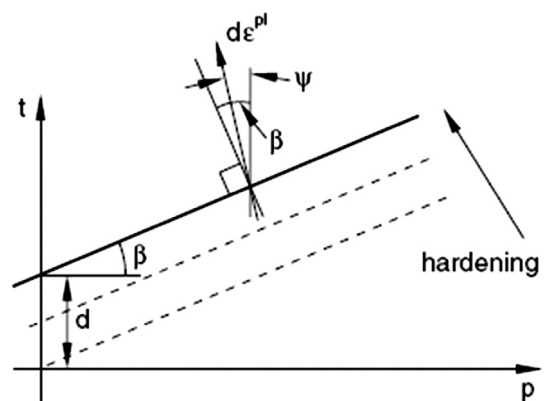


Figure 4: Yield surface and flow direction

Slika 4: Meja plastičnosti in smer toka materiala

where σ_c is the uniaxial compression yield stress, σ_t is the uniaxial tension yield stress and τ is the shear stress.

(2) Plastic flow

G is the flow potential, chosen in this model as:

$$G = t - p \tan \psi_1 \quad (12)$$

where $\psi_1(\theta, f_i)$ is the dilation angle in the $p - t$ plane. A geometric interpretation of ψ is shown in the $p - t$ diagram of **Figure 4**. In the case of the hardening defined for the uniaxial compression, this flow-rule definition precludes the dilation angles $\tan \psi > 3$. This restriction is not seen as a limitation since it is unlikely that it will apply to real materials.

(4) Non-associated flow

The non-associated flow implies that the material stiffness matrix is not symmetric; therefore, the unsymmetrical matrix storage and solution scheme should be used. If the difference between β and ψ is not large and the region of the model, in which the inelastic deformation is occurring is confined, it is possible that a symmetric approximation of the material stiffness matrix will give an acceptable rate of convergence and the unsymmetrical matrix scheme may not be needed.

5 LOADING FORM OF DYNAMIC COMPACTION

According to the previous research and test demonstrations, in the process of a pounder's collision with and impact on a foundation, the contact stress has only one significant peak value on the time-history curve and its duration is very short, around 0.1 s. The impact load is simplified into the load of the triangle form, as seen on **Figure 5**. The values of t_n , t_r , P_{\max} from this figure can be measured in the test fields or estimated with the following formulas:

$$P_{\max} = \frac{V_0 \sqrt{mS}}{\pi r^2} \quad t_n = \pi \sqrt{\frac{m}{S}} \quad t_r = \left(\frac{1}{4} \approx \frac{1}{2} \right) t_n \quad (13)$$

where V_0 is the landing speed of the pounder, m is the pounder quality, r is the pounder radius and S is the elastic constant:

$$S = 2rE(1 - \mu^2) \quad (14)$$

As the deformation modulus of the soil is being continuously adjusted, the contact stress and the contact time also undergo continuous changes. We fully considered these changes in the simulation, adjusting, on the basis of the deformation modulus, the contact stress and the contact time for each analysis step, where one pounder strike is defined as one analysis step, lasting for 0.3 s, so that the total analysis time is 2.1 s.

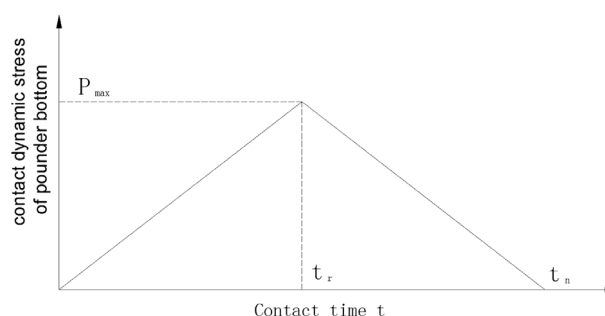


Figure 5: Strong-pounder dynamic-effect model
Slika 5: Model dinamičnega učinka močnega tolkača

6 PROJECT APPLICATION

A section of the railway branch between DaLanPing and BaoShuiGang (CK12+ 000 ~ CK17+300) is involved in a blowing-sand-reclamation project applying to a littoral area with the total length of the dynamic compaction area set to be 150 m.

The section from DK15+315.64 to DK15+515.64 was regarded as the test section. According to the depth range covered with the standard penetration test, the area was geotechnically divided into 3 layers: the filling sand, the fine sand and the mud.

7 NUMERICAL ANALYSIS

7.1 Analysis model

With the ABAQUS finite-element software, simulating the foundation of blowing sand reclamation and using a dynamic-compaction method, we built two three-dimensional entity models on the basis of the finite-element model and infinite-finite element coupling model, aiming to simulate the dynamic compaction process for the test section.

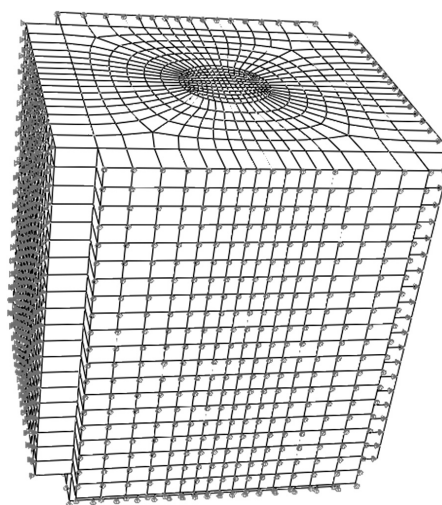


Figure 6: Finite-element method
Slika 6: Metoda končnega elementa

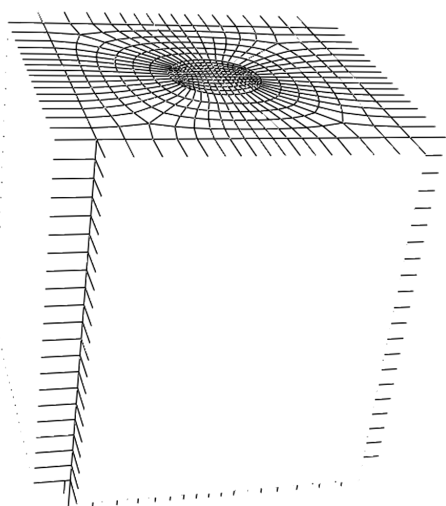


Figure 7: Coupling method of an infinite-finite element
Slika 7: Združena metoda neskončnega-končnega elementa

The factors influencing the foundation of blowing sand reclamation, included in the dynamic-compaction method, are many and the deformation characteristics of the soil body are also very complicated, so we introduced the following assumptions:

- 1) The soil body in the model can be regarded as homogeneous, isotropic and elastic-plastic infinite spatial.
- 2) No effects of the groundwater need to be considered.
- 3) The pouncer is simplified into a force, that is, a force is applied on the soil body.
- 4) The interface between the above force and the tangential force of the blowing sand reclamation can be ignored.

The finite-element model (model 1) is based on the following parameters: the width of the top surface of the roadbed is 20 m, the width of the bottom surface is 40 m, the height is 10 m, the length is 10 m, and the grid size is 1 m. The tamper weight is 150 kN, the tamping energy is 2600 kN m.

The infinite-finite-element coupling model (model 2) is based on the finite-element model. The boundary elements for four weeks and the bottom elements can be replaced with the spatial infinite elements. As the infinite elements belong to the boundary elements, we do not need to set the boundary conditions, as shown in **Figures 6** and **7**.

7.2 Material model parameters

The physical and mechanical parameters of different sections between the top and the bottom of the filling-sand layer are presented in **Table 1**.

Table 1: Physical and mechanical parameters of the filling-sand layer
Tabela 1: Fizikalni in mehanski parametri plasti polnilnega peska

Sand layer	E/MPa	μ	$\beta/^\circ$	K	$\psi/^\circ$	ε_p	σ/kPa
0~1 m	8	0.3	58.5	0.778	0	0	100

Table 2: Settlement of dynamic compaction (cm)

Tabela 2: Posedanje pri dinamičnem kompaktiranju (cm)

times	test	model 1	model 2
1	35.7	36.0	40.0
2	19.0	21.0	25.0
3	16.7	12.0	14.0
4	12.3	10.0	12.0
5	8.7	5.0	7.0
6	6.0	3.0	5.5
7	3.0	1.0	2.0
total	101.4	88.0	105.5

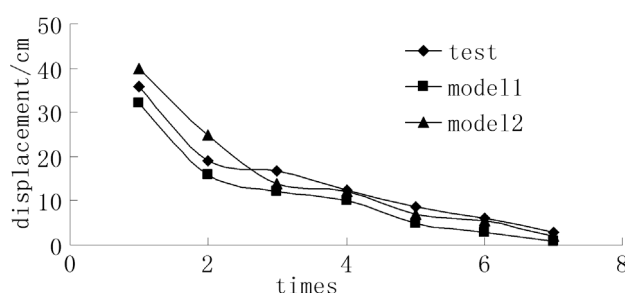


Figure 8: Relation curve of dynamic pit settlement and times
Slika 8: Odvisnost krivulje dinamičnega posedanja od ponovitev

1~2 m	14.5	0.3	58.5	0.778	0	0	140
2~5 m	19	0.3	58.5	0.778	0	0	180
5~6 m	8	0.3	58.5	0.778	0	0	100
6~8 m	14.5	0.3	58.5	0.778	0	0	140
8~12 m	18	0.3	58.5	0.778	0	0	180

We simulated and analyzed the dynamic compaction process for different test sections with two models, and compared the analysis results with the measured values of the field dynamic-penetration test. The surface-settlement data of dynamic compaction for the process of 7 strikes is presented in **Table 2** and the dynamic-compaction settlements are plotted in **Figure 8**.

As shown in the above figure and table, in the numerical analysis of consolidating the foundation's capacity for blowing sand reclamation, the settlement amount for model 1 using the finite-element method is smaller than for model 2 using the infinite-finite element method with the infinite element as the boundary condition. The values of model 2 are close to the measured values of the field test, showing that this model can simulate the practical boundary conditions well by introducing infinite elements to the analysis model.

In the process of dynamic compaction, when the number of the rammer strikes is 7, the settlement tends to be stable and the measured value is 3 cm, reaching the settlement requirement of dynamic compaction.

8 CONCLUSIONS

On the basis of an analysis of the foundation's capacity for blowing sand reclamation carried out with the

dynamic-compaction method, and a comparison of its results with the measured values, we can draw the following conclusions:

- 1) The model can simulate the practical conditions well by introducing the infinite elements as boundaries;
- 2) The boundary conditions have a big influence on the calculation results of the finite-element method;
- 3) Compared with the measured values, the values of model 2 that used the infinite element as the boundary condition are close to the measured values;
- 4) If the number of the rammer strike is 7, the settlement tends to be stable, reaching the requirement of dynamic compaction.

Acknowledgements

Xie thanks the National Natural Science Foundation of China (No.: 51068001), the Systematic Project of the Guangxi Key Laboratory of Disaster Prevention and Structural Safety – the Scientific Research (2012ZDX04), the

Technology Development Key Project of Guangxi (No.: 0816006-7 and No.: 0992027-12) and the Scientific Research Foundation of the Guangxi University (No.: XBZ100762).

9 REFERENCES

- ¹ J. Li, W. F. Teng, Estimation of construction parameters of dynamic compaction method based on 3D soil dynamic numerical simulation, *Yangtze River*, 42 (2011) 15, 50–52
- ² W. Li, Q. Gu, L. Su, B. Yang, Finite element analysis of dynamic compaction in soft foundation, *Procedia Engineering*, 12 (2011), 224–228
- ³ K. Mostafa, Numerical modeling of dynamic compaction in cohesive soils, A Dissertation Presented to The Graduate Faculty of The University of Akron, 2010, 2–3
- ⁴ J. P. Borg, J. R. Cogar, A. Lloyd, A. Ward, D. Chapman, K. Tsembe-lis, Computational simulations of the dynamic compaction of porous media, *International Journal of Impact Engineering*, 33 (2006), 109–118
- ⁵ L. Chen, Application and Research of Ground Treatment of Encircling the Sea to Land Project, *Special Structure*, 27 (2010) 2, 1–5

EXPERIMENTAL STUDY ON THE ROLE OF THE VIBRATION DAMPING AND ENERGY ABSORPTION OF FLEXIBLE FUNCTION LAYERS

EKSPERIMENTALNA ŠTUDIJA VLOGE DUŠENJA VIBRACIJ IN ABSORPCIJE ENERGIJE V GIBLJIVIH FUNKCIONALNIH PLASTEH

Bin Yang^{1,2,3}, Jinhua Huang¹, Sihao Mo^{1,2,3}, Ping Wu^{1,2,3}

¹College of Civil Engineering and Architecture, Guangxi University, 530004 Nanning, China

²Key Laboratory of Disaster Prevention and Structural Safety of Ministry of Education, 530004 Nanning, China

³Guangxi Key Laboratory of Disaster Prevention and Engineering Safety, 530004 Nanning, China
yangbin5612@163.com

Prejem rokopisa – received: 2013-01-27; sprejem za objavo – accepted for publication: 2013-02-19

In order to solve the pavement-slab breakdowns caused by a poor vibration damping and energy absorption of cement-concrete rigid structures with a lean concrete base, this study proposes an addition of a flexible function layer between the lean concrete base and the concrete pavement slab to form a "rigid+flexible+rigid" structure. The conducted experiments use a dynamic signal-testing and analyzing system to collect the frequency signals from the pavement-structure vibration when a small pavement-slab structure is subjected to a ball-drop impact. The results reveal how much vibration is damped out and how much energy is absorbed by adding a flexible function layer. According to the contrastive tests, the pavement-slab vibration is a declining process under an impact load. The vibration damping is more significant with an increase in the thickness of the function layer, but it becomes slower if the layer reaches a certain thickness. The tests also show that a flexible function layer has a significant role in the vibration damping and energy absorption. Therefore, the cement-concrete pavement structure designed with a flexible function layer can greatly reduce the slab breakdowns caused by the wheel-impact vibrations.

Keywords: cement-concrete pavement, flexible function layer, vibration damping and energy absorption, dynamic response

Da bi rešili problem pokanja plošč pločnikov, ki ga povzroči slabo dušenje vibracij in absorpcija energije betonskih togih konstrukcij z osnovo iz pustega betona, ta študija predlaga dodatek gibljive funkcionalne plasti med podlago iz pustega betona in ploščo pločnika, da se vzpostavi "togo-giblivo-togo" strukturo. Pri opravljenih preizkusih je bil uporabljen analizi sistem za preizkušanje dinamičnih signalov in za registracijo frekvenčnih signalov iz vibracij pločnika, če je bil ta izpostavljen udarcu pri padcu krogle. Rezultati odkrivajo, koliko vibracij je zadušenih in koliko energije se absorbira z dodatkom gibljive funkcionalne plasti. Na osnovi preizkusov je vibracija pločnika pri udarcu pojemajoč proces. Učinek dušenja vibracij je večji z naraščajočo debelino funkcionalnega sloja in postane manjši pri določeni debelini plasti. Preizkusi so tudi pokazali, da ima gibljivi funkcionalni sloj veliko vlogo pri dušenju vibracij in pri absorpciji energije. Zato se pri strukturi cementnega pločnika z gibljivim funkcionalnim vmesnim slojem lahko močno zmanjša pokanje plošč, ki ga povzročijo udarci pri vibraciji koles.

Ključne besede: pločnik iz cementa, gibljiva funkcionalna plast, dušenje vibracij in absorpcija energije, dinamično odzivanje

1 INTRODUCTION

Many countries have adopted the idea of a rigid base or semi-rigid base for their cement-concrete pavements because this pavement structure has advantages, such as a high degree of rigidness, superior strength and a large load capacity. However, this pavement structure has inferior vibration-damping and energy-absorption capabilities, and thus, the impact of wheel vibrations can easily damage the concrete pavement slab. Therefore, the current study proposes an addition of a flexible vibration-damping function layer between the rigid or semi-rigid base and the concrete pavement slab to form a "rigid+flexible+rigid" pavement structure to solve the problem stated above. The addition of a flexible function layer can significantly reduce the vibration impact of the wheel load on the cement-concrete pavement, improving the working conditions of the pavement and extending the life cycle of a highway.

Some researchers have conducted studies on the flexible function layer of a cement concrete pavement. Ma, Yi, and He (2004)¹ analyzed the influence of the function layer on the surface concrete materials and its mechanical performance. H. Miao (2009)² conducted a mixture-accumulative deformation test, an interlayer shear-strength test and a water-damage test for the function layer in an MTS material testing system. Yao et al. (2009)³ introduced methods for an interlayer shear-strength test, torsion test, and pull-out test by combining the application research of a waxed curing agent and the function layer of a slurry-sealing layer. Wang (2009)⁴ analyzed the mixture types of different function layers and the results of the interlayer shear-strength tests under different environment temperatures using different dealing measures for different layers.

Although flexible function layers have been applied in some pavements around the world, the existing research on the flexible function layers added to cement-

concrete pavements lacks depth, especially with respect to the vibration-damping and energy-absorption effects of these layers. The current experiment mainly aims to compare the vibration-damping and energy-absorption effects produced under the circumstances of cement-concrete pavements with and without a flexible function layer. This experiment analyzed the declining rule of the vibration response in the pavement structure and explored the vibration-damping and energy-absorption effects of the flexible function layer using a ball-drop impact test and a dynamic signal-test instrument to collect the signal data from the vibration-frequency domain of the pavement structure.

2 TEST METHODS

2.1 Comparison of the structure types of the test models

Figure 1 shows the two test structure models used in the experiment: **Figure 1a** refers to the pavement structure when the concrete slab was placed directly onto a lean concrete base and **Figure 1b** refers to the pavement structure when a flexible vibration-damping function layer was added between the concrete slab and the lean concrete base. The test piece was 62.5 cm long and 50 cm wide. The cement-concrete pavement slab used the C30 asphalt concrete, having a resilience modulus of 31.000 MPa and a thickness of 5 cm. The lean concrete base used the C15 asphalt concrete, having a resilience modulus of 21.000 MPa and a thickness of 4 cm. The flexible vibration-damping function layer used the AC-10 asphalt concrete, having a resilience modulus of 1.400 MPa and the thicknesses of 2 cm and 4 cm. The bottom layer of the pavement structure was a 2 cm thick rubber cushion.

2.2 Material-mixing ratio for the flexible vibration-damping function layer

In line with the *Technical Specifications for Construction of Highway Asphalt Pavements* (JTG F40-2004)⁵ relating to the grading scope of the mineral aggregates of a dense-graded asphalt concrete mixture, the experiment used AC-10 as the mixture for the flexible function layer to be tested. The design of the grading is shown in **Table 1**.

The asphalt was the AH-70 matrix asphalt, whose specifications are listed in **Table 2**. The quantity used in the experiment was based on the best amount of the

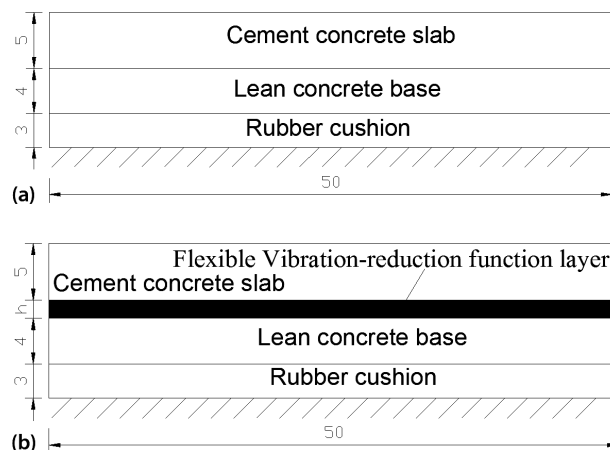


Figure 1: Comparison test model dimensions (cm): a) pavement structure without a flexible vibration-damping function layer, b) pavement structure with a flexible vibration-damping function layer
Slika 1: Primerjava dimenzij preizkusnih modelov (cm): a) struktura pločnika brez gibljivega funkcionalnega sloja za dušenje vibracij, b) struktura pločnika z gibljivim funkcionalnim slojem za dušenje vibracij

Table 2: Asphalt-performance indices

Tabela 2: Značilne lastnosti asfalta

Asphalt test	Test result	Technical requirement
Ductility of 10 °C/mm	300	200
Ductility of 15 °C/mm	837	400
Ductility of 25 °C/mm	1401	–
Penetration at 25 °C/0.1 mm	72.7	60≈80
Softening point (°C)	48.4	45
Flash point (°C)	266	260
Specific gravity (g/cm ³)	1.029	Actual record

AC-10 asphalt mixture determined with a Marshall test. The Marshall-test piece was prepared in accordance with the *Standard Test Methods of Asphalt and Asphalt Mixtures for Highway Engineering* (JTJ 052-2000)⁶. According to the test, the best amount of the AC-10 asphalt was 5.0 %.

3 BALL-DROP VIBRATION TESTS

3.1 Layout of the vibration measuring points

The experiment adopted the ball-impact test⁷ proposed by the American Concrete Institute (ACI) to implement a vibration impact to the pavement. A steel ball was used to provide the source of a vibration signal. **Figure 2** shows the stipulated vibration test. The measuring points were located within the pavement slab, speci-

Table 1: Mineral-aggregate gradation of AC-10

Tabela 1: Razporeditev zrnatosti v AC-10

Mesh Source	Quality percentage (%) with the following mesh size (mm)								
	13.2	9.5	4.75	2.36	1.18	0.6	0.3	0.15	0.075
Specification allowance	100	90≈100	45≈75	30≈58	20≈44	13≈32	9≈23	6≈16	4≈8
Actual value	100	95	60	40	30	25	16	12	6

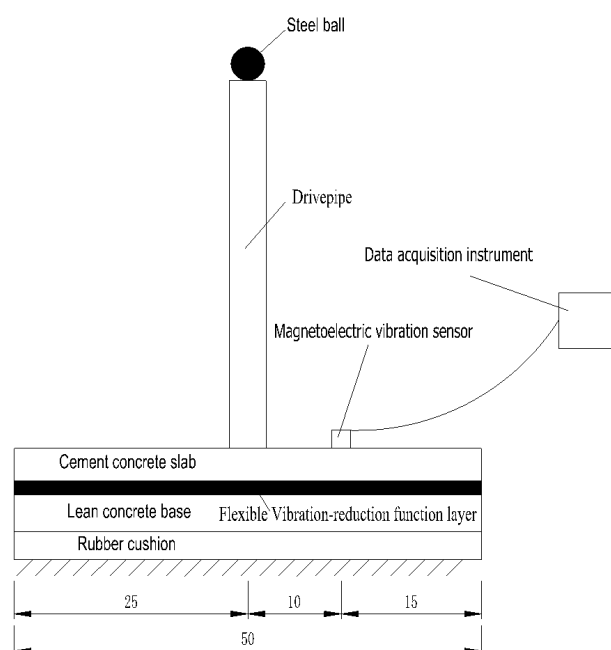


Figure 2: Schematic diagram of data acquisition (cm)
Slika 2: Shematski prikaz zbiranja podatkov (cm)

fically, at the midpoint and corners. A time-domain analysis was conducted on the basis of the vibration signals from the measuring points to investigate the vibration-response rule of the pavement structure. **Figure 3** shows the selection of the measuring points. In this test, the sample frequency was 5.000 Hz, the analyzing frequency was 1.950 Hz and the testing orientation was vertical.

The ball-drop heights of the steel ball in this test were set at (40, 60, 80, 100, 120, and 140) cm to simulate the wheel vibrations and test the load-declining rule of the pavement under different working conditions.

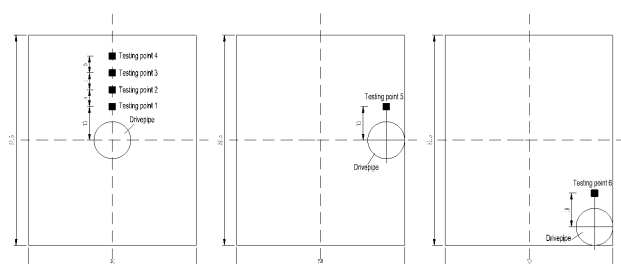


Figure 3: Layout of vibration measuring points (cm)
Slika 3: Razporeditev točk za merjenje vibracij (cm)

3.2 Testing instruments

The main testing instruments included, among others, a dynamic signal-testing instrument, a signal-testing and analyzing system, a magnetic-electric vibration sensor and a steel ball, as shown in **Figures 4** and **5**.

4 ANALYSIS OF THE RESULTS OF THE VIBRATION-DAMPING AND ENERGY-ABSORPTION TESTS OF THE FLEXIBLE FUNCTION LAYER

4.1 Contrastive analysis of the measured vibration-waveform signals

The measured waveforms at various ball-drop heights of the steel ball were the same, except for the occurrence of a significant variation at the peak. In the current study, the data analysis was only applied to the tests, in which the measuring point was within the slab and the ball-drop height was 60 cm. **Figure 6** shows the measured waveform signal from the cement-concrete pavement slab with and without the flexible function layer. **Table 3** shows the comparison results for the measured vibration data from the pavement slab with and without the flexible function layer.

In this study, the declining rate = (maximum peak – attenuation peak)/maximum peak, representing the decline of the pavement slab. A bigger declining rate indicates that the declining effect is more significant. As

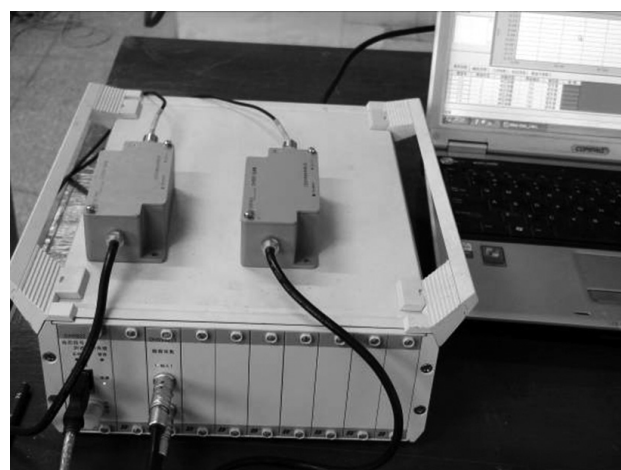


Figure 4: Dynamic signal test instrument
Slika 4: Preizkusna naprava za dinamične signale

Table 3: Measured vibration-data comparison table of the pavement slabs with and without a flexible function layer

Tabela 3: Primerjalna tabela izmerjenih vibracij na plošči pločnika z gibljivim funkcionalnim slojem in brez njega

Structure type of the pavement slab	Max peak (mm)	Min peak (mm)	Attenuation peak (mm)	Attenuation time (s)	Difference between the max and min peaks (mm)	Declining rate
Without a flexible function layer	0.227	-0.664	0.141	0.268	0.941	37.89 %
With a flexible function layer	0.140	-0.373	0.082	0.287	0.513	41.43 %

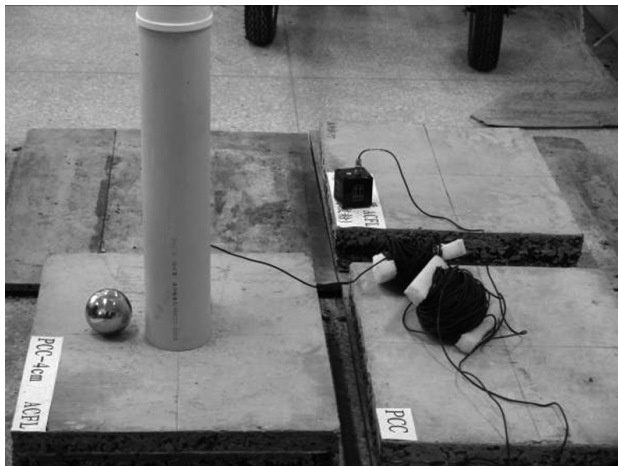


Figure 5: Steel ball and sleeve
Slika 5: Jeklena krogla in vodilo

can be seen in **Figure 6**, the time-domain curve of the vibration signal of the pavement slab under the load impact fluctuated in the following way: the vibration signal first achieved its maximum peak as the impact occurred, then decreased to its minimum value and eventually came close to zero through a declining process with several fluctuation cycles. The fluctuation showed that the vibration of a pavement slab under the load impact was a declining process.

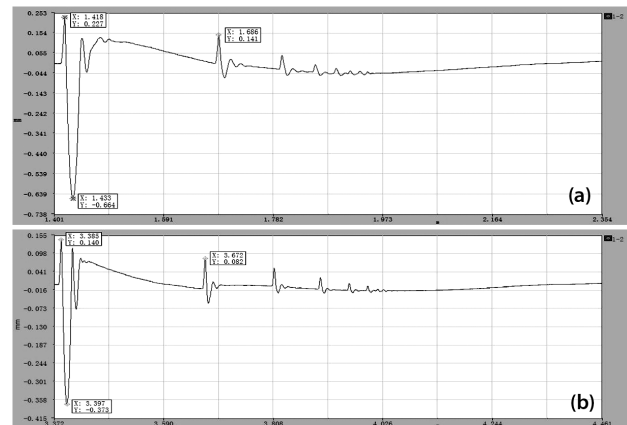


Figure 6: Time-domain waveform comparison diagram of the pavement slab with and without a flexible function layer: a) pavement structure without a flexible vibration-damping function layer, b) pavement structure with a flexible vibration-damping function layer

Slika 6: Primerjava časovnega poteka vala v plošči z gibljivim funkcionalnim slojem in brez njega: a) struktura pločnika brez gibljivega funkcionalnega sloja za dušenje vibracij, b) struktura pločnika z gibljivim funkcionalnim slojem za dušenje vibracij

As can be seen in **Table 3**, the addition of a flexible function layer decreased the maximum value of the vertical vibration response, the minimum absolute value of the vertical vibration response and the attenuation peak from (0.227, 0.664 and 0.141) mm to (0.140, 0.373

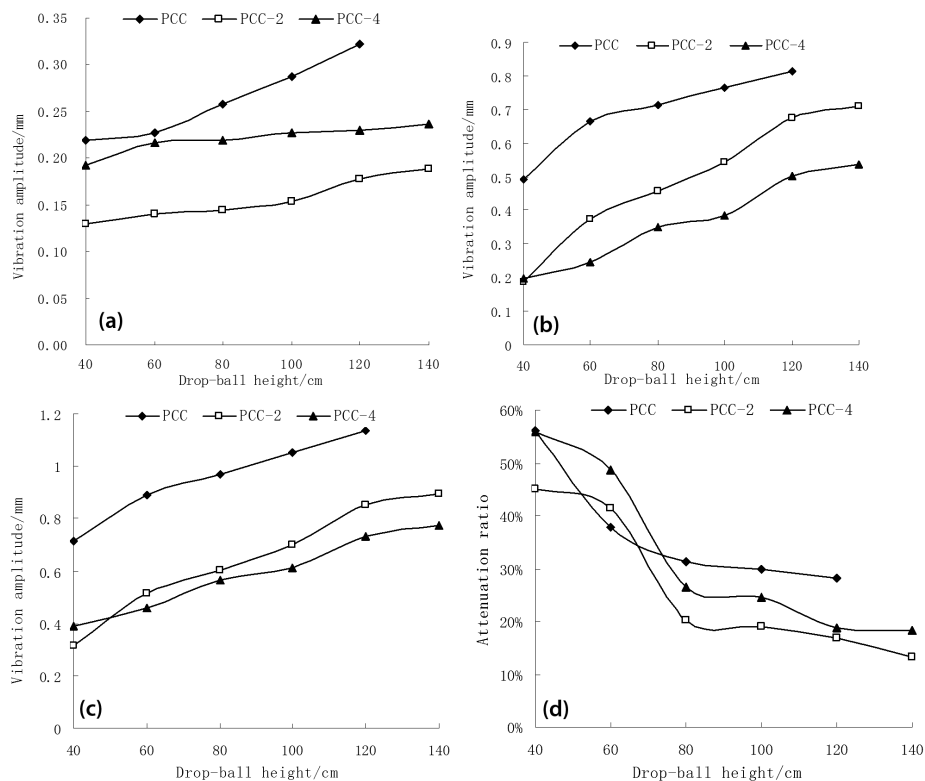


Figure 7: Vibration response variation diagram with changes in the thickness of the flexible function layer: a) the maximum peak, b) the absolute value of the minimum peak, c) the difference between the maximum and minimum peaks, d) attenuation value

Slika 7: Spreminjanje odziva na vibracije s spreminjanjem debeline gibljivega funkcionalnega sloja: a) maksimalne vrednosti, b) absolutne vrednosti minimuma, c) razlika med maksimalno in minimalno vrednostjo, d) vrednost dušenja

and 0.082) mm, respectively. Moreover, their amplitude reductions were 62.1 %, 78.0 % and 72.0 %, respectively. The difference between the maximum and minimum peaks of the pavement structure was reduced from 0.941 mm to 0.513 mm. Therefore, the addition of a flexible function layer in the cement-concrete pavement can efficiently reduce the vibration response of the pavement slab.

4.2 The variation rule of the vibration response with respect to the thickness of the flexible function layer

First, the magnetic-electric vibration sensor was placed onto the slab and then the pavement structure (PCC) was impacted from the ball-drop heights of (40, 60, 80, 100, 120 and 140) cm. We designed one pavement structure with a 2 cm flexible function layer (PCC-2) and another pavement structure with a 4 cm flexible function layer (PCC-4) to examine the effecting rule of the pavement-vibration responses of the flexible function layers with different thicknesses.

Figure 7 shows the images of the variation rule of the maximum peak, the absolute value of the minimum peak as well as the attenuation peak, the attenuation time, the difference between the maximum peak and the minimum peak and the declining rate of the vibration responses of the flexible function layers with different thicknesses. Since the pavement structure without a flexible function layer (PCC) was already broken under the ball drop from the height of 140 cm, only five data points were collected for the PCC curves on Figures 7a to d.

Figure 7a shows the variation diagram of the maximum peak of the pavement vibration response with respect to the changes in the thickness of the flexible function layer. As can be seen, the maximum peak of the vibration response increased when the ball-drop height was higher. Moreover, initially the maximum peak of the vibration response significantly decreased and later the

decrease became slower as the thickness of the flexible function layer increased.

The absolute value of the minimum peak of the vibration response increased with the increasing ball-drop height, but declined with the increase in the thickness of the flexible function layer, as shown in Figure 7b. Taking the 80 cm ball-drop height as an example, the absolute values of the vibration responses for PCC, PCC-2 and PCC-4 were (0.712, 0.457 and 0.348) mm, respectively. Compared with PCC, PCC-2 displayed a reduction of 35.8 %, and compared with PCC-2, PCC-4 displayed a reduction of 23.8 %.

The difference between the maximum and minimum values of the structure-vibration response increased with the increasing ball-drop height, but declined with the increase in the thickness of the flexible function layer, as shown in Figure 7c. In other words, initially the vibration amplitude reduced significantly with the increasing thickness, but became slower when a certain thickness was achieved.

The declining rate of the vibration response declined with the increasing ball-drop height, as shown in Figure 7d. Taking PCC-4 as an example, the declining rate decreased from 55.96 % to 18.22 % when the ball-drop height was gradually increased from 40 cm to 140 cm. Moreover, initially the declining rate reduced significantly with the increase in the ball-drop height, but the reduction later turned to be less significant.

4.3 Variation rule of the vibration response with respect to the change in the impact height

First, a magnetic-electric vibration sensor was placed onto the slab and then the test piece was impacted, with the ball-drop height set at (40, 60, 80, 100, 120 and 140) cm, to investigate the variation rule of the vibration response with respect to the changing ball-drop height.

Figures 8 to 10 show the variation curves for the ball-drop heights when the pavement structure was

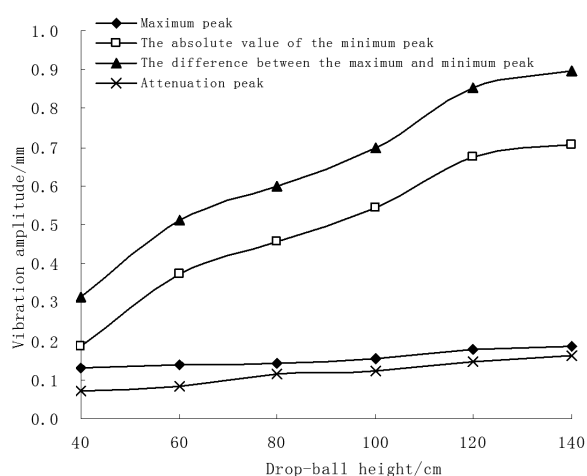


Figure 8: Variation rule of PCC vibration amplitude
Slika 8: Spreminjanje PCC-amplitude vibracij

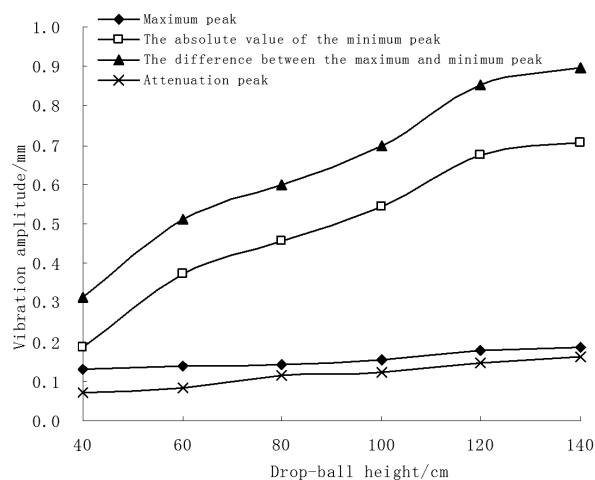


Figure 9: Variation rule of PCC-2 vibration amplitude
Slika 9: Spreminjanje PCC-2-amplitude vibracij

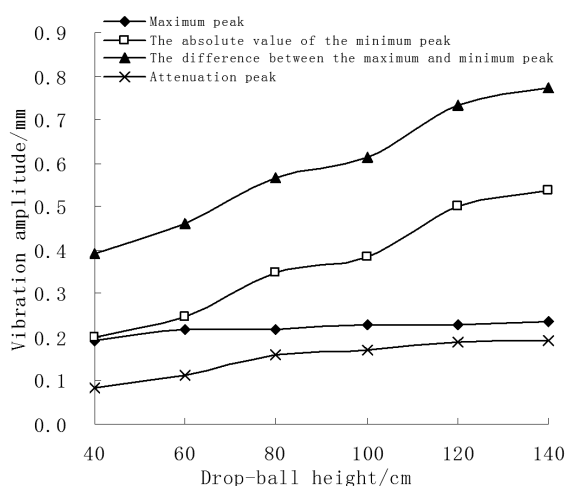


Figure 10: Variation rule of PCC-4 vibration amplitude

Slika 10: Spreminjanje PCC-4-amplitude vibracij

designed without a flexible function layer (PCC), with a 2 cm thick flexible function layer (PCC-2) and with a 4cm thick flexible function layer (PCC-4), respectively.

As can be seen in **Figures 8 to 10**, the vibration response amplitude assumed a linear growth trend with the increasing ball-drop height. Taking PCC-2 as an example, the maximum peak, the absolute value of the minimum peak, the difference between the maximum and minimum peaks and the attenuation peak increased from (0.129, 0.186, 0.315, and 0.071) mm to (0.188, 0.708, 0.896, and 0.163) mm, respectively, when the ball-drop height was increased from 40 cm to 140 cm. Moreover, the corresponding amplification rates were (0.0006, 0.0052, 0.0058 and 0.0009) mm/cm, respectively.

4.4 Analysis of the pavement-slab breakdowns

The pavement slab without a flexible function layer appeared to break down under the impact vibration of the steel ball when the ball-drop height was set to 140 cm, as shown in **Figure 11a**, whereas the pavement slab with a 2 cm thick flexible function layer remained unchanged, as shown in **Figure 11b**. These results show that the addition of a flexible function layer to a rigid pavement structure has a significant effect on the vibration damping and energy absorption and efficiently reduces the breakdowns caused to the pavement.

5 CONCLUSIONS

- 1) The pavement vibration under the impact load was a declining process. The measured vibration-waveform signals remained consistent, except for the occurrence of a significant variation in the vibration peak.
- 2) The maximum peak of the structure vibration response increased with an increase in the thickness of the flexible function layer. Initially, the vibration amplitude had larger reductions, but the reduction

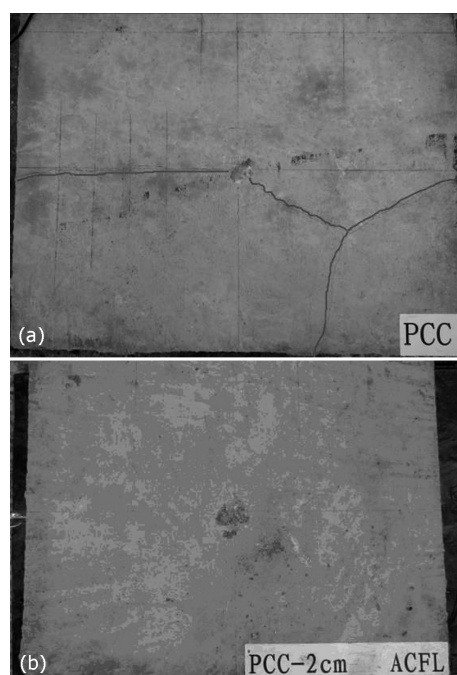


Figure 11: Crack comparison diagram of the pavement slab with and without flexible function layer: a) pavement structure without flexible vibration-damping function layer, b) pavement structure with flexible vibration-damping function layer

Slika 11: Primerjava slike razpok na plošči za pločnik z gibljivo funkcionalno plastjo in brez nje: a) struktura pločnika brez gibljivega fleksibilnega sloja za dušenje vibracij, b) struktura pločnika z gibljivim fleksibilnim slojem za dušenje vibracij

became slower when the flexible function layer achieved a certain thickness.

- 3) The vibration-response amplitude assumed a linear growth with the increasing ball-drop height.
- 4) The test results show that a flexible function layer has a significant effect on the vibration damping and energy absorption. The cement-concrete pavement structure with a flexible function layer can efficiently reduce the breakdowns and cracks to the pavement caused by the wheel-impact vibrations.

Acknowledgments

The project was supported by National Natural Science Foundation of China (51168005, 51268003), Key Project of Guangxi Science and Technology Lab Center (LGZX201107), Natural Science Foundation of Guangxi (2012GXNSFAA053205) and Foundation Project of Key Laboratory of Disaster Prevention and Engineering Safety of Guangxi (2012ZDX08).

6 REFERENCES

- ¹ Y. Ma, Experiment study and calculating analysis of insulating-layer cement concrete Pavement structure, Chongqing Communication University, China, 2004, 15–34
- ² H. Miao, Research on asphalt mixture functional layer for cement concrete pavement, Changan University, China, 2009, 36–62

- ³ Y. Jialiang, Y. Jianbo, Z. Qisen, Experimental study of emulsified wax curing agent and asphalt slurry seal as bond breaker media in cement concrete pavement, *China Civil Engineering Journal*, (2009) 10, 127–131
- ⁴ W. Xiangheng, Research on Interfacial Shearing Failure and Function Layer for Asphalt Pavement, Changan University, China, 2009, 36–43
- ⁵ The Ministry of Communications of the People's Republic of China, Technical Specifications for Construction of Highway Asphalt Pavements (JTG F40-2004), People's Communication Press, 2004
- ⁶ The Ministry of Communications of the People's Republic of China, Standard Test Methods of Asphalt and Asphalt Mixtures for Highway Engineering (JTJ 052-2000), People's Communication Press, 2000
- ⁷ ACI-544.2R-1989 Measurement of Properties of Fiber Reinforced Concrete, 1989

ABRASIVE WEAR BEHAVIOUR OF SiC_p-REINFORCED 2011 Al-ALLOY COMPOSITES

VEDENJE KOMPOZITA Al ZLITINE 2011, OJAČANE Z DELCI SiC_p, PRI ABRAZIJI

Mehmet Uzkut

Turgutlu Vocational School, Celal Bayar University, Manisa, Turkey
mehmet.uzkut@cbu.edu.tr

Prejem rokopisa – received: 2013-02-05; sprejem za objavo – accepted for publication: 2013-02-21

In this study, the abrasive wear behaviour of aluminium-alloy (Al-2011) SiC-particle-reinforced composites was investigated and compared with that of the matrix alloy. The experimental variables were the SiC-particle proportion, sliding distance and abrasive grit size. Al-2011 reinforced composites containing volume fractions (7, 14 and 21) % SiC_p were fabricated with the vortex method. Sliding-wear tests were carried out using a pin-on-disc abrasive-test machine where a sample slides against a SiC abrasive of different grit sizes at a fixed speed, under the load of 4 N at room conditions. The results show that the wear resistance of the composites was significantly larger than that of the Al-2011 alloy; it increased with the increasing SiC-particle proportion and decreased with the increasing abrasive grit size.

Keywords: abrasive wear, metal-matrix composites, vortex method, SiC particle

V tej študiji je bila preiskovana abrazijska obraba kompozita aluminijeve zlitine (Al-2011), ojačane z delci SiC in primerjana z osnovno zlitino. Eksperimentalne spremenljivke so bile: delež delcev SiC, dolžina drsenja in velikost zrn v drsni plošči. Kompoziti zlitine Al-2011 s prostorninskim deležem (7, 14 in 21) % SiC_p so bili izdelani po metodi vrtnca (vorteksa). Preizkusi abrazije so bili izvršeni na napravi "pin-on disc" za preizkus abrazije, kjer vzorec drsi po plošči iz SiC z različno velikostjo zrn, pri določeni hitrosti in obtežbi 4 N pri sobni temperaturi. Rezultati kažejo, da je obrabna odpornost kompozita veliko večja kot pri zlitini Al-2011 in narašča z naraščanjem vsebnosti SiC-delcev ter se zmanjšuje z večanjem zrn abrazijske plošče.

Ključne besede: abrazijska obraba, kompozit s kovinsko osnovo, metoda vortex, delci SiC

1 INTRODUCTION

Aluminium-matrix composites (AMCs) reinforced with ceramic particles exhibit better mechanical properties than unreinforced aluminium alloys^{1,2} and have been used as tribological parts in the automobile, defence and aerospace industries due to their excellent combination of higher specific strength and hardness, improved wear and higher elevated-temperature strength as compared with their base alloys.³ AMCs find potential applications in the automobile components like pistons, brake drums, cylinder liners, crankshafts, etc.⁴⁻⁶ These components showed sliding as well as abrasive wear against their counter surface during the treatment. Particulate-reinforced aluminium-alloy composites have shown a significant improvement in the tribological properties, including the abrasive-wear resistance.^{7,8} Therefore, considerable attention have been paid to the particulate AMCs with respect to tribological applications because of the advantages of AMCs such as good wear resistance, light weight and high load-carrying capacity. Some investigations show that these composites have a potential for being used in abrasive-wear conditions.⁹⁻¹² The high wear resistance of particulate-reinforced AMCs is a result of the ceramic-particle content, which considerably decreases the wear of the metal matrix. For the AMCs reinforced with ceramic particles, it has been commonly agreed that an increase in the particle content

increases the wear resistance.¹³⁻¹⁵ Accordingly, the application of SiC- or Al₂O₃-particle-reinforced AMCs in the automotive and aircraft industries is gradually increasing, used for connecting rods, cylinder heads, pistons, etc., where the tribological properties of the materials are vital.¹⁶

The investigations about this subject reveal that the wear resistance of the particle-reinforced composites is affected by many factors such as the applied load, particle size, particle content, sliding speed, sliding distance, hardness of particles and the properties of the matrix alloy.¹⁷ Consequently, the wear behaviour of the composites has not been fully established. The aim of the present work is to investigate the effect of the SiC-particle content, abrasive size, applied load and sliding distance on the wear behaviour of SiC-particle-reinforced 2011 aluminium-alloy composites.

2 EXPERIMENTAL WORK

2.1 Materials and characterization

In the present study, an Al-Cu alloy (Al-2011) and AMCs (Al-2011-SiC_p) containing varying amounts of SiC particles were used. The Al-2011 alloy contains about mass fractions 4 % Cu, 0.5 % Si, 0.7 % Mn, 0.7 % Mg and the rest is aluminium. The approximate size of SiC was 64 µm. The volume fractions of the SiC parti-

cles were (7, 14 and 21) %. AMCs were prepared with the vortex method. An unreinforced 2011 Al-matrix alloy specimen was also produced with the same method. **Table 1** shows the microstructural characteristics and properties of the tested materials.

Table 1: Microstructural characteristics and properties of the tested materials

Tabela 1: Mikrostrukturne značilnosti in lastnosti preizkušanih materialov

Sl. No.	Material (SiC in volume fractions)	Brinell hardness (BHN)	Density (g/cm ³)
1	Al-2011	97	2.748
2	Al-2011- 7 % SiC	109	2.803
3	Al-2011- 14 % SiC	120	2.858
4	Al-2011- 21 % SiC	125	2.913

The test specimens were prepared with the standard metallographic techniques for microstructural investigations. The samples were examined using a scanning electron microscope (SEM). A typical microstructure of 64 μm , 21 % volume fraction of SiCp-reinforced 2011 Al-alloy composite is shown in **Figure 1**.

2.2 Wear tests

In order to determine the wear behaviour of the composites and aluminum alloy, a pin-on-disc with a sandpaper device was used. A schematic representation of the abrasive-wear test is shown in **Figure 2**.

In this study, SiC sandpapers fixed on a rotating disc were used as the abrasive material. The specimens were loaded against the abrasive surface of the sandpaper with a bell-crank mechanism. Three groups of composites and the aluminum-matrix alloy were tested in the study. The wear tests were carried out at room temperature. The test specimens were abraded under the applied load of 4 N against the abrasive SiC sandpapers of (23, 36 and 52) μm . The cylindrical test specimens with a 6.35 mm diameter and 20 mm length were prepared. The total sliding distance was 600 m. The other test parameters were: the rotating speed of the disc was 350 r/min and the track diameter of the emery paper was 130 mm. Before each

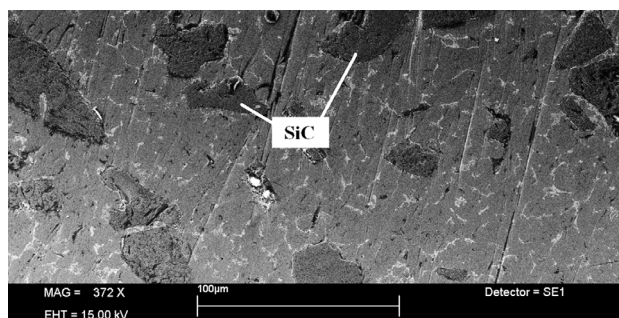


Figure 1: Microstructure of the volume fraction 21 % SiCp-reinforced 2011 Al-alloy composite with the size of 64 μm

Slika 1: Mikrostruktura kompozita zlitine Al 2011, ojačane z volumenskim deležem 21 % delcev SiC z velikostjo 64 μm

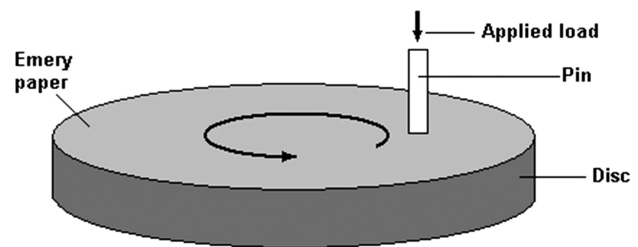


Figure 2: Schematic representation of the abrasive-wear test
Slika 2: Shematska predstavitev preizkusa abrazijske obrabe

test, the wear surface of a specimen was ground with the 500-grade abrasive paper, making sure that each of the specimens had the same contact area and surface roughness. A new abrasive paper was used for each of the tests. Before and after every test, the specimens were cleaned with acetone and then dried with a heat blower. An electronic balance with a sensitivity of 0.1 mg was used for measuring the weights of the pin specimens. Each test was performed four times. An outlier test result for each test group was removed and not included in the average calculation. Then the average of the tests was used. The wear weight losses were obtained from the weight differences for the specimens measured before and after the tests. Then, using the known densities of the Al-2011 and SiC, the wear volume losses of the specimens were calculated.

3 RESULTS AND DISCUSSION

Figure 3 shows the effect of the sliding distance on the wear volume loss of the composites with three

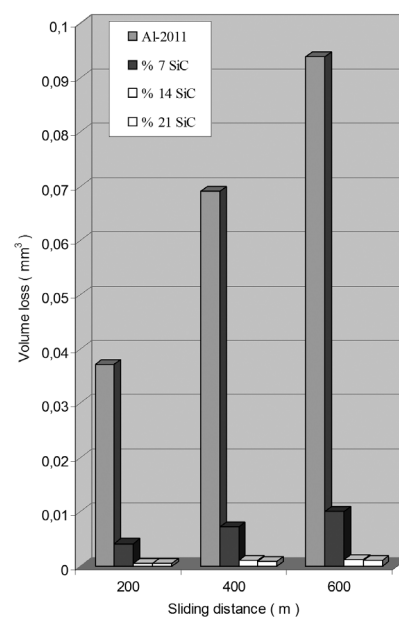


Figure 3: Volume loss as a function of the sliding distances of (200, 400 and 600) m, at 4 N, for the 52 μm SiC abrasive

Slika 3: Zmanjšanje volumna v odvisnosti od razdalje drsenja (200, 400 in 600) m pri 4 N po SiC-abrazivu z velikostjo zrn 52 μm

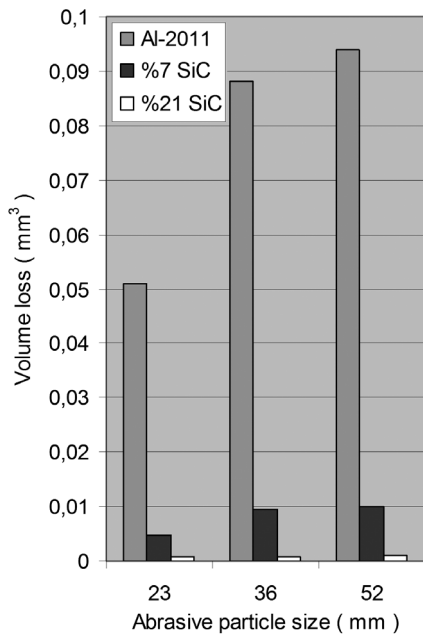


Figure 4: Fluctuation of the wear volume loss with the abrasive grit sizes at the sliding distance of 600 m

Slika 4: Spreminjanje volumna zaradi obrabe v odvisnosti od velikosti abrazijskih zrn pri razdalji drsenja 600 m

different SiC-particle contents and the matrix alloy. It reveals that the wear volume loss increases with the increasing sliding distance and decreases with the increasing SiC-particle content.¹⁸ The wear volume loss of the 2011 Al-alloy was much higher than that of the

composites in the experiment as shown in **Figure 3**. It rises about linearly with the sliding distance, while the volume loss of the composites rises only slightly. It can be inferred from the figure that for the 600 m sliding distance the approximate rates of increase in the wear resistance of the composite, in comparison with that of the 2011 Al-alloy, are 9.4, 76.6 and 92.9 for (7, 14 and 21) % volume fractions of fine SiC reinforcement, respectively. It shows that the wear resistance can be improved with an increase in the SiC content.¹⁹

The addition of only 7 % SiC particle to the 2011 Al-alloy was very effective at decreasing the wear volume loss. The reason for this is the fact that the SiC particles raised the hardness of the matrix alloy as shown in **Table 1**. It is clear from this table that the hardness of the composite increased due to the addition of the SiC particles. The wear volume loss of the composites reinforced with the SiC particles increased slightly with the increasing sliding distance. As shown in **Figure 3**, Al-2011-21 % SiC composite showed the lowest wear volume loss, while the highest wear volume loss was observed for the Al-2011-7 % SiC composite.

The correlation between the wear volume loss and the SiC abrasive grit size is given in **Figure 4**. The reinforcing SiC particles were very effective in increasing the wear resistance against the SiC abrasives of the emery. The wear volume loss of the composites was much smaller than that of the matrix alloy. In addition, the highest wear volume loss was obtained for the Al specimen with 7 % SiC against the emery with the 52 μm SiC abrasive. Adversely, the lowest wear volume loss was observed for the Al specimen with 21 % SiC used against the emery with the 23 μm SiC abrasive. Consequently, the two important parameters for the wear volume loss are the particle content and the abrasive grit size of the emery used.

The surface of the 2011 Al-alloy worn at an applied load of 4 N and against an abrasive with the size of 52 μm is shown in **Figure 5a**. It was defined by an intense plastic deformation and an explicit evidence of ploughing and cutting. A large amount of continuous wear grooves and the flakes present in some places along the grooves were observed on the worn surface. As the SiC abrasive of the emery was much harder than the unreinforced Al-2011 alloy, the abrasive could penetrate and cut the surface. Therefore, too much wear volume loss occurred as shown in **Figure 5a**. **Figure 5b** shows the worn surface of the 21 % SiCp-reinforced composite at an applied load of 4 N and the abrasive size of 52 μm . It represents the continuous wear grooves without any SiC particles. As the SiC particles have a very high wear resistance, they look like protrusions on the worn surface.²⁰ These protruded SiC particles resist the abrasive effect of the abrasive medium. Consequently, **Figure 5b** shows a larger wear volume loss on the Al-alloy region of the composite than on the reinforcement region of the composite.

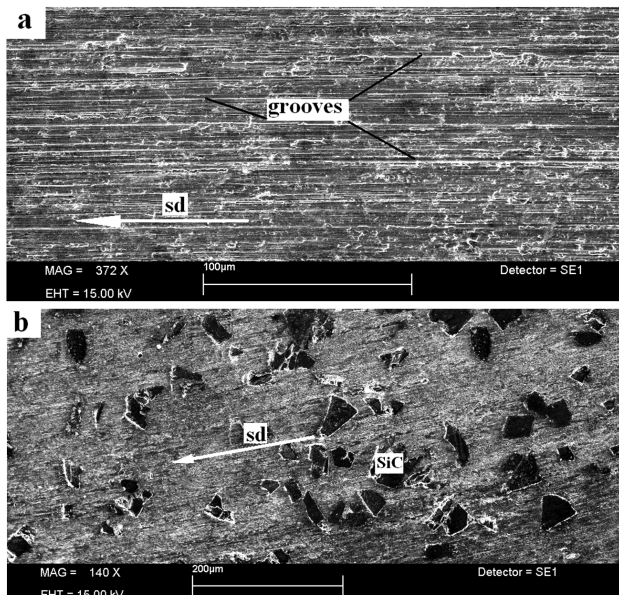


Figure 5: Surfaces worn against the 52 μm SiC abrasive at an applied load of 4 N and the sliding distance of 600 m: a) Al matrix alloy, b) volume fraction 21 % SiCp composite, sd: sliding direction

Slika 5: Obrabljeni površini pri SiC-abrazivu z velikostjo delcev 52 μm pri uporabi obtežbe 4 N in razdalji drsenja 600 m: a) osnovna Al-zlitina, b) kompozit z volumenskim deležem 21 % SiC delcev, sd: smer drsenja

One of the important factors of the investigated composites is the hardness impact on the wear mechanism. The SiC particles in a composite save the softer matrix during the abrasive sliding and make the composite harder. Consequently, due to the particle reinforcement only limited deformation occurred on the surface.

4 CONCLUSIONS

1. The wear resistance of the 2011 Al-alloy composites was much higher than that of the unreinforced 2011 Al-alloy.
2. The wear volume loss of the 2011 Al-alloy increased linearly with the increasing sliding distance. But the volume loss of the 2011 Al-alloy composites was much smaller than that of the 2011 Al-alloy.
3. The high wear resistance of the 2011 Al-alloy composites was largely dependent on the excellent wear resistance and high hardness of the SiC particles.
4. The SiC particles on the worn surfaces of the composites looked like protrusions due to their high hardness and wear resistance.
5. The wear resistance of the 2011 Al-alloy composites increased with the increasing SiC-particle content.
6. The wear resistance of the 2011 Al-alloy composites decreased with the increasing abrasive grit size of the emery used.

5 REFERENCES

- ¹ K. M. Shorovordi, A. S. M. A. Haseeb, J. P. Celis, Velocity effects on the wear, friction and tribochemistry of aluminum, MMC sliding against phenolic brake pad, *Wear*, 256 (2004), 1176–1181
- ² R. K. Uyyuru, M. K. Surappa, S. Brusethaug, Tribological behavior of Al-SiC-SiC_p composite/automobile brake pad system under dry sliding conditions, *Tribology International*, 40 (2007), 365–373
- ³ K. Shibata, H. Ushio, Tribological application of MMC_s for reducing engine weight, *Tribol. Int.*, 27 (1994), 39–41
- ⁴ R. Molins, J. D. Bartaut, Y. Beivenu, *Mater. Sci. Eng. A*, 135 (1991), 111
- ⁵ E. D. Nussbaum, *Light Metal Age*, 2 (1997), 54–57
- ⁶ T. Zenuer, P. Stojnov, H. Ruppert, A. Engels, *Mater. Sci. Technol.*, 14 (1998), 1857–63
- ⁷ T. L. Ho, M. B. Peterson, Wear formulation of aircraft brake material sliding against steel, *Wear*, 43 (1977), 199–210
- ⁸ M. K. Surappa, S. V. Prasad, P. K. Rohatgi, Wear and abrasion of cast Al-alumina particle composites, *Wear*, 77 (1982), 295–312
- ⁹ A. Banerji, S. V. Prasad, M. K. Surappa, P. K. Rohatgi, Abrasive wear of cast aluminium alloy-zircon particle composites, *Wear*, 82 (1982), 141–151
- ¹⁰ S. V. Prasad, P. K. Rohatgi, T. H. Kosel, Mechanisms of material removal during low stress and high stress abrasion of aluminum alloy-zircon particle composites, *Mater. Sci. Eng.*, 80 (1986), 213–220
- ¹¹ K. J. Bhansali, R. Mehrabian, Abrasive wear of aluminum matrix composites, *J. Met.*, 32 (1982), 30–34
- ¹² B. K. Prasad, S. V. Prasad, A. A. Das, Abrasion-induced micro structural changes and material removal mechanisms in squeeze-cast aluminum alloy-silicon carbide composites, *J. Mater. Sci.*, 27 (1992), 4489–4494
- ¹³ K. G. Basavakumar, P. G. Mukunda, M. Chakraborty, Dry sliding wear behavior of Al-12Si and Al-12Si-3Cu cast alloys, *Mater Des.*, 30 (2009) 4, 1258–1267
- ¹⁴ F. A. Davis, T. S. Eyre, The effect of silicon content and morphology on the wear of aluminum-silicon alloys under dry and lubricated sliding conditions, *Tribol. Int.*, 27 (1994), 171–181
- ¹⁵ A. Somi Reddy, B. N. Pramila Bai, K. S. S. Murthy, S. K. Bisvas, Wear and seizure of binary Al-Si alloys, *Wear*, 171 (1994), 115–127
- ¹⁶ S. V. Prasad, R. Asthana, Aluminum metal-matrix composites for automotive applications: tribological considerations, *Tribol. Lett.*, 17 (2004), 445–453
- ¹⁷ A. P. Sanmino, H. J. Rack, Dry sliding wear of discontinuously reinforced aluminum composites; review and discussion, *Wear*, 189 (1995), 1–19
- ¹⁸ B. N. Pramila Bai, B. S. Ramasesh, M. K. Surappa, Dry sliding wear of A356-Al-SiC_p composites, *Wear*, 157 (1992), 295–304
- ¹⁹ D. P. Mondal, S. Das, High stress abrasive wear behaviour of aluminium hard particle composites: Effect of experimental parameters, particle size and volume fraction, *Tribology International*, 39 (2006), 470–478
- ²⁰ V. K. Kant, B. N. Pramila Bai, S. K. Bisvas, Wear mechanism in a hyper-eutectic aluminum silicon alloy sliding against steel, *Scr. Metal. Mater.*, 24 (1990), 267–271

INFLUENCE OF WELD-PROCESS PARAMETERS ON THE MATERIAL CHARACTERIZATION OF THE FRICTION-STIR-WELDED JOINTS OF THE AA6061-T₆ ALUMINIUM ALLOY

VPLIV PARAMETROV POSTOPKA VARJENJA NA LASTNOSTI TORNO-VRTILNO VARJENIH SPOJEV ALUMINIJEVE ZLITINE AA6061-T₆

Hiralal Patil¹, Sanjay Soman²

¹Department of Mechanical Engineering, GIDC Degree Engineering College, Abrama-Navsari, India

²Department of Metallurgy & Material Engineering, Faculty of Engineering & Technology, M. S. University of Baroda, India
hspatil12@rediffmail.com, hspatil28@gmail.com

Prejem rokopisa – received: 2013-02-13; sprejem za objavo – accepted for publication: 2013-03-08

Friction-stir welding (FSW), a solid-state innovative joining technique, is being widely used for joining aluminium alloys for the aerospace, marine, automotive industries and many other applications of commercial importance. FSW trials were carried out using a vertical machining centre (VMC) on an AA6061 alloy. The main objective of the present work was to evaluate the weld-processing parameters of FSW for the AA6061-T₆ alloy and to determine the properties of the obtained joints with respect to the welding speed. The experiments were conducted by varying the welding speed between 55–70 mm/min and the rotating speed was fixed at 1700 r/min. The tensile properties, microstructure, microhardness, fractography and corrosion resistance of the FSW joints were investigated in this study. The result showed that there was a variation in the grain size in each weld zone depending upon the material and the process parameters of FSW in a joint. The coarsest grain size was observed in the heat-affected zone (HAZ), followed by the thermo-mechanically affected zone (TMAZ) and the nugget zone (NZ). The maximum tensile strength of 184 MPa and the highest joint efficiency of 49.32 % were obtained on the joint fabricated at the welding speed of 55 mm/min.

Keywords: friction-stir welding, AA6061 aluminium alloy, mechanical and metallurgical characterization, corrosion

Torno-vrtilno varjenje (FSW) je inovativna tehnika spajanja v trdnem stanju za spajanje aluminijevih zlitin za letalstvo, pomorsko, avtomobilsko industrijo in mnoge druge komercialno pomembne uporabe. FSW-preizkusi so bili izvedeni na vertikalnem obdelovalnem stroju (VMC) z zlitino AA6061. Glavni cilj tega dela je bila ocena varilnih parametrov pri FSW-postopku pri zlitini AA6061-T₆ in določitev lastnosti dobljenih spojev glede na hitrost varjenja. Preizkusi so bili izvršeni pri različnih hitrostih varjenja 55–70 mm/min, pri čemer je bila hitrost rotacije stalna pri 1700 r/min. V tej študiji so bile preizkušene natezna trdnost, mikrostruktura, mikrottrdota, fraktografija in korozijska odpornost FSW-spojev. Rezultati so pokazali, da se je v vsaki coni varjenja spreminjala velikost zrn, kar je posledica materiala in procesnih parametrov pri FSW-spoju. Najbolj groba zrna se opazi v toplotno vplivani coni (HAZ), sledi ji termomehansko vplivano področje (TMAZ) in drobnozrnato področje (NZ). Največja natezna trdnost 184 MPa in največja učinkovitost spajanja 49,32 % sta bili doseženi pri spoju s hitrostjo varjenja 55 mm/min.

Ključne besede: torno-vrtilno spajanje, aluminijeva zlitina AA6061, mehansko-metalurška karakterizacija, korozija

1 INTRODUCTION

AA6061-T₆ alloys are high-strength aluminium (Al), magnesium (Mg) and silicon (Si) alloys containing manganese to increase their ductility and toughness. The alloys of this class are readily weldable, but they suffer from a severe softening in the heat-affected zone (HAZ) because of the dissolution of the Mg₂Si precipitates during the thermal cycle. It is therefore appropriate to overcome or minimize the HAZ softening with respect to the fusion welding in order to improve the mechanical properties of a weldment.¹ In addition, a poor solidification microstructure and porosity in the fusion zone should also be overcome. Compared to many of the fusion-welding processes that are routinely used for joining structural alloys, friction-stir welding (FSW) is an emerging solid-state joining process, in which the material that is being welded does not melt and recast.

FSW is a solid-state process based on plastic deformation. FSW is a continuous, hot-shear, autogenous process involving a non-consumable rotating tool of a material harder than the substrate material. Defect-free welds with good mechanical properties have been made of a variety of aluminium alloys, even those previously thought not to be weldable. When alloys are friction-stir welded, the phase transformations occurring during the cooling down of a weld are of a solid-state type. Due to the absence of the parent-metal melting, the new FSW process is found to have several advantages over the fusion welding.^{2–4} In this process a special pin/slug rotating at a high speed penetrates to the centre of the two pieces to be joined. The heat generated through friction makes the material soften into a paste-like phase (plasticize).⁵ Plastic deformation causes the edges of the material to mix together and fuse, hence the term "fric-

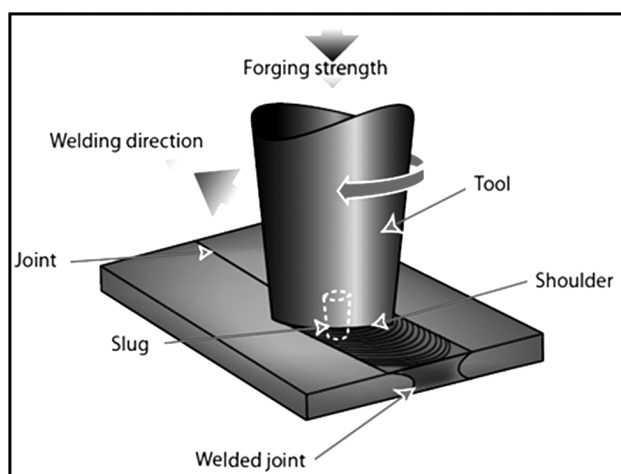


Figure 1: Principle of the FSW process

Slika 1: Princip FSW-postopka

tion-stir weld". The presence of a retaining wall exerts sufficient force to prevent the semi-molten mixture from flowing out of the joint area. This creates a press forging effect behind the material which has been softened and mixed. Welding by plastic deformation is the technique of choice when maintaining the original properties of the metal is all-important. Since the tool heats the material to a paste-like consistency, and not the liquid state, the properties of the material are not degraded to the same degree as they are when fusion occurs. **Figure 1** explains the working principle of the FSW process.

FSW has a quality advantage of making the weld strength and ductility either identical or better than those of the base-metal alloy.⁶ The tensile strength of FSW welds is directly proportional to the welding speed.⁷ Friction-stir processing (FSP) is a new microstructural modifications technique. FSP has become an efficient tool for homogenizing and refining the grain structure of a metal sheet. The tensile strength of the friction-stir welds is affected by the weld parameter. The grain structure within the friction-stir processing is fine and equiaxed compared to TMAZ.⁸ An optimization of the FSW parameters in different conditions of a base material and the microstructures of the as-welded condition are compared with the post-weld heat-treated microstructures welded in the annealed and T_6 condition.⁹ FSW joints usually consist of four different regions as shown

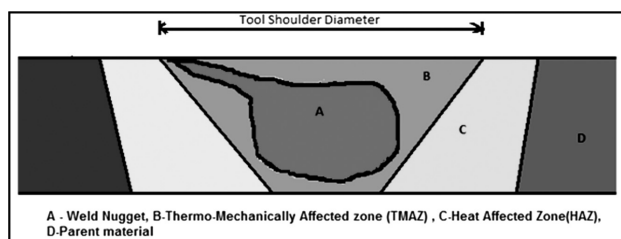


Figure 2: Different regions of a FSW joint

Slika 2: Različna področja v FSW-spoju

in **Figure 2**. They are: A-weld nugget (WN), B-thermo-mechanically affected zone (TMAZ), C-heat-affected zone (HAZ) and D-parent material (PM). The formation of the above regions is affected by the material flow behaviour under the action of rotating a non-consumable tool.¹⁰ However, the material flow behaviour is predominantly influenced by the FSW tool profiles, FSW tool dimensions and FSW process parameters.^{11,12}

The weld zones are more susceptible to corrosion than the parent metal.¹³⁻¹⁸ Generally, it has been found that friction-stir (FS) welds of aluminium alloys such as 2219, 2195, 2024, 7075 and 6013 did not exhibit an enhanced corrosion of the weld zones. FSWs of aluminium alloys exhibit intergranular corrosion mainly located along the nugget's heat-affected zone (HAZ) enhanced by the coarsening of the grain-boundary precipitates. Coarse precipitates and wide precipitate-free zones promoted by the thermal excursion during the welding are correlated with the intergranular corrosion. The effect of the FSW parameters on the corrosion behavior of friction-stir welded joints was reported by many researchers.^{16,18} The effect of the processing parameters such as the rotation speed and traverse speed on the corrosion behavior of the friction-stir processed, high-strength, precipitation-hardenable AA2219-T87 alloy was investigated by Surekha et al.¹⁸ The available literature focuses on the effect of tool profiles and tool shoulder diameter on the FSW zone formation. Hence, in this investigation an attempt has been made to understand the effect of the welding speed on the material characterization of AA6061 in terms of mechanical properties, metallurgical behaviour and corrosion analysis. This paper presents the effects of different welding speeds on the weld characteristics of AA6061- T_6 fabricated with a hexagonal tool-pin profile. The weld characteristics include UTS, YS and a fraction of elongation, microhardness, fractography, microstructure and corrosion of AA6061- T_6 joints.

2 EXPERIMENTAL DETAILS AND PROCESS CONDITIONS

The rolled plates with a thickness of 5 mm, made of AA6061 aluminium alloy, were cut into the required shapes (300 mm × 150 mm) by power hacksaw cutting and grinding. The chemical composition and mechanical properties of the parent metal are presented in **Table 1**. A square-butt joint configuration was prepared to fabricate the FSW joints. The initial joint configuration was obtained by securing the plates in the position using mechanical clamps. The direction of welding was normal to the rolling direction. The single-pass welding procedure was adopted to fabricate the joints. In the present work a hexagonal, tool-pin profile was used for the welds, made of cold-work die steel (**Figure 3**). The machine used for the production of the joints was a vertical machining centre.

Table 1: Chemical composition and mechanical properties of AA6061-T₆**Tabela 1:** Kemijska sestava in mehanske lastnosti AA6061-T₆

Chemical composition								
Element	Si	Fe	Cu	Mn	Mg	Cr	Zn	Ti
Content	0.62	0.45	0.2	0.18	1.05	0.09	0.03	0.07
Mechanical properties								
Tensile strength (MPa)		Yield strength (MPa)		Elongation (%)		Hardness (HV)		
Min	Max	Min	Max	Min	Max			
300	–	241	–	6	–	95		
328.57	335.71	282	296	11	11.8	98		

**Figure 3:** Geometry of the hexagonal tool-pin profile used in the present study**Slika 3:** Geometrija šestokotne konice, uporabljene pri preiskavah

The welding parameters and tool dimensions are presented in **Table 2**. The welded joints were sliced, using a pantograph machine, to the required dimensions to prepare the tensile specimens. American Society for Testing of Materials (ASTM E8-04) guidelines were followed when preparing the test specimens. The tensile test was carried out in a 400 kN capacity, mechanically controlled, universal testing machine.

Table 2: Welding conditions employed to join the AA6061 plates**Tabela 2:** Pogoji varjenja, uporabljeni pri spajanju AA6061-plošč

Weld process parameter	Value
Rotational speed (r/min)	1700
Welding speed (mm/min)	55, 60, 65, 70
Tool depth (mm)	4.6
Tool shoulder diameter (mm)	18
Tilt angle (degree)	0
Hexagonal shape (mm)	6

All the welded samples were visually inspected to verify a presence of possible macroscopic external defects, such as surface irregularities, excessive flash and surface-open tunnels. By using a radiographic unit, an X-ray radiographic inspection was carried out on the FSW samples. For the radiographic test, ⁶⁰Co & Ir192 were used as a radioactive source. The film used was Agfa D-4 and the radiographic films indicated a defect-free weld as well as a weld with defects like insufficient fusion and cavity.

The mechanical properties of the test welds were assessed with the tensile tests; the ultimate tensile stress (UTS), yield strength (YS) and the fraction of elongation

were also measured with the tensile test. The micro-indentation hardness test as per ASTM E-384:2006 was used to measure the Vickers hardness of the FSW joints. The Vickers micro-hardness indenter is made of diamond in the form of a square-based pyramid. The test load applied was 100 g and the dwell time was 15 s. The indentations were made in the midsections of the plates, across the joint. The tensile-fracture surfaces were analyzed using scanning electron microscopy.

The metallographic specimens were cut out mechanically from the welds, embedded in resin and mechanically ground and polished using abrasive disks and cloths with a water suspension of diamond particles. The chemical etchant was the Keller's reagent. The microstructures were observed with an optical microscope.

Potentiodynamic polarization tests were used to study the pitting corrosion behavior of AA6061 alloys. In the tests, the cell-current readings were taken during a short, slow sweep of the potential. The sweep was taken in the range of 0.5 V to 1 V. The potentiodynamic scan was performed at the scan rate of 0.5 mV/s.

3 RESULT AND DISCUSSION

3.1 Mechanical properties

The mechanical and metallurgical behavior of AA6061 was studied in this research. The transverse tensile properties of FSW joints such as yield strength, tensile strength, percentage of elongation and joint efficiency are presented in **Figure 4**. The strength and ductility in the as-welded condition are lower than in the case of the parent metal in the T₆ condition.

The heat input in the weld area is affected by the welding conditions like the welding speed and rotational speed. At a constant rotational speed of 1700 r/min (**Figure 5**), a higher welding speed resulted in a lower heat input per unit length of the weld, causing a lack of stirring in the friction-stir processing zone and poor tensile properties. A lower welding speed resulted in a higher temperature and a slower cooling rate in the weld zone causing grain growth and precipitates. Most of the joint fractures at the retreating side are due to the variation in the temperature distribution and the flow of the material in the weld zone with the corresponding hardness distribution and strained region. It can be observed that the flows of the parent material on the

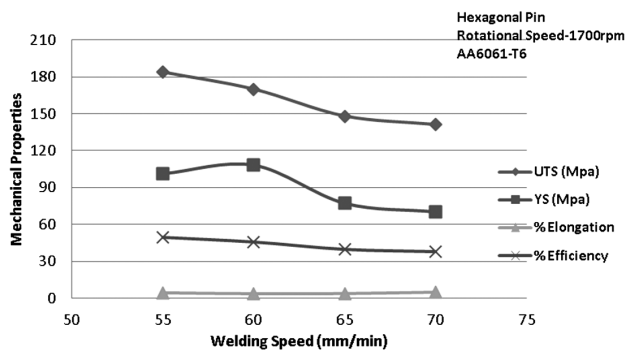


Figure 4: Effect of the welding speed on the mechanical properties of AA6061-T₆

Slika 4: Vpliv hitrosti varjenja na mehanske lastnosti AA6061-T₆

advancing side and the retreating side are different. The material on the retreating side never enters the rotational zone, but the material on the advancing side forms a fluidized bed near the pin and rotates around it (**Figure 6**). The downward (axial) force was found to be independent of the process parameter values for this experimental-data set, providing the position control. It has been observed that the axial force is a quality indicator for friction-stir welds. An insufficient axial force indicates a lack of the shoulder pressure and can also indicate a lack of the containment of the surface flash and/or voids.

During FSW the heat is assumed to be produced mainly through the friction between the tool shoulder and the plate surface. Therefore, the heat is no longer concentrated to a narrow line, but is generated across a broad band having the width of the tool shoulder. Hence, the tangential velocity of the rotating tool-shoulder surface is high at the periphery; the strongest temperature gradients are not expected to be found in the weld line but at the edges of the shoulder resulting in a thermal softening. The location of the soft band is at the retreating side, where the over-aging precipitates cause a failure in this region. Hence, the welding speed must be optimized to get an FSP region with fine precipitates uniformly distributed throughout the matrix. Of the four

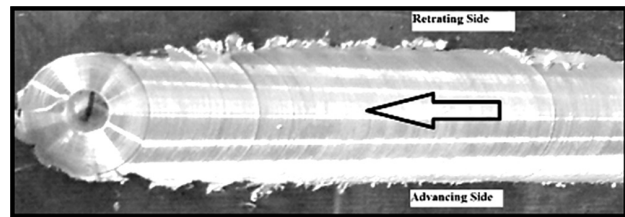


Figure 6: Friction-stir welded joint of AA6061-T₆

Slika 6: Torno-vrtilni varjeni spoj AA6061-T₆

different welding speeds (55–70 mm/min), the joints fabricated at the welding speed of 55 mm/min exhibited superior tensile properties – the ultimate tensile strength of 184 N/mm² and the joint efficiency of 49.32 %. The combined effect of a higher number of the pulsating, stirring actions during the metal flow and an optimum welding speed may be the reason for the superior tensile properties of the joint fabricated at a welding speed of 55 mm/min using a hexagonal, pin-profiled tool (**Figures 4 and 5**).

In FSW, microhardness also reflects the state of the precipitates within the weld nugget (WN) since the alloy composition is fixed and the changes in the microhardness must result primarily from the changes in the precipitates and the grain size. The microhardness plots for the welds of the AA6061 alloy performed with different welding speeds can be seen in **Figure 7**. The results show that the friction-stir-processed area has an equivalent Vickers hardness value with respect to the parent material.

3.2 Metallographic analysis

Based on the optical microstructural characterization of the grains and precipitates, three distinct zones were identified: the weld-nugget zone, the thermo-mechanically affected zone (TMAZ) and the heat-affected zone (HAZ). Microstructural details of the parent metals (PM) and similar joints are presented in **Figures 8 to 10**. The parent material revealed grains of unequal sizes and was found to be distributed in the matrix with the grains tending to be rather elongated. The frictional heat pro-

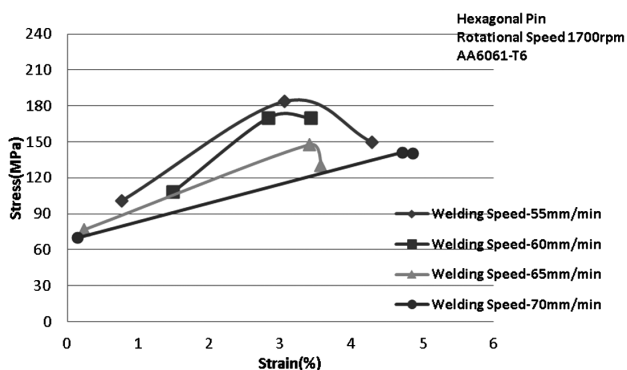


Figure 5: Engineering stress-strain curves for AA6061-T₆ with a hexagonal pin

Slika 5: Inženirske krivulje napetost – raztezek za AA6061-T₆ pri šestkotni konici

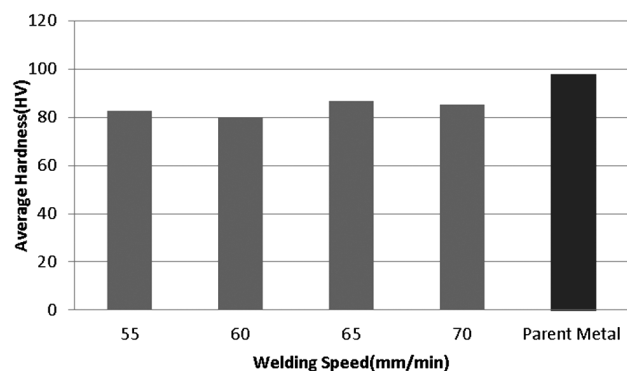


Figure 7: Effect of the welding speed on the microhardness of AA6061-T₆

Slika 7: Vpliv hitrosti varjenja na mikrotrdoto AA6061-T₆

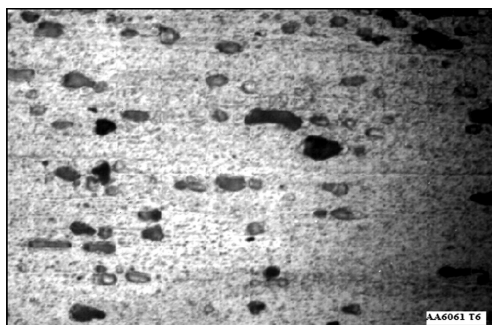


Figure 8: Optical micrograph of the AA6061 parent metal
Slika 8: Mikrostruktura osnovnega materiala AA6061

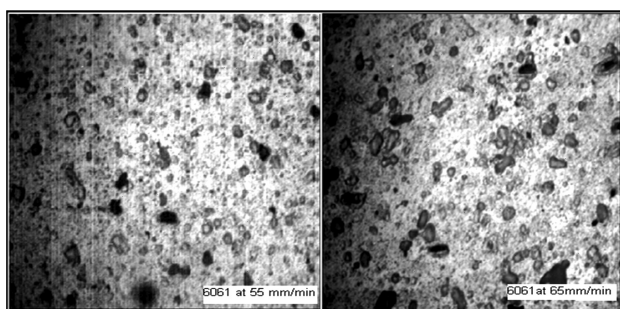


Figure 9: Optical micrograph of AA6061 at 55 mm/min and 65 mm/min

Slika 9: Mikrostruktura spoja AA6061 pri 55 mm/min in 65 mm/min

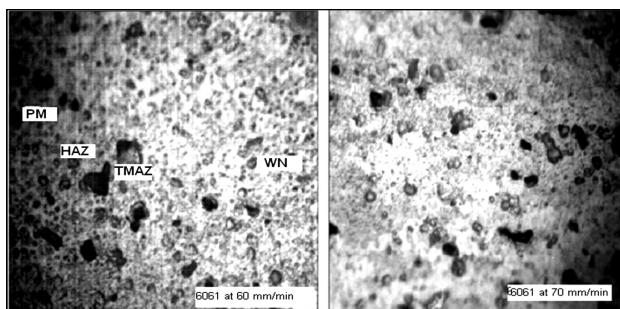


Figure 10: Optical micrograph of AA6061 at 60 mm/min and 70 mm/min

Slika 10: Mikrostruktura spoja AA6061 pri 60 mm/min in 70 mm/min

vided by the rubbing of the tool shoulder and the mechanical stirring of the material by the tool nib, and the adiabatic heat arising from the deformation induced a dynamic recrystallization, showing a transition of aluminium from the parent material to the FSW zone with a clean decrease in the grain size.

3.3 Fractography analysis

An examination of the tensile-fracture surfaces of AA6061 was done at low magnification as well as at higher magnification in order to identify the fracture mechanisms. The SEM observations of the fracture surfaces of the tensile-test specimens revealed the best bonding characteristics of the FSW joints. The fracture surface was found to have very fine dimples revealing a

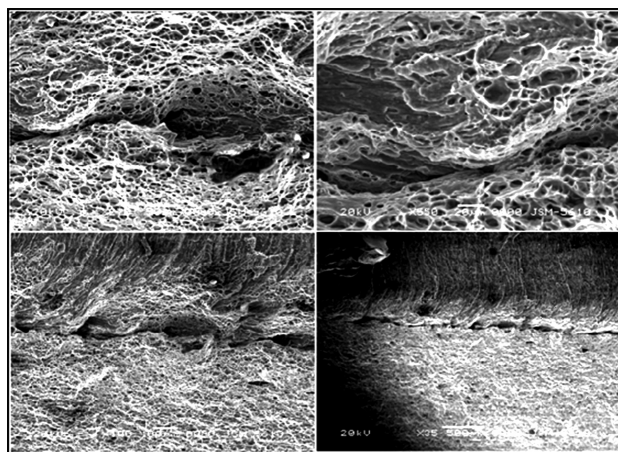


Figure 11: SEM images of the tensile-fracture surface of AA6061 at 65 mm/min

Slika 11: SEM-posnetki preloma pri natezni obremenitvi AA6061 pri 65 mm/min

very ductile behaviour of the material before the failure as shown in **Figure 11**.

3.4 Corrosion behaviour

The potentiostatic polarization curves for the base alloy and FSW samples in 3.5 % NaCl at room temperature are given in **Figures 12** and **13**. It is shown that the corrosion behavior of the parent alloy significantly differs from that of the welded joints.

Table 3: Result analysis of the corrosion test

Tabela 3: Rezultati pri korozijskih preizkusih

Material of the FSW joint	Welding speed (mm/min)	$I_{corr}/(\mu A/cm^2)$	E_{corr}/mV	Corrosion rate (mpy)
6061T ₆ -6061T ₆	55	471 nA/cm ²	-841	215.3 E ⁻³
6061T ₆ -6061T ₆	60	202.0 nA/cm ²	-789	92.23 E ⁻³
6061T ₆ -6061T ₆	65	3.34	-1.35V	1.526
6061T ₆ -6061T ₆	70	1.35	-1200	617.7 E ⁻³
PM AA6061T ₆	—	1.820	-1160	832.1 E ⁻³

From **Table 3** it is clear that the pitting potentials of the corrosion-test samples at various process parameters indicate a greater corrosion resistance of the weld metal than of the base metal. This is attributed to the precipitates present in the alloy promoting the matrix dissolution through a selective dissolution of aluminium from the particles. These precipitate deposits are highly cathodic compared to the metallic matrix, initiating the pitting on the surrounding matrix and also enhancing pit growth. During the FSW process only the coarse precipitates could nucleate and grow but not the finer ones. This supported the formation of a passive film, which remained more intact on the surface of the sample. It is also found that in AA6061 and at 65 mm/min, the corrosion resistance is very poor. The poor pitting-corrosion resistance of a weld joint is due to a difference in the pitting potentials across the weld region, or the stir

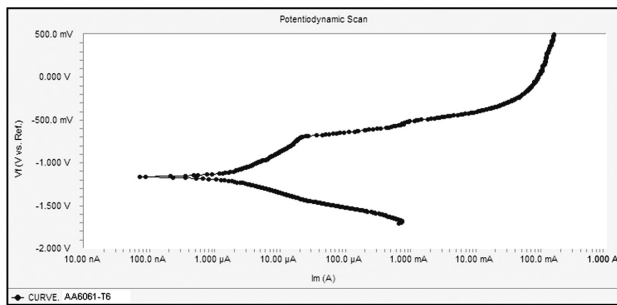


Figure 12: Polarization curves of the AA6061-T6 parent metal
Slika 12: Polarizacijska krivulja osnovne zlitine AA6061-T6

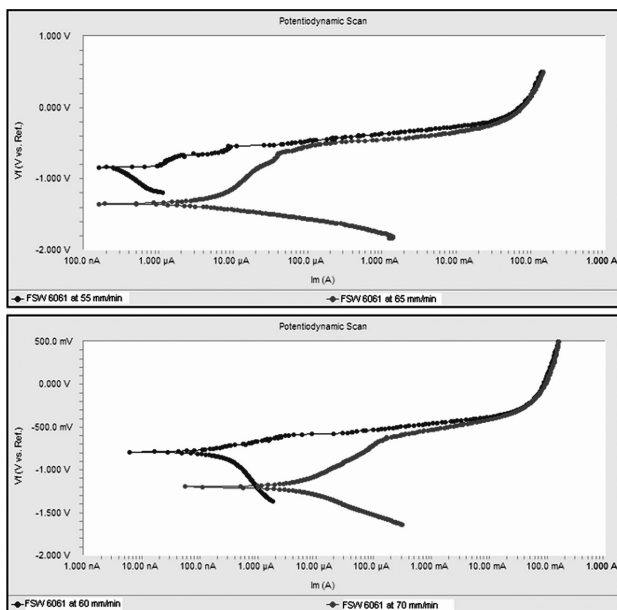


Figure 13: Polarization curves of AA6061 at the welding speeds of 55–70 mm/min
Slika 13: Polarizacijske krivulje AA6061 pri hitrostih varjenja 55–70 mm/min

nugget, caused by the inhomogeneity of the microstructures in these regions. All the FSW samples show a passivation after a longer time of an exposure to the corrosion media. At 65 mm/min, AA6061 has the highest active potential (−1.35 V). The active E_{corr} increased with the increasing weld speed.

4 CONCLUSIONS

The mechanical and metallurgical behavior of AA6061 was studied in this paper. The joints were produced at different welding speeds from 55 mm/min to 70 mm/min and the constant rotational speed of 1700 r/min. The downward force was observed to be constant at 11 kN and it was found to be independent of the weld process parameter for all the produced joints. The tensile strength of a FSW joint is lower than that of the parent metal. With an increase in the welding speed above the critical value, the tensile strength and the fraction of elongation decrease due to a low heat input at the constant downward pressure and the tool rotational speed.

Of the four different welding speeds (55–70 mm/min), the joints fabricated at the welding speed of 55 mm/min exhibited superior tensile properties of 184 N/mm² (UTS) and the joint efficiency of 49.32 %. The microstructural changes induced by the FSW process were clearly identified in this study. FSW of AA6060-T₆ resulted in dynamically recrystallized zones, TMAZ and HAZ. A softened region has clearly occurred in the friction-stir-welded joints, due to dissolution of the strengthening precipitates. The fracture surface appears to have very fine dimples revealing a very ductile behaviour of the material before the failure. The corrosion rate is increased by increasing the welding speed of the FSW tool.

5 REFERENCES

- K. Elangovan, V. Balasubramanian, S. Babu, Predicting tensile strength of friction stir welded AA6061 aluminium alloy joints by a mathematical model, *Materials and Design*, 30 (2009), 188–193
- W. M. Thomas et al., Friction stir welding, International Patent Application, No. PCT/GB92/02203 and GB Patent Application No. 9125978.8, December 1991, US Patent No. 5,460,317, 1991
- P. L. Threadgill, Friction stir welding – The state of the art, TWI, Bulletin 678, UK, 1999
- M. Peel, A. Steuwer, M. Preuss, P. J. Withers, Microstructure, mechanical properties and residual stresses as a function of welding speed in AA5083 friction stir welds, *Acta Mater*, 51 (2003), 4791–801
- R. S. Mishra, Z. Y. Ma, Friction stir welding and processing, *Materials Science and Engineering: R: Reports*, 50 (2005), 1–78
- N. Li, T. Y. Pan, R. P. Cooper, D. Q. Houston, Z. Feng, M. L. Santella, FSW of magnesium alloy AM60, 19 *Magnesium Technology 2004*, Edited by A. A. Luo, TMS (The Minerals, Metals & Materials Society), 2004
- J. Adamowski, M. Szkodo, Friction Stir Welds (FSW) of aluminum alloy AW6082-T6, *Journal of Achievement in Materials and Manufacturing Engineering*, 20 (2007) 1–2, 403–406
- R. Palanivel, P. Koshy Mathews, N. Murugan, Influences of tool pin profiles on the mechanical and metallurgical properties of FSW of dissimilar alloys, *International Journal of Engineering Science and Technology*, 2 (2010) 6, 2109–2115
- M. Indira Rani, R. N. Marpu, A. C. S. Kumar, A study of process parameters of friction stir welded AA 6061 aluminum alloy in O and T6 conditions, *ARPJ Journal of Engineering and Applied Sciences*, 6 (2011) 2, 61–66
- L. E. Murr, R. D. Flores, O. V. Flores, J. C. McClure, G. Liu, D. Brown, Friction-stir welding: microstructural characterization, *Mater Res Innov.*, 1 (1998) 4, 211–23
- H. Liu, H. Fujii, M. Maeda, K. Nogi, Heterogeneity of mechanical properties of friction stir welded joints of 1050-H 24 aluminium alloy, *J. Mater. Sci. Lett.*, 22 (2003), 441–4
- H. J. Liu, H. Fujii, M. Maeda, K. Nogi, Mechanical properties of friction stir welded joints of 1050-H 24 aluminium alloy, *Sci. Technol. Weld Join*, 8 (2003) 6, 450–4
- C. S. Paglia, K. V. Jata, R. G. Buchheit, A cast 7050 friction stir weld with scandium: microstructure, corrosion and environmental assisted cracking, *Material Science Engineering- A*, 424 (2006), 196–204
- R. W. Fonda, P. S. Pao, H. N. Jones, C. R. Feng, B. J. Connolly, A. J. Davenport, Microstructure, mechanical properties, and corrosion of friction stir welded Al 5456, *Material Science Engineering- A*, 519 (2009), 1–8
- D. A. Wadson, X. Zhou, G. E. Thompson, P. Skeldon, L. Djapic Oosterkamp, G. Scamans, Corrosion behaviour of friction stir

welded AA7108 T79 aluminium alloy, *Corrosion Science*, 48 (2006), 887–897

¹⁶ M. Jariyaboon, A. J. Davenport, R. Ambat, B. J. Connolly, S. W. Williams, D. A. Price, The effect of welding parameters on the corrosion behaviour of friction stir welded AA2024–T351, *Corrosion Science*, 49 (2007), 877–909

¹⁷ P. S. Pao, S. J. Gill, C. R. Feng, K. K. Sankaran, Corrosion-fatigue crack growth in friction stir welded Al 7075, *Scripta Materiala*, 45 (2001), 605–612

¹⁸ K. Surekha, B. S. Murty, R. K. Prasad, Effect of processing parameters on the corrosion behaviour of friction stir processed AA2219 aluminium alloy, *Solid State Sciences*, 11 (2009), 907–91

COMPOSITIONAL AND MICROSTRUCTURAL ANALYSES OF Fe-Pd NANOSTRUCTURED THIN FILMS

ELEMENTNA IN MIKROSTRUKTURNA ANALIZA NANOSTRUKTURNIH TANKIH PLASTI Fe-Pd

Zoran Samardžija, Kristina Žužek Rožman, Darja Pečko, Spomenka Kobe

Jožef Stefan Institute, Department for Nanostructured Materials, Jamova cesta 39, 1000 Ljubljana, Slovenia
zoran.samardzija@ijs.si

Prejem rokopisa – received: 2013-02-15; sprejem za objavo – accepted for publication: 2013-03-19

Fe-Pd thin films with various compositions and thicknesses were produced with electrodeposition using the constant potentials from -1.0 to -1.3 V. The FEGSEM and AFM analyses revealed a smooth, nanostructured surface morphology of the films, with more granular features appearing at more negative potentials. The high-resolution FEGSEM images of the film cross-sections and complementary calculations using the data from the EDS thin-film analyses were used to determine the film thicknesses, showing that ultrathin films 50 nm to 120 nm were obtained. The chemical compositions of the films were measured with a quantitative, EDS electron-probe microanalysis using two independent approaches: (i) a low-voltage analysis (LVEDS) and (ii) a variable-voltage analysis with a dedicated thin-film-analysis (TFA) method. Both approaches were properly modified and optimized on the basis of the Monte Carlo simulation data. The results showed that the composition of the Fe-Pd films was close to the preferred equiatomic $\text{Fe}_{50}\text{Pd}_{50}$ stoichiometry (which is important for achieving good magnetic properties) and was obtained at -1.3 V and -1.2 V. At the more positive potentials, the Fe-Pd films became Pd rich. The best agreement between the LVEDS and TFA quantitative results was achieved for the Fe-Pd films that were thicker than 80 nm, and a slight discrepancy within the ± 10 % relative between the LVEDS and TFA values was observed for the films thinner than 70 nm. The faster LVEDS approach is suitable for routine analyses of numerous Fe-Pd samples, to obtain the information about a film composition in a short time. The more demanding TFA approach was found to be very appropriate for accurate compositional analyses of the Fe-Pd ultrathin films and for determining the film thickness.

Keywords: Fe-Pd films, electron-probe microanalysis, FEGSEM, EDS, AFM

Tanke plasti na osnovi zlitine Fe-Pd z različno sestavo in debelino smo pripravili z metodo elektronanosa pri konstantnih potencialih od $-1,0$ V do $-1,3$ V. S FEGSEM- in AFM-preiskavami morfologije smo ugotovili, da je površina plasti gladka in sestavljena iz nanodelcev, katerih velikost narašča z uporabo bolj negativnih potencialov. Debelino plasti smo določili iz visokoločljivostnih FEGSEM-posnetkov prereзов plasti in dodatno z izračuni na osnovi podatkov iz EDS-analiz. Sintetizirane plasti Fe-Pd so imele debelino med 50 nm in 120 nm. Kemijsko sestavo takšnih ultratankih plasti smo določili s kvantitativno elektronsko mikroanalizo z EDS z uporabo dveh neodvisnih metod: (i) z analizo pri nizki pospeševalni napetosti (LVEDS) in (ii) analizo pri spremenljivih napetostih s posebnim postopkom za analizo tankih plasti (TFA). Analitski metodi smo priredili in optimirali na osnovi izračunov, narejenih s simulacijo Monte Carlo. Zaželeno stehiometrijo $\text{Fe}_{50}\text{Pd}_{50}$, ki je pomembna s stališča doseganja dobrih magnetnih lastnosti, je bila dobljena pri potencialih $-1,3$ V in $-1,2$ V, medtem ko so bile plasti, narejene pri bolj pozitivnih napetostih, bogate s Pd. Rezultati kvantitativnih analiz LVEDS in TFA so bili konsistentni in so se odlično ujemali za plasti Fe-Pd, ki so bile debelejšje od 80 nm. Pri plasteh, tanjših od 70 nm, smo ugotovili majhen odmik rezultatov LVEDS v primerjavi s TFA, in sicer v okviru relativne razlike ± 10 %. Hitrejša LVEDS-metoda je primerna za rutinske analize in določanje sestave večjega števila Fe-Pd-vzorcev. Zahtevnejša metoda TFA je bolj natančna in večstranska, saj poleg analize sestave ultratankih Fe-Pd-plasti omogoča tudi določanje debeline le-teh.

Ključne besede: tanke plasti Fe-Pd, elektronska mikroanaliza, FEGSEM, EDS, AFM

1 INTRODUCTION

Thin films made from Fe-Pd alloys with a stoichiometry close to the equiatomic Fe/Pd ratio and an ordered $L1_0$ phase have attracted a lot of attention because of their large magnetocrystalline anisotropy (1.8 MJ/m^3) and the consequent good hard-magnetic properties, which can be retained even at the nanoscale.¹ Such properties make these materials suitable for high-density, perpendicular, magneto-recording media or for the nano-devices in nanoelectromechanical systems (NEMS).¹⁻³ Fe-Pd thin films can be prepared by electroplating, which is a cost-effective and efficient method, with a possibility of tailoring a film composition and morphology via simple experimental adjustments. An electrochemical synthesis of Fe-Pd thin films basically depends on the preparation of a stable electrolyte and,

recently, successful Fe and Pd co-depositions were performed in a citrate-based bath.⁴ Different kinds of thin-film applications would require thin films with well-defined properties resulting from an electrochemical processing. The initial Fe- and Pd-ion concentrations, the applied potential, the deposition time, etc., are the parameters that influence a film chemical composition, thickness, surface roughness and microstructure, all of which have an impact on the final properties.

In order to investigate the influence of the parameters of an electrodeposition process on the composition and microstructure of Fe-Pd thin films and to define the composition-property relations, it is important to perform a reliable microstructural and compositional characterization of the as-deposited films.

For this purpose a high-resolution field-emission-gun scanning electron microscope (FEGSEM) combined

with an electron-probe microanalysis (EPMA) using energy-dispersive X-ray spectroscopy (EDS) can be used as an appropriate characterization tool. However, since the thickness of Fe-Pd films is in the submicrometer/nanometer range, the analytical procedure for the quantitative EDS measurements is not straightforward and it requires special attention in order to achieve precise and accurate analytical results.^{5–7} For this reason, in this work, we propose two advanced, independent and optimized EDS procedures that were applied to determine the chemical composition of thin Fe-Pd films with high confidence. The high-resolution FEGSEM imaging and atomic-force microscopy (AFM) were employed to study the quality of the film surfaces, the surface morphology and the film thickness.

2 EXPERIMENTAL WORK

The Fe-Pd thin films were produced with an electro-deposition from an electrolyte based on palladium chloride PdCl_2 2 mM, iron chloride FeCl_2 18 mM, ammonium citrate $(\text{NH}_4)_2\text{C}_6\text{H}_6\text{O}_7$ 0.2 mM and $\text{NH}_3(\text{aq})$ 0.5 M with $\text{pH} = 9$.^{4,8} The potentiostatic co-deposition of Fe and Pd was performed at the potentials of -1.00 , -1.10 , -1.15 , -1.20 and -1.30 V measured vs. an Ag/AgCl electrode, for 300 s, onto a SiO_2 -glass substrate that was plasma-sputtered with Cr 40 nm and Au 100 nm metallic layers.

The characterization of the Fe-Pd samples was carried out in a FEGSEM JEOL JSM-7600F equipped with a high-efficiency, silicon drift EDS detector (SDD) X-Max 20 and an INCA microanalysis suite from Oxford Instruments. FEGSEM micrographs were recorded using secondary electrons (SE) or backscattered electrons in the compositional contrast mode (BSE-COMPO). Complementary AFM images were recorded with a Veeco diDimension 3100 scanning probe microscope in the tapping mode. To avoid the charging in the SEM the film cross-sections were coated with a 3 nm-thick amorphous carbon conductive layer in a Gatan PECS 682. After considering the complex, stratified arrangement of the samples, i.e., the Fe-Pd/Au/Cr metal-

lic layers on the SiO_2 substrate, Monte Carlo (MC) simulations were performed in order to decide on the optimum experimental conditions for the quantitative EDS analyses.^{9,10} Consequently, two independent SEM/EDS experimental set-ups were applied:

- a low-voltage EDS analysis (LVEDS) of the low-energy $\text{Fe-L}\alpha$ (0.704 keV) and $\text{Pd-L}\alpha$ (2.838 keV) spectral lines at the SEM accelerating voltage of 6.5 kV,
- variable-voltage analyses at (13, 15, 17 and 19) kV of all the elements present in the Fe-Pd films and in the substrate, by measuring the spectral lines of $\text{Fe-K}\alpha$ (6.403 keV), $\text{Pd-L}\alpha$, $\text{Au-M}\alpha$ (2.123 keV), $\text{Cr-K}\alpha$ (5.414 keV), $\text{Si-K}\alpha$ (1.740 keV) and $\text{O-K}\alpha$ (0.523 keV), followed by an off-line EDS-data processing with a dedicated thin-film analysis method (TFA).¹¹

To improve the accuracy of the quantitative analysis, the EDS-SDD detector response was properly calibrated at each applied accelerating voltage using Co and Si as standard reference materials. The EDS spectra were quantified using the $\text{XPP-}\Phi(\rho z)$ matrix-correction procedure.¹¹

3 RESULTS AND DISCUSSION

The SEM micrographs of the surfaces of the two representative Fe-Pd films deposited at -1.0 V and -1.3 V are shown in **Figure 1**. We found that at a higher absolute value of the applied voltage (≥ 1.2 V) the surfaces of the films become more granular, with bubble-like features (**Figure 1b**), which is due to an increased cathodic hydrogen evolution, whereas at lower absolute voltages (≤ 1.15 V) smoother nanostructured films were obtained (**Figure 1a**). Characteristic surface-profile parameters were determined from the corresponding AFM images, acquired from the $2\text{ }\mu\text{m} \times 2\text{ }\mu\text{m}$ sized regions on the samples, as presented in **Figure 2**. The three-dimensional image analyses revealed that the maximum profile height difference (z) was 40 nm at -1.0 V and 105 nm at -1.3 V, with the respective average-roughness (R_a) values of 2 nm and 10 nm. These data were taken into account in order to apply a suitable EDS measurement strategy that effectively diminishes

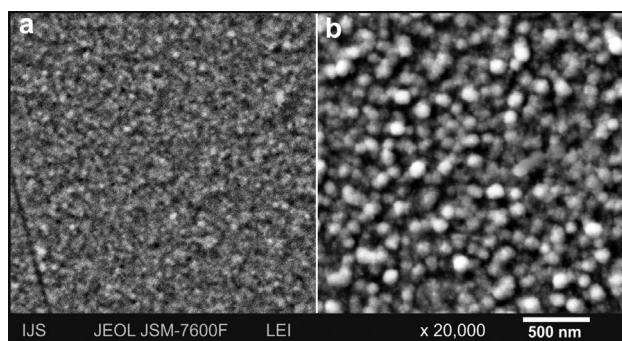


Figure 1: FEGSEM SE micrographs of the surface morphology of Fe-Pd films: a) deposited at -1.0 V, b) deposited at -1.3 V

Slika 1: FEGSEM SE-posnetka morfologije površine plasti Fe-Pd: a) plast, nanosena pri $-1,0$ V, b) plast, nanosena pri $-1,3$ V

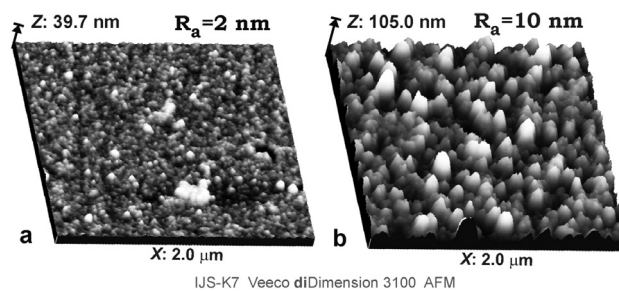


Figure 2: AFM images of Fe-Pd films deposited at: a) -1.0 V and b) at -1.3 V

Slika 2: AFM-posnetka plasti Fe-Pd, nanosenih pri: a) $-1,0$ V in b) $-1,3$ V

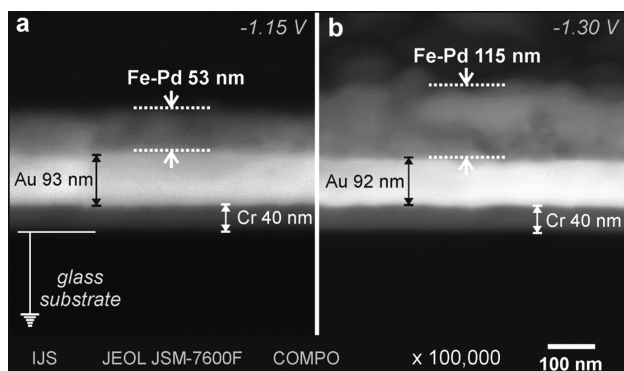


Figure 3: FEGSEM BSE-COMPO micrograph of the cross-sections of Fe-Pd films: a) deposited at -1.15 V, b) deposited at -1.3 V
Slika 3: FEGSEM BSE-COMPO-posnetek prečnega prereza plasti Fe-Pd: a) plast, nanesena pri -1.15 V, b) plast, nanesena pri -1.3 V

the influence of the roughness on the spectral-data acquisition.

The high-resolution compositional contrast micrographs of the cross-section samples of the Fe-Pd films deposited at -1.15 V and -1.3 V are shown in **Figure 3**. This imaging mode emphasizes the grey-level differences between the materials/elements according to the differences in their (average) atomic numbers. So, the micrographs clearly revealed the layered structure of the samples with a Fe-Pd film on the top of the Au/Cr/SiO₂ substrate. The thickness of individual metallic layers was measured directly from the images, taking six random positions on the samples with the average values given on the images (**Figure 3a, b**). The results obtained for all the analysed samples showed that the Fe-Pd films have the thicknesses in the range from 50 nm to 120 nm.

On the basis of the MC calculations the applied voltage 6.5 kV for the LVEDS set-up was found to be an appropriate compromise choice that ensures a sufficiently small size of the X-ray analytical volume and a

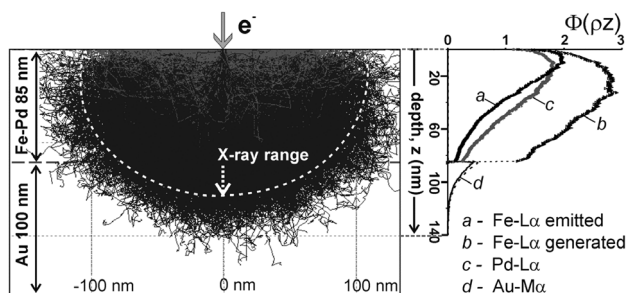


Figure 4: Results of the Monte Carlo simulation performed for the 85-nm-thick Fe-Pd film sample at the beam energy 6.5 keV. The image shows the size of the electron interaction volume in the x - z projection, the estimated size of the X-ray generation range and the $\Phi(\rho z)$ depth-distribution intensity curves for the Fe-L α , Pd-L α and Au-M α spectral lines.

Slika 4: Rezultati simulacije Monte Carlo za vzorec plasti Fe-Pd debeline 85 nm pri energiji elektronov 6,5 keV. Slika prikazuje velikost interakcijskega volumna elektronov v projekciji x - z , oceno velikosti področja nastanka rentgenskih žarkov in $\Phi(\rho z)$ -krivulje globinske porazdelitve intenzitet za spektralne črte Fe-L α , Pd-L α in Au-M α .

large enough overvoltage ratio to maintain a level of ≥ 2 for the highest X-ray energy analysed, i.e., the L₃-edge excitation energy of the Pd-L α radiation. Consequently, using the LVEDS the analytical procedure gets closer to the conventional bulk-sample EPMA situation, as illustrated in **Figure 4**, showing the MC results for the 85-nm-thick Fe-Pd film. The maximum X-ray generation depth at 6.5 kV (X-ray range) is ≈ 110 nm, suggesting that some Au-M α X-rays may still be generated from the Au-layer beneath the Fe-Pd film on the top, especially in the case of the films thinner than 100 nm. The $\Phi(\rho z)$ depth-distribution curves given in **Figure 4** also show a minor Au-M α contribution, together with the principal contributions of the Pd-L α and Fe-L α lines. The X-ray intensity calculations revealed that a high absorption of the Fe-L α radiation occurs with ≈ 60 % of the generated X-rays being absorbed in the Fe-Pd matrix, whereas this effect is negligible for the Pd-L α line. Even so, an acceptable accuracy of the quantitative LVEDS can be achieved, since it is expected that the XPP matrix correction is capable of compensating for the strong absorption effects, like those present here for the Fe-L α line.

The comparison of the characteristic EDS spectra acquired from the Fe-Pd film 85 nm using the LVEDS and TFA approaches is shown in **Figure 5**. As predicted from the MC calculations, the spectrum 6.5 kV has two main peaks, Fe-L α and Pd-L α , and a minor Au-M α peak. The appearance of the small O-K α peak is (most likely) due to a partial film-surface oxidation upon the film preparation. The Au-M and O-K contributions were then neglected in the quantification and calculation of the Fe/Pd stoichiometry. The spectrum 19 kV (and also the spectra at (13, 15 and 17) kV) shows the peaks of all the elements from the film and the substrate: Fe, Pd, Au,

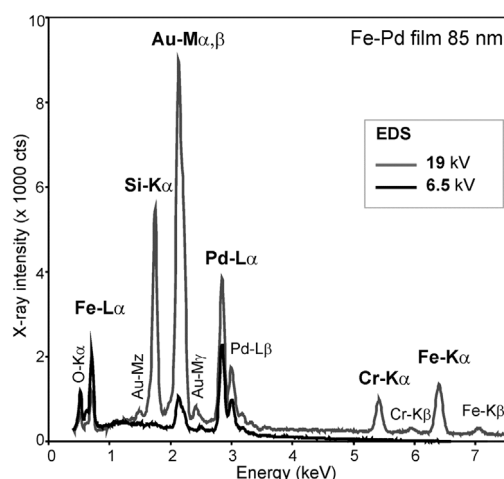


Figure 5: Comparison of the EDS spectra at 6.5 kV and 19 kV, obtained from the Fe-Pd film 85 nm, with marked analytical spectral lines used for the LVEDS and/or TFA methods

Slika 5: Primerjava EDS-spektrov pri 6,5 kV in 19 kV, ki so bili pridobljeni iz 85 nm tanke plasti Fe-Pd, z označenimi analitskimi spektralnimi črtami, ki so bile uporabljene za metodi LVEDS in/ali TFA

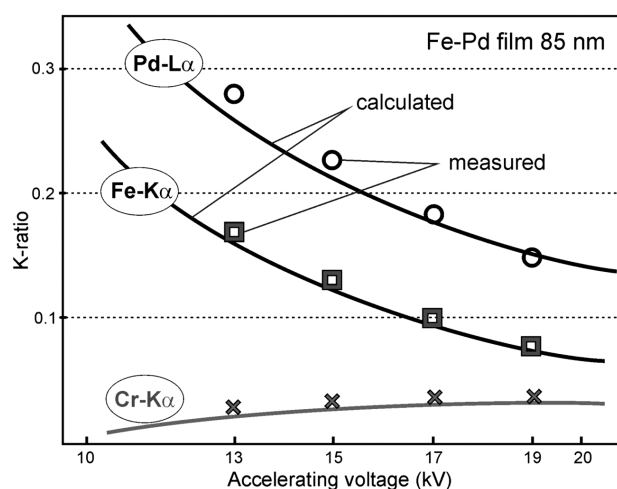


Figure 6: Calculated and measured Fe, Pd and Cr k -ratio values versus the accelerating voltage, obtained using EDS-TFA analyses

Slika 6: Izračunane in izmerjene vrednosti k -razmerij za Fe, Pd in Cr v odvisnosti od pospeševalne napetosti, dobljene z analizami EDS-TFA

Cr and Si. In the case of the TFA, we found, with the MC calculations, that the $O-K\alpha$ radiation from the SiO_2 substrate is fully absorbed in the upper layers at all the applied voltages. The EDS-TFA spectra were subsequently processed to obtain the dependence of the measured and calculated k -ratios versus the voltage, as shown in **Figure 6** for Fe, Pd and Cr. The excellent fit obtained for the measured and calculated values verifies the correctness of the TFA experimental set-up and ensures that a reliable quantitative compositional analysis of the Fe-Pd films can be achieved. Consequently, the true X-ray depth distributions were computed for the stratified Fe-Pd/Au/Cr/ SiO_2 specimens, which then allowed us to calculate the Fe-Pd film thicknesses with high confidence as well.

The reliability of the TFA was first assessed with a comparison of the film-thickness results for the inter-

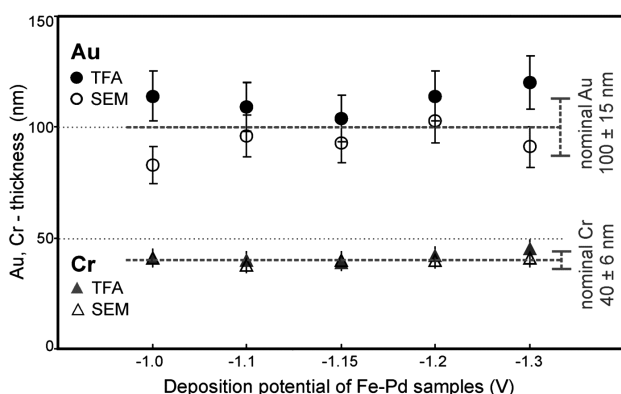


Figure 7: Measured thickness values for the Au and Cr intermediate layers, determined directly from the SEM images and calculated from the TFA data

Slika 7: Izmerjene vrednosti debelin vmesnih plasti Au in Cr, določene neposredno iz SEM-posnetkov in izračunane na osnovi podatkov iz analiz TFA

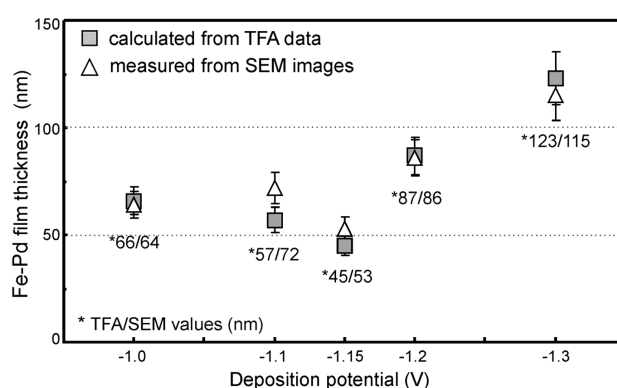


Figure 8: Thickness of the Fe-Pd films versus the applied deposition potential, determined from the SEM images and from the TFA data

Slika 8: Debelina plasti Fe-Pd v odvisnosti od napetosti nanašanja, določene iz SEM-posnetkov in na osnovi podatkov iz analiz TFA

mediate Au and Cr layers that were obtained from the SEM images and from the TFA calculations, as shown in **Figure 7**. Taking into account that the inherent precision of the plasma-sputtering device is $\leq \pm 15\%$ relative, the experimentally determined values for the Au- and Cr-layer thicknesses were fully consistent with their declared/nominal values, which was an additional proof of the accuracy of the TFA method. The results of the thickness determination for the Fe-Pd films are given in **Figure 8**. The comparison of the SEM and TFA values showed a very good agreement between the two datasets, i.e., similar thickness values were independently determined with both methods. Thus, under the applied electrodeposition conditions, the ultrathin Fe-Pd films with the thicknesses between ≈ 50 nm and 120 nm were produced.

A summary of the results of the EDS quantitative elemental analyses performed by the LVEDS and TFA is given in **Figure 9**. The composition of the Fe-Pd films close or equal to the preferred equiatomic $Fe_{50}Pd_{50}$

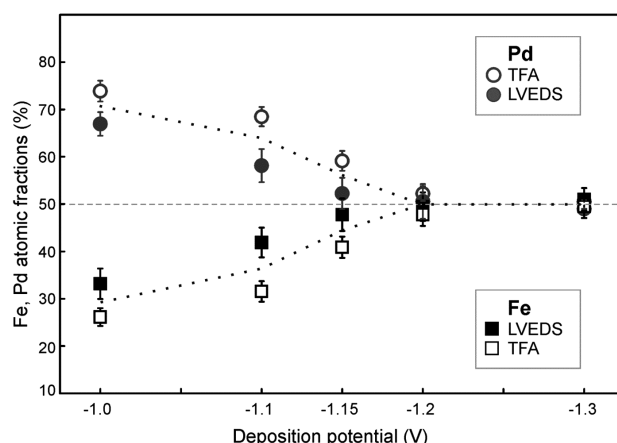


Figure 9: Fe and Pd elemental atomic fractions (%) versus the deposition potential of the analysed Fe-Pd films, as determined from the quantitative LVEDS and TFA methods

Slika 9: Atomski deleži (%) za Fe in Pd v odvisnosti od napetosti nanašanja analiziranih vzorcev plasti Fe-Pd, določeni iz kvantitativne analize z metodami LVEDS in TFA

stoichiometry was obtained at higher absolute deposition potentials, i.e., at -1.2 V and -1.3 V. At lower absolute potentials (i.e., ≥ -1.15 V) the Fe-Pd films are Pd rich due to the more positive reduction potentials of the Pd-complex in comparison with the Fe-complex. It is evident that the best agreement between the LVEDS and TFA quantitative data is achieved for the Fe-Pd films that are thicker than ≈ 80 nm, whereas for the films below 70 nm, a certain discrepancy is present. This discrepancy, in the case of the very thin Fe-Pd samples, is due to the additional X-ray excitations originating from the substrate (Au), even at 6.5 kV, where the bulk-sample analysis approximation becomes less correct. Namely, both the Pd- $L\alpha$ radiation excited from the Fe-Pd layer and a certain quantity of the primary-beam electrons can produce the Au- $M\alpha$ X-rays, either by the secondary fluorescence or by the primary ionization process. Furthermore, the photons of the Au- $M\alpha$ partially contribute to the extra Fe- $L\alpha$ excitations by the secondary fluorescence as well. Since these effects are complicated and difficult to calculate, they are neglected in the LVEDS approach and, therefore, the seemingly higher Fe concentrations in the very thin Fe-Pd samples were obtained with the LVEDS analysis, as compared to the TFA. Subsequently, a correct analysis of the Fe-Pd films can be performed using the procedures designed for the bulk-like samples (LVEDS), when no extra radiations are emitted due to the fluorescence of the substrate excited by the film. Even so, these discrepancies between the LVEDS and TFA quantitative results are relatively small and within ± 10 % relative.

4 CONCLUSIONS

The composition and microstructure of the electrodeposited Fe-Pd thin films were studied by the FEGSEM, EDS and AFM. The Fe-Pd films had a nanostructured surface morphology with an increased roughness at higher absolute values of the deposition potential. The film thickness varied from 50 nm to 120 nm. In order to analyse the chemical composition of such ultrathin Fe-Pd layers on the Au/Cr/SiO₂ substrate, two specially designed quantitative EDS methods were applied, i.e., the LVEDS and TFA. The LVEDS approach gave good accuracy for the Fe-Pd films thicker than 80 nm and reasonable results for the thinner films (< 70 nm), being

within the ± 10 % relative difference in comparison with the TFA quantitative results. Since the LVEDS approach is quicker, it is suitable and acceptable for a routine control of the Fe/Pd stoichiometry for a large number of the samples produced in laboratory experiments every day. The optimized, dedicated TFA approach was found to be a very appropriate and accurate method for a quantitative compositional analysis of the Fe-Pd thin films and for the film-thickness determinations as well. Since reliable and accurate quantitative results can be achieved for any film thickness, we recommend using this, admittedly more demanding, TFA approach, particularly for analysing ultrathin Fe-Pd films.

Acknowledgements

This work was supported by the Slovenian Research Agency (ARRS) within project J2-4237 "Electron microscopy and microanalysis of materials on submicrometer scale" and program P2-0084 "Nanostructured materials".

5 REFERENCES

- ¹ F. M. Takata, G. Pattanaik, W. A. Soffa, P. Sumodjo, G. Zangari, *Electrochem. Commun.*, 10 (2008), 568–571
- ² X. L. Fei, S. L. Tang, R. L. Wang, H. L. Su, Y. W. Du, *Solid State Commun.*, 141 (2007), 25–28
- ³ C. Issro, W. Püschl, W. Pfeiler, P. F. Rogl, W. A. Soffa, M. Acosta, G. Schmerber, R. Kozubski, V. Pierron-Bohnes, *Scripta Mater.*, 53 (2005), 447–452
- ⁴ S. C. Hernandez, B. Y. Yoo, E. Stefanescu, S. Khizroev, N. V. Myung, *Electrochim. Acta*, 53 (2008), 5621–5627
- ⁵ J. I. Goldstein, D. E. Newbury, D. C. Joy, C. E. Lyman, P. Echlin, E. Lifshin, L. Sawyer, J. R. Michael, *Scanning Electron Microscopy and X-Ray Microanalysis*, 3rd ed., Kluwer Academic Publishers, New York 2003, 453
- ⁶ R. A. Waldo, M. C. Militello, S. W. Gaarenstroom, *Surf. Interface Anal.*, 20 (1993), 111–114
- ⁷ G. F. Bastin, J. M. Dijkstra, H. J. M. Heijligers, D. Klepper, *Microbeam Analysis*, 2 (1993), 29–43
- ⁸ D. Pečko, K. Žužek Rožman, P. J. McGuinness, B. Pihlar, S. Kobe, *J. App. Phys.*, 107 (2010), 09A712
- ⁹ D. Drouin, A. R. Couture, D. Joly, X. Tastet, V. Aimez, R. Gauvin, *Scanning*, 29 (2007), 92–101
- ¹⁰ Z. Samardžija, K. Žužek Rožman, S. Kobe, *Mater. Charact.*, 60 (2009), 1241–1247
- ¹¹ J. L. Pouchou, F. Pichoir, *Electron Probe Quantitation*, Plenum Press, New York 1991, 31

EVALUATION OF THE EFFECTS OF SURFACE TREATMENTS ON DIFFERENT DENTAL CERAMIC STRUCTURES

OCENA VPLIVA OBDELAVE POVRŠINE RAZLIČNIH DENTALNIH KERAMIK

**Ergül Ertürk¹, Mehmet Dalkiz², Emre Özyilmaz³, H. Zehra Akbaş⁴,
H. Ali Çetinkara⁴, Halil Aykul³**

¹Turkish Gelibolu Army Hospital, Dental Service, Gelibolu, Turkey

²Mustafa Kemal University, Dentistry Faculty, Hatay, Turkey

³Hitit University, Engineering Faculty, Dept. of Mechanical Engineering, Çorum, Turkey

⁴Mustafa Kemal University, Arts and Science Faculty, Hatay, Turkey
erturktural@hotmail.com

Prejem rokopisa – received: 2013-02-20; sprejem za objavo – accepted for publication: 2013-03-05

The surface treatments applied to porcelain materials can be different overglaze methods, chemical interactions and polishing techniques. The aims of these methods are the most durable restoration and the smoothest surface. The smoothness attained with these processes is important due to the following reasons: reduction of the bacteria remaining in the pores of a surface, improvement of gingival health and esthetic view, and prevention of an abrasion of the opposite canal.

The aim of this study is to assess different surface-finishing operations that are applied to widely used porcelains in prosthetic dentistry using SEM (a scanning electron microscope). In the experiments seven different surface finishing operations (sandpaper, rubber, Sof-Lex, HP paste, autoglaze, overglaze and ion exchange) were applied to four different commercial porcelains (IPS d. SIGN, Antagon, Ceramco 3, Vitadur Alpha). The effects of various surface-finishing operations on porcelain are micro-morphologically evaluated (a SEM analysis). The results showed that the smoothest surfaces were obtained with the overglaze and autoglaze, followed by HP paste, rubber, Sof-Lex and sandpaper. In addition, the smoothness values of HP paste proved that it can be safely used in clinical surface-finishing operations.

Keywords: dental porcelain, SEM, surface finishing

Pri obdelavi površine porcelanskih materialov lahko uporabljamo različne metode: glaziranje v peči, kemijske interakcije in tehnike poliranja. Namen teh metod je največja zdržljivost, kot tudi najbolj gladka površina. Gladkost, dobljena pri teh postopkih, je pomembna zaradi naslednjih razlogov: zmanjšanje števila bakterij, ki ostajajo v porah na površini, izboljšanje zdravlja obzobnega tkiva, boljši estetski videz, preprečevanje obrabe.

Namen te študije je oceniti površine pri različnih postopkih obdelave porcelana, ki se uporablja v protetičnem zobozdravstvu, z metodo SEM (vrstična elektronska mikroskopija). Pri eksperimentih je bilo uporabljeno sedem različnih operacij obdelave površine (brusni papir, guma, Sof-Lex, HP-pasta, samoglaziranje, preglaziranje in izmenjava ionov) pri štirih različnih komercialnih porcelanih (IPS d. SIGN, Antagon, Ceramco 3, Vitadur Alpha). Učinek različnih operacij obdelave površine na porcelanih je bil mikro-morfološko ocenjen s SEM-analizo. Rezultati so pokazali, da je bila najbolj gladka površina dosežena s prepolariziranjem in z avtoglaziranjem, nato s HP-pasto, gumo, softlexom in brusnim papirjem. Dodatno je gladkost pri uporabi HP-paste pokazala njeno varno uporabo pri klinični obdelavi površine.

Ključne besede: dentalni porcelan, SEM, obdelava površine

1 INTRODUCTION

Dental porcelain restorations have two main disadvantages: these restorations have a brittle structure and they cause abrasion on the opposite teeth. Brittleness is mostly caused by the fractures that develop along the porcelain surface. These fractures are micro-fractures caused by porosity, oven heating or the process, with which the prosthesis is adapted to the patient. The existence of micro-fractures has the effect of accelerating the fractures by reducing the bending resistance under the chewing loads. It was concluded that the abrasion effect observed on the teeth of the opposite occlusion is proportional to the hardness and roughness of the porcelain surface. Therefore, when porcelain is preferred in dental restorations, aforementioned disadvantages should be minimized. For that purpose, certain measures are

taken to strengthen the internal structure of the porcelain and various surface treatments are applied to solve this problem.¹⁻⁶

The applied surface processes can be listed as follows: different overglaze techniques, chemical interactions and polishing techniques. With these methods we aim to achieve the most durable restoration and the smoothest surface possible. The smoothness attained with these processes are important due to the following reasons: reduction of the bacteria remaining in the pores of a surface, improvement of gingival health and esthetic view, and prevention of an abrasion of the opposite canal.⁷⁻¹³

A determination of the most suitable porcelain surface, in terms of the mechanical properties under the chewing loads and surface composition created via various surface-finishing operations, is a continuously

researched and developed subject. The aim of this study is to assess different surface-finishing operations that are applied to widely used porcelains in prosthetic dentistry using SEM (a scanning electron microscope).

2 MATERIALS AND METHODS

In our study, three metal-supported commercial porcelains [IPS d. SIGN (Ivoclar Schaan, Liechtenstein), Antagon (Elephant Hoorn, Holland), Ceramco 3 (DeguDent GmbH, USA)] and a porcelain without any support [Vitadur Alpha (Vita, Germany)] were used.

Following the instructions of the producers, porcelain dough was mixed. The steel mould prepared to maintain the standards was placed on a vibrator device (Vibratör R2, Degussa, Germany). This step was repeated until the mould was full. For the condensation process, the vibration was provided by the vibrator.

For the production of the porcelain discs with a diameter of 7 mm and a thickness of 2 mm, later observed with SEM, a special cylindrical mould was used. The piston of the mould was pulled down by 3 mm and was fixed at this position. The porcelain dough, prepared in accordance with the producers' instructions, was put into the mould via a spatula. With the help of vibration, the condensation was carried out and the water that rose to the surface was taken away. Then, the porcelain discs were taken out by pushing the piston.

These porcelain-dough specimens were laid onto a 3 mm asbestos plate and placed in an oven following the instructions provided by the manufacturers. For any porcelain type of a given surface treatment 10 specimens were treated in the oven (**Table 1**).

The finishing of all of the porcelain blocks and discs were carried out using a handpiece at a speed of 15000 r/min and using a diamond-granule cylinder burr. The surfaces used for observing the discs and cylinders were ground for 30 min with the 220- and 360-grade abrasive papers. Porcelain discs were machined to the dimensions of 7 mm × 2 mm. Finally, an adequate smoothness and parallelism of the surfaces were maintained (**Figure 1**).

To one surface of all the specimens, 500-grade abrasive paper (waterproof silicon-carbide paper, England) was applied for 30 s. The opposite surfaces were marked. All the porcelain specimens were cleaned using an ultrasonic cleaning device (Euronda, Eurosonic Energy, Italy) and an ultrasonic cleaning solution (Sultan Che-

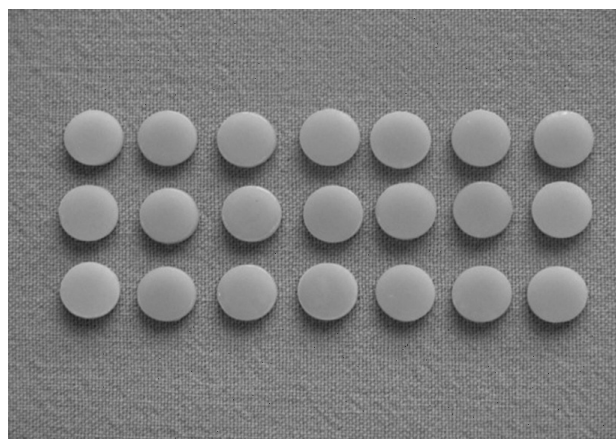


Figure 1: Specimens prepared for the SEM analysis

Slika 1: Vzorci, pripravljeni za SEM-analizo

mist Inc., Englewood, USA). All the porcelain specimens were grouped with respect to their manufacturers. Then, ten porcelain blocks and ten discs were separated from each manufacturer group to form the following groups: sandpaper, rubber, Sof-Lex, paste, autoglaze, overglaze and ion-exchange.

- 1. Sandpaper group:** After processing this group using the 500 grade for 30 s, no further steps were applied. The surface was being cleaned with steam bath and ultrasonic cleaners for 10 min.
- 2. Rubber group:** The appropriate surfaces of the discs and cylinders of this group were ground at 15000 r/min for 20 s using Cerashine porcelain rubbers (Diatec, Switzerland). The rubber remnants were removed from the surface with a steam bath and ultrasonic cleaners.
- 3. Sof-Lex group:** The Sof-Lex polishing rubber (3M ESPE, USA) was applied to the appropriate surfaces of the discs and cylinders of this group. 1982C, 1982M, 1982F and 1982SF grade discs were applied, respectively, for 10 s in accordance with the manufacturer's instructions.
- 4. Paste group:** Using the HP paste (Heraeus Kulzer, Germany), the surfaces of the discs and blocks of this group were polished. In accordance with the manufacturer's instructions, this paste was applied using a bristle brush at the speed of 15000 r/min and for 20 s. After the completion of the process, the porcelain blocks and discs were cleaned under flowing water.

Table 1: Numbers of porcelain discs (D) used for different surface-finishing operations

Tabela 1: Porazdelitev števila (D) uporabljenih porcelanskih ploščic glede na obdelavo površine

	Sandpaper	Rubber	Sof-Lex	HP-paste	Autoglaze	Overglaze	Ion-exchange	Total
	D	D	D	D	D	D	D	D
IPS d. SIGN	10	10	10	10	10	10	10	70
ANTAGON	10	10	10	10	10	10	10	70
CERAMCO 3	10	10	10	10	10	10	10	70
VITADUR ALPHA	10	10	10	10	10	10	10	70
TOPLAM	40	40	40	40	40	40	40	280

Table 2: Time-temperature table for the autoglaze group**Tabela 2:** Tabela čas-temperatura za skupino Autoglaze

Porcelain types	Initial temperature (°C)	Heating temperature (min.)	Temperature increasing rate (°C/min)	Highest temperature (°C)	Dwell duration (min)	Vacuum initiation (°C)
IPS d. SIGN	403	4	60	870	1	450
Antagon	500	3	60	895	1	–
Ceramco 3	650	3	45	920	1	–
Vitadur Alpha	600	3	60	940	1	–

Table 3: Time-temperature table for the overglaze group**Tabela 3:** Tabela čas-temperatura za skupino Overglaze

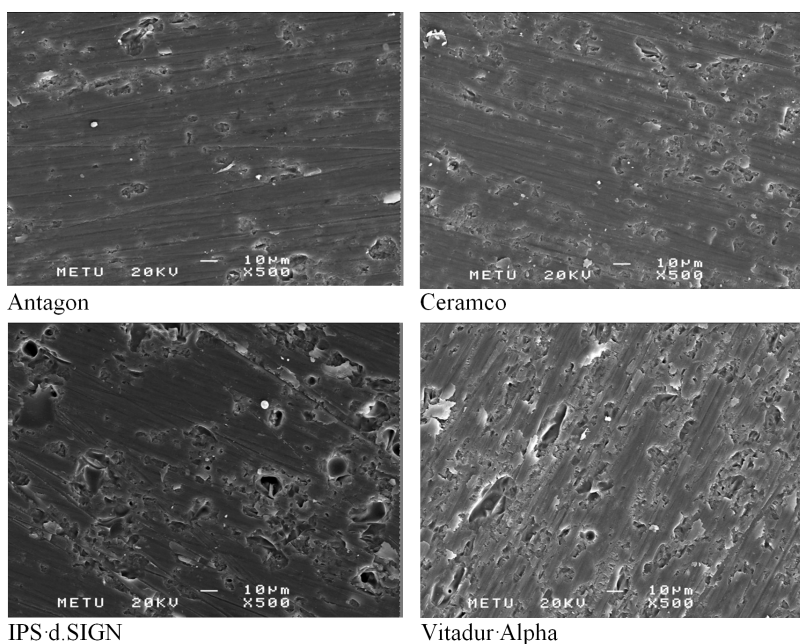
Porcelain types	Initial temperature (°C)	Heating temperature (min)	Temperature increasing rate (°C/min)	Highest temperature (°C)	Dwell duration (min)	Vacuum initiation (°C)
IPS d. SIGN	403	4	60	830	1	450
Antagon	500	3	60	895	1	–
Ceramco 3	650	3	55	925	1	–
Vitadur Alpha	600	3	60	920	1	–

Then, they were being cleaned in the ultrasonic cleaner for 10 min.

5. Autoglaze group: According to the manufacturers' instructions, the cylinders and discs of this group were autoglazed according to the oven programs given in **Table 2**.

6. Overglaze group: For this group of porcelain discs and blocks, the glazing powders and liquids of the manufacturers were used. A glaze powder and liquid were mixed together and this mixture was applied using a grade-1 sable brush in such a way that it covered all the surface. At the end they were kept in the oven as described in the instructions provided by the manufacturer (**Table 3**).

7. Ion-exchange group: In order to use a dual ion exchange, 10 % mol LiCl and 90 % mol NaCl ion-exchange solution (Merck, Germany) was prepared. The surfaces of porcelain blocks and discs were covered with this ion-exchange solution using a spatula in such a way that it formed a 1 mm layer. The covered blocks were kept in the oven at 750 °C and for 30 min. For the second stage of the ion exchange, the temperature was reduced to 450 °C and kept in the oven for another 30 min. After being cooled at room temperature, these porcelain blocks and discs were being cleaned of the salt on the surface under flowing water and in the ultrasonic cleaner for 10 min. The porcelain blocks and discs,

**Figure 2:** Surface views of sandpaper-finished specimens**Slika 2:** Videz površine vzorcev, obdelanih z brusnim papirjem

whose surface processes were completed, were placed into plastic containers.

2.1 Evaluation of the surface-finishing operations on the test specimens with SEM

In order to qualitatively evaluate the surface operations of these porcelain discs, their single surfaces were covered with 250 Angstroms of gold using a gold-covering device (Hummer VII, Anatech Ltd., USA). The surface was scanned using an electron microscope (Jeol, JSM-6 6400, Japan). For all of the specimens, the vol-

tage, inclination-angle and magnification values were kept constant. Each porcelain specimen was magnified 100, 500 and 2000 times.

3 RESULTS

The results of the SEM analysis are summarized under 7 headings.

a) Results of the specimens finished using sandpaper

All the porcelain specimens were prepared in accordance with the instructions provided by the manu-

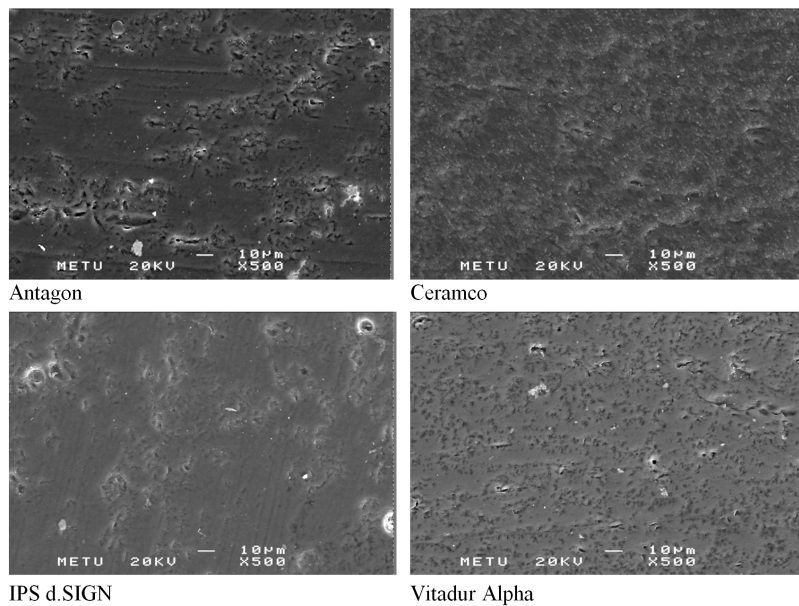


Figure 3: Surface views of rubber-finished specimens

Slika 3: Videz površine vzorcev, obdelanih z gumo

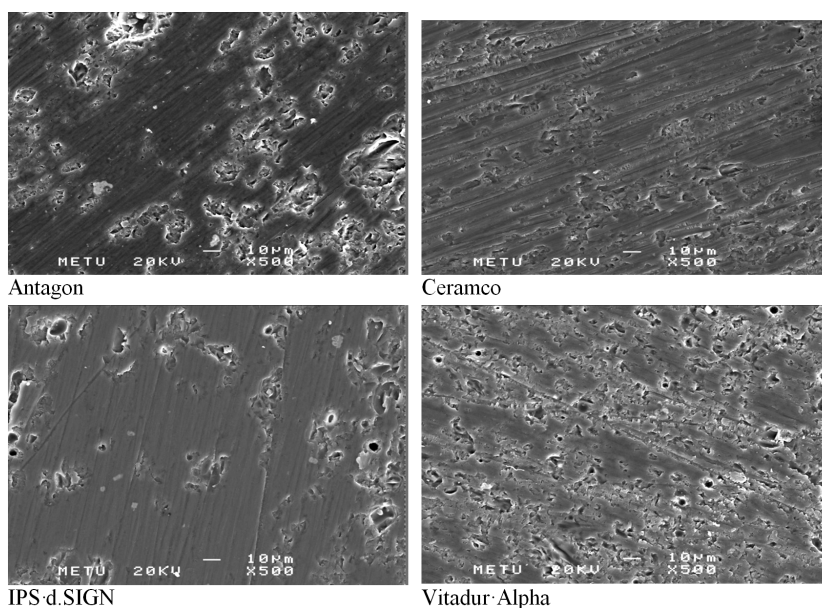


Figure 4: Surface views of Sof-Lex-finished specimens

Slika 4: Videz površine vzorcev, obdelanih s soflexom

facturers. These specimens were magnified 500 times and analyzed. It was found that a sandpapering operation can smooth the surface but it leaves deep scratches on the surface and cannot eliminate the porosity or fill in the gaps. In addition, no difference was observed between the porcelains of four manufacturers (Figure 2).

b) Results of the specimens finished using rubber

With the analysis it was found that the finishing operation carried out by using rubber could create smoother surfaces compared to sandpaper. However, it was not successful in removing the sandpaper and the finishing

scratches. Moreover, it could not fill in the gaps that developed during the water vaporization (Figure 3).

c) Results of the specimens finished with Sof-Lex

After the examination of the Sof-Lex finished specimens, it was seen that the results were quite similar to the result obtained for the rubber-finished specimens. The Sof-Lex finished specimens were of a similar surface quality and this technique also failed to fill in the gaps that developed during the water evaporation (Figure 4).

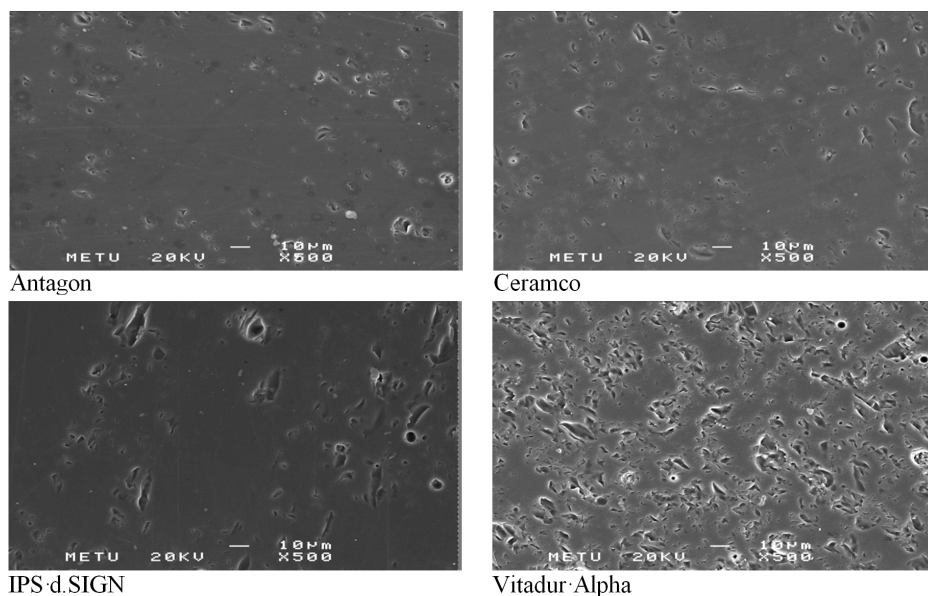


Figure 5: Surface views of HP-paste-finished specimens

Slika 5: Videz površine vzorcev, obdelanih s HP-pasto

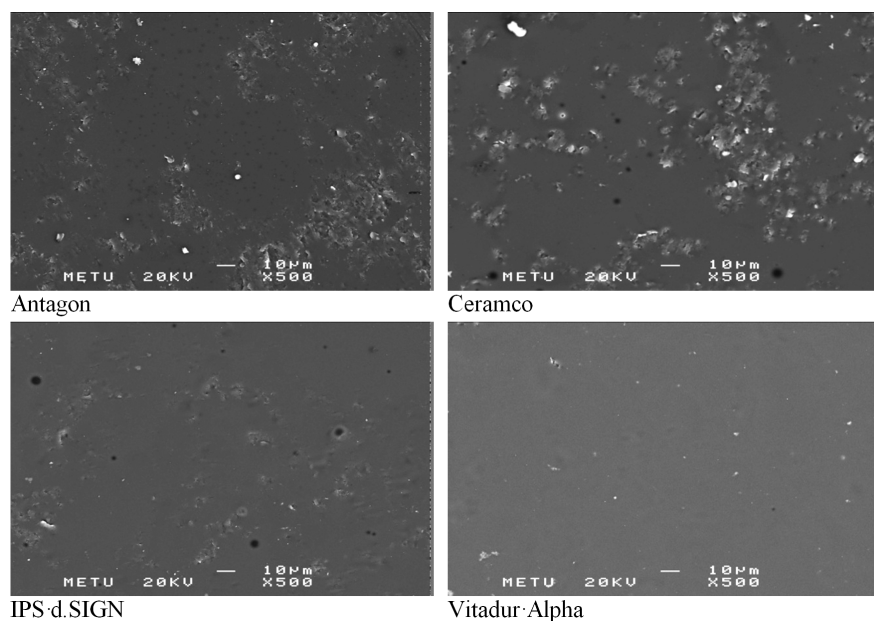


Figure 6: Surface views of autoglaze-finished specimens

Slika 6: Videz površine vzorcev, obdelanih s samoglaziranjem

d) Results of the specimens finished using HP paste

The examination of the HP-paste-finished specimens revealed that this finishing technique could eliminate the sandpaper and the finishing scratches but failed to fill in the gaps that developed during the water evaporation (Figure 5).

e) Results of the autoglaze-finished specimens

The autoglaze operation removed all of the scratches that emerged due to the finishing operations and filled in most of the gaps that developed during the water evaporation. In addition, it vitrified the surface and the struc-

ture of the porcelain specimens to some extent (Figure 6).

f) Results of the overglaze-finished specimens

The examination of the overglaze-finished porcelain specimens showed that all the finishing scratches and water-evaporation gaps were removed. In addition, this finishing process provided a perfect vitrification of both the surface and the structure. It was observed that, among all the groups, this surface-finishing process provided the best surface properties (Figure 7).

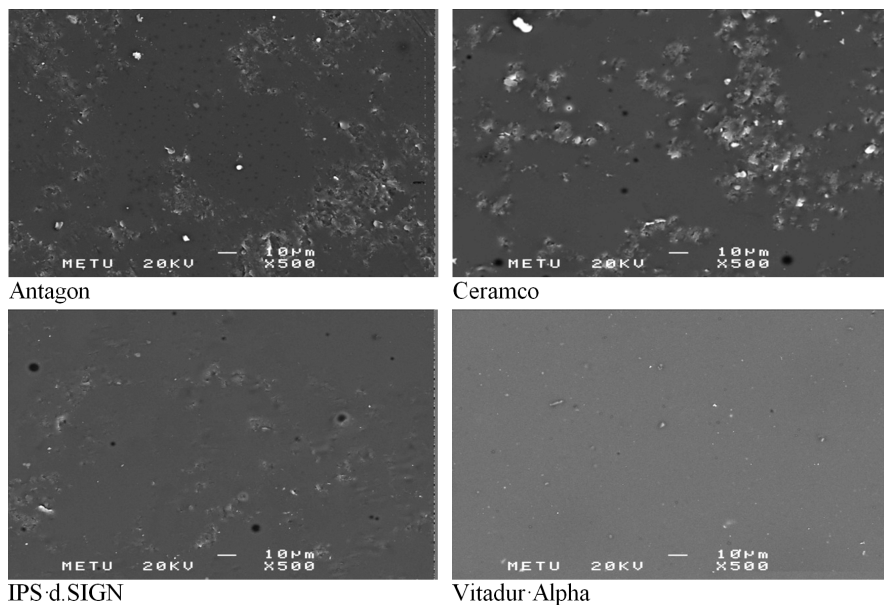


Figure 7: Surface views of overglaze-finished specimens
Slika 7: Videz površine vzorcev, obdelanih s preglaziranjem

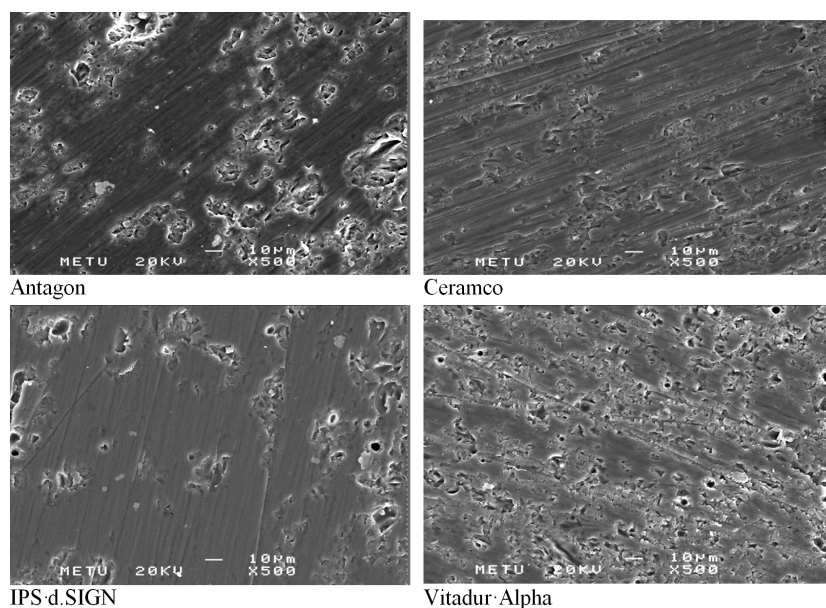


Figure 8: Surface views of ion-exchange-finished specimens
Slika 8: Videz površine vzorcev, obdelanih z izmenjavo ionov

g) Results of the ion-exchange finished specimens

The last group of the specimens was the ion-exchange group. The specimens of this group had the third best surface quality after the overglazed and autoglazed specimens. On the other hand, the ion-exchange application caused these specimens to deform and made some interior fractures to propagate to the surface (**Figure 8**).

4 DISCUSSION

Dental porcelains are the most preferred restorative materials thanks to their bio-compatible structures, perfect esthetic results and the capability of being used in various dental applications.¹⁴ By implementing the appropriate surface-finishing operation needed for porcelain restorations, an aggregation of the agents that cause plaque and staining is prevented, the mechanical irritations of the surrounding soft tissue are eliminated and an abrasion on the contact surfaces of the neighboring and opposite teeth can be reduced.

Although porcelains are generally recognized as bio-compatible materials, they have a porous and brittle structure. In order to increase both strength and bio-compatibility of dental porcelains, many surface treatments are applied. These are the techniques of polishing, glazing and ion-exchange treatments. The aim of this study is to investigate the effects of these surface-finishing operations on dental porcelains and compare them with the results from the literature.

Various surface-finishing operations were investigated by many researchers.^{15,16} Sof-Lex, rubber and autoglaze processes were examined^{7,17} and the polishing methods and effects of the glazing techniques using the SEM method were studied.¹⁸ The effectiveness of polishing using various grain-sized diamond burrs and diamond-grained pastes was studied.¹⁹ In addition, diamond-added pastes and glazing treatments were also researched.¹² Some researchers investigated the polishing methods and autoglaze treatment.^{20–22} They compared the porcelains, to which autoglaze was applied, using SEM.

Scientists tested the resistances of the porcelains that had undergone different surface treatments, employing the three-point bending test. In addition, they also evaluated these specimens' surface qualities and the fracture zones with a SEM analysis.

The SEM method was used in order to compare different surface treatments.¹⁶ SEM was used to evaluate the effects of polishing using diamond-added pastes after machining with different-grained diamond burrs.¹⁹

In prosthetic restorations, shiny surfaces are one of the desired qualities along with the esthetics and functioning. While, for many dental materials, the polishing and finishing provide a sufficient surface shine, for dental porcelains that can only be obtained by employing the glazing techniques. Nowadays, in dentistry, many low-temperature porcelains and reduced-hardness porcelains are in use. Depending on the instructions of the manu-

facturers, the surface treatments of these porcelains may vary. For this reason, in our study, we examined different porcelains that are widely used in the Turkish dentistry.

In the surface-finishing operations of porcelain restorations, the sequences of the processes are quite important. By using the feldspathic porcelain, crack emergence was avoided on the polished and autoglazed surfaces.²³ However, microcracks occurred during the autoglaze treatment following the polishing. It was found that these microcracks may cause surface roughness and that a repetition of any surface treatment may result in a porous structure instead of a shiny surface. In our study, all the specimens were machined with the same burrs and sandpapered in the same manner. Then, the last required surface-finishing operation was carried out.

It was concluded that the autoglaze treatment provides a better surface than the polishing^{15,17,21} but it was also stated that polishing creates a shinier surface than the autoglaze technique.²² In our study, while the creation of the smoothest surface using the HP paste contradicts the findings of Campbell et al.¹⁵ and Patterson et al.¹⁷, it resembles the results from the study by Wright et al.²² This contradiction might have been caused due to the difference between the methods of observation as, during the SEM analysis, the smoothest surfaces were observed on the autoglazed and overglazed specimens.

In the study, in which different polishing and glazing methods are compared,¹⁸ it is reported that, according to the SEM-analysis results, the autoglaze treatment provided the smoothest surfaces. Similarly, in this study, it was concluded, on the basis of a SEM analysis, that the overglaze treatment provided the smoothest surfaces. The SEM analysis of our study is similar to their results.

Motro et al.²⁴ concluded that, when compared to the autoglaze, the polishing systems are also clinically acceptable. Wright et al.²² and Patterson et al.¹⁷ stated that the polishing techniques lead to smoother surfaces than the autoglaze techniques; however, they are not a substitute of the autoglaze. These results reveal that HP pastes can be used for restoring the porcelain, whose glaze structure was damaged. In spite of this, Campbell et al.¹⁵ and Dalkiz et al.²¹ reported that the autoglaze operations are more suitable for producing smoother surfaces. These results contradict what we found in our study.

It was observed that there is no significant difference between Sof-Lex and polishing rubbers in terms of surface smoothness.^{25–28} It was determined that Sof-Lex discs are more suitable for creating smoother surfaces than the diamond-added pastes.¹⁴ After using SEM, Giordano et al.⁷ and Yilmaz et al.²⁰ found that the glaze treatments provide the smoothest surface, while Sof-Lex and rubber provide less smooth surfaces. In our study, with respect to the SEM findings, we found that Sof-Lex discs provide less smooth surfaces than the diamond-added HP paste and that our result contradicts the one of the above-mentioned scholars. This contradiction may be

attributed to the use of different pastes of different manufacturers.

5 CONCLUSIONS

Dental porcelains are the most widely preferred restoration materials thanks to their desired properties, such as the optical properties, being esthetic restorative materials, bio-compatible, resisting chewing loads, etc. Surface-finishing operations are very important for porcelains because these treatments increase the tissue compatibility by reducing the abrasive effect of porcelains, eliminating staining and plaque aggregation. Hence, when the effects of different surface-finishing treatments are evaluated, the following conclusions can be made:

From a morphological point of view, the overglaze and then the autoglaze are the most appropriate techniques to create the smoothest surfaces. In descending order, HP paste, rubber, Sof-Lex and sandpaper are increasingly less favorable for a finishing operation on a porcelain surface.

From a micromorphological point of view, certain finishing techniques generate similar surface qualities on all the porcelains.

6 REFERENCES

- ¹ A. M. Al-Wahadni, D. M. Martin, An in Vitro Investigation into the Wear Effects of Glazed, Unglazed and Refinished Dental Porcelain on an Opposing Material, *J. Oral Reh.*, 26 (1999), 538–546
- ² J. R. Ariel, Contemporary materials and technologies for All – Ceramic Fixed Partial Dentures: A Review of the Literature, *J. Prosth. Dent.*, 92 (2004) 2, 557–562
- ³ G. Clyde, Dental Ceramics. *Br. Dent. J.*, 164 (1988) 9, 231–246
- ⁴ H. Fischer, M. Schafer, R. Marx, Effect of Surface Roughness on Flexural Strength of Veneer Ceramics, *J. Dent. Res.*, 82 (2003) 12, 972–973
- ⁵ J. R. Mackert, S. W. Twiggs, C. M. Russell, A. L. Williams, Evidence of a Critical Leucite Particle Size for Microcracking in Dental Porcelains, *J. Dent. Res.*, 80 (2001) 6, 1574–1579
- ⁶ I. Denry, J. A. Holloway, Ceramics for Dental Applications: A Review, *Materials*, 3 (2010) 1, 351–368
- ⁷ R. Giordano, M. Cima, R. Pober, Effect of Surface Finish on the Flexural Strength of Feldspathic and Aluminous Dental Ceramics, *Int. J. Prost.*, 8 (1995) 4, 311–319
- ⁸ M. Guazzato, M. Albakry, L. Quanch, M. V. Swain, Influence of Grinding, Sandblasting, Polishing and Heat Treatment on the Flexural Strength of a Glass-Infiltrated Alumina-Reinforced, Dental Ceramic. *Biomaterials*, 25 (2004) 11, 2163–60
- ⁹ J. G. Ironside, M. V. Swain, Definitions of Mechanical Properties, *J. Austr. Ceram. Society*, 34 (1998) 2, 78–91
- ¹⁰ G. Isgro, P. Pallav, J. M. Van Der Zel, A. J. Feilzer, The Influence of the Veneering Porcelain and Different Surface Treatments on the Biaxial Flexural Strength of a Heat-Pressed Ceramic, *J. Prosth. Dent.*, 90 (2003) 5, 465–73
- ¹¹ K. Kawai, M. Inoue, Y. Tsuchitani, Effect of Ion-Exchange Treatment on Mechanical Properties of New Dental Ceramics, *Am. J. Dent.*, 16 (2003) 5, 347–350
- ¹² L. H. Klausner, G. T. Charbeneau, Polished Versus Autoglazed Porcelain Surfaces, *J. Prost. Dent.*, 47 (1982) 2, 157–162
- ¹³ R. T. Williamson, R. E. Kovarig, R. J. Mitchell, Effects of Grinding, Polishing, and Overglazing on the Flexure Strength of a High-Leucite Feldspathic Porcelain, *Int. J. Prost.*, 9 (1996) 1, 30–37
- ¹⁴ R. Haroon, Evaluation of the surface roughness of a standard abraded dental porcelain following different polishing techniques, *Journal of Dental Sciences*, 7 (2012) 2, 184–189
- ¹⁵ S. D. Campbell, Evaluation of Surface Roughness and Polishing Techniques for New Ceramic Materials. *J. Prosth. Dent.*, 61 (1989), 563–568
- ¹⁶ M. Jung, O. Wehlen, J. Klimek, Finishing and Polishing of Indirect Composite and Inlays In-Vivo, *Occlusal Surfaces, Oper. Dent.*, 29 (2004) 2, 131–141
- ¹⁷ C. J. Patterson, W. D. R. Stirrups, Efficacy of a Porcelain Refinishing System in Restoring Surface Finish after Grinding with Fine and Extra-Fine Diamond Burs, *J. Prost. Dent.*, 68 (1992), 402–406
- ¹⁸ N. Yoshiharu, H. Satoru, S. Hideaki, The effect of surface roughness on the Weibull distribution of porcelain strength, *Dental Materials Journal*, 29 (2010) 1, 30–34
- ¹⁹ W. J. Finger, M. D. Noack, Post Adjustment Polishing of CAD-CAM Ceramic with Luminescence Diamond Gel, *Am. J. Dent.*, 13 (2000) 1, 8–12
- ²⁰ K. Yilmaz, P. Ozkan, Profilometer evaluation of the effect of various polishing methods on the surface roughness in dental ceramics of different structures subjected to repeated firings, *Quintessence International*, 41 (2010) 7, 125–131
- ²¹ M. Dalkiz, C. Sipahi, B. Beydemir, Effects of Six Surface Treatment Methods on the Surface Roughness of a Low-Fusing and an Ultra Low-Fusing Feldspathic Ceramic Material, *Journal Of Prosthodontics-Implant Esthetic and Reconstructive Dentistry*, 18 (2009) 3, 217–222
- ²² M. D. Wright, R. Masri, C. F. Driscoll, E. Romberg, G. A. Thompson, D. A. Runyan, Comparison of Three Systems for The Polishing of an Ultra-Low Fusing Dental Porcelain, *J. Prosth. Dent.*, 92 (2004) 5, 486–490
- ²³ M. J. Edge, W. C. Wagner, Surface Cracking Identified in Polished and Self-Glazed Dental Porcelain, *J. Prosth.*, 3 (1994) 3, 130–133
- ²⁴ P. F. K. Motro, P. Kursoglu, E. Kazazoglu, Effects of Different Surface Treatments on Stainability of Ceramics, *J. Prosth. Dent.*, 108 (2012) 4, 231–237
- ²⁵ J. Martinez - Gomis, J. Bizar, J. M. Anglada, J. Samso, M. Peraire, Comparative Evaluation of Four Finishing Systems on One Ceramic Surface, *Int. Prost.*, 16 (2003) 1, 74–77
- ²⁶ D. Glavina, I. Skrinjaric, S. Mahovic, M. Majstorovic, Surface Quality of Cerec CAD - CAM Ceramic Veneers Treated With Four Different Polishing Systems, *Eur. J. Paediatr. Dent.*, 5 (2004) 2, 60–67
- ²⁷ M. Guazzato, M. Albakry, S. P. Ringer, M. V. Swain, Strength, Fracture Toughness and Microstructure of a Selection of All-Ceramic Materials. Part I. Pressable and Alumina Glass- Infiltrated Ceramics, *Dent. Mater.*, 20 (2004) 5, 441–448
- ²⁸ M. Guazzato, L. Quanch, M. Albakry, M. V. Swain, Influence of Surface and Heat Treatments on the Flexural Strength of Y-TZP Dental Ceramic, *J. Dent.*, 33 (2005) 1, 9–18

MICROTOMOGRAPHY IN BUILDING MATERIALS

MIKROTOMOGRAFIJA GRADBENIH MATERIALOV

Aleš Česen, Lidija Korat, Alenka Mauko, Andraž Legat

Zavod za gradbeništvo Slovenije, Dimičeva ulica 12, 1000 Ljubljana, Slovenija
ales.cesen@zag.si

Prejem rokopisa – received: 2012-05-14; sprejem za objavo – accepted for publication: 2013-03-13

X-ray computed microtomography (micro CT) is now widely available for a non-destructive evaluation of various building materials. It can provide information on the internal structure of small samples, with the maximum resolution of about 1 μm . For this study, samples of different building materials, such as concrete, mortar, steel, soils and asphalt composites, were selected. Their microstructure and pathology (corrosion) were determined mainly from the applicative point of view.

Keywords: X-ray computed microtomography, micro CT, 3D, imaging, building materials

Rentgenska računalniška mikrotomografija (mikroCT) je postala široko uporabna za nedestruktivne analize različnih gradbenih materialov. Zagotavlja informacije o notranji strukturi manjših vzorcev z največjo ločljivostjo 1 μm . V tej študiji so bili izbrani različni materiali, kot so beton, malta, jeklo, zemljina in asfaltni kompozit. Glavni cilj tega prispevka je oceniti mikrostrukturo in patologijo (korozijo) gradbenega materiala z uporabo rentgenske mikrotomografije, predvsem z vidika uporabe.

Ključne besede: rentgenska računalniška mikrotomografija, mikroCT, 3D, slikovna obdelava, gradbeni material

1 INTRODUCTION

Since the end of the 19th century, when Wilhem Conrad Röntgen discovered the existence of X-rays,¹ huge developments have occurred in their application. Computed tomography was introduced in the late 1970s,² following the evolution of computer science. CTs were most commonly used in the fields of medicine and industry. In recent years a big step forward, in this field, has been accomplished with the introduction of micro- and nanotomography,^{3,4} giving a totally new perspective to material science.

Micro-computed tomography (micro CT) is an X-ray-based imaging technique that can provide 3D views of the internal structures of investigated specimens. As the expression "micro" indicates, this technique makes it possible to achieve a spatial resolution that is better than one micron. The main advantages of tomography are that the specimens normally do not have to be specially prepared and that the method is non-destructive. Thus, the same specimen can be investigated under different conditions (e.g., monitoring the degradation processes during the ageing of a material, or any other changes to the material made under force or temperature loads). Like other methods, microtomography, too, has its limits.⁵ In the case of denser materials (with high Z values) and larger specimens, the scanning time quickly increases up to several hours or even several days. In order to increase the scanning speed, it is necessary to sacrifice a certain degree of image quality. The size of the specimens also has an impact on the final resolution, although the size is not a critical parameter and it is possible to achieve good spatial resolution even in the case of large specimens.

2 EXPERIMENTAL WORK

2.1 X-ray computed micro CT: the principles

Every tomograph consists of three basic parts; an X-ray source, a sample stage and a detection system. The X-ray source is usually an X-ray tube, in which electrons are accelerated by a known voltage and then they collide with the target (anode). The effect of a rapid braking of an electron as it hits its target is the high-energy electromagnetic radiation (Bremsstrahlung radiation), i.e., the X-rays. The problem is that this kind of radiation contains the whole energy spectrum of photons, up to the accelerating voltage. In any material, the photons of different energies have different absorption coefficients. The effect is known as "the beam hardening" and it makes a homogenous material look denser at the edges than it really is. This problem can be avoided with the use of the synchrotron radiation resulting in the monochromatic radiation with a very narrow energy spectrum. Additionally, the synchrotron radiation flux is many orders of magnitude greater than the radiation emitted by conventional X-ray tubes. In this way the scanning time can be significantly shortened.^{6,7} The detector system is another crucial part of each microtomograph. In order to detect the photons that make up X-rays, they have to be converted into visible light using an appropriate scintillator. A scintillator is a special kind of material which emits visible photons when excited by ionizing radiation. Between a scintillator and a CCD detector, there can be an optical system allowing an optical as well as a geometrical magnification. This greatly improves the resolution achieved for larger specimens. The best results and finest resolution can, however, only be obtained for reasonably small specimens. Unlike in the medical or

industrial CTs, the source and detector in a microtomograph are stationary during the scan – the specimen stage rotates around the vertical axis during the scanning process. In this way 2D absorption radiographs of a specimen are taken from every sample-orientation angle. These are then reconstructed in 3D in order to obtain a view of the interior structure of the material.

In its basic form, tomographic reconstructions provide 3D information about X-ray absorption. In this way, each 3D pixel (voxel) represents a piece of the matter with a certain X-ray absorption factor. Due to the different absorption factors of different phases in a specimen, it is easy to detect certain features, such as voids and grains of different compositions. By using a further image analysis, it is possible to determine the values of many different parameters, such as the pore-size distribution and the orientation of features as well as their volumes and areas, all of which are important for a good understanding of material properties and functionality.

2.2 X-ray computed micro CT: the building materials

Microtomography is a very useful technique for the building-material studies. In the case of smaller, specially prepared specimens, the technique is entirely non-destructive. This means that it is possible to study the same specimen at different ageing periods, or, for instance, before and after the temperature or pressure loads have been applied. Very good information can be obtained about how a building material may behave in different exposure environments. For instance, we can monitor a cement hydration process, or the growth of the cracks in concrete under load, 3D crack distribution in steel after a stress-corrosion cracking⁸ or a loss of material due to steel corrosion.^{9,10} Although there are literally endless possibilities, as with every measuring technique, there are also certain limitations, mainly with regard to the specimen size and the type of specimen material. Clearly, the weight and size of the test specimen must not exceed the nominal table capacity. These limitations vary from system to system, but, roughly, a test specimen can have a weight of up to several kilograms and a size in the order of a few decimeters. Although some tomography systems can achieve very fine resolutions in the case of larger samples, for the best results, smaller samples are much more appropriate. In practice, if a resolution of under a micron is needed, the sample size is usually limited to a few millimeters in diameter. Additionally, the X-ray absorption is an exponential function of the sample thickness. Thus, the scanning time is highly dependent on the sample size.

As already suggested, some types of materials are more appropriate than others for the tomography. In the case of the microtomograph that has been installed at the Slovenian National Building and Civil Engineering Institute (ZAG), the highest acceleration voltage is 150 kV. This voltage is certainly sufficient for investigating the materials such as concrete, stone, mortars, glass,

ceramics, wood and polymers. However, there are limitations in the case of the materials such as steel, copper and other denser metals. In order to investigate the materials of this kind, very small samples are needed in order to obtain a strong enough signal from the detector. Otherwise, the scanning time can be unreasonably long and the signal-to-noise ratio can be too low to provide qualitative information.

2.3 X-ray computed micro CT: the experimental procedure (image acquisition, processing and analysis)

In this study, the X-ray energy was set to different values. For the purpose of studying steel corrosion in concrete, using different methods, different concrete specimens with the dimensions of 450 mm × 100 mm × 55 mm with two embedded longitudinal reinforcement steel bars of the B500B quality were prepared. The specimen described in this paper was cyclically exposed to a 3.5 % solution of NaCl for a period of 4 years. The beam energy was set to the highest available value (150 kV, 66 μ A), due to the high density of the steel embedded in the concrete. 5000 images were recorded in order to get a good-quality 3D reconstruction (**Figures 1 and 2**). In the case of the tested concrete sample (**Figure 3**), the beam energy was set to a value of 140 kV and the intensity was kept constant at 70 μ A. Using a high-precision rotation stage, different projection images were taken at different views, with different exposure times per projection during the 360° rotation. In the case of the concrete sample, 4000 images were taken at different views with an exposure time of 3 seconds per projection. These projections were acquired with a CCD camera, and an optical magnification objective with a nominal power of 0.39 was used. The pixel resolution under these

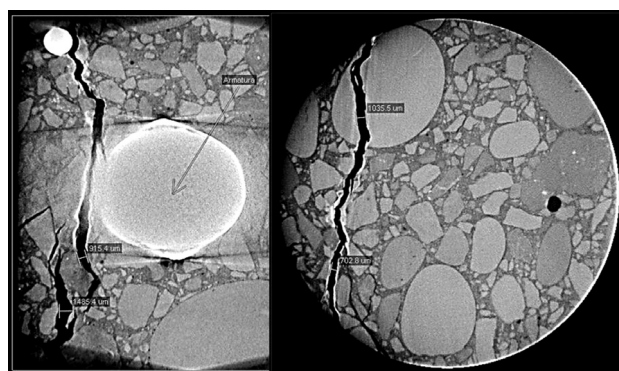


Figure 1: 2D slice in the XY direction of the steel bar embedded in the concrete (left image). A layer of the secondary corrosion products is visible on the surface of the embedded bar (the bright layer) as well as on the surface of the newly formed crack (left and right image). The cracks in the concrete cover were formed due to the increased volume of the secondary corrosion products.

Slika 1: 2D-rezina v XY-smeri jeklene armature (levo) v betonu. Na sliki so vidne plasti sekundarnih korozijskih produktov, in sicer tako na površini armature kot tudi v nastali razpoki v betonu (leva in desna slika). Razpoke v betonu so nastale zaradi povečane prostornine sekundarno nastalih korozijskih produktov.

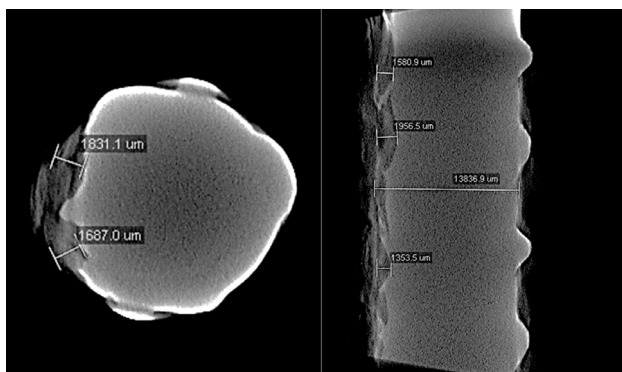


Figure 2: Horizontal (left) and vertical (right) cross-sections of the corroded steel bar. Approximately two millimeters of the bar was corroded due to the exposure.

Slika 2: Horizontalni (levo) in vertikalni (desno) prerez korodirane jeklene armaturne palice. Približno dva milimetra palice je bilo korodirane zaradi izpostavitve.

conditions was 29 μm . In the case of the mortar sample (**Figure 4**), the beam energy was set to a value of 80 kV. 1600 projections with an exposure time of 4 seconds were taken during the 360° rotation, and a 0.39-times optical magnification objective was used. The pixel resolution under these conditions was 19 μm . In order to investigate the cracks in a humid soil sample (**Figure 4**), the sample was embedded in a 2 mm thick glass capillary. The beam energy was then set to 60 kV and the intensity was kept constant at 166 μA . The sample was rotated during the 360° rotation, and 1000 images with a 25 s exposure time were recorded. With an optical magnification of 20, the final pixel resolution of 1.2 μm was obtained.

3 RESULTS AND DISCUSSION

The concrete cover of the embedded steel bar (**Figures 1 and 2**) was 1.0 cm. After four years of exposure, the first cracks became visible on the surface. Using the

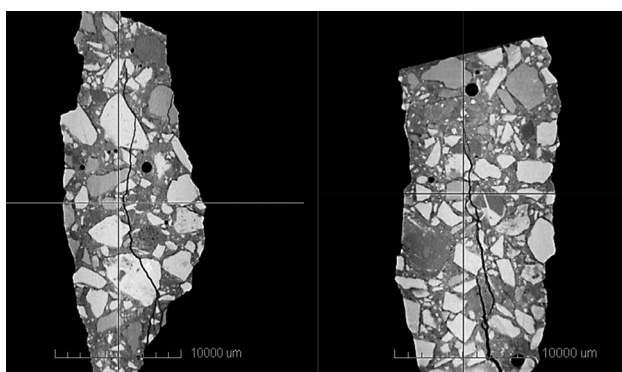


Figure 3: Vertical cross-sections of a piece of concrete approximately 3.0 cm in size. The cementitious matrix, at least two types of aggregate grains, air voids and cracks are presented in the image with different greyscale values.

Slika 3: Vertikalna prereza približno tri centimetre velikega kosa betona. Na sliki so z različnimi sivinskimi vrednostmi prikazani cementna matrika, vsaj dva tipa agregatnih zrn, zračne pore in razpoke.

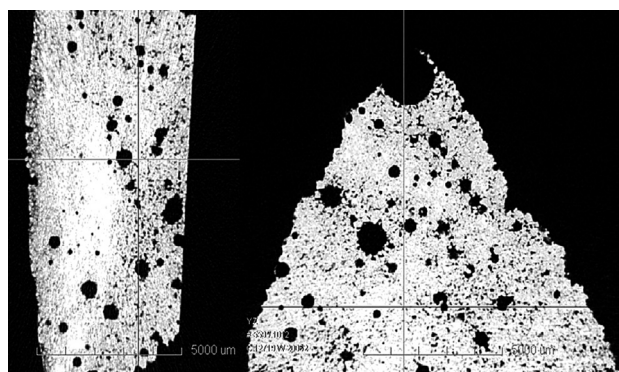


Figure 4: Vertical slices of the mortar specimen in the XY and YZ directions

Slika 4: Vertikalni rezini cementne malte z vidnimi zračnimi porami (črna faza) in cementno matriko (svetlejša faza)

tomography technique, it was possible to clearly detect and measure the cracks induced by the corrosion of the steel reinforcement. In the vicinity of the bars, the crack width was around 1 mm. The images of the reconstructed slices were somewhat blurred and of a lower quality, very close to the steel, which was a consequence of a very high contrast in the X-ray absorption between the steel bars and the surrounding concrete. Nevertheless, the loss of material on the bars was clearly visible. As expected, only the upper side of the reinforcement, which was closer to the exposed concrete surface, was highly corroded. Up to almost 2 mm of steel was corroded.

The representative slices in the XY direction (left) and the XZ direction (right) obtained from the concrete specimen are shown in **Figure 3**. As shown in this figure, the background (i.e., the surrounding air) is shown as dark voxels. The same dark voxels in the reconstructed greyscale image also correspond to the

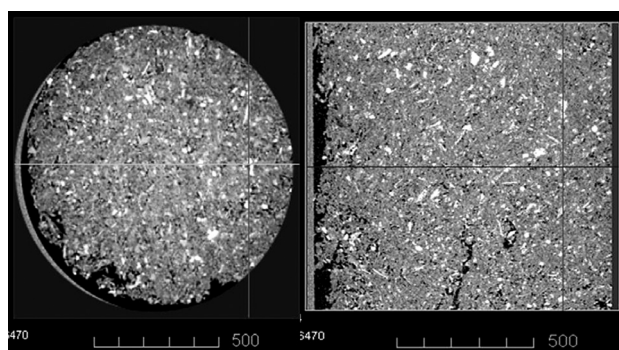


Figure 5: Horizontal slice (left) and a vertical slice in the XZ direction (right) of the humid-soil specimen in a glass capillary, partly visible on the left image. Different inorganic (brighter) and organic (darker) components are visible in the figure, as well as the cracks and air voids. A snapshot of a 3D representation of the soil structure is given in **Figure 6**.

Slika 5: Horizontalna (levo) in vertikalna (desno) rezina v smeri XZ mokre zemljine v stekleni kapilari, ki je vidna delno na sliki levo. Na sliki so vidne različne anorganske (svetlejša) in organske (temnejša) komponente, kot tudi razpoke in zračne pore. Izrez iz 3D-predstavitve materiala je podan na **sliki 6**.

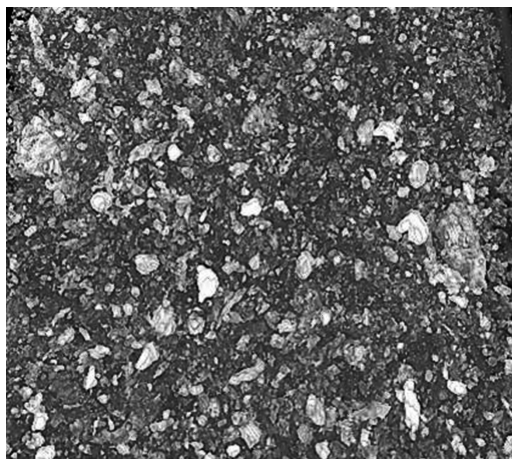


Figure 6: Snapshot of a 3D representation of the soil structure
Slika 6: Izrez iz 3D-predstavitve vzorca zemljine

low-density phases such as air voids or pores. The brighter voxels denote the high-density phases, e.g., the cementitious matrix and aggregate grains as the phases with the highest density. The representative slices show different distributions of aggregate particles, with the typical diameters in excess of 50 μm . A large crack is visible in the XY and XZ directions. Thus, in this case the orthoslices show a clear presence of large aggregate particles, the cementitious matrix and air-void porosity. **Figure 4** shows reconstructed slices of the mortar. The brighter voxels denote the high-density phases of sand particles that are smaller than 0.5 mm. The light-to-dark-grey patches indicate the cementitious matrix. The dark voxels in the reconstructed greyscale image correspond to the air voids or pores with the diameters in excess of 1000 μm .

The first images of the soil sample in a glass capillary, only 2 mm thick, were taken with a 20-times optical magnification (**Figures 5 and 6**). To see different inorganic and organic components as well as cracks, further images were taken at a higher optical (40-times) magnification distinguishing the organic matter from the air pores and the fluid in these pores.

4 CONCLUSIONS

As can be seen from the results of the experimental study presented in this paper, the micro CT technique is a powerful technique for an in-situ monitoring of the microstructure evolution of different types of building materials. Both heterogenous and homogenous materials can be analyzed using the microtomographic technique, which makes this tool important for a non-destructive three-dimensional characterization. Additional techniques such as scanning electron microscopy can be used to identify individual phases. With the addition of the recently developed nanotomography and with possible phase identification, tomography has become an indispensable tool in the building pathology, as well as in all the individual fields of material science.

5 REFERENCES

- ¹ O. Glasser, Wilhelm Conrad Röntgen and the early history of the Roentgen rays, C. C. Thomas, Springfield, Ill., 1934
- ² E. N. Landis, D. T. Keane, X-ray microtomography, *Materials Characterization*, 61 (2010), 1305–1316
- ³ P. A. Midgley, E. P. W. Ward, A. B. Hungria, J. M. Thomas, Nanotomography in the chemical, biological and material sciences, *Chem. Soc. Rev.*, 36 (2007), 1477–1494
- ⁴ T. Hashimoto, X. Zhou, C. Lou, K. Kawano, G. E. Thompson, A. E. Hughes, P. Skeldon, P. J. Withers, T. J. Marrow, A. H. Sherry, Nanotomography for understanding materials degradation, *Scripta Materialia*, 63 (2010), 835–838
- ⁵ J. Y. Buffiere, E. Maire, J. Arien, J. P. Masse, E. Boller, In Situ Experiments with X ray Tomography: An Attractive Tool for Experimental Mechanics, *Experimental Mechanics*, 50 (2010), 289–305
- ⁶ E. Gallucci, K. Scrivener, A. Groso, M. Stamparoni, G. Margaritondo, 3D experimental investigation of the microstructure of cement pastes using synchrotron X-ray microtomography (μCT), *Cement and Concrete Research*, 37 (2007), 360–368
- ⁷ N. Burlion, D. Bernard, D. Chen, X-ray microtomography: Application to microstructure analysis of a cementitious material during leaching process, *Cement and Concrete Research*, 36 (2006), 346–357
- ⁸ T. J. Marrow, L. Babout, B. J. Connolly, D. Engelberg, G. Johnson, J. Y. Buffiere, P. J. Withers, R. C. Newman, High-resolution, in-situ, tomographic observations of stress corrosion cracking, *Environment-Induced Cracking of Materials*, 2 (2008), 439–477
- ⁹ M. Beck, J. Goebbels, A. Burkert, B. Isecke, R. Bässler, Monitoring of corrosion processes in chloride contaminated mortar by electrochemical measurements and X-ray tomography, *Materials and Corrosion*, 6 (2010), 475–479
- ¹⁰ T. S. Sprague, X-ray Tomography for Evaluation of Damage in Concrete Bond, Master Thesis, The University of Washington, 2006

INFLUENCE OF THERMOMECHANICAL PROCESSING ON THE COLD DEFORMABILITY OF LOW-CARBON STEEL

VPLIV TERMOMEHANSKE PREDELAVE NA HLADNO PREOBLIKOVALNOST MALOGLJIČNEGA JEKLA

Besim Baručija¹, Mirsada Oruč¹, Omer Beganović¹, Milenko Rimac¹, Sulejman Muhamedagić²

¹Institute of Metallurgy "Kemal Kapetanović" Zenica, University of Zenica, Travnička cesta 7, Zenica, Bosnia and Herzegovina

²Faculty of Metallurgy and Materials, University of Zenica, Travnička cesta 7, Zenica, Bosnia and Herzegovina
miz@miz.ba

Prejem rokopisa – received: 2012-08-31; sprejem za objavo – accepted for publication: 2013-01-29

The group of steels intended for the production of bolts and nuts from the production programme of the Zenica Steel Plant, Zenica, nowadays called Arcelor Mittal Zenica, includes, among others, the steel C8C according to EN 10263-2. In this paper, the results of testing the above-mentioned steel, with the nitrogen content of more than 0.007 %, manufactured within a specifically defined technological programme, are presented. The testing of the rolled bars with a diameter of 12 mm is focused, among the mechanical and metallographic tests, especially on the technological compression test in the cold state that is normally performed as an additional control test in the production. The cold compression of the test samples has been performed in four degrees of deformation and at two different speeds of compressing tools. We determined the dependence of the resistance to deformation of the material on the degree and speed of deformation. The surface inspection of the tested samples was performed with visual control with the aim to determine deformability of the bars produced in this way.

Keywords: low-carbon steel, deformation testing, compression, visual control

Skupina jekel, namenjena za izdelavo vijakov in matic iz proizvodnega programa Železarne Zenica iz Zenice, danes Arcelor Mittal Zenica, vsebuje med drugim tudi jeklo C8C, skladno s standardom EN 10263-2. V članku so predstavljeni rezultati preizkušanja omenjenega jekla z vsebnostjo dušika več kot 0,007 %, izdelanega po posebni tehnologiji. Preizkušanje valjanih palic premera 12 mm je poleg metalografskih in mehanskih preizkusov usmerjeno predvsem na tehnološki tlačni preizkus v hladnem, kar se navadno izvaja kot dodatni kontrolni preizkus v proizvodnji. Preizkus hladnega stiskanja vzorcev je bil izврšen s štirimi stopnjami deformacije in pri dveh hitrostih stiskanja. Določena je bila odvisnost med odpornostjo proti deformaciji materiala, stopnji deformacije in hitrosti deformacije. Ocena površine preizkušancev je bila izvršena z vizualnim nadzorom z namenom, da se ugotovi deformabilnost palic.

Ključne besede: maloogljično jeklo, preizkus deformacije, stiskanje, vizualni nadzor

1 INTRODUCTION

Aluminum is used as a deoxidizing agent during the production of low-carbon steels included in the standard EN 10263-2. This type of deoxidation creates favorable conditions for obtaining the steels with a high capability of being shaped in the cold state. Parallel to the process of binding oxygen to aluminum, aluminum also binds nitrogen in aluminum nitride (AlN) precipitates that, according to the known Zener mechanism of the grain boundary pinning,¹ block the growth of the austenite grains in the process of static and dynamic recrystallization and during the thermomechanical rolling process. In the usual process of thermomechanical rolling, according to the original MORGAN technology for the wire rolling mill, we obtain the steel with a fine-grained microstructure (ASTM8–ASTM10). The microstructure of this type of steel is characterized with the increased values of the yield strength and with a high resistance to plastic deformation and decreased plasticity.² Insufficient plasticity of this steel type is the result of strengthening through a reduction of the ferrite-grain size, the presence

of aluminum in the crystal lattice and the presence of aluminum nitride precipitates.

Sensitivity of this steel to cold deformation depends on the manner of nitrogen binding in the steel. Namely, if nitrogen is interstitially dissolved in the α -Fe crystal lattice during the process of natural aging, it will bind to iron in Fe₄N. This is directly connected to an increased sensitivity of the steel to cold deformation. This sensitivity increases with an increase in the nitrogen content in the steel. But, if nitrogen is in the form of aluminium nitride then the sensitivity of the steel to cold deformation decreases.

Particle precipitates and grain boundaries are obstacles for dislocation motion. With an increased number of these obstacles, the resistance of the steel to deformation increases and the plasticity of the steel decreases. Non-coherent precipitates are weaker obstacles for dislocation motion than coherent precipitates because dislocations, during their motion round the non-coherent precipitates, form Orowan loops around such precipitates.³ The formation of Orowan loops represents the initial reaction of the dislocation with the precipitates and a continuation of

the plastic deformation, which is accompanied by a deformation strengthening, a further reaction. The external load to be applied to cause the initial reaction and to reach the yield stress represents a measure of precipitation hardening, while an additional increase in the load, allowing a continuation of the reaction represents a measure of deformation strengthening.

2 EXPERIMENTAL WORK

Sixteen experimental heats with a weight of 120 t were produced in the LD converters. The chemical compositions of all the heats are within the permissible limits for the steel C8C according to the standard EN 10263-2 (**Table 1**).

Table 1: Chemical composition according to standard EN 10263-2
Tabela 1: Kemijska sestava, skladna s standardom EN 10263-2

Steel	Content of elements in mass fractions (w/%)					
	C	Si _{max}	Mn	P _{max}	S _{max}	Al
C8C	0.06–0.10	0.10	0.25–0.45	0.020	0.025	0.020–0.060

All the produced heats were hot rolled into the semi-products with the dimensions of 115 mm × 115 mm × 12000 mm, and then into the wires with the diameters from 6 mm to 12 mm using a MORGAN – USA wire rolling mill. Eight heats were processed according to the original technological prescriptions defined by MORGAN and the remaining eight heats were processed according to the corrected prescriptions related to the heating of semi-products and the corrected prescription related to the thermomechanical treatment (rolling and cooling). In the phase of the semi-product heating a longer stay of a semi-product in the walking-beam furnace was provided for by increasing the rolling rhythm from 13 s to 16 s, depending on the diameter of the rolled wires. A longer stay of the semi-products in the walking-beam furnace enables the coarsening of the aluminium nitride precipitates. By reducing the semi-product temperature in the walking-beam furnace by 50 °C we reduced the possibility of a complete dissolution of the aluminium nitride precipitates in the matrix after achieving Ostwald ripening⁴ at a temperature above 1150 °C. Through an equable rolling rhythm it was provided that the final rolling temperature was between 950–980 °C with the aim of creating the conditions for the static and dynamic recrystallization of the austenite so as to ensure coarse grains in the structure after the phase austenite-ferrite transformation, which is more suitable for further cold plastic deformation. The reduction of the cooling speed after the final rolling pass by stopping the forced cooling and the reduction of the speed of the STELMOR conveyor from 25 m/min to 19 m/min had similar effects. A slow cooling of the rolled wire provides better conditions for the static recrystallization and a growth of the recrystallized austenitic

grains. Also, according to Beeghly,^{5,6} a lower cooling rate creates favourable conditions for a precipitation of aluminium nitride particles in the temperature interval of 950–750 °C in the steel matrix. In this way we prevented dissolution of the nitrogen in the ferrite crystal lattice that is a result of the natural aging process in the steel and of the intense deformation strengthening of the steel during the cold plastic deformation.

The size of the secondary grain of the wire produced with the new manufacturing technology is between 6 and 8 per ASTM scale, which is 1 to 2 grades less than the size of the secondary grain of the wire produced with the original MORGAN technology. A microstructural analysis indicates that for both production technologies the ferrite content in the material is between 93 % and 95 % and perlite is between 5 % and 7 %, depending on the carbon content of each heat, in other words, if the carbon content is high the content of perlite is high too. The tensile properties of the hot rolled wires produced with both technologies (old and new) are in accordance with the prescribed values according to the standard EN 10263-2 for the steel C8C. The tensile-strength and yield-strength values for the wires produced with the new technology are lower by 12 MPa to 21 MPa in comparison with the wires produced with the old technology. The values for the elongation and reduction of the area of the wires produced with the new technology are higher by 2.8 % to 4.8 % in comparison with the wires produced with the old technology.^{7,8}

3 RESULTS AND DISCUSSION

The testing of the steel plasticity in industrial conditions was carried out with a compression test in the cold state on the samples with a height of $h_0 = 1.5d_0$ (d_0 – diameter of a rolled wire). The final height was one-third of h_0 .

The estimation of the sample surfaces after cold compression was conducted by using a rating of 0 to 3, where the ratings of 0 and 1 indicated a satisfactory surface and the ratings of 2 and 3 an unsatisfactory one. The shallow grooves that occur as rolling scars as well as the typical fiber surface cracks that mostly appeared on the test samples with a surface estimation of 0 and 1 are not considered as surface defects. The results of the estimation of the tested samples' surface condition after the cold compression for the old and new manufacturing technologies are given in **Table 2**. The test results clearly indicate that the ability for cold forming of the wires produced with the new technology increased much more than the ability of the wires produced with the old manufacturing technology.

The compression test at room temperature in the laboratory conditions was carried out on a SINTECH 10/D (USA) tester at the Polytechnic University of Turin. We tested the rolled wires with a diameter of 12 mm made from the heats 350871 and 350866. The chemical compositions of these heats are given in **Table 3**.

Table 2: Summary review of the estimation of the sample surfaces after the cold compression test of the rolled wires with the diameters of 6 mm to 12 mm, produced with the old and new technologies**Tabela 2:** Pregled ocene površine po hladnem stiskanju valjane žice s premerom od 6 mm do 12 mm, izdelane po stari in novi tehnologiji

Techno- logy	Number of rolled coils for plasticity testing	Estimation of the sample surface after the cold compression test (n_0, n_1, n_2, n_3)/%								Sum of the coils with the plasticity esti- mation of 0 and 1		Sum of the coils with the plasticity estimation of 2 and 3	
		0		1		2		3					
		n_0	%	n_1	%	n_2	%	n_3	%	$n_0 + n_1$	%	$n_2 + n_3$	%
Old	509	71	13.9	113	22.2	127	24.9	198	38.9	184	36.2	325	63.8
New	581	306	53.2	251	47.7	14	2.4	10	1.7	557	95.9	24	4.1

Note: n_0, n_1, n_2, n_3 are numbers of defect classification

Table 3: Chemical compositions of the tested heats**Tabela 3:** Kemijska sestava preizkušanih talin

Heat	C	Si	Mn	P	S	Cu	Cr	Ni	Al	N
	w/%									
350866	0.07	0.05	0.39	0.015	0.013	0.06	-	0.02	0.047	0.0114
350871	0.08	0.05	0.38	0.010	0.012	0.06	0.02	0.02	0.047	0.0112

The original height of the tested samples was $h_0 = 24$ mm. It means that the ratio between the original height and the diameter ($h_0 = 2d_0$) was not standardized. The cold compression was carried out in four compression degrees and at two deformation speeds (0.5 mm/s and 1.0 mm/s). All the relevant parameters of the process that were measured or calculated are shown in **Tables 4** and **5**. These tables give the estimations of the tested sample surfaces according to the accepted criteria for industrial conditions with the aim of achieving estimation coherence.⁷

The degree of deformation is calculated according to the following equation:

$$\varphi = \ln\left(\frac{h_0}{h}\right) \quad (1)$$

where h_0 is the original height of a sample before the compression, h is the height of a sample after the compression.

The resistance of steel to deformation is calculated according to the following equation:

$$k_f = \frac{F \cdot h}{A_0 \cdot h_0} \left(\frac{N}{\text{mm}^2} \right) \quad (2)$$

where F is the compression force (N), A_0 is the original cross-section of a tested sample before the compression.

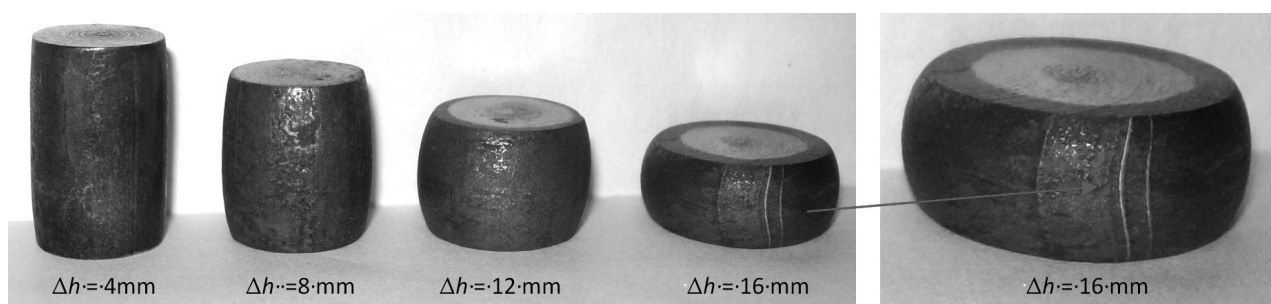
The results of the plasticity testing conducted on the nonstandard samples ($h_0 = 2d_0$) at room temperature and with different degrees and rates of deformation indicate that the low-carbon steel, which deoxidized due to aluminum and was produced with the new thermomechanical process on the MORGAN wire rolling mill, is very plastic (**Tables 4** and **5**). We observed and recorded the defects with the ratings of 0 or 1, but the 0 rating is the dominant surface-condition estimation. At the compression-tool speed of 0.5 mm/s, which is the standard requirement, the 0 rating was recorded for the third and fourth deformation degrees, and at the tool speed of 1.0 mm/s, which is a nonstandard requirement, it was determined that the surface condition rating of 0 related to the second and third deformation degrees, while rating 1 related to the fourth degree of deformation. The ratings

Table 4: Results of the compression testing at room temperature of the wires with a diameter of 12 mm from the heat 350866 for the testing speeds of 0.5 mm/s and 1.0 mm/s**Tabela 4:** Rezultati stiskanja pri sobni temperaturi za žico premera 12 mm iz taline 350866 pri hitrostih preizkusa 0,5 mm/s in 1,0 mm/s

Sample number	Average compression force	Reduction of height	Compres- sion speed	Time of compression	Deformation rate	Degree of deformation	Average resistance to deformation	Surface estimation after compression [Exist (+), Nonexist (-)]			
	F/N	$\Delta h/\text{mm}$	$v/(\text{mm/s})$	t/s	$\dot{\varphi}/\text{s}^{-1}$	φ	$k_f/(\text{N/mm}^2)$	0	1	2	3
1.1–4.1	69519	4	0.5	8	0.1823	2.279×10^{-2}	512.2	–	–	–	–
1.2–4.2	103039	8	0.5	16	0.4055	2.534×10^{-2}	607.4	–	–	–	–
1.3–4.3	140591	12	0.5	24	0.6931	2.888×10^{-2}	621.5	+	–	–	–
1.4–4.4	218922	16	0.5	32	1.0986	3.433×10^{-2}	645.2	+	–	–	–
1.5–4.5	71785	4	1.0	4	0.1823	4.557×10^{-2}	528.9	–	–	–	–
1.6–4.6	105292	8	1.0	8	0.4055	5.068×10^{-2}	621.0	+	–	–	–
1.7–4.7	142252	12	1.0	12	0.6931	5.776×10^{-2}	628.9	+	–	–	–
1.8–4.8	224235	16	1.0	16	1.0986	6.866×10^{-2}	660.9	–	+	–	–

Table 5: Results of the compression testing at room temperature of the wires with a diameter of 12 mm from the heat 350871 for the testing speeds of 0.5 mm/s and 1.0 mm/s**Tabela 5:** Rezultati stiskanja pri sobni temperaturi za žico premera 12 mm iz taline 350871 pri hitrostih preizkusa 0,5 mm/s in 1,0 mm/s

Sample number	Average compression force	Reduction of height	Compression speed	Time of compression	Deformation rate	Degree of deformation	Average resistance to deformation	Surface estimation after compression [Exist (+), Nonexist (-)]			
	F/N^*	$\Delta h/mm$	$v/(mm/s)$	t/s	$\dot{\varphi}/s^{-1}$	φ	$k_p/(N/mm^2)$	0	1	2	3
1.1–4.1	71431	4	0.5	8	0.1823	2.279×10^{-2}	526.3	–	–	–	–
1.2–4.2	104098	8	0.5	16	0.4055	2.534×10^{-2}	613.9	–	–	–	–
1.3–4.3	141983	12	0.5	24	0.6931	2.888×10^{-2}	627.6	+	–	–	–
1.4–4.4	221047	16	0.5	32	1.0986	3.433×10^{-2}	651.5	+	–	–	–
1.5–4.5	72764	4	1.0	4	0.1823	4.557×10^{-2}	536.3	–	–	–	–
1.6–4.6	106957	8	1.0	8	0.4055	5.068×10^{-2}	630.5	+	–	–	–
1.7–4.7	143398	12	1.0	12	0.6931	5.776×10^{-2}	633.9	+	–	–	–
1.8–4.8	227316	16	1.0	16	1.0986	6.866×10^{-2}	669.9	–	+	–	–

**Figure 1:** Surfaces of cold compressed specimens of the wire with a diameter of 12 mm from the heat No. 350866 (surface-defect rating 1 after the fourth degree of deformation, $\Delta h = 16$ mm, the tool speed of the testing machine is 1 mm/s)**Slika 1:** Površina hladno stisnutih vzorcev žice premera 12 mm iz taline št. 350866 (površinska napaka, označena z 1 po četrti stopnji deformacije, $\Delta h = 16$ mm, hitrost orodja na preizkusnem stroju 1mm/s)

of 0 and 1 relate to small, shallow surface defects resulting from the rolling scars (**Figure 1**).

4 CONCLUSION

The new thermomechanical rolling process on the MORGAN wire rolling mill, applied to the low-carbon steel C8C, provides a better grain-boundary migration, set with Zener's criteria, during the heating process and during the dynamic and static recrystallization, that is, the coarsening of the austenite grains and, consequently, the growth of the secondary grains. Also, the precipitates of aluminum nitride have a tendency towards Ostwald ripening. The coarser aluminum nitride precipitates, which have no coherent link with the matrix, are lower barriers to the movement of dislocations during the plastic deformation due to the Orowan mechanism. This, in combination with the coarser secondary structure, taking into account the Hall-Petch equation, ensures lower values of the upper yield stress and a lower defor-

mation resistance and high ductility of the steel C8C wire in the cold state.

5 REFERENCES

- ¹ C. Zener (quoted by C.S. Smith), Trans. Am. Inst. Min. Engrs., 175 (1948), 15–51
- ² N. J. Petch, JISI, 174 (1953), 25–28
- ³ E. Orowan, M. Cohen (eds), Dislocation in Metals, American Institute of Mining and Metallurgical Engineers, New York 1954, 128–134
- ⁴ A. Prikhodovsky, Prediction of the size distribution of precipitates, Steel Research, 72 (2001), 11/12
- ⁵ H. F. Beeghly, Analytical Chemistry, 21 (1949), 1513–1521
- ⁶ H. F. Beeghly, Analytical Chemistry, 24 (1952), 1095–1100
- ⁷ B. Baručija, Mehanizmi djelovanja aluminijumnitrida na hladnu deformabilnost niskougljeničnog čelika umirenog sa aluminijumom kod sadržaja azota >70 ppm, Ph. D. Thesis, Univezitet u Zenici, 2010
- ⁸ B. Baručija, M. Oruč, O. Beganović, M. Rimac, Uticaj aluminijumnitrida na hladnu deformabilnost niskougljeničnog čelika za izradu vijaka, IX Naučni/stručni simpozij sa međunarodnim učešćem "Metalni i nemetalni materijali", Zenica, BiH, 2012

OXIDATION OF THE Al_2O_3 - TiB_2 COMPOSITES PRODUCED WITH THE REDUCTION-COMBUSTION SYNTHESIS TECHNIQUE

OKSIDACIJA KOMPOZITA Al_2O_3 - TiB_2 , IZDELANEGA S TEHNIKO REDUKCIJSKE ZGOREVNE SINTEZE

Nuri Ergin, Yigit Garip, Ozkan Ozdemir

Sakarya University, Technology Faculty, Department of Metallurgy and Materials Engineering, 54187 Esentepe Campus, Sakarya, Turkey
nargin@sakarya.edu.tr

Prejem rokopisa – received: 2012-08-31; sprejem za objavo – accepted for publication: 2013-03-04

In this study, Al_2O_3 - TiB_2 composites were synthesized in an electrical resistance furnace in open atmosphere under the uniaxial pressure of 150 MPa at 1200 °C for 4 h, using the reduction-combustion synthesis technique. The initial powder mixture used in this study is $\text{Al}+\text{TiO}_2+\text{B}_2\text{O}_3$. TiB_2 , Al_2O_3 and some trace phases were found in the produced composites using the X-ray diffraction analysis. The densities of the samples were measured using the Archimedes' technique. The relative density was determined as 94.2 % for the composites. The oxidation properties of the composites were examined in open atmosphere at 600 °C, 800 °C and 1000 °C after up to 64 h. The activation energy of the composite was calculated to be 90 kJ/mol.

Keywords: composite, sintering, reduction combustion synthesis, oxidation

V tej študiji je bil sintetiziran kompozit Al_2O_3 - TiB_2 v električni uporovni peči z normalno atmosfero pri enoosnem tlaku 150 MPa in 4 h pri 1200 °C z uporabo tehnike redukcijske zgorevne sinteze. Začetna mešanica prahov, uporabljena v tej študiji, je bila $\text{Al}+\text{TiO}_2+\text{B}_2\text{O}_3$. Z rentgensko difrakcijo so bili v izdelanem kompozitu odkriti TiB_2 , Al_2O_3 in nekaj faz v sledovih. Gostota vzorcev je bila izmerjena z Arhimedovo tehniko. Relativna gostota kompozita je bila 94,2-odstotna. Oksidacijske lastnosti kompozita so bile preiskane na zraku po 64 h na temperaturah 600 °C, 800 °C in 1000 °C. Izračunana aktivacijska energija kompozita je bila 90 kJ/mol.

Ključne besede: kompozit, sintranje, redukcijska zgorevna sinteza, oksidacija

1 INTRODUCTION

Reduction (thermite type) combustion synthesis (RCS) is one of the three main types of combustion synthesis from the viewpoint of chemical nature.¹ The in-situ synthesis is used for fabricating the metal- or ceramic-matrix composites.² As the reinforcements are generated directly from the chemical reaction within the matrix, the composites show many excellent advantages, such as a clean reinforcement-matrix interface, fine and thermodynamically stable reinforcement, good compatibility and high bonding strength between the reinforcement and the matrix, and low fabrication costs.³ When TiC or TiB_2 are combined with Al_2O_3 , the composite, without a significant drop in the hardness, has a better oxidation resistance and possesses a superior mechanical strength and fracture toughness than TiC or TiB_2 alone. Researchers have chosen reduction (thermite type) combustion synthesis systems like $\text{TiO}_2/\text{Ti}-\text{B}_2\text{O}_3/\text{B}-\text{Al}$, $\text{Nb}-\text{B}-\text{Al}-\text{Nb}_2\text{O}_5$, $\text{ZrO}_2-\text{B}_2\text{O}_3-\text{Al}$, TiO_2-Al for fabricating the Al_2O_3 based in-situ composites.⁴⁻⁶ The main objective of the present study is to investigate the synthesis of the Al_2O_3 - TiB_2 in-situ composites produced from TiO_2 , B_2O_3 and Al precursors with the one-step, pressure-assisted, reduction-combustion technique, and the oxidation properties of the produced composites.

2 EXPERIMENTAL DETAILS

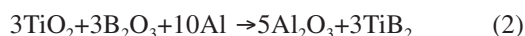
The Al_2O_3 - TiB_2 in-situ composite was densified by uniaxial loading during the reaction. TiO_2 (98.8 % purity, 1 μm), B_2O_3 (99.99 % purity, less than 38 μm) and Al (99 % purity, 15 μm) were used in the powder mixtures to produce the TiB_2 - Al_2O_3 composites using the aluminothermic reduction. The mixed powders were pressed in a cylindrical mold, then the in-situ composite was formed in an electrical resistance furnace in open atmosphere under a uniaxial pressure of 150 MPa, at 1200 °C, with a heating rate of 20 °C/min and for 4 h. To examine the relative density, the Archimedes' method with a sensitive balance (0.0001 g) was applied. The specimens were polished with the emery papers (up to 1200 grit) and, finally, with a diamond paste up to 1 μm before the oxidation test. The oxidation properties of the samples were investigated at 600 °C, 800 °C and 1000 °C for (4, 16, 32 and 64) h in open atmosphere. Each sample was carefully weighed before and after the oxidation test to determine the weight changes. The morphology and nature of the oxide layer and the phases formed in the oxidized layers of the samples, tested at 600 °C, 800 °C and 1000 °C for 64 h, were characterized using the SEM and XRD analyses. In order to understand the kinetics of the oxidation, the data were analyzed using the parabolic law:

$$\left(\frac{\Delta w}{A}\right)^2 = k_p t \quad (1)$$

where Δw is the change in the weigh, A is the surface area of the sample, t is the oxidation time and k_p is the parabolic rate constant.⁷

3 RESULTS AND DISCUSSION

The composite produced with the pressure-assisted RCS is compact and dense. This technique is more advantageous than the classic two-step production methods. The aluminothermic reaction results in the Al₂O₃-TiB₂ composite according to the following reaction:



TiB, TiO₂ and the Al₅BO₉ trace phases, along with the major Al₂O₃ and TiB₂ peaks, were observed during the XRD analysis (**Figure 1**). The Al₂O₃-TiB₂ composite with the calculated volume proportions of Al₂O₃ (71 %) and TiB₂ (27 %) was obtained with a synthesizing system of 3TiO₂-3B₂O₃-10Al.⁸ In the present study, the relative densities of the samples, synthesized under a pressure of 150 MPa and at 1200 °C for 4 h, were measured as 94.2 %.

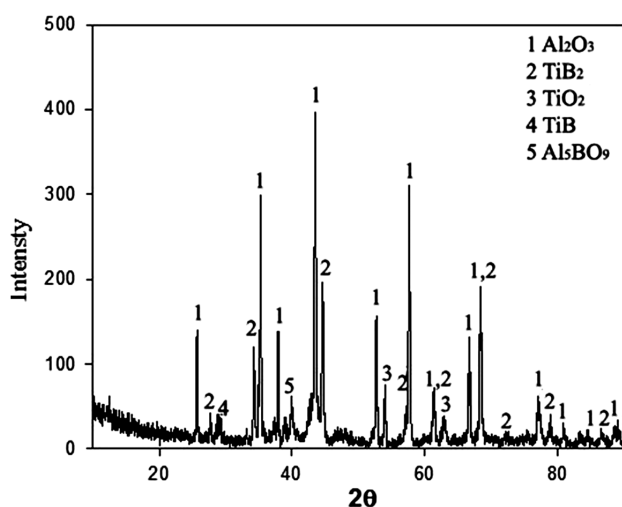


Figure 1: XRD diffraction patterns of the synthesizing at 1200 °C for 4 h

Slika 1: Rentgenska difrakcija sintetiziranega kompozita po 4 h na 1200 °C

Table 1: Variation in the weight gain as a function of the process time and temperature

Tabela 1: Spreminjanje prirastka mase v odvisnosti od časa in temperature procesa

Time (h)	Weight change (g/cm ²)		
	600 °C	800 °C	1000 °C
4	0.587	1.493	2.322
16	0.618	2.899	3.277
32	0.709	3.123	3.738
64	0.782	3.322	4.371

The mass change of the oxidized samples during the oxidation treatment at 600 °C, 800 °C and 1000 °C as a function of the process time for the Al₂O₃-TiB₂ composites occurred parabolically with the process time. The mass changes of the composites during the oxidation test at 600 °C, 800 °C and 1000 °C, lasting for 4–64 h, are listed in **Table 1**.

The parabolic rate constant was calculated from the slope of the plots that was drawn from the square of the mass change versus the treatment time of the composites. The parabolic rate constants (k_p) of the composites during the oxidation tests at 600 °C, 800 °C and 1000 °C are $0.322 \cdot 10^{-5} \text{ g}^2/(\text{cm}^4 \text{ s})$, $5.98 \cdot 10^{-5} \text{ g}^2/(\text{cm}^4 \text{ s})$, and $9.59 \cdot 10^{-5} \text{ g}^2/(\text{cm}^4 \text{ s})$, respectively. The temperature dependence of the parabolic rate constant (k_p) follows an Arrhenius-type expression, $k_p = k_0 \exp(-Q/RT)$. The slope of the plots that was drawn from the $L_n K_p$ -values versus $1/T$ is to give the Q/R -value. In the present study, the calculated value of the activation energy was approximately 90 kJ/mol in the temperature range of 600–1000 °C, for the Al₂O₃-TiB₂ composite.

Tampieri and Bellosi⁹ have reported the activation energy of 230 kJ/mol ($T = 400\text{--}900$ °C) and 40 kJ/mol ($T = 900\text{--}1100$ °C) for the monolithic TiB₂. An activation energy of 110.56 kJ/mol was reported for the temperature range of 750–950 °C by Murthy et al.¹⁰ Murthy et al. explained that the vast difference in the activation energy for the TiB₂ oxidation with the temperature is due to the change in the mechanism caused by the evaporation of B₂O₃ at higher temperatures. The SEM images of the oxidized surfaces of the composites at 1000 °C for 64 h are shown in **Figure 2**. The cracks, along with the coarsening of the oxide, were observed on the surface of the sample oxidized at 1000 °C. The results presented are consistent with the study of Murthy et al.⁷ A large volume expansion was seen during the oxidation of the composites. During the oxidation process, the TiB₂ phase oxidized and, subsequently, changed to the TiO₂ phase. During the oxidation, the transformation of the TiB₂ phase to TiO₂ causes a cracking of the oxide layer, resulting in an increase in the active area for further oxidation.⁷ Because of the active area formed by the cracks, the oxide layer was thought to accelerate this mechanism. The oxide layer was charac-

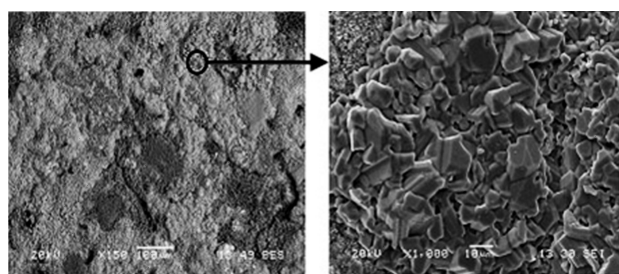


Figure 2: SEMs of the oxidized surfaces of the composites at 1000 °C after 64 h

Slika 2: SEM-posnetka oksidirane površine kompozita po 64 h na 1000 °C

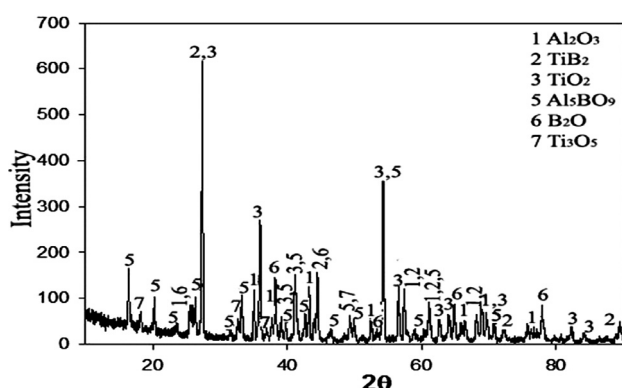
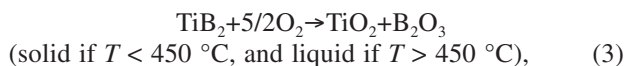


Figure 3: XRD patterns of the oxidized surfaces of the composite specimens at 1000 °C after 64 h

Slika 3: Rentgenska difrakcija oksidirane površine vzorca po 64 h na 1000 °C

terized by the presence of the surface cracks, probably caused by either the large volume expansion of B_2O_3 or the thermal stresses generated during the cooling.¹¹ The X-ray diffraction patterns of the oxidized undoped and doped composites at 1000 °C for 64 h are given in **Figure 3**.

The phases formed in the oxidized layer of the composite materials at 1000 °C after 64 h were the TiO₂, B₂O, Al₃BO₉ and Ti₃O₅ phases, besides the Al₂O₃ and TiB₂ phases. Possible reactions of TiB₂, B₂O₃ and Al₂O₃ are:



TiO₂ is a semi-protective oxide formed at a high temperature. Depending on the defect concentration, the growth of TiO₂ is governed by either an outward diffusion of the interstitial Ti ions or an inward diffusion of the oxygen ions via the vacancies.¹¹ It is possible that B₂O₃ has the dominant effect on the oxidation of the TiO₂ phase.

4 CONCLUSION

This study reports on the oxidation properties of an $\text{Al}_2\text{O}_3\text{-TiB}_2$ in-situ composite obtained with the pressure-assisted, reduction-combustion synthesis of the thermite mixtures. The mass (the weight gain) of the oxidized samples during the oxidation treatment in open atmosphere at 600 °C, 800 °C and 1000 °C as a function of the process time (up to 64 h) for the $\text{Al}_2\text{O}_3\text{-TiB}_2$ composites was changing parabolically with the process time. The activation energy of the composites was calculated to be 90 kJ/mol.

Acknowledgement

This work was supported by SAU Scientific Research Foundation (Project No: 2009-50-01-043).

5 REFERENCES

- ¹ A. Varma, A. S. Mukasyan, Powder Metal Technologies and Applications, ASM Handbook, volume 7, ASM International, 1988, 523–40
- ² S. C. Tjong, Z. Y. Ma, Materials science and Engineering: Reports, 29 (2000) 49, 113
- ³ H. Zhu, H. Wang, L. Ge, S. Chen, S. Wu, Transactions of Nonferrous Metals Society of China, 17 (2007), 590–4
- ⁴ E. Y. Gutmanas, I. Gotman, Ceramics International, 26 (2000), 699–707
- ⁵ W. Deqing, Journal of the European Ceramic society, 29 (2009), 1485–92
- ⁶ D. Vallauri, V. A. Shcherbakov, A. V. Khitev, F. A. Deorsola, Acta Materialia, 56 (2008), 1380–1389
- ⁷ T. S. Murthy, J. K. Sonber, C. Subramania, R. K. Fotedar, M. R. Gonal, A. K. Suri, Int. J. of Refr. Met. and Hard Materials, 27 (2009), 976–984
- ⁸ M. A. Meyers, E. A. Olevsky, J. Ma, M. Jamet, Materials Science and Engineering A, 311 (2001), 83–99
- ⁹ A. Tampieri, A. Bellosi, Journal of Materials Science, 28 (1993), 649–53
- ¹⁰ T. S. Murthy, J. K. Sonber, C. Subramania, R. K. Fotedar, M. R. Gonal, A. K. Suri, Int. J. of Refr. Met. and Hard Materials, 28 (2010), 529–40
- ¹¹ D. B. Lee, Y. C. Lee, D. J. Kim, Oxidation of Metals, 56 (2001), 177–89

OPTIMISATION OF THE SLAG MODE IN THE LADLE DURING THE STEEL PROCESSING OF SECONDARY METALLURGY

OPTIMIRANJE ŽLINDRE V PONOVCU PRI IZDELAVI JEKLA PO POSTOPKU SEKUNDARNE METALURGIJE

Ladislav Socha¹, Jiří Bažan¹, Karel Gryc¹, Jan Morávka², Petr Styrnal³,
Václav Pilka⁴, Zbygněv Piegza⁴

¹VŠB – Technical University of Ostrava, FMME, Department of Metallurgy and Foundry, 17. listopadu 15/2172, 708 33 Ostrava – Poruba, Czech Republic

²Materiálový a Metalurgický Výzkum, s.r.o., Pohraniční 693/31, 706 02 Ostrava, Czech Republic

³JAP Trading, s.r.o., Karpentná 146, 739 94 Třinec, Czech Republic

⁴Třinecké Železářny, a.s., Průmyslová 1000, 739 70 Třinec – Staré Město, Czech Republic
ladislav.socha@vsb.cz

Prejem rokopisa – received: 2012-10-15; sprejem za objavo – accepted for publication: 2013-03-19

Optimisation of the slag mode in the ladle with the help of briquetted fluxing agents, based on Al_2O_3 under various technological conditions is the object of this paper. The aim of the industrial experiments was to assess the possibility of achieving the optimum chemical composition of the slag that would improve the kinetic conditions of the refining ladle slag during the treatment in secondary metallurgy units. Industrial experiments were focused on comparing the influences of different slag-making agents such as lime (CaO), briquetted fluxing agents and deoxidation agents forming calcium carbide (CaC_2) and granular aluminium ($\text{Al}_{\text{granul}}$). During the evaluation of the slag mode in the ladle, samples of the steel from different technological places under operational conditions were taken to assess the desulphurization degree. The samples of the slag for evaluating the chosen parameters, such as basicity, the content of easily reducible oxides, the proportion of $\text{CaO}/\text{Al}_2\text{O}_3$ and the Mannesmann index, were taken too. Further, the temperature and the oxygen activity in the steel were continuously measured too. The results mentioned in this paper represent the basic information about the possibilities of the slag-mode optimisation in the ladle using different proportions of the slag-making additions, briquetted fluxing agents as well as the deoxidation agents within secondary metallurgy.

Keywords: secondary metallurgy, slag, fluxing agents, steel, desulphurization

Predmet tega članka je optimiranje žlindre v ponovci z briketiranim talilom na osnovi Al_2O_3 v različnih tehnoloških razmerah. Namen preizkusov je bil ugotoviti možnosti za doseganje optimalne kemijske sestave žlindre, ki bi omogočile izboljšanje kinetičnih razmer rafinacijske ponovčne žlindre med postopkom sekundarne metalurgije. Eksperimenti so bili usmerjeni v primerjavo vpliva različnih gradnikov žlindre, kot so apno (CaO), briketirano talilno sredstvo in dezoksidacijsko sredstvo, ki tvori kalcijev karbid (CaC_2), in aluminij v zrnih ($\text{Al}_{\text{granul}}$). Za oceno žlindre v ponovci so bili odvzeti vzorci jekla iz različnih mest med postopkom za ugotavljanje stopnje razžvepljanja. Vzeti so bili tudi vzorci žlindre za določanje izbranih parametrov, kot so bazičnost, vsebnost oksidov, ki se jih da lahko reducirati, razmerje $\text{CaO}/\text{Al}_2\text{O}_3$ in Mannesmannov indeks. Zvezno sta bila merjena tudi temperatura in aktivnost kisika v jeklu. V članku omenjeni rezultati so osnovna informacija o možnostih optimiranja ponovčne žlindre z različnimi deleži dodatkov, ki tvorijo žlindro, briketiranih talil in dezoksidantov pri procesih sekundarne metalurgije.

Ključne besede: sekundarna metalurgija, žlindra, talilno sredstvo, jeklo, razogljčenje

1 INTRODUCTION

The ladle slag presents an important factor influencing the steel cleanliness in secondary metallurgy units. It can accelerate the reactions during a steel treatment between the slag and the metal, such as desulphurization and absorption of non-metallic inclusions. The process of forming ladle slag within secondary metallurgy depends on the quantity of the used slag-making agents (CaO and the fluxing agents based on Al_2O_3), the method of steel deoxidation, the intensity of stirring, the corrosion (wear) of the ladle lining and the quantity of the overflowing slag. A formed mixture of individual oxides represents slag, the composition of which distinctly influences its viscosity, as well as its refining abilities. During a steel treatment the chemical composition of slag is modified with other

additions of slag-making agents, and also by decreasing the contents of easily reducible oxides in order to create a sufficiently basic, liquid slag with a low melting point, contributing to an increase in metallurgical processes. One of the possibilities of fulfilling these requirements within secondary metallurgy is the optimisation of the slag mode in the ladle¹⁻³.

Slag in a ladle is a poly-componential melt whose properties are influenced by the temperature, oxygen activity in slag and in steel, and, above all, by its chemical composition. It was found in literature⁴⁻⁶ that the optimum composition of the slag for the steel deoxidised by aluminium and designated for secondary-metallurgy treatment should have the following oxide proportion: approx. 60 % CaO , 30 % Al_2O_3 , less than 6 % SiO_2 and less than 1 % FeO .

The paper relates to the works of the authors⁷⁻⁹ that focused on using the briquetted fluxing agents (based on Al_2O_3) under plant conditions. The plant experiments aimed at comparing different variants of the proportion of the slag-making agents and deoxidising agents, and at evaluating the achieved optimum chemical composition of the slag, thus enhancing the kinetic conditions of the ladle slag during the treatment in secondary metallurgy units.

2 CHARACTERISTICS OF PLANT EXPERIMENTS AND INDIVIDUAL VARIANTS

Plant experiments for optimising the slag mode were realised during the treatment of steel in the secondary metallurgy units. An evaluation of the influence of the slag-making additions, fluxing agents and the method of deoxidising the steel on the chemical compositions and refining abilities of the slags was made in the following units:

- a homogenization station – HS (blowing of argon),
- a ladle furnace – LF (heated with an electric arc).

Altogether 21 melts were realised under plant conditions, made of unalloyed structural steel S355 in various modifications, the chemical composition of which is given in **Table 1**. It should be mentioned that the plant experiments involved 3 modifications of steel S355, while different maximum contents of sulphur in the steel were required (mass fractions 0.012 % and 0.015 %).

Different variants of the experiments were proposed for creating active slag in the ladle for the treatment in secondary-metallurgy units. These variants differed not only in the used slag-making agents, but also in the

quantity of the additions charged into the ladle. Altogether four variants were proposed, in which the following additions were used: lime (CaO), calcium carbide (CaC_2), granular aluminium ($\text{Al}_{\text{granular}}$) and two types of the fluxing agent, A and B, based on Al_2O_3 . **Table 2** gives the basic characteristics of individual variants.

It follows from **Table 2** that two fluxing agents based on Al_2O_3 were chosen for the plant experiments for all the proposed variants. These fluxing agents contain the same basic components, but they differ in the contents of Al_2O_3 , CaO and in the type of the used bonding agent. **Table 3** gives their basic chemical compositions. Moreover, calcium carbide (CaC_2) was added in order to reduce the contents of easily reducible oxides in the case of a penetration of the furnace slag by the BOF. Granular aluminium ($\text{Al}_{\text{granular}}$) was used for ensuing deep deoxidation; this deoxidation agent was also added in order to reduce the influence of alloying additions and the transition of the formed oxides into the slag in the ladle. The last item is represented by two different doses of lime (CaO) that served as the basic component for the ladle slag.

During the treatment of the steel in the secondary-metallurgy units (HS and LF), the samples of the steel and slag were taken at the following technological places: in the ladle after tapping them from the basic oxygen furnace (BOF) and after their arrival to the homogenization station (sample HS_{start}), before their departure from the homogenization station to the ladle furnace (sample HS_{end}), at the beginning of the treatment in the ladle furnace (sample LF_{start}) and at the end of treatment in the ladle furnace (sample LF_{end}). In the case

Table 1: Basic chemical composition of steel S355 in mass fractions, w/%

Tabela 1: Osnovna kemijska sestava jekla S355 v masnih deležih, w/%

Grade	Range	Chemical composition (w/%)					
		C	Mn	Si	P	S	Al
S355	Min.	xxx	xxx	xxx	xxx	xxx	0.010
	Max.	0.22	1.60	0.55	0.035	0.035	0.060

Table 2: Characteristics of individual variants of industrial experiments

Tabela 2: Značilnosti posameznih variant industrijskih preskusov

Variant of experiment	Additions of slag-making agents (kg)				
	Fluxing agent A	Fluxing agent B	CaC_2	$\text{Al}_{\text{granular}}$	CaO
A	400	xxx	xxx	150	1200
B	xxx	300	100	150	1200
C	400	xxx	100	300	1200
D	xxx	300	100	200	1500

Table 3: Basic parameters of the used fluxing agents in mass fractions, w/%

Tabela 3: Osnovni parametri uporabljenih talil v masnih deležih, w/%

Type of fluxing agent	Chemical composition (w/%)					Used binder	Strength (MPa)
	Al_2O_3	CaO	MgO	Fe_2O_3	SiO_2		
Fluxing agent A	55	15	4	1.5	2	organic	8 – 15
Fluxing agent B	65	11	6	xxx	3.5	sodium silicate	8 – 15

of taking the samples of steel, an analysis of sulphur contents was made, while the analysis of the slag samples was focused on the basic types of oxides and the slag.

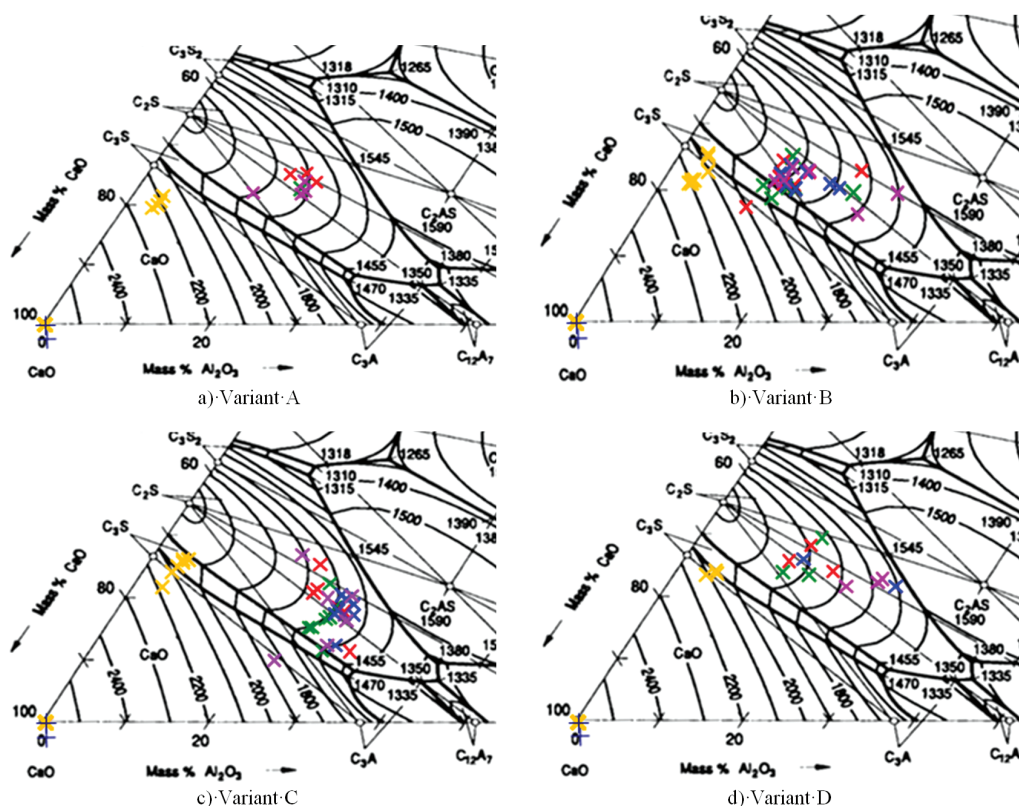
3 RESULTS DISCUSSION

An assessment of the influence of individual variants of the slag-making agents and deoxidation agents on the chemical compositions of the slags was realised in several stages. The first assessment dealt with the evolution of the chemical-composition changes in the ladle slags on the basis of analysing the samples that were taken during the treatment in two secondary-metallurgy units (HS and LF). The obtained results of the chemical-composition changes for individual variants were processed using ternary diagrams presented in **Figures 1a to 1d**^{10,11}.

It follows from the ternary diagrams for CaO-Al₂O₃-SiO₂ that, in the case of variant A (**Figure 1a**), the temperatures of the slag melting in the ladle vary during the whole treatment in the area above 1800 °C. This may be explained with the low contents of Al₂O₃, approx. 15 % of the slag, with the simultaneously increased contents of SiO₂ in the range from 18 % to 20 %, and with the content of CaO of approx. 49 %. It may be

assumed that the remelt loss of FeSi or FeSiMn, used during the tapping as an alloying addition, might have contributed to the increased contents of SiO₂. Furthermore, it follows from the ternary diagram that, in the course of the treatment, the chemical composition gets slightly modified and the ladle slags approach the boundary area of the melting temperature of 1600 °C. This phenomenon may be explained with the addition of aluminium (Al_{granular}) to the ladle furnace, when the content of easily reducible oxides was reduced.

In variant B (**Figure 1b**) a more distinct evolution of the chemical-composition changes in the slags is visible, but in this case the temperature of the melting slag also varies in the area above 1800 °C. This change may be explained with the low contents of Al₂O₃ in the slag, approx. 13 %, while the contents of SiO₂ were lower than in the previous variant, approx. 17 %, and the contents of CaO varied within the interval from 51 % to 54 %. In this case it may be stated that a lower addition of fluxing agent B had a negative impact on the quantity of Al₂O₃ in the slag, although this fluxing agent contains higher contents of Al₂O₃. However, in the case of several heats, the area of the melting temperature was achieved in the range from 1600 °C up to 1800 °C, namely, in the slags exiting the ladle furnace. This phenomenon may be explained with the additions of lime (CaO), fluxing agent



Note: yellow – BOF slag (sample LD_{end}), red – slag from the homogenization station (sample HS_{start}), green – slag from the homogenization station (sample HS_{end}), blue – slag from the ladle furnace (sample LF_{start}), violet – slag from the ladle furnace (sample LF_{end})

Figure 1: Parts of the ternary diagram for the CaO-Al₂O₃-SiO₂ composition of the ladle slag^{10,11}

Slika 1: Deli ternarnega diagrama CaO-Al₂O₃-SiO₂ sestav žilindre iz ponovce^{10,11}

B and aluminium ($\text{Al}_{\text{granular}}$), resulting in a modification of the chemical composition of the slag.

In the case of variant C (**Figure 1c**) it may be stated that the chemical composition of the slags varies, from the beginning, in the area of the melting temperatures from 1600 °C to 1800 °C. For this variant the following contents of the basic oxides were achieved: approx. 21 % of Al_2O_3 , approx. 15 % of SiO_2 and between 45 % and 50 % of CaO . In this case a positive influence of the bigger additions of fluxing agent A was clearly confirmed, as well as of a double quantity of aluminium ($\text{Al}_{\text{granular}}$) ensuring deep deoxidation. Certain heats move, however, at the boundary of the melting temperature from 1400 °C to 1800 °C. This may be explained with a gradual dissolution of individual components of the ladle slag, and also with the additions of lime (CaO), fluxing agent A and aluminium ($\text{Al}_{\text{granular}}$) to the ladle furnace, with the aim of modifying the chemical composition and creating a refining slag.

The biggest change in the chemical composition of the slags during the treatment is shown for the last variant – D (**Figure 1d**). The main part of individual components varies; however, it does so in the area of the melting temperatures above 1800 °C. This may be explained with the low contents of Al_2O_3 , approx. 13 %, and with the simultaneously increased content of SiO_2 , approx. 21 %, while CaO varies within the range from approx. 46 % up to 52 %. In this case it may be stated that the lower contents of Al_2O_3 in the slag actually represent a lower addition of fluxing agent B, added during the tapping. It may also be assumed that the remelt loss of FeSi , used during the tapping as an alloying element, as well as a possible lower addition of aluminium ($\text{Al}_{\text{granular}}$) during the tapping, contributed to the increased content of SiO_2 . It also follows from the ternary diagram that several slags exiting the ladle furnace reach a low level of the melting point, 1600 °C. This phenomenon may be explained with the additions of fluxing agent B and of aluminium ($\text{Al}_{\text{granular}}$), added to the ladle furnace in order to increase the content of Al_2O_3 in the slag and to reduce the contents of easily reducible oxides.

Apart from an evaluation of the chemical composition of the slags with the ternary diagrams, an evaluation of the achieved degrees of desulphurisation (η_s), the values of oxygen activity in the steel ($a_{[\text{O}]}$) and the basic parameters of the slags was also made. **Table 4** gives the results for the investigated parameters of the degrees of desulphurisation representing the degrees of desulphurisation for individual technological operations, which took place during the treatment of the steel.

It is evident from **Table 4** that the degrees of desulphurisation had different values for different variants. The total degree of desulphurisation ($\eta_s \Sigma$) varied within the range from approx. 49 % to 57 % (**Table 4**). This is related to the lower initial contents of sulphur in the metal, ranging from approx. 0.025 % up to 0.036 %, and to the required sulphur contents in the steel, ranging from 0.012 % and 0.015 %. It is appropriate to point out that the plant experiments were run in the heats that were not designated for a treatment in a vacuum station (RH) and that their working temperatures varied within the interval from 1572 °C up to 1582 °C.

Variant C (**Table 4**) achieves the best results for continuous desulphurisation. It may be assumed that, in this variant, a gradual dissolution of the slag-making agents takes place during individual technological operations, accompanied by a formation of a liquid refining slag, successfully participating in the steel desulphurisation (45 % to 50 % of CaO , approx. 21 % of Al_2O_3 and approx. 15 % of SiO_2). This trend is confirmed also with the results from the ternary diagram, representing the temperatures of the melting slag (**Figure 1c**).

The oxygen activity in the steel ($a_{[\text{O}]}$) that is an important thermodynamic parameter influencing the steel desulphurisation is the next monitored parameter. The values achieved for individual variants are listed in **Table 5**. It follows from these results that, at the beginning of the steel treatment in the homogenization station (HS_{start}), the oxygen activity varies between 8×10^{-6} to approx. 10×10^{-6} . A decrease in the oxygen activity occurs due to the subsequent treatment in the homogenization station (HS) and the ladle furnace (LF) ranging from approx. 2.5×10^{-6} to 3.0×10^{-6} , as determined in the ladle furnace at the end of the treatment (LF_{end}). This decrease is different for individual variants and the difference in the oxygen-activity decrease is caused by different quantities of deoxidation agents including

Table 4: Degree of desulphurisation during the treatment of steel in secondary metallurgy

Tabela 4: Stopnja razžvepljanja med obdelavo jekla s postopkom sekundarne metalurgije

Variant of experiment	Degree of desulphurisation during the treatment of steel (%)				
	η_s LD	η_s HS	η_s LADLE	η_s LF	$\eta_s \Sigma$
A	27.54	xxx	xxx	16.58	56.72
B	13.79	5.53	18.57	26.65	50.97
C	17.07	12.09	15.99	29.91	55.97
D	11.57	4.63	4.91	37.15	49.47

Note: η_s – degree of desulphurisation: $\eta_s = [\text{S}_{\text{start}}] - [\text{S}_{\text{end}}] / [\text{S}_{\text{start}}] \cdot 100$, η_s LD – degree of desulphurisation during the tapping from the LD converter, η_s HS – degree of desulphurisation in the homogenization station, η_s LADLE – degree of desulphurisation in the ladle during the transport between HS and LF, η_s LF – degree of desulphurisation in the ladle furnace, $\eta_s \Sigma$ – overall degree of desulphurisation

calcium carbide (CaC_2) and granular aluminium ($\text{Al}_{\text{granular}}$).

The best results for the continuous decrease in the oxygen activity were achieved for variant C (**Table 5**). In this variant, an increased addition of granular aluminium ($\text{Al}_{\text{granular}}$) was positive, ensuring deep deoxidation of the steel. Apart from this deoxidation agent, calcium carbide (CaC_2) was also used, dissolving gradually and supporting the next decrease in the oxygen activity and easily reducible oxides during the steel treatment in the homogenization station ($\text{HS}_{\text{start}} - \text{HS}_{\text{end}}$) and the transport of the ladle with steel to the ladle furnace (LF_{start}).

Table 5: Monitored parameter of steel – oxygen activity in steel

Tabela 5: Prikaz parametrov aktivnosti kisika v jeklu

Variant of experiment	Oxygen activity in steel – a_{O}/ppm			
	HS_{start}	HS_{end}	LF_{start}	LF_{end}
A	xxx	3.50	xxx	2.75
B	8.38	6.75	6.13	2.67
C	10.29	4.14	3.14	2.86
D	10.33	9.00	6.33	2.67

Apart from the degree of desulphurisation and oxygen activity, an evaluation of the investigated parameters of the slags was also made. The results are presented in **Table 6** showing the basicity, the content of easily reducible oxides, the proportion of $\text{CaO}/\text{Al}_2\text{O}_3$ and the Mannesmann index.

It is clear from the comparison of individual basicity values B1 (**Table 6**) that variants A and D may be included into the group of medium basicity, and variants B and C belong to the group of strongly basic slags. The achieved values are related to the contents of CaO and SiO_2 . The resulting degrees of desulphurisation

($\eta_s \Sigma$) for individual variants cannot be, however, substantiated only on the grounds of basicity. This is why an evaluation of the other parameters was also started.

The content of easily reducible oxides was investigated for the ladle slags (**Table 6**). In this case significantly higher contents were determined for variants B, C and D. These higher contents prove that the furnace slag penetrated into the ladle at the end of the tapping. An addition of calcium carbide (CaC_2) to variants B, C and D was manifested with a gradual reduction of these oxides during its dissolution. This process was supported in the ladle furnace by the additions of aluminium ($\text{Al}_{\text{granular}}$). It may be presumed that a certain quantity of easily reducible oxides is created due to a partial deoxidation and the alloying of the steel.

In the case of the calcium-aluminous proportion it is evident that all the variants (**Table 6**) achieve the values exceeding the optimum for this parameter (approx. 2.0 to 2.5). Variant C achieves the most stable values, as this parameter varies within the range of approx. 2.1 to 2.5. In the case of variant A, this proportion varies within the range of approx. 3.1 to 3.4, which is caused by the low contents of Al_2O_3 in the slag, approx. 15 %. At the beginning of the experiment, variants B and D achieved the values >4 , which is again confirmed with the low contents of Al_2O_3 in the slag, approx. 12 %. Later, the values for these variants decrease during the treatment, which is caused by the gradual dissolution of fluxing agent B and aluminium additions ($\text{Al}_{\text{granular}}$), while only variant D approached the optimum value.

The last investigated parameter was the Mannesmann index (**Table 6**), the optimum value of which varies within the range from 0.15 to 0.30. It follows from the

Table 6: Investigated parameters of the slags during the secondary-metallurgy treatment of steel

Tabela 6: Preiskovani parametri v žlindri med obdelavo jekla s postopki sekundarne metalurgije

Variant of experiment	Place of taking the sample	Basic parameters of the ladle slags			
		B1	ERO	C/A	MM
A	HS_{start}	2.30	2.91	3.15	0.15
	HS_{end}	2.56	4.72	3.07	0.17
	LF_{start}	xxx	xxx	xxx	xxx
	LF_{end}	2.64	1.32	3.45	0.18
B	HS_{start}	2.97	8.77	4.51	0.26
	HS_{end}	3.09	5.56	4.41	0.25
	LF_{start}	2.89	4.44	4.0	0.22
	LF_{end}	2.93	1.75	3.73	0.21
C	HS_{start}	3.14	9.62	2.38	0.16
	HS_{end}	3.68	3.39	2.40	0.18
	LF_{start}	3.23	2.42	2.13	0.14
	LF_{end}	3.70	2.17	2.47	0.18
D	HS_{start}	2.29	14.27	4.25	0.21
	HS_{end}	2.39	7.01	4.40	0.20
	LF_{start}	2.34	5.70	3.20	0.15
	LF_{end}	2.44	1.85	2.37	0.12

Note: B1 – basicity: $\text{B1} = (\text{CaO})/(\text{SiO}_2)$, ERO – content of easily reducible oxides: $\text{ERO} = (\text{FeO}) + (\text{Fe}_2\text{O}_3) + (\text{MnO}) + (\text{Cr}_2\text{O}_3) + (\text{V}_2\text{O}_5) + (\text{P}_2\text{O}_5)$, C/A – proportion: $\text{C/A} = (\text{CaO})/(\text{Al}_2\text{O}_3)$, MM – Mannesmann index: $\text{MM} = ((\text{CaO})/(\text{SiO}_2))/(\text{Al}_2\text{O}_3)$

results that in variants A and C, it slightly increases, which is caused by the gradual dissolution of fluxing agent A and aluminium additions ($Al_{granular}$) used to reduce the easily reducible oxides, accompanied by the formation of Al_2O_3 in the slag. The achieved values vary in the range from approx. 0.15 to 0.18, corresponding to the lower degrees of desulphurisation of 57 % and 56 %. However, in the remaining variants, B and D, the values decrease in the course of treatment, which is caused by the increasing contents of Al_2O_3 in the slag. This increase is caused by important additions of fluxing agent B containing Al_2O_3 and aluminium ($Al_{granular}$), used to reduce the easily reducible oxides. As a result of this increase, the values of the MM index decrease, which is manifested by the achieved degrees of desulphurisation, 51 % and 49 %.

4 CONCLUSIONS

Experiments were made under plant conditions to obtain relevant information about the behaviour and influence of fluxing agents A and B, as well as the additions of calcium carbide (CaC_2) and aluminium ($Al_{granular}$) on the chemical compositions of the ladle slags. It is possible to draw the following conclusions from the obtained results:

- it follows from the ternary diagrams for $CaO-Al_2O_3-SiO_2$ that variant C approached the optimum composition of the slag according to the findings from the literature, in which the following contents were achieved: 45 % to 50 % of CaO , approx. 21 % of Al_2O_3 and approx. 15 % of SiO_2 ;
- the lowest areas of the melting temperatures of the ladle slags were achieved with variant C, namely, within the range from 1600 °C to 1800 °C, while some heats varied around the boundary of the melting temperature of 1400 °C;
- it follows from the results for desulphurisation degree that variant C approached the optimum formation of the liquid refining slag, participating in desulphurisation during individual technological operations;

- it follows from the achieved values for the oxygen activity that a higher quantity of deoxidation agents was positively reflected in the lower values of the oxygen activity in the beginning phases of the steel treatment in the homogenization station and ladle furnace;
- to ensure deep desulphurisation of the steel by applying aluminium ($Al_{granular}$) during the tapping, the remelt loss of the alloying additions of $FeSi$ and $FeSiMn$ was reduced, which was manifested with the lower contents of SiO_2 in the ladle slag;
- in the next stage of our research the attention will be focused on confirming these results by producing different steel grades.

Acknowledgements

The work was carried out with the support of the Czech Ministry of Industry and Trade within the frame of the program MPO-TIP and the projects with the reg. No. FR-TI2/319 and reg. No. FR-TI1/240.

5 REFERENCES

- ¹ A. Ghost, A. Chatterjee, *Ironmaking and Steelmaking: Theory and Practice*, 1st ed., PHI Learning Private limited, 2008, 472
- ² R. J. Fruehan et al., *The Making, Shaping and Treating of Steel*, 11th edition, AISE Steel Foundation, Pittsburgh 2010, 768
- ³ R. Dudek, L. Dobrovský, J. Dobrovská, *Metallurgija*, 48 (2009) 4, 239–242
- ⁴ E. Kawecka-Cebula, *Metallurgy and Foundry Engineering*, 22 (1996) 3, 169–182
- ⁵ E. Kawecka-Cebula, Z. Kalicka, J. Iwanciw, *Metallurgy and Foundry Engineering*, 22 (1996) 4, 267–280
- ⁶ K. Michalek, L. Čamek, Z. Piega et al., *Archives of Metallurgy and Materials*, 55 (2010) 4, 1159–1165
- ⁷ L. Socha, J. Bažan, P. Machovcak et al., *Hutnické listy*, 65 (2012), 8–13
- ⁸ L. Socha, J. Bažan, K. Gryc et al., *Conference on Metallurgy and Materials: Metal 2011*, 2011, 163–169
- ⁹ L. Socha, J. Bažan, K. Gryc et al., *Hutnik - Wiadomości Hutnicze*, (2011) 9, 772–774
- ¹⁰ M. Allibert et al., *Slag atlas*, 2nd edition, Verein Stahleisen GmbH, Düsseldorf 1995, 616
- ¹¹ K. Gryc, K. Stránský, K. Michalek et al., *Mater. Tehnol.*, 46 (2012) 4, 403–406

STUDY ON THE MECHANICAL AND RADIATION-SHIELDING PROPERTIES OF BORIDED AISI 304 STAINLESS STEELS

ŠTUDIJA MEHANSKIH LASTNOSTI IN ZAŠČITNIH SPOSOBNOSTI NERJAVNEGA JEKLA AISI 304 PRED SEVANJEM

Adnan Çalik¹, Serdar Karakaş¹, Nazım Uçar², İskender Akkurt², Adem Turhan¹

¹Manufacturing Engineering Department, Faculty of Technology, Suleyman Demirel University, Isparta, Turkey

²Department of Physics, Arts and Science Faculty, Suleyman Demirel University, Isparta, Turkey
nazmucar@yahoo.com

Prejem rokopisa – received: 2012-12-03; sprejem za objavo – accepted for publication: 2013-01-31

The boriding effect on the tensile properties, microhardness and radiation shielding has been studied. While boriding increased the hardness of the AISI 304 steel from 240 HV_{0.1} to the maximum value of 1 740 HV_{0.1}, the elongation and the maximum stress clearly showed decreasing values. Borided specimens were more capable at stopping the high-energy photons and boriding improved the radiation-shielding properties of the AISI 304 steel. From the obtained results, it has been concluded that the borided AISI 304 stainless steel can be used as radiation shielding for γ -rays.

Keywords: boriding, radiation shielding, mechanical properties, stainless steel

Preučevan je bil učinek boriranja na natezne lastnosti, mikrotvrdoto in zaščito pred sevanjem. Medtem ko boriranje poveča trdoto jekla AISI 304 iz 240 HV_{0.1} na maksimalno 1740 HV_{0.1}, raztezek in maksimalna napetost izkazujejo padajoče vrednosti. Borirani vzorci so bolj odporni proti zaustavljanju visokoenergijskih protonov. Boriranje jekla AISI 304 poveča zaščito pred sevanjem. Iz dobljenih rezultatov lahko sklenemo, da je jeklo AISI 304 mogoče uporabiti za zaščito pred sevanjem rentgenskih žarkov.

Ključne besede: boriranje, zaščita pred sevanjem, mehanske lastnosti, nerjavno jeklo

1 INTRODUCTION

Austenitic stainless steels have high chromium contents and are commonly used as engineering materials.^{1,2} Considering their use as engineering materials, the main problem with austenitic stainless steels is their relatively poor wear resistance, yield strength, fracture and impact toughness.^{3,4} In recent years, extensive studies have been carried out on the improvement of the mechanical properties of these materials. Stainless steels are found to be well suited and established for surface treatments such as nitriding and boriding.⁵ One of the surface-treatment techniques is boriding, a thermo-chemical surface treatment in which boron atoms diffuse into the surface of the work piece to form hard borides with the base material.⁶⁻⁹ Corresponding to this, Tabur et al.¹⁰ showed that the borided steels exhibit a surface hardness of over 2000 HV and provide an improved abrasive and adhesive wear resistance due to the hard boride phases and a diffusion of boron into the steel substrate, respectively.

In addition to the microhardness studies, it has been shown that tensile properties change with boriding due to a surface modification as expected when considering a plastic deformation of materials. Corresponding to this, it has been shown that the Young's modulus increases with an increase in the boriding processing time.¹¹ The increase in the boriding time from 2 to 6 h causes an increase in Young's modulus from 125 GPa to 241 GPa,

from 240 GPa to 396 GPa and from 276 GPa to 397 GPa. Finally, according to the mechanical investigation, the optimum mechanical properties were obtained after 2 h of the boriding processing time. One can understand that the mechanical properties change with boriding due to a surface modification as expected when considering a plastic deformation of materials.

In recent years, boron has been used as an alternative for radiation shielding, although heavy metals such as lead have been used for this purpose.¹²⁻¹⁴ According to¹⁴, the borided AISI 316L and microalloyed stainless steels, especially in the middle energy region, have radiation shielding properties that are similar to those of lead, the standard shielding material. In the above-mentioned studies, the linear attenuation coefficients of steel were measured at photon energies of (662, 1170 and 1332) keV. It was clearly seen that the radiation shielding properties of steel were improved with a boriding process. Over the past 40 years, boriding has become an increasingly better surface-protection method. Thus, most of the previously reported experimental studies of borided steels have been devoted to mechanical properties. No study on the radiation shielding of borided AISI 304 stainless steels has been reported in the literature. The main goal of this study is to investigate the radiation-shielding properties of borided AISI 304 stainless steels.

2 EXPERIMENTAL METHODS

The substrates used for this study were the AISI 304 stainless steels. The chemical composition of the test material is listed in **Table 1**.

The boriding of the AISI 304 steels was achieved in a solid medium using the powder-pack method. In this method, a commercial Ekabor-III boron source and an activator (ferro-silicon) were thoroughly mixed to form the boriding medium. The test samples and pack were then heated in an electric resistance furnace for 3 h at 1200 K under atmospheric pressure. After this process, the borided samples were removed from the furnace and cooled in air. Borided steels were sectioned from one side and prepared metallographically with emery paper up to 1200-grit and then polished, using alumina pastes 3 μm . The surfaces of the polished samples were etched with 4 % Nital before the tests. The thicknesses of the diffusion layers of borided AISI 304 steels were observed with optical microscopy.

Borided steels were tested for tension with a universal tester with a capacity of 5 kN and a gauge length of 11 mm. The hardness measurements were made using a Vickers microhardness tester with a load of 100 g. Finally, to investigate the radiation-shielding properties of borided AISI 304 steels, the linear attenuation coefficients (μ) of steel were measured before and after boriding the steel at photon energies of 662 keV and 1250 keV obtained from ^{137}Cs and ^{60}Co γ -ray sources, respectively. For this purpose, the γ -rays through the steel were detected using a gamma spectrometer that consists of an approximately 76 mm \times 76 mm NaI(Tl) detector connected to a multichannel analyzer (MCA). The detector system communicates with a PC using the Genie 200 software. If N and N_0 are the measured count rates in the detector with and without an absorber of thickness x (cm), respectively, then the absorption coefficient μ can be extracted with the standard equation:

$$N = N_0 e^{-\mu x}$$

The slope of the $\ln(N/N_0)$ versus x plot gives μ . Further experimental details were described in¹⁵.

3 RESULTS AND DISCUSSION

As seen in **Figure 1**, optical examinations revealed that the boride layer on the surface of the steel has a columnar morphology due to many alloying elements in the AISI 304 stainless steel.

The boride-layer thickness varied between 15 μm and 20 μm . In other words, the rate of the boron diffusion into the surface of a substrate was low. The thickness of

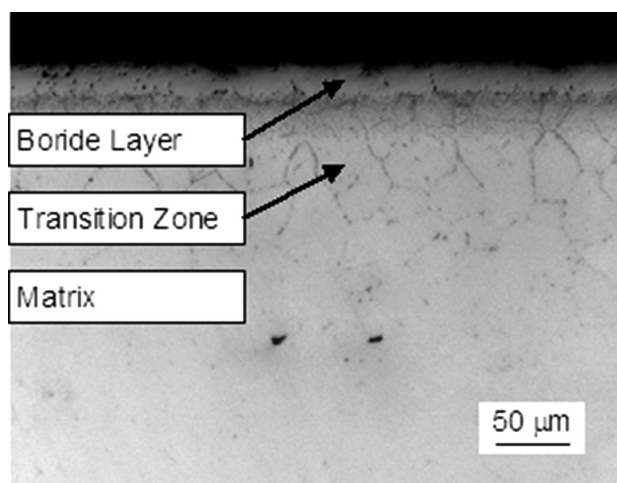


Figure 1: Optical micrograph of a cross-section of the borided AISI 304 stainless steel

Slika 1: Posnetek prečnega prereza boriranega nerjavnega jekla AISI 304

the transition region was also very small (the average of 100 μm) and the grain growth was not introduced in the transition regions of borided steels. This is because boron does not dissolve significantly in the boride layer during the boriding.

To compare the mechanical properties of borided and untreated AISI 304 stainless steels, elongation and microhardness tests were performed on the samples. While the microhardness values in the matrix varied between 241 $\text{HV}_{0.1}$ and 285 $\text{HV}_{0.1}$, they reached 1099–1123 $\text{HV}_{0.1}$ and 1650–1740 $\text{HV}_{0.1}$ in the transition zone and the boride layer, respectively. We say that the

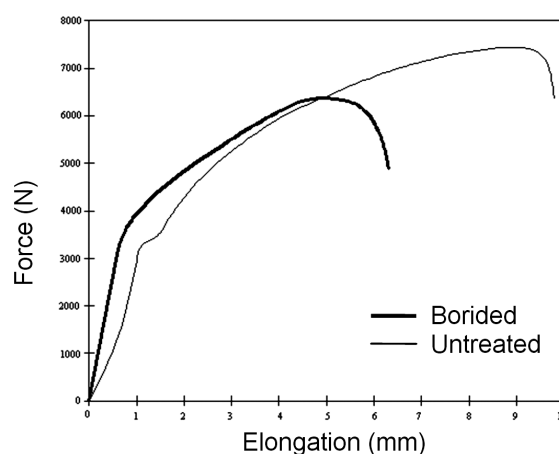


Figure 2: Load-elongation curve of borided and untreated AISI 304 stainless steels

Slika 2: Krivulja sila – raztezek boriranega in neobdelanega nerjavnega jekla AISI 304

Table 1: Chemical composition of the AISI 304 stainless steel (w/%)

Tabela 1: Kemijska sestava nerjavnega jekla AISI 304 (w/%)

C	Ni	Cr	Mn	P	S	Si	Cu	Mo	Nb	Fe
0.044	8.03	18.26	1.5	0.032	0.0003	0.47	0.38	0.38	0.022	Bal.

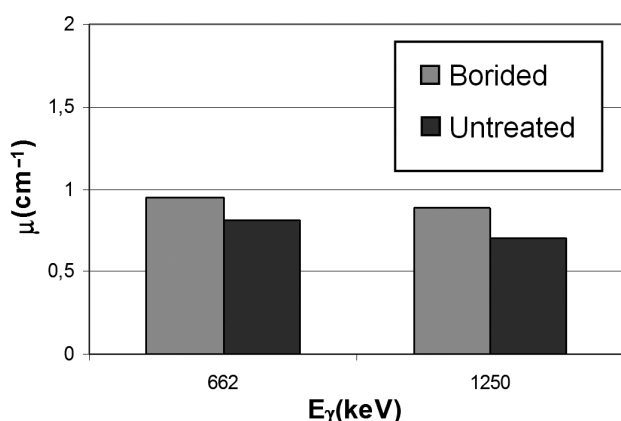


Figure 3: Linear-attenuation coefficients for borided and untreated AISI 304 stainless steels

Slika 3: Linearni koeficient slabljenja pri boriranem in neobdelanem nerjavnem jeklu AISI 304

microhardness values of the boride layer are higher than those of the matrix because of the presence of a hard Fe_2B phase. Meanwhile, a high microhardness value is mainly due to the mono phase (Fe_2B) in the boride layer.

In addition to the microhardness results, boriding also affects the tensile properties of AISI 304 steels. It can be seen on **Figure 2** that there is a minor increase in the yield stress in the borided steels in comparison with the untreated ones. In general, it has been indicated that the boriding process increases the yield stress due to a surface modification, as obtained from the microhardness results.^{16,17} In the present study, it is evident from this figure that both the maximum stress and elongation are decreased drastically by a factor close to 15 % and 25 %, respectively. On the basis of these results, we can say that the microstructure has become very coarse occurring in a brittle mode after the boriding. The same results have been also obtained for many other borided steels.^{11,18,19}

Now let us consider the radiation-shielding properties of borided AISI 304 stainless steels. The linear attenuation coefficients (μ) of the steel were measured at photon energies of 662 keV and 1250 keV obtained from ^{137}Cs and ^{60}Co γ -ray sources, respectively. This measurement was performed before and after the boriding. This is shown in **Figure 3** where it can be clearly seen that the boriding processes increased the linear attenuation coefficients. We say that borided AISI 304 stainless steels can be used as radiation shielding in many industrial applications. However, the increase in micrometers with the boriding is limited due to a small diffusion layer of the borided AISI 304 stainless steel. By comparing the experimental results obtained with the present study with

the results for the borided AISI 316L¹⁴ and microalloyed stainless steels,²⁰ we can say that in our case the increase in micrometers is smaller than in the other cases. From these results, we also concluded that a thicker boride layer is needed to stop higher energy photons and that the boriding improved the radiation-shielding capability of the steel. It has to be remembered that the increasing temperature and time increase the boride-layer thickness of borided steels resulting in an excellent radiation-shielding performance.

4 CONCLUSIONS

To sum up, the maximum stress and elongation clearly showed a decrease, while the yield stress displayed a slight increase. In addition, the microhardness and linear-attenuation coefficient increased because of the hard boride phases in the boride layer and the boride-layer thickness.

5 REFERENCES

- M. C. M. Farias, R. M. Souza, A. Sinatora, D. K. Tanaka, *Wear*, 263 (2007), 111
- U. Sen, S. Sen, *Mater. Character.*, 50 (2003), 261
- P. A. Dearnley, G. Aldrich-Schmith, *Wear*, 256 (2004), 491
- L. Shi, D. O. Northwood, *Acta Mater.*, 43 (1995), 453
- S. Taktak, *J. Mater. Sci.*, 41 (2006), 7590
- A. Ozsoy, Y. M. Yaman, *Scr. Metall. Mater.*, 29 (1993), 231
- N. E. Maragoudakis, G. Stergioudis, H. Omar, H. Paulidou, D. N. Tsipas, *Mater. Lett.*, 53 (2002), 406
- R. H. Biddulph, *Thin Solid Films*, 45 (1977), 341
- M. Carbuicchio, L. Bardani, G. P. Palombarini, *J. Mater. Sci.*, 15 (2007), 711
- M. Tabur, M. Izciler, F. Gul, I. Karacan, *Wear*, 266 (2009), 1106
- O. Culha, M. Toparli, T. Aksoy, *Adv. Eng. Softw.*, 40 (2009), 1140
- J. E. Martin, *Physics for Radiation Protection: A Handbook*, 2nd ed., Wiley, 2008, 660–661
- N. E. Hertel, Georgia Tech Project No. 25066KY, Nuclear and Radiological Engineering Program, G. W. Woodruff School of Mechanical Engineering, Georgia Institute of Technology, Atlanta, 2007
- I. Akkurt, A. Calik, H. Akyildirim, *Nuclear Engineering and Design*, 241 (2011), 55
- S. Akbunar, MSc thesis, Suleyman Demirel University, 2008
- M. Bektes, A. Calik, N. Ucar, M. Keddari, *Mater. Characterization*, 233 (2010)
- A. Calik, O. Sahin, N. Ucar, *Acta Phys. Polonica A*, 115 (2009), 694
- A. Calik, O. Sahin, N. Ucar, *Z. Naturforsch.*, 63a (2008), 1
- P. Novak, V. Filip, A. Michalcova, *Metal*, Brno, Czech Republic, 2012
- I. Akkurt, H. Akyildirim, A. Calik, O. B. Aytar, N. Ucar, *Arab. J. Sci. Eng.*, 36 (2011), 145

